UNIVERSITÀ DEGLI STUDI DI NAPOLI FEDERICO II

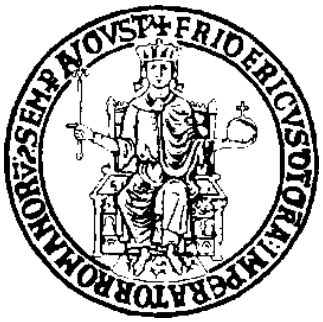

SCUOLA POLITECNICA E DELLE SCIENZE DI BASE

Department of Industrial Engineering

DOCTORAL THESIS

DECARBONIZING MARINE SECTOR THROUGH ADVANCED COMBUSTION STRATEGIES AND ALTERNATIVE FUELS: A CFD-BASED INVESTIGATION

Tutor
Prof. Maria Cristina Cameretti
Prof. Roberta De Robbio

Ph.D. Candidate
Marco Palomba

Ph.D. School Coordinator
Prof. Michele Grassi

XXXVIII CYCLE

Index

Index of figures

Index of tables

Nomenclature

AFR	Air-to-Fuel Ratio
ATDC	After Top Dead Centre
BESS	Battery Energy Storage System
BMEP	Brake Mean Effective Pressure
BSFC	Brake Specific Fuel Consumption
BTDC	Before Top Dead Centre
BTE	Brake Thermal Efficiency
CCS	Carbon Capture and Storage
CFD	Computational Fluid Dynamics
CFL	Courant–Friedrichs–Lewy
CHP	Combined Heat and Power
CI	Compression Ignition
CR	Compression Ratio
DF	Dual Fuel
DMC	Discrete Multi-Component
DOI	Duration of Injection
ECA	Emission Control Area
EDM	Eddy Dissipation Model
EGR	Exhaust Gas Recirculation
EVC	Exhaust Valve Closing
EVO	Exhaust Valve Opening
FDM	Finite Difference Method
FEM	Finite Element Method
FMEP	Friction Mean Effective Pressure
FVM	Finite Volume Method
GHG	Greenhouse Gas
HPDI	High-Pressure Direct Injection
HR	Heat Release
HRF	High-Reactivity Fuel
HRSG	Heat Recovery Steam Generator
HT-PEMFC	High Temperature-Proton Exchange Membrane Fuel Cell
ICE	Internal Combustion Engine

IMO	International Maritime Organization
IMEP	Indicated Mean Effective Pressure
IVC	Inlet Valve Closing
IVO	Inlet Valve Opening
KH	Kelvin-Helmholtz
LES	Large Eddy Simulation
LFS	Laminar Flame Speed
LHV	Lower Heating Value
LNG	Liquefied Natural Gas
LRF	Low-Reactivity Fuel
MC	Main Chamber
PC	Pre-Chamber
PID	Proportional–Integral–Derivative
PM	Particulate Matter
PSA	Pressure Swing Adsorption
RANS	Reynolds-Averaged Navier–Stokes
RCCI	Reactivity-Controlled Compression Ignition
RNG	Renormalization Group
ROHR	Rate Of Heat Release
RT	Rayleigh-Taylor
SCR	Selective Catalytic Reduction
SI	Spark Ignition
SOC	State of Charge
SOI	Start of Injection
SMR	Steam Methane Reforming
ST	Spark Timing
TDC	Top Dead Centre
TFS	Turbulent Flame Speed
TKE	Turbulent Kinetic Energy
TKI	Turbulent-Kinetics Interaction
UHC	Unburned Hydrocarbons

Greek Symbols

α	Air-To Fuel Ratio
α_S	Parameters Function of the Equivalence Ratio
α_{st}	Stoichiometric Air-to Fuel Ratio
β_S	Parameters Function of the Equivalence Ratio
Γ	Turbulent Stress
Δ	Variation
δ	Flame Thickness
ε	Dissipation Rate
ε_u	Empirical Coefficient accounting that only a Portion of the Fuel Cell's Generated Heat is Recoverable
$\varepsilon_{FC/SMR}$	Efficiency of the Natural Gas to Hydrogen Conversion System
η_{FC}	Efficiency of the Fuel Cell
$\eta_{FC/SMR}$	Efficiency of the Fuel Cell and Methane Reformer System
η_{ICE}	Efficiency of the ICE
η_{gl}	Overall Electrical Efficiency
θ	Variable Within the Control Volume
κ	Correlation Factor Defined by Ra and Reitz
$\tilde{\kappa}$	Favre Mean Flame Front Curvature
ρ	Density of the Fluid
ρ_b	Density of the Burned Mixture
ρ_k	Density and Internal Energy of The Mixture inside The Kernel
ρ_L	Liquid Density
ρ_u	Density of the Unburned Mixture
Λ_{KH}	Wavelength of the Fastest-Growing Mode of KH Breakup
Λ_{RT}	Wavelength of the Fastest-Growing Mode of RT Breakup
λ	Excess Air Ratio
λ_{th}	Thermal Conductivity
μ	Dynamic Viscosity
μ_l	Liquid Viscosity
μ_t	Turbulent Viscosity
σ	Viscous Forces

σ_ε	Turbulent Prandtl Number for ε
σ_k	Turbulent Prandtl Number for k
Σ	Surface Tension
τ_{chem}	Chemical Time Scale
τ_{mix}	Turbulent Scalar Mixing Time Scale
τ_{KH}	Breakup Time Scale of KH Breakup
τ_{RT}	Breakup Time Scale of RT Breakup
υ	Kinematic Viscosity
ϕ	Equivalence Ratio
Ω_{KH}	Growth Rate of the Fastest Wave Growing on the Surface of the Droplet of KH Breakup
Ω_{RT}	Growth Rate of the Fastest Wave Growing on the Surface of the Droplet of RT Breakup
ω	Dissipation Rate
$\dot{\omega}_i$	Rate of Production or Consumption of Species k per Unit Volume due to Chemical Reactions

Latin Symbols

A	Boundary of the Volume
A_{cf}	1D Model User Input
A_L	Laminar Flame Area
A_T	Turbulent Flame Area
B_{cf}	1D Model User Input
B_{KH}	Size Constant of KH Breakup
B_M	Spalding Number
B_{RT}	Size Constant of RT Breakup
C	Courant Number
$C_{1\varepsilon}$	RNG k–ε Model Constant
$C_{2\varepsilon}$	RNG k–ε Model Constant
C_μ	RNG k–ε Model Constant
C_{cf}	1D Model User Input
C_{KH}	Time Constant of KH Breakup

$\bar{C}_p$	Average Specific Heat of the Gas Mixture Including Fuel Vapor
C_{PL}	Liquid Specific Heat at Constant Pressure
C_{RT}	Time Constant of RT Breakup
c_1	Dimensionless Function of the Mean Piston Speed
c_2	Dimensionless Function of the Mean Piston Speed
Da	Damköhler Number
D	Initial Droplet Diameter
$D_{species}$	Diffusion Species of Fuel Species
$D_{i,m}$	Mass Diffusion Coefficient
$D_{i,T}$	Thermal Diffusion Coefficient
D_T	Turbulent Diffusivity
E_{oc}	Open Circuit Voltage
E_n	Nerst Potential
F	Faraday Constant
$\vec{F}$	External Body Forces
G	Scalar G
G_k	Production of TKE due to Velocity Gradients
$\vec{g}$	Gravitational Body Force
g_m	The Mass Transfer Coefficient
$h_{i,eff}$	Heat Transfer Coefficient inside the Droplet
h_u	Enthalpy of the Unburned Mixture
I	Specific Internal Energy
I_c	Discharge Current
I_d	Charge Currents
I_u	Fuel Utilization Index
i_0	Exchange Current Density
J	Total Heat Flux
J_i	Diffusive Flux of Species k
K	Stretch Rate
K_c	Nominal Cell Voltage Coefficient
Ka	Karlovitz Number
k	Turbulent Kinetic Energy

k_{mol}	Molecular Thermal Conductivity
k_{Pl}	Planck's Constant
k_t	Turbulent Thermal Conductivity
L	Characteristic Length for a Given Geometry
$L(T_S)$	Latent Heat of the Fuel at the Surface
L_b	Markstein Length
LHV_{H_2}	LHV of Hydrogen
LHV_{NG}	LHV of Natural Gas
LHV_{pf}	LHV of the Primary Fuel
LHV_{sf}	LHV of the Secondary Fuel
$\bar{M}$	Molar Mass of the Gas Mixture
$\dot{m}$	Mass Flow Rate
$\dot{m}_f$	Vaporization Rate of The Droplet
$\dot{m}_{H_2}$	Flow Rate of Hydrogen
$\dot{m}_{ICE}$	Engine Mass Flow Rate
$\dot{m}_{NG}$	Flow Rate of Natural Gas
m_{pf}	Mass of the Primary Fuel
m_{sf}	Mass of the Secondary Fuel
$\dot{m}_{SMR}$	Flow Rate of Natural Gas Entering The SMR
n	Engine Speed
Nu	Nusselt Number
P_{aux}	Power from the Auxiliaries
P_{el_FC}	Electric Power of the FC
P_{el_ICE}	Electric Power of the ICE
p	Fluid Pressure
p_0	Pressure at Standard Conditions
p_{H2}	Partial Pressure of Hydrogen
p_{max}	Maximum In-Cylinder Pressure
p_{mot}	Motored In-Cylinder Pressure
p_{O2}	Partial Pressure of Oxygen
p_r	Reference Pressure
p_u	Pressure of the Unburned Mixture

$\dot{Q}^c$	Source Term due to Chemical Heat Release
$\dot{Q}^s$	Source Term due to Spray Interactions
Q_{cf}	1D Model User Input
$\dot{Q}_{FC}$	Fuel Cell Thermal Power
$\dot{Q}_L$	Thermal Power Entering the Droplet
$\dot{Q}_{spk}$	Electrical Energy Discharge Rate
$\dot{Q}_U$	Thermal Output
q_0	Heat Transfer occurring from the Outer Gas to The Surface
q_i	Heat Transfer occurring from the Inside of the Droplet to the Surface
q_W	Wall Heat Flux
R	Specific Gas Constant
R_{add}	Additional Term Derived from the RNG Theory to Account for the Interaction between Dissipation and Mean Strain
R_i	Mass Rate of Creation or Depletion of Chemical Species i by Chemical Reaction
$R_{i,k}$	Reaction Rate
R_u	Universal Gas Constant
Re	Reynolds Number
r_c	Radius of Child Droplet
r_P	Radius of Parent Droplet
Sc_t	Schmidt Number
S_i	Rate of Creation by Addition from the Dispersed Phase
S_L	Laminar Flame Speed
S_{L0}	Laminar Flame Speed at Standard Conditions
S_m	Mass Added to the Continuous Phase from a Dispersed Phase
S_{plasma}	Plasma Flame Speed
S_T	Turbulent Flame Speed
Sh	Sherwood Number
T	Fluid Temperature
T_0	Temperature at Standard Conditions
T_{FC}	Fuel Cell Temperature.
T_d	Droplet Inlet Temperature

T_g	Gas Temperature Near the Wall
T_r	Reference Temperature
T_S	Droplet Surface Temperature
T_{sur}	Surrounding Gas Temperature
T_u	Temperature of the Unburned Mixture
T_w	Wall Temperature
s	Engine Stroke
t	Time
t_η	Characteristic Time of Micro-Vortices
t_t	Characteristic Time of Turbulence of Macro-Vortices
U	Internal Energy
u	Velocity
u_k	Internal Energy of the Mixture inside the Kernel
V	Control Volume
V_a	Activation Voltage Drop
V_{batt}	Total Output Voltage of the Battery Pack
V_{cell}	Actual Voltage of a Single Cell in the Stack
V_D	Cylinder Displacement
V_{drop}	Drop Voltage due to the Internal Resistance
V_r	Reference Volume
v_c	Characteristic Velocity of the Piston
v_m	Mean Piston Speed
x_r	Percentage of Inert in Unburned Mixture
$Y_{F,s}$	Fuel Mass Fraction at the Droplet Surface
$Y_{F,\infty}$	Fuel Mass Fraction far away from the Droplet Surface
Y_i	Mass Fraction of Species i
$Y_{k,eq}$	Equilibrium Mass Fraction of Species k
y_{F0}	Mass Fractions of Fuel at the Interface
y_{FSur}	Mass Fractions of Fuel far away the Droplet

Introduction

The maritime sector represents the backbone of global trade, with approximately 70% of the world's goods transported by sea [1], as illustrated in Figure 1. However, the steady growth of international shipping has made its contribution to greenhouse gas (GHG) emissions and air pollution increasingly significant.

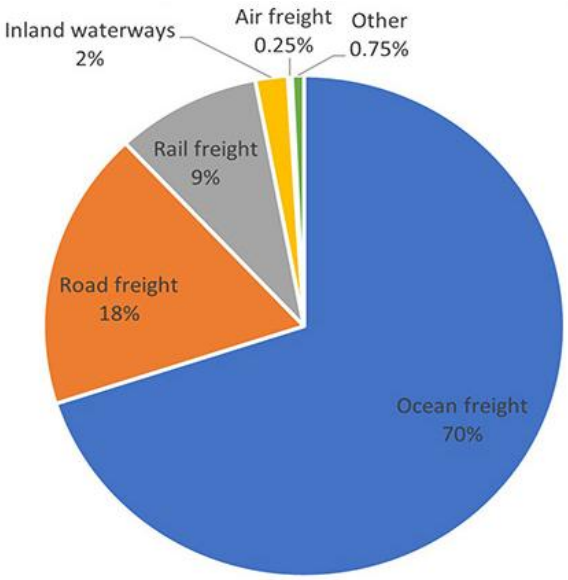

Figure 1: Global freight transport by mode of transport

Currently, marine CO_2 emissions account for about 11% of the total emissions from the transport sector (Figure 2). Moreover, among the various maritime activities, the transportation sector is the second-largest source of emissions after offshore oil operations (Figure 3).

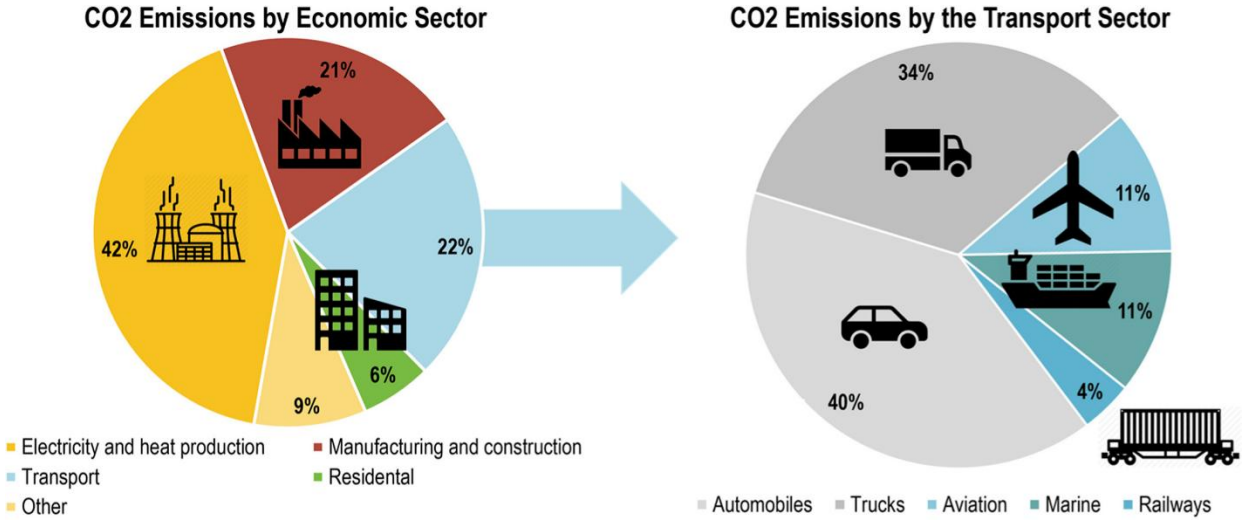

Figure 2: CO_2 distribution by sector [2]

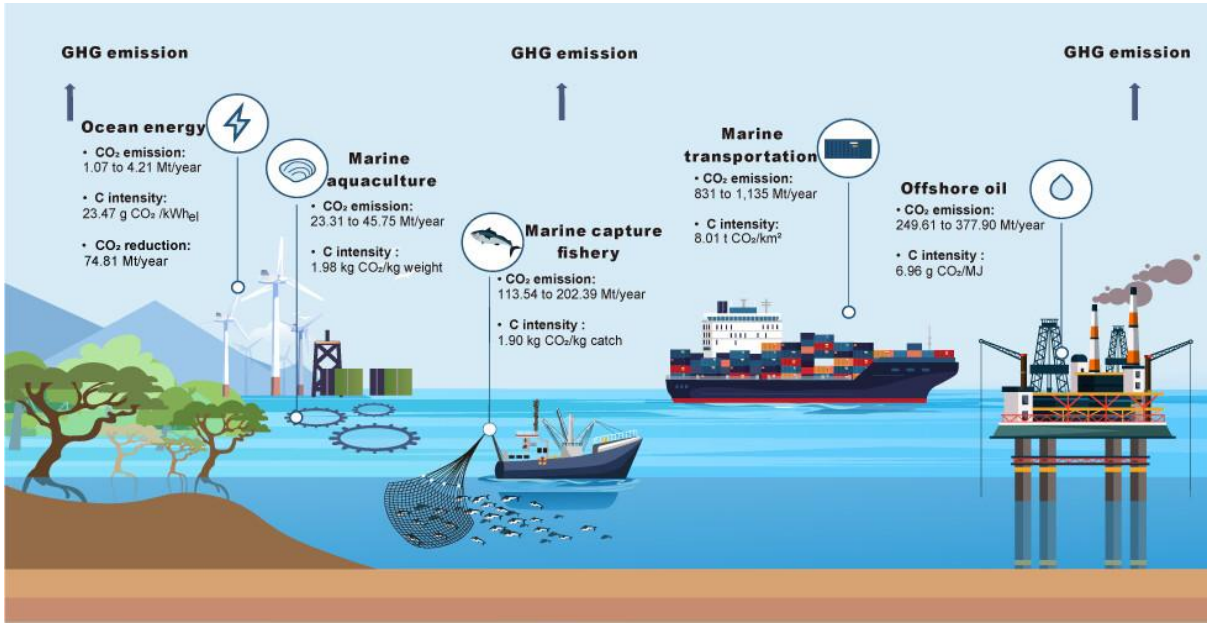

Figure 3: GHG emissions and carbon intensity associated with different marine sectors [3]

In response to these environmental challenges, the maritime industry is undergoing a profound transformation, driven by international climate goals and an increasingly stringent regulatory framework. The International Maritime Organization (IMO), a specialized agency of the United Nations, plays a central role in governing the safety, security, and environmental performance of international shipping.

A key milestone in this process is the IMO Initial GHG Strategy (2018), which aims to reduce total GHG emissions from international shipping by at least 50% by 2050 compared to 2008 levels, with the ultimate objective of achieving full decarbonization within this century. To meet these goals, several mandatory measures have been introduced under MARPOL Annex VI, targeting both CO_2 and other pollutants such as NO_x and SO_x. Regarding CO_2, the main regulatory instruments (Figure 4) include [4]:

- Energy Efficiency Design Index (EEDI) – mandatory efficiency standards for newly built ships, expressed in terms of minimum energy efficiency per capacity mile.
- Energy Efficiency Existing Ship Index (EEXI) – applying similar efficiency requirements to existing ships.
- Carbon Intensity Indicator (CII) – introduced in 2023, this operational measure evaluates carbon intensity based on actual fuel consumption and cargo transported.

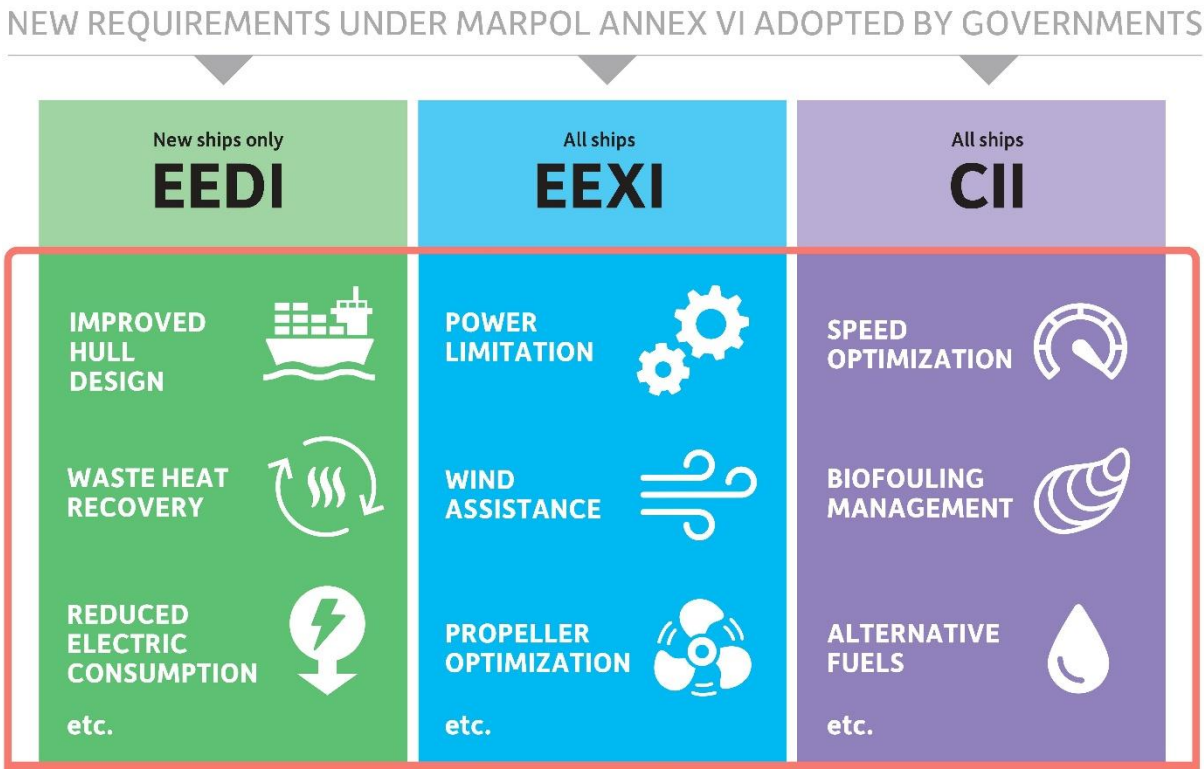

Figure 4: New regulatory requirements under MARPOL Annex VI for GHG reduction in the shipping sector and strategies to meet the targets [5]

Beyond CO_2, MARPOL Annex VI also establishes global and regional limits for sulfur oxides (SO_x), nitrogen oxides (NO_x), and particulate matter (PM). Key measures include:

- Global sulfur cap – since January 1, 2020, the sulfur content in marine fuels has been limited to 0.5% m/m, down from 3.5%.
- IMO Tier II and Tier III standards – defining NO_x limits based on engine speed and date of manufacture, with Tier III requiring up to an 80% reduction compared to Tier I for ships built after 2016.
- Emission Control Areas (ECAs) – specific regions where stricter limits apply: 0.1% sulfur and NO_x Tier III compliance.

Currently, the Baltic Sea, North Sea, and Mediterranean Sea are designated SO_x ECAs, while the North American and U.S. Caribbean Sea ECAs regulate both NO_x and SO_x emissions. From 1 March 2026, the Canadian Arctic and Norwegian Sea will also become dual NO_x and SO_x ECAs. Additional areas may be added in the future. Within ECAs, pointed out in Figure 5, emission limits are significantly stricter than in other regions.

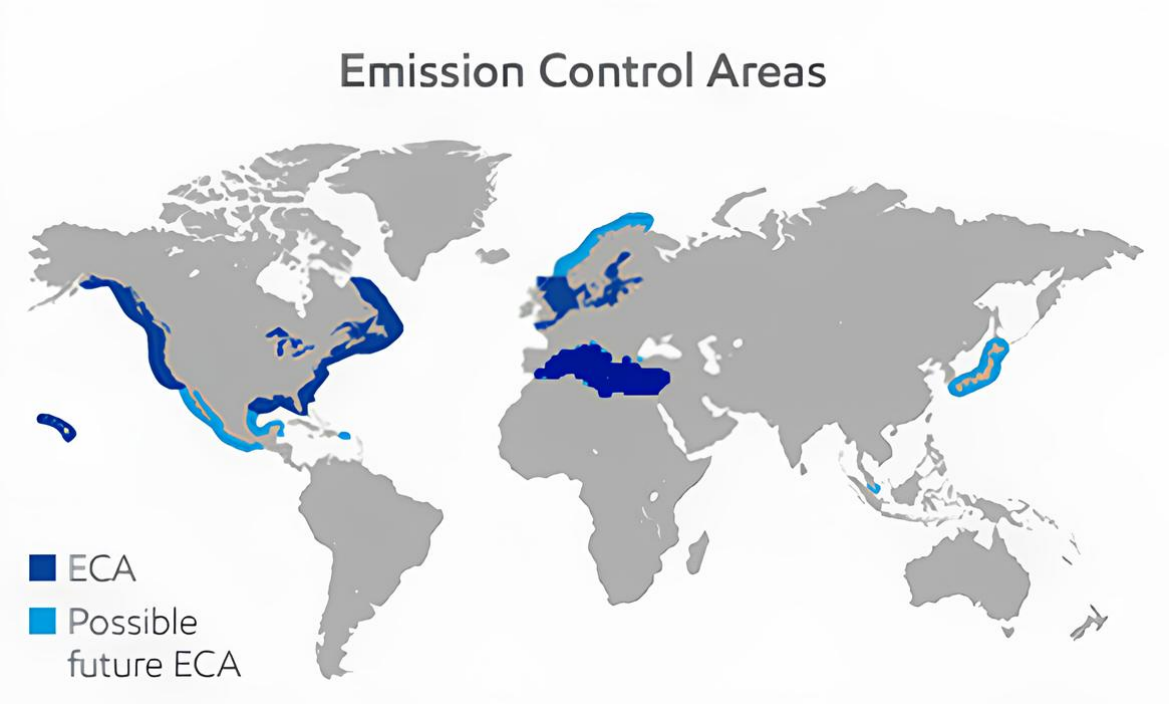

Figure 5: Current and possible future ECAs [6]

Given this evolving regulatory landscape, the adoption of cleaner propulsion technologies and low-emission fuels has shifted from being an option to becoming a strategic imperative for shipping companies, engine manufacturers, and naval architects. To comply with regulations and meet decarbonization targets, the maritime sector is investing in a wide range of technological solutions, including:

- Exhaust after-treatment systems – such as Selective Catalytic Reduction (SCR) for NO_x abatement, Exhaust Gas Recirculation (EGR) to lower peak combustion temperatures, and particulate filters for PM reduction.
- Alternative fuels – including liquefied natural gas (LNG), methanol, ammonia, hydrogen, and biofuels, each with specific advantages and challenges compared to conventional marine diesel.
- Combustion system innovations – such as lean-burn spark ignition (SI) engines with pre-chamber (PC) ignition, dual fuel (DF) compression ignition (CI) engines, variable valve timing, advanced turbocharging, and optical diagnostics for better control and monitoring.

- Hybrid-electric propulsion systems – integrating internal combustion engines (ICEs) with batteries and electric drives to optimize operating conditions and enable zero-emission operation in ports or ECAs.
- Digitalization and automation – including real-time emissions monitoring, AI-based engine control, and predictive maintenance to enhance compliance and reliability.

Among these various technological pathways, this thesis focuses on two interrelated areas of the alternative fuels and combustion system innovations.

In particular, alternative fuels such as methane, hydrogen, ammonia, methanol, and ethanol have distinct physical and chemical properties that significantly affect combustion behavior, ignition stability, flame propagation, and emission characteristics. Their use in marine propulsion requires careful adaptation of engine architectures and combustion strategies to minimize CO_2, NO_x, and unburned hydrocarbons (UHC).

To fully exploit the potential of these fuels, innovative combustion systems have been developed to overcome the limitations of conventional SI and CI operation, with particular attention to DF CI operation and PC SI configurations. Through detailed 3D Computation Fluid Dynamic (CFD) simulations, this thesis investigates how advanced combustion concepts interact with selected alternative fuels under realistic operating conditions, providing fundamental insights into their behavior in future-ready marine propulsion systems.

The structure of the thesis is as follows:

- **Chapter 1** presents the theoretical foundations necessary to understand the operation of ICEs for marine propulsion, with an emphasis on alternative combustion strategies.
- **Chapter 2** describes the key physical and chemical properties of the fuels investigated.
- **Chapter 3** details the numerical CFD models and the physical and chemical phenomena inside the combustion chamber, including how these are represented and applied.
- **Chapter 4** provides a comprehensive state-of-the-art review of alternative fuels used in innovative combustion systems.
- **Chapter 5** focuses on DF CI operation and related simulations.
- **Chapter 6** examines CFD simulations of conventional SI engines and alternative SI concepts employing PC ignition.
- **Chapter 7** proposes an innovative marine system based on onboard hydrogen production through fuel cells.

Chapter 1

1. THEORETICAL BACKGROUND ON ICE FOR MARINE PROPULSION

In this chapter, the theoretical foundation necessary to understand the operation of ICEs for marine propulsion are established. Particular emphasis is placed on the fundamental differences between SI and CI engines, and the way in which alternative combustion strategies, such as PC ignition and DF operation, are integrated into these frameworks to support decarbonization efforts in the maritime sector.

1.1 Classification of Marine Propulsion Engines

ICEs have been the cornerstone of marine propulsion systems for over a century [7]. Their ability to convert chemical energy into mechanical work with relatively high efficiency, scalability, and robustness makes them particularly well-suited for maritime operations. However, the diversity of vessel sizes, operating conditions, and environmental regulations has led to a broad spectrum of engine types and configurations. Marine engines are typically classified into two categories based on their operating cycle and speed [8]:

- Two-stroke low-speed engines: operate at speeds typically below 200 rpm and are directly coupled to the propeller shaft. Their simple design, high torque output, and superior fuel economy make them ideal for large vessels. They use uniflow scavenging and often rely on crosshead designs to reduce frictional losses.
- Four-stroke medium-speed engines: operating in the range of 400–1200 rpm, these engines are used in smaller vessels, auxiliary power systems, and diesel-electric configurations. They offer better load flexibility and dynamic response compared to their two-stroke counterparts.

1.2 CI Engines in Marine Applications

CI engines, commonly referred to as diesel engines, remain the primary technology driving large-scale marine propulsion. Their unmatched thermal efficiency, robustness, and adaptability to heavy and varied fuel types have made them the propulsion system of choice for the vast majority of ocean-going vessels. From large container ships and bulk carriers to tankers

and cruise liners, CI engines dominate the propulsion landscape due to their reliability, long service intervals, and fuel flexibility.

1.2.1 The DF Combustion

In recent years, growing environmental pressure and fuel diversification have led to the rapid development of DF engine technology. These engines combine the benefits of CI combustion with the use of gaseous fuels, such as methane, hydrogen, or ammonia, supplemented by a pilot injection of liquid fuel, usually marine diesel oil.

The combustion process DF CI engines is more complex than in traditional diesel engines. It involves a pilot-ignited, premixed-diffusion hybrid regime, where the premixed gaseous charge exhibits flame propagation behavior, while the pilot injection creates local ignition kernels and hot spots [19].

Examining in detail the combustion process of DF engines, it is typically characterized by three distinct phases, as illustrated in Figure 1.1.

Initially, the pilot combustion phase occurs when a small quantity of High-Reactivity Fuel (HRF), typically diesel, is injected near the end of the compression stroke. This phase is marked by a sharp and narrow heat release peak, which results from the rapid auto-ignition and diffusion-controlled combustion of the pilot fuel. The primary function of this phase is to provide a localized high-temperature zone capable of reliably igniting the premixed charge of gaseous fuel and air. In DF operation, the pilot fuel often contributes only 5–10% of the total energy input, but its role is critical for stable combustion.

Following pilot ignition, the second phase, known as premixed combustion, dominates the heat release profile. During this phase, the premixed gaseous fuel–air charge, introduced during the intake process and thoroughly homogenized with the incoming air, is ignited and burns rapidly through the propagation of multiple flame fronts across the combustion chamber. The resulting heat release is typically broader and less steep compared to the pilot peak, reflecting the flame propagation throughout the cylinder. The intensity and timing of this premixed phase are highly dependent on several factors, including the substitution ratio, the degree of premixing, and the ignition delay between the pilot injection and the onset of gaseous fuel combustion. A longer ignition delay tends to promote a higher proportion of premixed charge combustion, which can increase the heat release rate but may also elevate the risk of abnormal combustion phenomena, such as knock, particularly in smaller DF engines [20].

The third and final phase, referred to as diffusion combustion, represents the tail end of the heat release process. This phase is characterized by a relatively low and prolonged rate of heat

release (ROHR), resulting from the burning of residual pilot fuel droplets and incompletely combusted gaseous fuel pockets. Unlike the earlier phases, diffusion combustion is governed primarily by the mixing of remaining fuel with available oxygen in the cylinder. It typically occurs during the expansion stroke. Although this phase contributes less to the overall energy output, it has significant implications for exhaust emissions, particularly nitrogen oxides (NO_x) and PM, due to localized high temperatures and fuel-rich zones.

Overall, the total heat release profile in DF combustion is the superposition of these three phases. It exhibits an initial rapid rise due to pilot combustion, a dominant broad peak from the premixed combustion of the gaseous fuel, and a trailing portion attributable to diffusion-controlled processes.

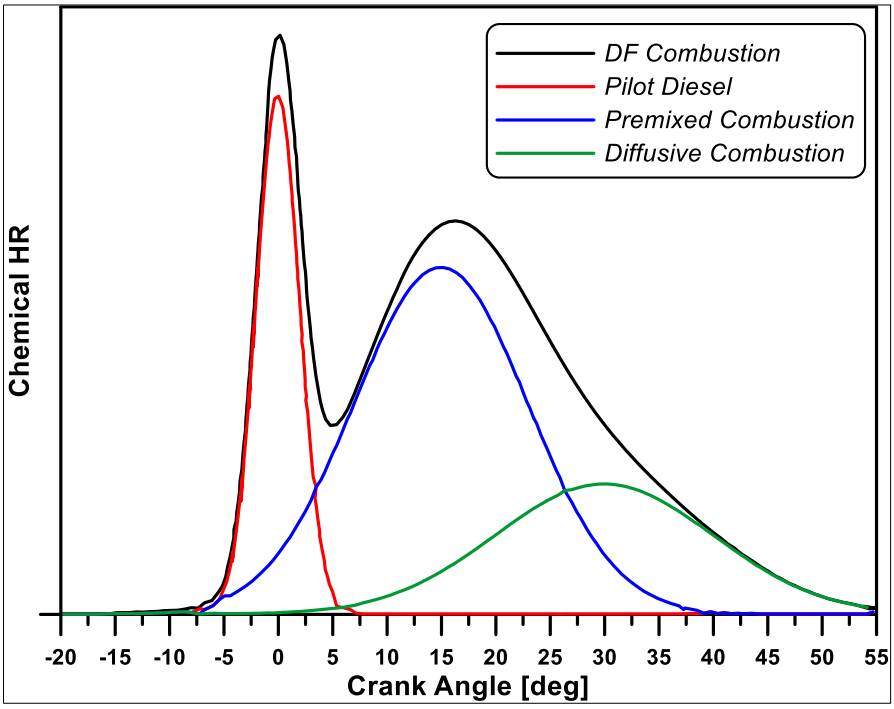

Figure 1.1: Typical chemical heat release for DF combustion

Figure 1.2 illustrates the sequential phases of combustion in a DF. In (a), the HRF injector delivers a small quantity of diesel fuel, forming localized diesel jets that act as ignition sources within the combustion chamber. Then, (b) depicts the multiple ignition points that develop as the diesel fuel auto-ignites, initiating combustion in the immediate vicinity of the jets. Finally, (c) shows the progression to the propagation of multiple flame fronts, where the ignition points serve as centers from which turbulent flames expand and consume the premixed low-reactivity fuel (LRF)–air mixture throughout the chamber.

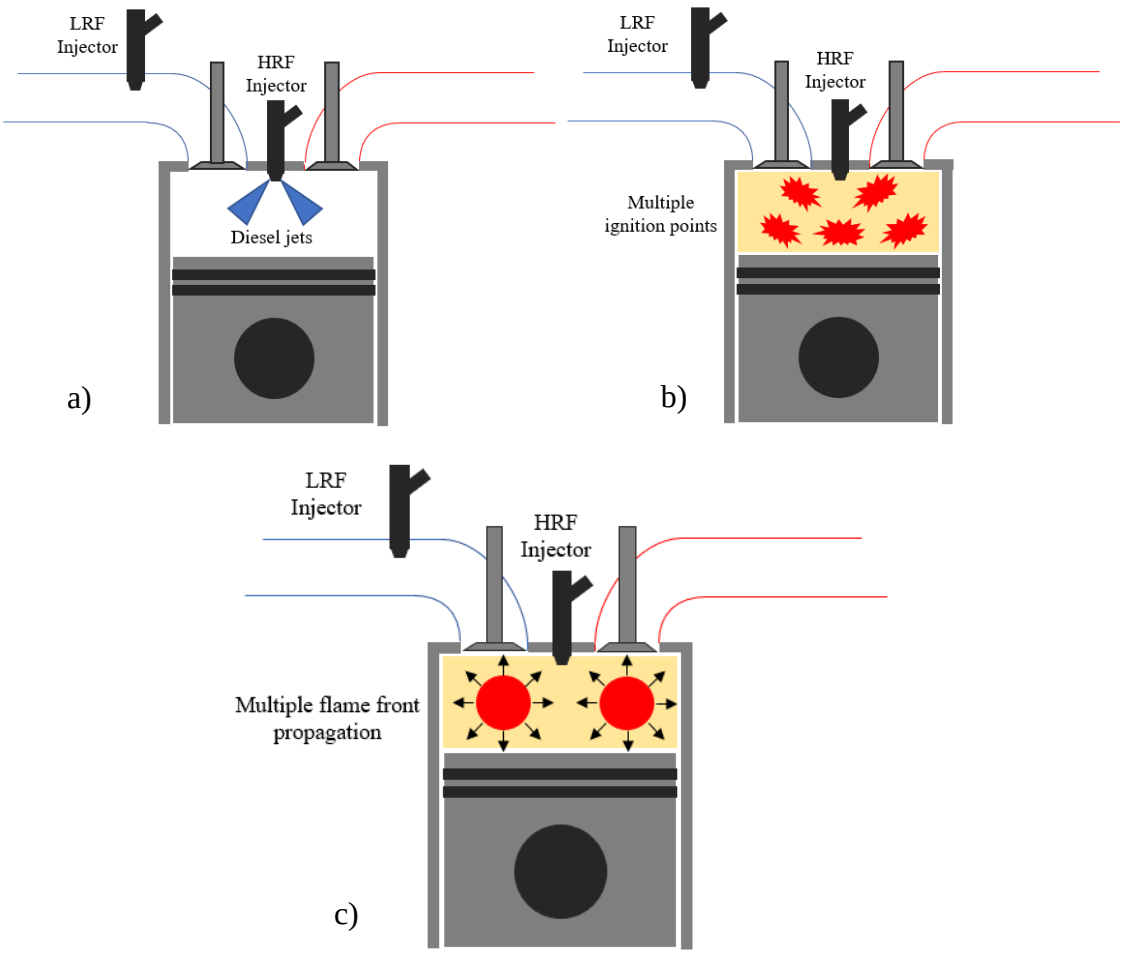

Figure 1.2: Illustration of combustion in DF engine.

A significant advantage of DF engines is their operational flexibility: they can switch between DF and full diesel modes depending on fuel availability or operational constraints, ensuring continuous operation even in ports or regions lacking gas infrastructure.

One major issue is the risk of knocking, resulting from the premature autoignition of the gaseous mixture under conditions of elevated pressure and temperature. Additionally, misfire or incomplete combustion can occur, particularly during lean operation or at low loads, where flame propagation may be insufficient to fully oxidize the charge. While DF strategies effectively reduce CO_2 and PM emissions, they introduce emission trade-offs, as unburned methane (methane slip) and NO_x formation remain persistent concerns. To manage these challenges, advanced control strategies are required, involving precise regulation of injection timing, pilot fuel quantity, air–fuel mixing, and the application of EGR to balance efficiency and emissions across a wide operating envelope [21].

Several engine manufacturers have successfully commercialized DF technologies for the marine sector, with notable examples including MAN Energy Solutions, Wärtsilä, and WinGD. These engines have been widely adopted across a variety of vessel types due to their flexibility

in utilizing both gaseous and liquid fuels. LNG carriers represent a primary application, as the engines can efficiently use boil-off gas from the cargo as the main energy source, thereby improving overall vessel energy efficiency. DF systems are also increasingly deployed on container ships and ferries operating within ECAs, where stringent air quality regulations necessitate the use of cleaner fuels to minimize NO_x, SO_x, and particulate emissions. Furthermore, these technologies are being explored in decarbonization pilot projects involving alternative fuels such as hydrogen or ammonia blends, positioning DF engines as a key transitional solution toward compliance with future low-carbon and zero-emission targets in maritime transport.

1.1.1 Marine Propulsion Systems: An Overview

ICEs are typically the core of marine propulsion systems and can be broadly classified into three categories [9]:

- Mechanical propulsion systems, where the mechanical output of the ICE is directly transmitted to the propeller shaft, typically achieved through a system of gears or couplings.
- Electric or diesel-electric systems, where ICEs drive generators to produce electricity, which is then used to power electric motors connected to the propeller.
- Hybrid and alternative systems, including fuel cells, batteries, and wind-assisted propulsion, which are emerging in low-emission or auxiliary roles.

Despite the increasing interest in electrification, mechanical propulsion systems powered by ICEs—especially medium-speed and low-speed engines—remain the industry standard for long-distance commercial vessels, bulk carriers, container ships, and tankers.

1.1.2 Criteria for ICE Selection in Ship Design

The selection of an ICE for marine propulsion is a complex decision that must take into account a wide range of technical, operational, regulatory, and economic factors. Each vessel presents unique challenges and requirements, making the choice of engine architecture and fuel strategy a highly context-dependent process.

One of the most critical parameters is the power demand of the vessel, which is determined by its size, hull form, displacement, and service speed. Large ocean-going ships, such as container carriers and crude oil tankers, typically require low-speed two-stroke CI engines capable of delivering several megawatts of power at low rotational speeds. These engines offer high thermal efficiency and are optimized for continuous operation over long distances. In contrast, smaller vessels such as ferries, offshore supply ships, and patrol boats may operate with four-

stroke medium-speed engines, where flexibility in power output and more dynamic load response is needed [10].

Fuel availability and logistical considerations also play a key role. The growing adoption of alternative fuels such as LNG, hydrogen, and methanol is closely linked to the development of port infrastructure and onboard storage capabilities [11]. For instance, DF engines that operate on LNG require cryogenic storage tanks, insulation systems, and specific safety protocols, which may not be feasible on all ship types or routes. Consequently, engine choice is often constrained by regional and global bunkering availability.

Another decisive factor is compliance with emission regulations, particularly in ECAs where limits on sulfur oxides (SO_x) and nitrogen oxides (NO_x) are much more stringent [12]. Engines must be selected and calibrated to meet the standards set by the IMO, especially Tier III NO_x limits [13]. This has led to the adoption of exhaust after-treatment systems (e.g., SCR, EGR) or alternative combustion approaches, such as lean-burn or PC ignition, which inherently produce fewer emissions [14].

The operational profile of the ship influences both the engine configuration and the control strategies employed. Vessels that operate continuously at steady speeds (e.g., tankers, bulk carriers) can be optimized for thermal efficiency at a fixed operating point [15]. In contrast, vessels with highly variable load conditions (e.g., ferries, tugboats) benefit from engines that can quickly respond to changes in demand, often necessitating more advanced fuel injection and air management systems [16].

Equally important are considerations related to engine efficiency and the potential for waste heat recovery. Higher efficiency not only reduces fuel consumption and operational costs but also helps minimize environmental impact. In many large ships, waste heat from the exhaust can be recovered through economizers or steam turbines, providing additional propulsion or electrical power [17].

Maintenance, reliability, and crew training are also central to the decision-making process. Engine manufacturers with global service networks and standardized components are often preferred, particularly for commercial fleets seeking to minimize downtime and spare parts inventory [18]. Moreover, the complexity of alternative combustion systems requires specialized knowledge and training for engine room personnel, which must be considered at the fleet management level.

Finally, the degree of integration with other onboard systems—such as electric propulsion, battery storage, or hybrid modules—can influence the engine type and control architecture. As

ships move toward digitalization and smart energy management, engines must increasingly interact with automation systems, emissions monitors, and hybrid control units.

In summary, engine selection for marine propulsion is a multidimensional optimization process. It must align with the ship's mission profile, regulatory constraints, operational flexibility, fuel strategy, and long-term sustainability goals. The PC SI engines and DF CI engines explored in this research have emerged precisely in response to these complex demands, offering innovative pathways toward cleaner and more efficient marine propulsion.

1.3 SI Engines in Marine Applications

While SI engines have traditionally played a limited role in large-scale marine propulsion, recent advancements in combustion control, fuel flexibility, and emission reduction strategies are revitalizing their relevance in the maritime sector. Particularly, the integration of PC ignition systems has significantly enhanced the viability of SI engines for marine applications using alternative fuels such as methane, hydrogen, methanol, and ammonia. These developments are especially important in the context of decarbonization, where cleaner combustion and adaptability to non-fossil fuels are imperative.

Historically, SI engines have been employed in small pleasure craft, outboard motors, and auxiliary generator sets where compact size, low cost, and low vibration are desirable [22].

However, their widespread adoption in commercial marine propulsion has been limited by several inherent challenges. Traditional stoichiometric SI designs have demonstrated lower thermal efficiency compared to CI engines, particularly at the large scales required for marine applications. Moreover, their power output capabilities have historically been insufficient for the demands of large vessels. Operation with very lean mixtures, which is desirable for reducing emissions and improving efficiency, has also been problematic due to poor flame stability, especially when using alternative LRFs. Finally, SI engines exhibit a heightened susceptibility to knock, particularly when operating with HRFs or under high-load conditions, further restricting their suitability for large-scale maritime propulsion systems.

Nevertheless, recent advances in lean-burn strategies, turbocharging, and PC ignition systems have expanded the operational envelope of SI engines, making them suitable for low-emission, high-efficiency marine applications [23].

In SI engines, combustion is initiated by a controlled spark generated by a spark plug at the end of the compression stroke. The spark ignites a homogeneous air-fuel mixture prepared during the intake phase, typically under stoichiometric or slightly lean conditions. The flame propagates through the mixture via deflagration, which is highly sensitive to turbulence,

equivalence ratio, and combustion chamber geometry. It is important to emphasize here, and it will remain relevant in the subsequent sections of this thesis, that the equivalence ratio is a key parameter in any combustion process. It is defined as:

$$\phi = \frac{\alpha_{st}}{\alpha} \tag{1.1}$$

Where α indicates the ratio between the air-to fuel ratio and α_{st} is the air-to fuel ratio in stoichiometric conditions. Moreover, the inverse of the equivalence ratio is commonly indicated as λ.

Unlike CI engines, where the fuel is injected directly into hot compressed air, SI engines rely on premixed combustion, which generally results in lower soot and NO_x emissions but may suffer from knock at high loads and incomplete combustion at lean conditions [24]. To avoid knocking, SI engines typically operate at lower compression ratios (8–12) compared to CI engines (14–22), which somewhat limits their peak thermal efficiency.

1.3.1 PC Ignition: Concept and Benefits

One of the most promising developments in SI combustion is the PC ignition system. In this configuration, a small auxiliary chamber—typically mounted on the cylinder head and connected to the main chamber (MC) via a set of small nozzles—is used to initiate combustion. A dedicated spark plug ignites a rich or near-stoichiometric mixture within the PC, producing high-pressure combustion gases that jet into the MC and ignite the lean mixture through turbulent jet ignition [25]. The design of the PC—its volume, nozzle configuration, and fueling strategy (passive vs. active)—plays a critical role in determining combustion phasing, stability, and emissions.

There are two main categories of PC systems, as shown in Figure 1.3:

- Passive PC (Figure 1.3a) relies on the natural migration of air-fuel mixture from the MC into the PC during the compression stroke. It is simpler and cost-effective but may offer less control over mixture stratification.
- Active PC (Figure 1.3b) is equipped with a separate fuel injector, allowing for tailored control of the PC equivalence ratio independently of the MC. This enables fuel stratification in the PC, enhances stability, and is particularly beneficial when operating with very lean or high-dilution conditions.

In both cases, the enhanced ignition and flame propagation characteristics lead to higher thermal efficiency and lower specific emissions compared to traditional SI operation.

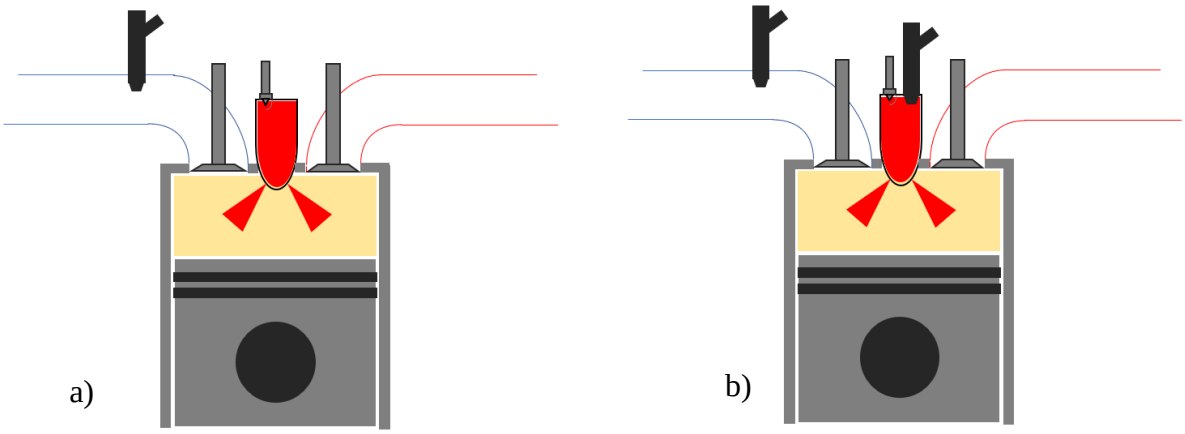

Figure 1.3: Passive vs active PC configuration.

In SI engines equipped with an active PC, the most used configuration, the combustion process is fundamentally characterized by two distinct phases, each associated with specific physical and chemical phenomena that enhance overall combustion efficiency, as shown in Figure 1.4. The first phase occurs within the PC itself, where a small volume of fuel-air mixture—often richer than the charge in the MC—is ignited by a centrally located spark plug. The confined geometry and high turbulence levels within the PC promote rapid flame kernel development, resulting in a fast and nearly complete combustion of the PC charge. This process generates a set of high-temperature, high-pressure reacting jets that are expelled through small orifices connecting the PC to the MC. These jets penetrate deeply into the lean or highly diluted mixture within the MC, serving as multiple ignition sources. The heat release during this stage is relatively small and appears as a narrow, early peak in the heat release rate profile. The second phase involves the bulk combustion of the MC charge, which is initiated by the turbulent reacting jets emerging from the PC. Unlike conventional SI combustion, where flame propagation proceeds spherically from a single ignition point, this phase is characterized by the simultaneous formation and propagation of multiple flame fronts throughout the MC. The jet-induced turbulence significantly accelerates the burn rate and promotes a more uniform combustion process. This results in a broader and more dominant peak in the ROHR curve, reflecting the rapid conversion of chemical energy to thermal energy. The distributed ignition pattern inherent to this combustion mode not only enables the stable operation of ultra-lean mixtures but also suppresses the onset of knock and reduces peak combustion temperatures, thereby lowering NO_x formation. As a consequence, the PC combustion strategy represents a highly effective means of improving thermal efficiency and achieving stringent emission targets in modern SI engines.

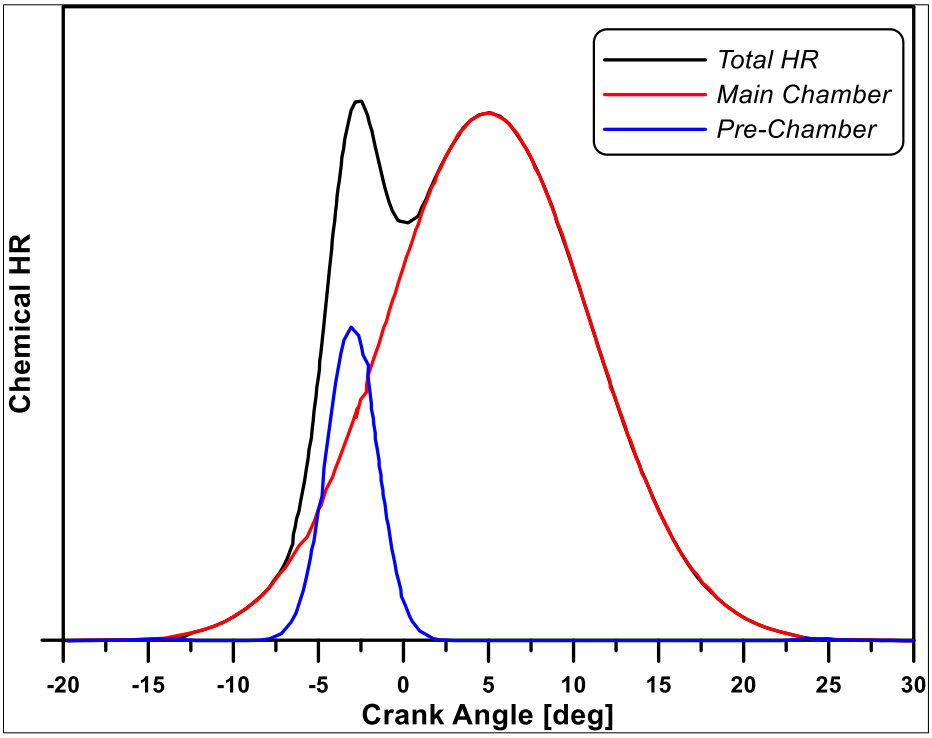

Figure 1.4: Typical chemical heat release for SI-PC combustion.

Figure 1.5 illustrates the key stages of PC combustion. In (a), a small quantity of fuel is injected into the PC and ignited by a spark plug, initiating the combustion of the rich PC mixture. In (b), combustion within the PC rapidly increases pressure and temperature, resulting in the generation of hot, reacting gases. Finally, in (c), these gases are expelled through orifices into the MC as turbulent jets, which ignite the lean or highly diluted mixture in the MC at multiple points, enabling distributed combustion and faster flame propagation.

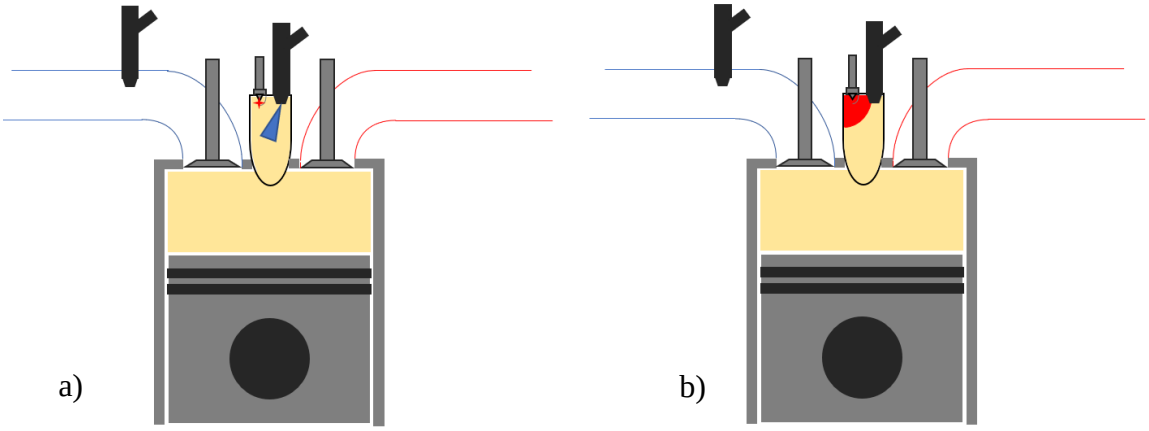

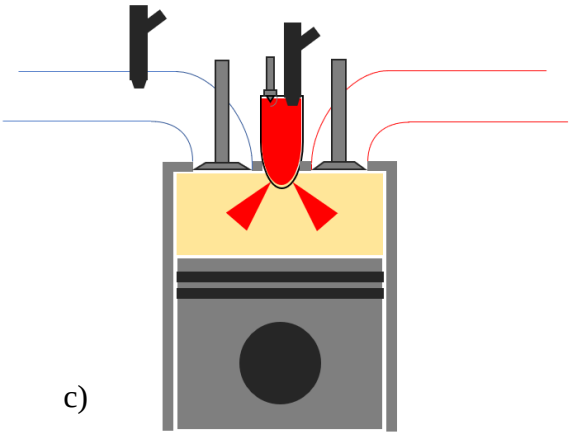

Figure 1.5: Illustration of combustion in PC engine.

The PC ignition system provides several key advantages over conventional SI approaches, making it particularly effective for modern high-efficiency combustion strategies. By generating hot turbulent jets that carry both thermal energy and active combustion radicals into the MC, the system substantially increases the available ignition energy. This enhances ignition reliability even under ultra-lean or highly diluted operating conditions. Furthermore, the jets promote intense turbulence and distributed ignition sites, leading to faster and more complete combustion across the entire chamber volume. This distributed combustion mechanism extends the lean burn capability of the engine, enabling stable operation at equivalence ratios below 0.6. Such ultra-lean operation effectively reduces peak combustion temperatures and suppresses NO_x formation. In addition, the PC configuration improves fuel flexibility by facilitating the combustion of LRFs such as methane and ammonia while also enabling safe and efficient operation with HRFs like hydrogen, which are prone to knock in conventional SI systems.

The integration PC ignition in SI engines is especially attractive for marine applications involving gaseous and alcohol-based fuels, where low carbon intensity and regulatory compliance are critical. When integrated with lean combustion strategies, PC ignition systems offer several advantages that directly address the challenges of modern marine propulsion. They enable significant reductions in NO_x emissions, achieving levels compliant with IMO Tier III regulations without relying on exhaust after-treatment technologies. Moreover, these systems facilitate stable combustion of LRFs such as methane and ammonia, which would otherwise struggle to ignite reliably in lean conditions. In addition, PC configurations support the use of hydrogen in ultra-lean mixtures without necessitating dilution with inert gases, thereby maximizing thermal efficiency while minimizing the formation of nitrogen-based pollutants.

Additionally, PC SI engines are well-suited for hybrid or electric propulsion architectures, where engine downsizing and thermal efficiency are prioritized over absolute power output.
However, a number of technical and operational challenges that must be addressed for successful implementation. One of the primary disadvantages lies in the increased system complexity and associated costs. Active PC configurations, which require dedicated fuel injection or spark systems within the PC, introduce additional components and control requirements compared to conventional SI engines. This added complexity not only raises manufacturing and maintenance costs but also demands advanced calibration strategies to ensure robust performance under varying operating conditions.
Furthermore, PC systems are prone to higher UHC emissions, particularly due to flame quenching and incomplete oxidation of trapped fuel-air mixtures within the small orifices and the PC volume itself.
The combustion process in PC systems is also highly sensitive to engine operating conditions. At very low loads or with highly diluted mixtures, insufficient jet penetration and energy can lead to misfire or incomplete combustion. Conversely, at high loads or when using HRFs such as hydrogen, the energetic jets may induce knocking phenomena, posing a risk to engine durability and performance.
Finally, the design of the PC and its connecting orifices requires careful optimization. If the PC volume is too large, it can lead to excessive trapped gases and increased UHC emissions, while overly small orifices may limit jet effectiveness or become susceptible to clogging due to soot deposits when liquid fuels are employed. These limitations highlight the importance of a holistic design and control approach to fully exploit the advantages of PC ignition while mitigating its inherent drawbacks.

1.4 Pollutant Emissions from Marine ICEs

ICEs used in marine propulsion are major contributors to air pollution, especially in coastal regions and high-traffic shipping lanes. The type and quantity of pollutants generated depend on multiple factors, including fuel composition, combustion strategy, operating conditions, and engine control parameters. Understanding the formation mechanisms and mitigation pathways of these emissions is critical for designing cleaner engines and complying with current and future environmental regulations.

This section provides an overview of the primary pollutants associated with marine SI and CI engines, with particular attention to how alternative fuels and advanced combustion systems such as DF and PC ignition influence their formation and control.

1.4.1 NO_x Emissions

Nitrogen oxides (typically NO and NO_2), collectively referred to as NO_x, are formed primarily through high-temperature reactions between nitrogen and oxygen during combustion. In marine engines, NO_x emissions are typically produced via [8]:

- Thermal NO_x (Zeldovich mechanism): dominant in high-temperature, stoichiometric or rich combustion zones.
- Prompt NO_x: occurs in fuel-rich zones, especially with hydrocarbon fuels.
- Fuel NO_x: negligible in most marine fuels, except for some biofuels.

The formation of NO_x in ICEs is governed by several key factors that directly influence the rate of thermal NO_x production. Among these, the peak combustion temperature plays a pivotal role, as NO_x formation is highly sensitive to temperature, particularly above 2000 K where the Zeldovich mechanism becomes dominant. Additionally, the residence time at high temperatures determines the extent to which nitrogen and oxygen molecules in the air dissociate and recombine to form NO_x species. The local equivalence ratio is equally critical, as stoichiometric and slightly rich mixtures tend to produce higher flame temperatures and, consequently, higher NO_x levels. Furthermore, the degree of air–fuel mixing and turbulence affects flame propagation characteristics, local temperature gradients, and the homogeneity of combustion, all of which contribute to NO_x formation dynamics.

To mitigate NO_x emissions, several strategies have been developed and widely implemented. Lean combustion is an effective approach as it lowers peak flame temperatures by operating with excess air, thereby reducing thermal NO_x formation. Similarly, EGR introduces a fraction of the exhaust gases back into the intake stream, which dilutes the oxygen concentration and increases the specific heat capacity of the charge, leading to reduced combustion temperatures and slower NO_x formation kinetics. On the after-treatment side, SCR systems chemically reduce NO_x to nitrogen and water using a reductant such as ammonia or urea, achieving high levels of NO_x abatement. Finally, advanced combustion techniques such as PC ignition facilitate the use of ultra-lean mixtures and promote distributed combustion with lower flame temperatures, further suppressing NO_x generation at the source.

In DF CI engines, NO_x emissions are reduced when gaseous fuels like methane or hydrogen are used in lean conditions, though they may increase under partial load or with hydrogen-rich mixtures due to high reactivity.

1.4.2 CO Emissions

CO is produced during incomplete combustion, especially in fuel-rich zones or at low temperatures. While CO levels in marine CI engines are typically low due to high combustion temperatures, SI engines (especially in lean-burn or partial load operation) can exhibit elevated CO levels.

In PC ignition systems, the formation of CO emissions is influenced by several interrelated factors tied to the combustion process. A primary determinant is the efficiency of jet-induced combustion in the MC, as incomplete oxidation within locally rich or lean zones can lead to elevated CO levels. The equivalence ratio plays a central role, with overly rich regions promoting incomplete combustion due to insufficient oxygen availability, while excessively lean areas can result in flame quenching and UHC that later oxidize to CO. Additionally, the extent of post-oxidation during the expansion and exhaust phases is critical, as residual CO formed during the main combustion event may undergo further oxidation if adequate temperatures and oxygen levels persist.

To mitigate CO emissions in PC systems, several strategies can be employed. Enhancing the turbulence and flame speed within the MC facilitates more complete combustion by promoting better air–fuel mixing and minimizing localized quenching zones. Avoiding overly lean mixtures is equally important, as regions with equivalence ratios below the lean flammability limit hinder complete oxidation and favor CO formation. Furthermore, careful optimization of spark timing (ST) and PC fueling is essential to ensure that combustion in both the PC and MC proceeds efficiently, avoiding conditions that lead to incomplete burn-out of the fuel. Together, these measures contribute to improved combustion completeness and a significant reduction in CO emissions, which is particularly relevant in engines targeting ultra-lean operation for higher thermal efficiency.

1.4.3 UHC Emissions

UHC emissions result from incomplete combustion of fuel. In particular, the presence of over-lean or over-rich regions within the combustion chamber can impede complete combustion; overly lean zones may fall below the lean flammability limit, while rich zones suffer from oxygen deficiency. Another important contributor is the existence of crevice volumes and regions of poor mixture homogeneity, where fuel–air pockets remain unburned due to limited

flame penetration or insufficient turbulence. These effects are particularly critical in engines operating with gaseous fuels such as methane, leading to the phenomenon commonly referred to as methane slip. Another significant source of UHC is flame quenching near cold walls, where heat loss to the chamber surfaces reduces local temperatures below the threshold required for sustained oxidation.

To address UHC emissions, several strategies can be employed. Optimizing injection timing and the pilot fuel quantity helps ensure that the combustion process initiates under favorable conditions and that flame propagation is sufficient to access all regions of the chamber. Enhancing in-cylinder mixing and turbulence improves charge homogeneity and reduces the occurrence of quenching-prone pockets. Additionally, for applications such as LNG-powered marine engines, the integration of oxidation catalysts or after-treatment systems has proven effective in oxidizing residual hydrocarbons in the exhaust stream, further minimizing methane slip and contributing to compliance with stringent emission regulations. These measures, applied individually or in combination, are critical for achieving low UHC levels while maintaining the efficiency advantages of PC combustion strategies.

1.4.4 PM and Soot

PM emissions represent a significant health and environmental challenge, particularly in sensitive areas such as ports and coastal regions where shipping activity is concentrated [26]. PM formation in ICEs originates primarily from the pyrolysis of hydrocarbons within fuel-rich regions of the combustion chamber, where insufficient oxygen availability leads to the formation of soot precursors. These nascent particles subsequently undergo coagulation and condensation during the expansion and exhaust phases, forming larger aggregates that are emitted into the atmosphere. In marine applications, diesel CI engines are the predominant source of PM emissions, owing to their reliance on heavy fuels rich in aromatic and long-chain hydrocarbons, which are prone to soot formation.

In contrast, the adoption of gaseous fuels in DF configurations, such as methane or hydrogen, can substantially reduce or even eliminate PM emissions due to the absence of soot-forming hydrocarbons in these fuels. Similarly, PC SI combustion systems operating on clean gaseous fuels or oxygenated alternatives (e.g., methane, methanol, ethanol) generate very low levels of soot, as the distributed ignition and lean operation inhibit the development of fuel-rich zones. However, it is worth noting that certain alcohol-based fuels may give rise to organic PM emissions, attributed to their high latent heat of vaporization and associated vaporization dynamics, which can create localized regions of incomplete combustion.

To mitigate PM formation, several strategies are employed. The most effective measures include switching to gaseous or oxygenated fuels, which inherently minimize soot precursors, and avoiding fuel-rich pockets through careful control of injection timing and mixture formation. Enhancing fuel–air mixing and combustion completeness is also critical, as it limits the occurrence of locally rich zones where pyrolysis could initiate. In specific applications, such as small-scale auxiliary engines, the use of diesel particulate filters provides an effective after-treatment solution, although their application in large marine engines remains limited due to operational and economic constraints.

1.4.5 Ammonia Slip and N_2O Emissions

The use of ammonia as a fuel in ICEs introduces a unique set of emission challenges that require careful consideration in both combustion system design and after-treatment strategies. One of the primary concerns is ammonia slip, defined as the presence of unreacted NH_3 in the exhaust gas. This phenomenon arises due to incomplete combustion, often exacerbated by the relatively low flame propagation speed and high ignition energy of ammonia, as well as operation at lower flame temperatures in lean-burn conditions. Ammonia slip presents significant environmental and health risks, contributing to atmospheric formation of secondary aerosols and exhibiting direct toxicity to humans and ecosystems [27]. To mitigate this issue, strategies aimed at ensuring complete in-cylinder oxidation are critical, including enhanced turbulence, optimized ignition systems, and precise control of the air–fuel equivalence ratio. Alternatively, downstream treatment technologies, such as selective catalytic oxidation, may be employed to eliminate residual NH_3 before exhaust release.

Another pollutant of concern is nitrous oxide (N_2O), a potent GHG with a global warming potential approximately 300 times that of CO_2 [28]. N_2O formation during ammonia combustion is highly sensitive to local combustion temperatures and the equivalence ratio. It is typically favored in regions with intermediate temperatures where NH_3 oxidation does not proceed to completion, allowing intermediate species to recombine into N_2O. Additionally, combustion phasing and the degree of stratification in ammonia–air mixtures significantly influence N_2O production. Both ammonia slip and N_2O emissions must therefore be carefully monitored and controlled in engines utilizing pure ammonia, ammonia–hydrogen blends, or DF configurations involving NH_3, particularly in maritime applications where stringent environmental regulations are progressively targeting these emerging pollutants.

1.4.6 CO_2 emissions

Although carbon dioxide (CO_2) is not classified as a pollutant in the conventional sense, it is the principal contributor to the greenhouse effect and thus a critical parameter in the environmental impact assessment of marine propulsion systems [29]. CO_2 emissions arise as a direct product of complete combustion, with their magnitude closely correlated to the carbon content of the fuel and the engine's specific fuel consumption. Among marine fuels, fossil diesel exhibits the highest carbon content, resulting in substantial CO_2 emissions per unit of energy produced. In contrast, methane, with its lower carbon-to-hydrogen ratio, emits less CO_2 than diesel for the same energy output. The utilization of hydrogen or ammonia as alternative fuels offers a distinct advantage in this regard, as their carbon-free molecular structures preclude CO_2formation entirely. Similarly, oxygenated fuels such as methanol and ethanol, derived from renewable sources, possess lower carbon content than diesel and represent a potential pathway toward carbon-neutral operation.

Strategies for reducing CO_2 emissions focus primarily on both fuel selection and improvements in engine efficiency. Enhancing thermal efficiency through advanced combustion techniques reduces the total fuel consumption and, consequently, the amount of CO_2 produced per unit of work. The adoption of low-carbon or carbon-free fuels directly lowers the carbon footprint of the propulsion system. Furthermore, optimizing combustion phasing and mixture preparation allows for leaner operation, minimizing both fuel consumption and CO_2 output. DF and PC combustion strategies contribute synergistically to these objectives: the former facilitates the substitution of high-carbon pilot fuels with gaseous alternatives, while the latter supports ultra-lean combustion and enables the stable use of low-carbon or carbon-free fuels. Together, these approaches provide an effective means of reducing the global warming potential of marine engines and achieving compliance with increasingly stringent international decarbonization targets.

Chapter 2

2. ALTERNATIVE FUELS

This chapter provides an overview of the five alternative fuels selected for this thesis—methane (natural gas), hydrogen, ammonia, methanol, and ethanol—which represent a diverse range of chemical families, reactivities, and emission potentials. Each of these fuels has been used in the computational studies developed in the later chapters, where their impact on ignition delay, flame development, and pollutant formation is analyzed in both DF CI engines and PC SI engines.

2.1 Key Physical and Chemical Properties of Fuels

The performance, efficiency, and emissions of ICEs engines are profoundly influenced by the physical and chemical properties of the fuel used. These properties characterize ignition behavior, combustion dynamics, air–fuel mixing, emission formation, and thermal efficiency, and are therefore central to engine design, control strategies, and numerical modeling.

This section introduces and discusses the most relevant fuel properties in the context of advanced marine combustion systems, with a specific focus on DF CI and PC SI operation.

The lower heating value (LHV) represents the net amount of energy released per unit mass or volume of fuel, excluding the latent heat of vaporization of water formed during combustion [30]. This parameter is a key determinant of the fuel consumption rate, as it directly defines the amount of fuel required to produce a given energy output. Moreover, the LHV influences engine thermal efficiency, since fuels with higher energy density can contribute to more compact and efficient engine designs.

The autoignition temperature is defined as the minimum temperature at which a fuel–air mixture will spontaneously ignite in the absence of an external ignition source. This parameter plays a critical role in determining combustion characteristics across different engine types. In CI engines, it directly influences the ignition delay, affecting both the timing and intensity of the premixed combustion phase, while in SI engines it is a key factor in defining the fuel's knock resistance, as lower autoignition temperatures can increase the likelihood of unwanted autoignition under high pressure and temperature conditions.

The laminar flame speed defines the rate at which a flame front propagates through a quiescent, premixed fuel–air mixture and is a fundamental property influencing combustion dynamics. In SI engines, it directly affects the overall combustion speed and efficiency, as higher flame

speeds enable faster energy release and more stable operation. For PC systems, the laminar flame speed determines the effectiveness of the turbulent jets in igniting the lean mixture within the MC, particularly under highly diluted conditions. Furthermore, this parameter is critical for achieving reliable lean burn operation, as fuels with low laminar flame speeds may exhibit poor flame propagation and increased susceptibility to misfire at ultra-lean equivalence ratios.

The stoichiometric air–fuel ratio (AFR) represents the mass of air necessary to achieve complete combustion of a unit mass of fuel without any excess oxygen or unburned fuel. This parameter has a direct impact on several aspects of engine operation and design. It influences the sizing and control of air management systems, as sufficient airflow must be provided to ensure proper combustion across various load conditions. The stoichiometric AFR also underpins the regulation of the equivalence ratio, which is critical for optimizing combustion stability, efficiency, and emissions. Additionally, it affects thermal loading within the combustion chamber, as deviations from stoichiometric conditions alter peak temperatures and, consequently, the formation of key pollutants such as NO_x and UHC.

The octane number quantifies a fuel's resistance to autoignition under high pressure and temperature, serving as a key indicator of its knock resistance in SI engines. A higher octane number allows operation at higher compression ratios and advanced ignition timing without the risk of premature combustion, which is essential for maximizing thermal efficiency. In contrast, the cetane number characterizes the ignition quality of a fuel in CI engines by measuring its propensity to autoignite after injection. Fuels with higher cetane numbers exhibit shorter ignition delays, promoting smoother and more predictable combustion.

Fuel properties play a fundamental role in shaping the emission profiles of ICEs, directly affecting the formation of key pollutants such as carbon dioxide CO_2, NO_x, UHC, CO, and PM. The carbon content of a fuel is the primary determinant of CO_2 emissions per unit of energy released, with higher carbon-to-hydrogen ratios leading to increased GHG output. Flame temperature and local stoichiometry significantly influence NO_x formation, as elevated temperatures and near-stoichiometric conditions favor the thermal NO_x production pathways. In addition, the completeness of combustion governs the levels of UHC, CO, and PM in the exhaust, with incomplete oxidation resulting in higher concentrations of these pollutants. Fuels with low reactivity or poor vaporization characteristics are particularly prone to incomplete combustion under certain operating conditions, further emphasizing the need to consider fuel properties when evaluating engine emissions.

2.2 Methane/Natural Gas

Methane (CH_4), the primary component of natural gas, is currently the most widely adopted alternative fuel in commercial marine applications [31]. Its relatively high availability, well-established distribution infrastructure, and lower carbon-to-hydrogen ratio compared to conventional fossil fuels make it a promising transitional fuel for reducing GHG emissions in the maritime sector. Methane is the dominant fuel in DF CI engines, which rely on a small pilot injection of diesel fuel to ignite a lean premixed methane-air mixture. Furthermore, methane can be used in SI engines, including those equipped with PC ignition systems, where its knock resistance and clean-burning characteristics are particularly advantageous.

Methane is a colorless and odorless gas under ambient conditions and possesses the simplest molecular structure among hydrocarbons, consisting of a single carbon atom bonded to four hydrogen atoms. Its LHV is approximately 50 MJ/kg, which is slightly lower than that of diesel fuel on a mass basis but offers a clear advantage on a per-carbon basis, as it produces significantly less CO_2 per unit of energy released. Methane exhibits a relatively high autoignition temperature of around 540 °C and a laminar flame speed of approximately 0.38 m/s at stoichiometric conditions [32]. It also has a stoichiometric air–fuel ratio of roughly 17.2 by mass. Its octane number exceeds 120, providing excellent resistance to knock in SI engines, while its cetane number of approximately 5 indicates poor autoignition performance in CI applications.

Due to the combination of high autoignition temperature and low cetane number, methane cannot reliably self-ignite under typical CI conditions and thus requires the use of a pilot fuel for ignition in DF configurations. Conversely, its superior knock resistance makes it ideally suited for SI engines, particularly when operating under lean or highly turbulent conditions where stable combustion is otherwise challenging to achieve.

In marine applications, methane is predominantly stored and transported in liquefied form as LNG, which is maintained at cryogenic temperatures of approximately −162 °C and near-atmospheric pressure [33]. This storage method allows for high energy density but introduces additional system complexity. LNG infrastructure onboard ships requires double-walled insulated tanks to minimize boil-off, as well as cryogenic pumps and vaporizers for fuel handling [34]. Specialized safety and venting systems are also essential to manage the risks associated with cryogenic storage and potential methane release, and all installations must comply with the International Code of Safety for Ships Using Gases or Other Low-Flashpoint Fuels (IGF Code) [35]. Despite these engineering challenges, LNG bunkering infrastructure has

expanded significantly in major ports worldwide, particularly in Europe and East Asia, driven by the need to comply with IMO sulfur emission limits and broader decarbonization initiatives within the maritime sector.

2.3 Hydrogen

Hydrogen (H_2) has emerged as one of the most promising energy carriers for enabling deep decarbonization in the maritime sector [36]. As a carbon-free fuel, its combustion ideally produces only water vapor, resulting in zero direct CO_2 emissions. Hydrogen can be produced through several pathways, each with distinct environmental and economic implications. The most common method today is steam methane reforming (SMR), which extracts hydrogen from natural gas but is associated with substantial CO_2 emissions unless combined with carbon capture and storage (CCS). Alternatively, hydrogen can be generated via water electrolysis, a process that uses electricity to split water into hydrogen and oxygen [37]. When the required electricity is sourced from renewable energy—such as wind, solar, or hydropower—the resulting "green hydrogen" enables a truly sustainable and circular energy cycle. Other emerging pathways include biomass gasification and thermochemical cycles driven by concentrated solar energy. Among these, electrolysis powered by renewables is particularly significant for the maritime sector, as it aligns with long-term climate goals and the drive towards fully decarbonized shipping. However, despite these environmental advantages, the deployment of hydrogen in ICEs presents significant technical, safety, and operational challenges, particularly in the demanding conditions of marine environments.

As the lightest element, hydrogen possesses a unique set of combustion-relevant properties that distinguish it from conventional hydrocarbon fuels [38]. Its LHV of approximately 120 MJ/kg makes it the highest energy carrier by mass, yet its volumetric energy density at ambient conditions is only about 10.8 MJ/Nm³, highlighting the challenges of storage and transportation. Hydrogen's autoignition temperature is approximately 560 °C, comparable to other gaseous fuels, but its laminar flame speed is exceptionally high at around 2.5 m/s, which significantly exceeds that of typical hydrocarbons. The stoichiometric AFR is approximately 34.3 by mass, reflecting the large quantity of air required for complete combustion. Furthermore, hydrogen's high diffusion coefficient enhances mixture uniformity, which is advantageous for combustion stability but simultaneously increases the risk of leakage and requires stringent safety measures. Its octane number exceeds 130, offering excellent knock resistance in SI operation and supporting ultra-lean combustion strategies.

The favorable combustion characteristics of hydrogen, particularly its high flame speed and diffusivity, enable rapid and complete energy release, which is especially beneficial for ultra-lean SI operation aimed at reducing NO_x emissions and improving thermal efficiency. However, these same properties introduce challenges, including an elevated risk of backfire, pre-ignition, and excessive NO_x formation in localized high-temperature regions if combustion is not carefully controlled.

In marine applications, hydrogen is typically stored either as compressed gas (CGH_2) at pressures between 350 and 700 bar or as cryogenic liquid (LH_2) at temperatures approaching −253 °C [39]. Both storage methods impose significant engineering requirements, including the use of robust, pressure-rated or heavily insulated tanks, venting and flame-arresting systems, and comprehensive safety protocols for leak detection and handling. Compliance with the IGF Code and classification society regulations is essential for onboard implementation. A key limitation in maritime contexts remains the low volumetric energy density of hydrogen, which demands substantial storage volumes and can compromise vessel payload capacity unless mitigated through advanced tank designs or integration of storage systems into the structural elements of the ship.

2.4 Ammonia

Ammonia (NH_3) is gaining increasing attention as a carbon-free fuel option for marine applications [40], particularly considering the international decarbonization targets set by the IMO and other regulatory bodies. Currently, ammonia is produced on an industrial scale almost exclusively through the Haber–Bosch process, which synthesizes NH_3 from nitrogen and hydrogen under high pressures and temperatures in the presence of a catalyst. Traditionally, the hydrogen used in this process is derived from fossil fuels, primarily via SMR of natural gas, resulting in significant CO_2 emissions and classifying this as “grey ammonia.” When CCS technologies are integrated with SMR, the resulting product is termed “blue ammonia,” offering a lower-carbon alternative. For truly sustainable applications, “green ammonia” can be produced by coupling the Haber–Bosch process [41] with hydrogen obtained from water electrolysis powered by renewable energy sources such as wind, solar, or hydropower. Emerging pathways, such as direct electrochemical synthesis of ammonia, are also being investigated to bypass the energy-intensive Haber–Bosch process entirely.

The ability of ammonia to be stored as a liquid at moderate pressures or cryogenic temperatures, combined with a globally established production, transport, and storage infrastructure due to its widespread use in the fertilizer and chemical industries, positions it as a promising and

potentially scalable fuel for the shipping sector [42]. By leveraging green ammonia, the maritime industry can significantly reduce its lifecycle GHG emissions and align with long-term decarbonization strategies.

Despite these advantages, ammonia presents significant combustion-related challenges that necessitate advanced ignition and combustion strategies. Its relatively low reactivity, high autoignition temperature of approximately 650 °C, and extremely low laminar flame speed of around 0.07 m/s hinder both spontaneous ignition and rapid flame propagation in conventional engine configurations [43]. These characteristics require assistance through the use of pilot fuels, fuel blending, or PC systems to achieve reliable and stable combustion. Moreover, ammonia exhibits a high latent heat of vaporization and a narrow flammability range ($\phi \approx 0.6$–1.4), which complicate lean burn operation and can result in flame quenching, especially under highly diluted or low-load conditions.

From a thermochemical perspective, ammonia has an LHV of approximately 18.6 MJ/kg, considerably lower than hydrocarbon fuels such as diesel or methane, though its octane number exceeds 100, indicating excellent knock resistance for SI operation. However, the cetane number of around 7 reflects poor ignition quality in CI engines, reinforcing the need for DF strategies where ammonia serves as the primary fuel supported by a small quantity of high-reactivity pilot fuel [44].

For onboard storage, ammonia can be handled in liquid state at −33 °C and atmospheric pressure or in pressurized tanks at ambient temperature, typically around 10 bar. Compared to hydrogen, ammonia offers a higher volumetric energy density of approximately 12.7 MJ/l, versus 8.5 MJ/l for liquid hydrogen, thus reducing the storage volume required to achieve equivalent vessel range. Furthermore, the existence of an extensive ammonia supply chain in major ports worldwide provides a strong logistical advantage for near-term adoption.

Nevertheless, the use of ammonia introduces significant safety and handling concerns due to its toxicity and corrosive nature. Onboard systems must incorporate double-walled tanks fabricated from corrosion-resistant materials, such as stainless steel, to prevent leakage and material degradation [45]. Ventilation and advanced leak detection systems are essential to mitigate health and environmental risks in the confined spaces of ship engine rooms. Full compliance with the IGF Code, including anticipated future updates specific to ammonia handling, will be required to ensure safe implementation. These considerations underscore the dual challenge of leveraging ammonia's environmental benefits while addressing the operational and safety complexities inherent to its use as a marine fuel.

2.5 Methanol

Methanol (CH_3OH), the simplest alcohol, is emerging as a viable alternative fuel for marine propulsion due to its renewable production potential, favorable combustion properties, and relatively straightforward storage requirements compared to gaseous fuels such as hydrogen or ammonia [46]. Industrially, methanol is predominantly produced from fossil sources through processes such as SMR of natural gas or coal gasification, where synthesis gas (a mixture of CO, CO_2, and H_2) is catalytically converted to methanol under high pressures and moderate temperatures. This conventional route, while cost-effective, is associated with substantial CO_2 emissions and is therefore classified as "grey methanol." By incorporating CCS into these processes, "blue methanol" can be obtained with a reduced carbon footprint.

For truly sustainable applications, "green methanol" can be synthesized using renewable hydrogen [47]—produced via water electrolysis powered by renewable energy sources—combined with captured CO_2 through catalytic hydrogenation. This pathway enables the recycling of atmospheric or industrial CO_2, effectively closing the carbon loop and significantly lowering lifecycle GHG emissions. Biomass gasification represents another renewable production route, where organic materials are thermochemically converted into synthesis gas for methanol synthesis. Emerging technologies, such as direct electrochemical reduction of CO_2 to methanol, are also under development as potential low-energy, decentralized alternatives to conventional catalytic processes.

Methanol's liquid state at ambient pressure and temperature eliminates the need for high-pressure or cryogenic storage systems, thereby simplifying onboard storage and bunkering logistics [48]. This characteristic, combined with its compatibility with existing fuel infrastructure and distribution networks, strengthens its position as a promising transitional fuel for the maritime sector in the pathway toward fully decarbonized shipping.

Furthermore, methanol's oxygenated molecular structure contributes to cleaner combustion, reducing soot and PM emissions relative to conventional hydrocarbons. However, its lower energy density, toxicity, and unique combustion characteristics require adaptations in engine design and control strategies to ensure efficient and safe operation.

Methanol exhibits several thermochemical and physical properties that distinguish it from hydrocarbon and gaseous fuels, each with significant implications for combustion performance and engine architecture [49]. With a LHV of approximately 19.9 MJ/kg—roughly half that of diesel fuel—methanol requires higher volumetric flow rates to achieve equivalent power output, which influences fuel injection and delivery system design. Its autoignition temperature

of around 470 °C is lower than that of methane and ammonia, enabling ignition in CI engines with the assistance of a pilot fuel. The laminar flame speed at stoichiometric conditions, approximately 0.43 m/s, is higher than methane yet much lower than hydrogen, supporting moderate flame propagation in SI operation but requiring careful control to avoid quenching in lean mixtures. The stoichiometric AFR of approximately 6.4 by mass reflects methanol's partially oxygenated nature, while its high-octane number of about 108 provides excellent knock resistance, allowing for operation at elevated compression ratios in SI engines.

A key characteristic of methanol is its high latent heat of vaporization, around 1100 kJ/kg, which induces significant charge cooling effects during vaporization [50]. This property can enhance volumetric efficiency but may also lead to wall wetting and incomplete combustion under certain conditions, particularly during cold starts or at low loads. Moreover, methanol is toxic and corrosive, requiring careful material selection for fuel system components, such as stainless steel and compatible polymers, to ensure durability and safety. Its hygroscopic nature, characterized by a tendency to absorb water from the surrounding environment, further necessitates protective measures to prevent corrosion and fuel degradation [51].

From an operational standpoint, methanol's liquid state at ambient temperature and pressure enables its storage in standard fuel tanks, provided material compatibility is ensured. This characteristic allows for relatively straightforward integration into existing bunkering and storage infrastructure, offering a logistical advantage over cryogenic or high-pressure fuels such as LNG, LH_2, or ammonia. Nonetheless, the toxicity of methanol demands the implementation of enhanced safety systems, including leak detection and ventilation measures, to protect crew health and minimize environmental risks. These considerations are particularly important in the confined environments of ship engine rooms and fuel storage areas.

2.6 Ethanol

Ethanol (C_2H_5OH), commonly referred to as ethyl alcohol, represents another promising alternative fuel for marine propulsion due to its renewable production potential, favorable combustion characteristics, and high compatibility with existing fuel infrastructure [52]. Industrially, ethanol is predominantly produced from biomass through fermentation processes, yielding bioethanol [53]. This pathway utilizes sugars and starches from crops such as sugarcane, corn, and wheat, or lignocellulosic biomass in advanced second-generation bioethanol production. The latter route reduces competition with food crops and enhances sustainability by converting agricultural residues and dedicated energy crops into fermentable sugars [54].

In addition to bio-based production, ethanol can also be synthesized via power-to-liquid processes, resulting in so-called e-ethanol. This method involves the catalytic hydrogenation of captured CO_2 using renewable hydrogen generated through water electrolysis powered by wind, solar, or other renewable energy sources. E-ethanol offers the advantage of integrating carbon recycling with renewable energy utilization, enabling near-zero lifecycle GHG emissions when implemented at scale. Emerging production technologies, such as gasification of municipal solid waste or direct electrochemical conversion of CO_2 to ethanol, are also under investigation as potential routes to sustainable ethanol synthesis.

Both bioethanol and e-ethanol pathways support the maritime sector's decarbonization efforts by offering drop-in compatibility with existing bunkering, storage, and distribution infrastructure. This, combined with ethanol's favorable physical properties and operational advantages, underscores its potential as a transitional and long-term solution for low-carbon marine propulsion. Similar to methanol, ethanol's liquid state at ambient pressure and temperature simplifies storage and handling, but its higher energy density provides a notable operational advantage by reducing volumetric fuel flow requirements and easing integration into existing bunkering systems [55]. In this thesis, ethanol is analyzed in the context of PC SI engines and DF CI systems to assess its combustion performance and emissions characteristics under marine-relevant operating conditions.

Ethanol exhibits several thermophysical properties that distinguish it from methanol and hydrocarbons, influencing its behavior in advanced combustion modes [56]. With a LHV of approximately 26.8 MJ/kg, ethanol has a higher energy content than methanol (19.9 MJ/kg) and approaches that of conventional hydrocarbon fuels, reducing the volumetric fuel flow necessary to achieve equivalent power output. Its autoignition temperature, around 365 °C, is relatively low, facilitating ignition in CI engines when assisted by a pilot fuel. The laminar flame speed at stoichiometric conditions is approximately 0.45 m/s, slightly higher than methanol, which supports efficient flame propagation and stable combustion in SI operation. Ethanol's stoichiometric AFR of about 9.0 by mass lies between that of methanol (6.4) and hydrocarbons such as methane (17.2). Its high-octane number, approximately 108, provides excellent knock resistance, enabling operation at elevated compression ratios in SI engines without detonation risk. The latent heat of vaporization of ethanol, around 840 kJ/kg, is lower than methanol's, resulting in a milder charge cooling effect that benefits cold start behavior but provides less enhancement to volumetric efficiency.

In terms of handling and operational characteristics, ethanol is less toxic and corrosive than methanol, which improves crew safety and reduces material compatibility challenges in fuel

system components. Its hygroscopic nature, however, necessitates careful water management to avoid contamination and phase separation during long-term storage, particularly in humid marine environments. Ethanol can be stored in conventional fuel tanks at ambient conditions, requiring only minor modifications to ensure compatibility with materials such as elastomers and metals in contact with the fuel. Compared to cryogenic or pressurized fuels such as LNG, liquid hydrogen, or ammonia, ethanol's physical state significantly simplifies onboard storage and refueling operations, reducing infrastructure complexity and associated costs.

2.7 Comparative Summary of Fuel Properties

The five alternative fuels analyzed in this chapter and used for marine applications—methane (CH_4), hydrogen (H_2), ammonia (NH_3), methanol (CH_3OH), and ethanol (C_2H_5OH)—exhibit markedly different physical, chemical, and combustion-relevant characteristics. These differences strongly influence their performance in marine ICEs and their suitability for advanced combustion strategies such as DF CI and PC SI. To facilitate a direct comparison, Table 2.1 summarizes the key thermochemical and combustion properties of these fuels, reported in the previous sections, highlighting their implications for engine design, combustion behavior, emissions, and storage requirements. This comparative table clearly illustrates the contrasting characteristics of these fuels. Hydrogen's exceptionally high gravimetric energy density is offset by its very low volumetric energy density in gaseous form, requiring cryogenic storage for marine use. Ammonia's low flame speed and high autoignition temperature necessitate enhanced ignition support such as pilot injection or PC systems. Methanol and ethanol, both oxygenated liquids at ambient conditions, offer easier handling and integration into existing fuel systems but require higher volumetric flow rates due to their lower LHVs relative to hydrocarbons. Methane, with a balanced energy density and established LNG infrastructure, represents a mature option for current DF marine engines. Finally, all alternative fuels exhibit a lower amount of CO_2 emitted per unit mass of fuel when compared to conventional diesel, which, based on the calculations presented, is characterized by an emission factor of approximately 3.16 kg CO_2 per kg of fuel. This difference arises primarily from their lower carbon content or, in some cases, the complete absence of carbon in their molecular structure. Fuels such as methanol, ethanol, and methane contain fewer carbon atoms per kilogram of fuel, resulting in proportionally lower CO_2 emissions during stoichiometric combustion. Other alternatives, including hydrogen and ammonia, do not contain carbon at all and therefore produce no direct CO_2 emissions upon oxidation. Consequently, when assessed on a mass-specific basis (kg CO_2 per kg of fuel), alternative fuels consistently demonstrate a

reduced carbon footprint relative to diesel, underscoring their potential contribution to the decarbonization of the transport and energy sectors.

Table 2.1: Fuel properties

Property	**CH_4**	**H_2**	**NH_3**	**CH_3OH**	**C_2H_5OH**
LHV [MJ/kg]	50	120	18.6	19.9	26.8
Autoignition Temperature [°C]	540	560	650	470	365
LFS [m/s]	0.38	2.5	0.07	0.43	0.45
Stoichiometric AFR	17.2	34.3	6.1	6.4	9
Octane Number	>120	>130	>100	>108	>108
Volumetric Energy Density [MJ/l]	35 (LNG)	8.5 (LH_2)	12.7	15.8	21.1
CO_2 emission factor [kg/kg_{fuel}]	2.75	0	0	1.38	1.91

Chapter 3

3. NUMERICAL MODELING

This chapter provides a comprehensive overview of the numerical modeling techniques employed to simulate the complex physical and chemical phenomena occurring within ICEs, with a particular emphasis on CFD. It begins by introducing the fundamentals of CFD and the governing equations that describe the conservation of mass, momentum, energy, and chemical species in reactive multiphase flows. Special attention is given to the numerical methods used to solve these equations, including the selection of solvers, mesh motion strategies, and the convergence and stability criteria adopted to ensure reliable and accurate results. Subsequently, the discussion focuses on the specific application of CFD to ICEs, highlighting how various sub-models—such as those for turbulence, atomization, vaporization, combustion, and heat transfer—are coupled within the numerical framework to account for the multiphysics and transient nature of engine processes. The focus is placed on the numerical modeling approach adopted in this PhD research, detailing the implemented models and providing a rationale for their selection in light of the engine configuration, operating conditions, and research objectives.

3.1 Computational Fluid Dynamics (CFD)

Today, CFD is widely used across numerous sectors, including aircraft, turbomachinery, automotive, and ship design. Beyond engineering applications, CFD has found relevance in disciplines such as meteorology, oceanography, astrophysics, biology, oil recovery, and architecture [57]. Different examples of CFD applications, different from ICEs applications, are reported in Figure 3.1.

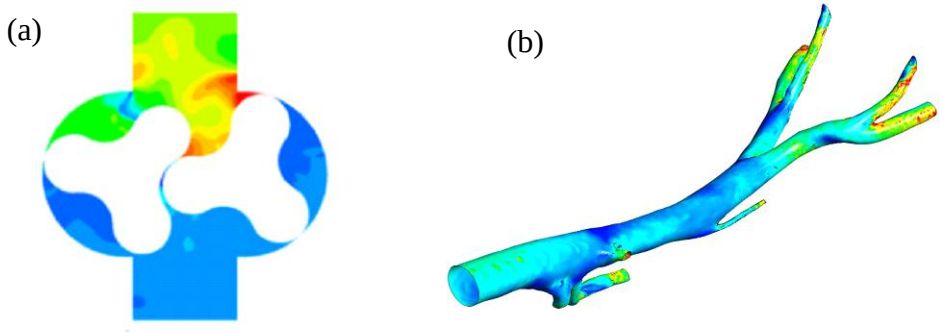

Figure 3.1: Example of applications of CFD: (a) a roots pump and an (b) human aorta [57]

Moreover, many numerical techniques developed within CFD are now employed to solve Maxwell's equations and in the field of aeroacoustics. As a result, CFD has evolved into a crucial tool not only for engineering design but also as an indispensable resource in scientific research. The accurate modeling of combustion processes in ICEs is critical for evaluating the performance and emissions of alternative fuels in marine propulsion applications. CFD has become an indispensable tool in this context, enabling detailed analysis of complex phenomena such as fuel injection, turbulent mixing, ignition, flame propagation, and pollutant formation under realistic engine operating conditions. Unlike experimental approaches, which are often constrained by cost, time, and safety considerations, CFD simulations provide a flexible and powerful framework for exploring a wide range of fuels, engine configurations, and combustion strategies.

The overall CFD workflow adopted in this study is schematically illustrated in Figure 3.2. The process begins with geometry preparation (computational domain) and mesh generation, followed by the selection of physical models encompassing turbulence, combustion, and spray dynamics. Subsequent steps involve defining boundary and initial conditions and configuring solver parameters to ensure numerical stability and convergence. The simulation phase is carried out as a fully transient calculation to capture the highly dynamic in-cylinder phenomena over the entire engine cycle. Post-processing then extracts key quantities of interest, including in-cylinder pressure traces, heat release rates, flame propagation characteristics, and pollutant formation trends. This structured workflow ensures a systematic and robust approach to analyzing alternative fuel combustion in marine engines.

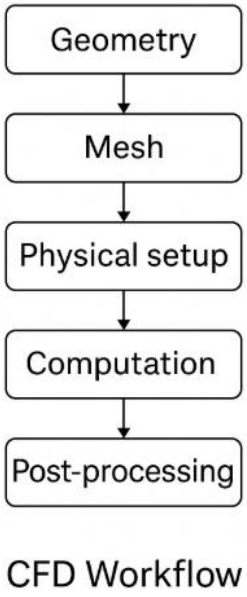

Figure 3.2: Schematics of CFD Workflow

3.2 Computational Grid

The computational grid in CFD plays a pivotal role in determining the fidelity and reliability of numerical simulations, especially in applications involving complex, multi-physics systems such as ICEs. The grid dimension must be defined to capture all relevant physical phenomena, from large-scale flow structures to small-scale features where critical interactions occur, such as fuel injection, turbulent mixing, and flame propagation. In engine modeling, this requires an accurate representation of the combustion chamber geometry, including piston bowls, cylinder heads, intake and exhaust ports, valves, and, when applicable, auxiliary components such as PCs and injector nozzles.

One of the key challenges in defining the computational grid for ICE simulations lies in balancing geometric detail with computational efficiency. High-fidelity geometrical models allow a more realistic prediction of in-cylinder flow patterns, spray-wall interactions, and combustion processes. However, excessive geometric complexity can lead to prohibitive computational costs. Simplifications such as the use of sector models or symmetry planes are often employed to reduce the domain size while preserving the dominant flow and combustion characteristics. These approaches are particularly effective in cases where the engine geometry and operating conditions exhibit high degrees of rotational symmetry. Conversely, full 360-degree models become necessary when simulating domains that are inherently asymmetric.

The generation of an appropriate computational mesh within the defined domain is equally critical [58]. Through the generation of a mesh, the physical fluid domain is divided into a number of discrete regions that are usually called cells or volumes. Thus, the physical domain is discretized. The mesh must resolve key regions where high gradients in velocity, temperature, and species concentrations are expected. These include boundary layers near solid surfaces, regions of spray breakup and evaporation, and flame fronts in premixed or partially premixed combustion modes. Near-wall refinement is typically implemented to adequately resolve the viscous sublayer and ensure accurate predictions of wall heat transfer and boundary layer behavior. Adaptive mesh refinement techniques may also be utilized to dynamically increase resolution in regions where sharp gradients of temperature, velocities or species are present.

The choice of mesh type also influences simulation, accuracy and stability. Structured meshes can provide high-quality grids with low numerical diffusion in simple geometries. A mesh is structured when the position of each individual cell can be uniquely determined by a set of indices. The cells of a structured mesh can be thought as elements of an array. For example, in two-dimensions each cell corresponds to a pair (i,j) of indices. In three-dimensions each cell

corresponds to a tern (i,j,k) of indices. Unstructured meshes offer greater flexibility for complex geometries. A mesh is defined ‘unstructured’ when its cells cannot be sort like the elements of an array. Specifically, for an unstructured mesh, the position of a cell cannot be determined from that of the adjacent cells. Finally, hybrid approaches, when the domain is divided into structured and unstructured portions, combining polyhedral cells in the bulk flow with refined hexahedral or tetrahedral cells in critical regions, are frequently employed to balance accuracy and computational cost. Figure 3.3 illustrates an example of a structured and unstructured mesh applied to a cubic form.

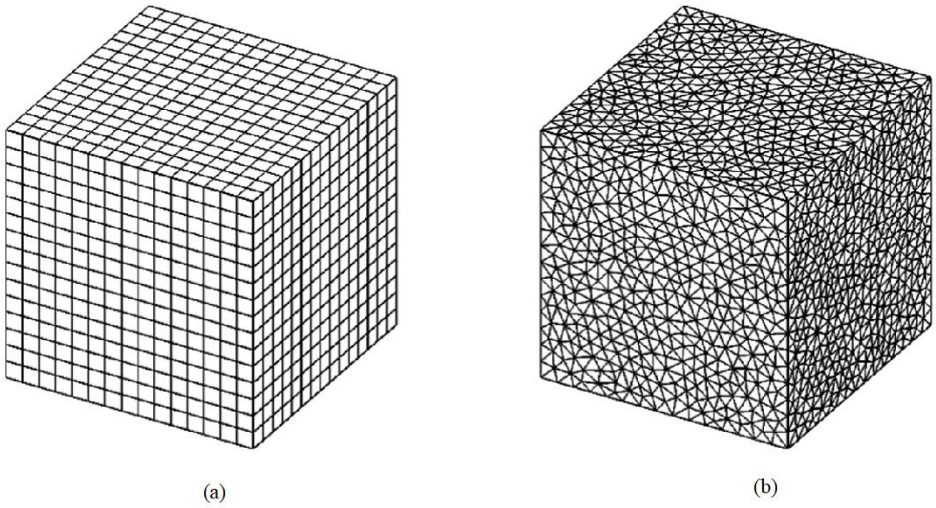

Figure 3.3: A three-dimensional structured (a) and unstructured mesh (b) [58]

In an ICE, since there is a piston that moves continuously and valves that open and closes, the in-cylinder mesh must be dynamic, i.e., the computational grid must change dynamically during the simulation.

A rigorous mesh independence study is an essential phase of the domain setup process. This involves performing simulations with progressively refined meshes and comparing key output parameters, such as peak cylinder pressure, heat release rates, and pollutant formation indices, to ensure that results are insensitive to further refinement. The outcome of this process defines the optimal mesh resolution that provides reliable results without excessive computational expense.

Ultimately, the development of the computational domain and mesh for ICE CFD simulations is a process that requires careful consideration of both physical and numerical aspects. It serves as the foundation for all subsequent modeling steps, enabling accurate predictions of in-cylinder phenomena.

3.3 Governing Equations

The motion of turbulent flows is governed by fundamental physical laws, which can be expressed through differential equations and solved using CFD. The selection of the governing equations depends on the specific problem under investigation. In the context of multispecies reactive flows, such as those occurring in ICEs, it is necessary to account for the conservation of mass, momentum, energy, and chemical species, along with an appropriate equation of state. The following sections utilize the conservative, compressible form of the governing equations [59].

3.3.1 Conservation of Mass

The continuity equation, or conservation of mass, for a compressible fluid, states that the rate of change of mass within a control volume is equal to the net mass flow into or out of the volume plus any mass generated or consumed within it.

$$\frac{\partial \bar{\rho}}{\partial t} + \nabla \cdot (\bar{\rho}\tilde{\boldsymbol{u}}) = S_m \tag{3.1}$$

Where $\bar{\rho}$ is the mean fluid density, $\tilde{u}$ is the ensemble average of the velocity field. The source S_m is the mass added to the continuous phase from a dispersed second phase (e.g., due to vaporization of liquid droplet).

3.3.2 Conservation of Momentum

It is the application of Newton's second law $\vec{F} = m\vec{a}$ applied to an infinitesimal control volume. It states that the rate of change of momentum of a fluid within a control volume is equal to the sum of the forces acting on the fluid within the volume.

$$\frac{\partial(\bar{\rho}\tilde{\boldsymbol{u}})}{\partial t} + \nabla \cdot (\bar{\rho}\tilde{\boldsymbol{u}}\tilde{\boldsymbol{u}}) = -\nabla\bar{p} + \nabla \cdot \boldsymbol{\sigma} - \nabla \cdot \Gamma + \bar{\rho}\vec{g} + \vec{F} \tag{3.2}$$

Where p is the static pressure, $\vec{g}$ is the gravitational body force, $\vec{F}$ are the external body forces acting on the flow accounting for interactions with the dispersed phase, σ are the viscous forces, representing the frictional forces due to fluid viscosity, which, can be expressed as:

$$\boldsymbol{\sigma} = \bar{\rho}\upsilon\left[\nabla\tilde{\boldsymbol{u}} + (\nabla\tilde{\boldsymbol{u}})^T - \frac{2}{3}(\nabla \cdot \tilde{\boldsymbol{u}})\boldsymbol{I}\right] \tag{3.3}$$

where υ is the kinematic viscosity.

The $\nabla \cdot \Gamma$ term is the turbulent stress (Reynolds or SGS Stress) and appears due to ensemble-averaging (RANS) or filtering (LES), capturing the effect of turbulent fluctuations. In RANS, it is called the Reynolds stress. In LES, it is called the Sub-Grid Scale (SGS) stress.

$$\Gamma = \bar{\rho}(\widetilde{\boldsymbol{u}\boldsymbol{u}} - \widetilde{\boldsymbol{u}}\widetilde{\boldsymbol{u}}) \tag{3.4}$$

3.3.3 Conservation of Energy

Based on the First Law of Thermodynamics, the change of internal energy has to be balanced by the pressure work and heat transfer. For the flow problems relevant to ICEs, the effects of convection, turbulent transport, turbulent dissipation, sprays, chemical reactions, and enthalpy diffusion of a multi-component flow should also be considered. The internal energy transport equation is:

$$\frac{\partial(\bar{\rho}\tilde{\boldsymbol{I}})}{\partial t} + \nabla \cdot \left(\bar{\rho}\tilde{\boldsymbol{u}}\tilde{\boldsymbol{I}}\right) = -\bar{p}\nabla \cdot \tilde{\boldsymbol{u}} - \nabla \cdot \boldsymbol{J} + \bar{\rho}\tilde{\varepsilon} + \dot{Q}^{c} + \dot{Q}^{s} \tag{3.5}$$

The left hand represents the local variation and transport in the total energy. $\tilde{I}$ is the specific internal energy, while the first three terms on the right-side of the equation accounts for energy transfer due to pressure, species diffusion and viscous dissipation. Finally, $\dot{Q}^{c}$ and $\dot{Q}^{s}$ are source terms due to chemical heat release and spray interactions, respectively.

3.3.4 Conservation of Chemical Species

The transport of chemical species in reacting flows is described by the species mass conservation equation, which accounts for convection, diffusion, and source terms due to chemical reactions. In its conservative, compressible form, the governing equation for species i can be written as:

$$\frac{\partial(\bar{\rho}Y_i)}{\partial t} + \nabla \cdot (\bar{\rho}\tilde{\boldsymbol{u}}Y_i) = -\nabla \cdot \boldsymbol{J_i} + \dot{\omega}_i \tag{3.6}$$

Where Y_i represents the mass fraction of species i. The term $\boldsymbol{J_i}$ denotes the diffusive flux of species, which accounts for both molecular diffusion and, where applicable, turbulent mixing. The source term $\dot{\omega}_i$ represents the rate of production or consumption of species i per unit volume due to chemical reactions and is typically determined from detailed or reduced chemical kinetics models. This equation forms part of the system of conservation equations that govern multispecies reactive flows, and its accurate solution is crucial for predicting the evolution of species concentrations, heat release, and pollutant formation in ICEs.

3.3.5 Ideal Gas Equation

To close the system of governing equations describing reactive multispecies flows, an equation of state is required to relate thermodynamic variables such as pressure, temperature, and density. In this work, the ideal gas law is employed due to its computational efficiency and adequacy for the pressure and temperature ranges typical of ICE simulations. The equation is expressed as:

$$\bar{p} = \bar{\rho} R T \tag{3.7}$$

Where R is the constant gas mixture and T the temperature. The specific gas constant R is elated to the universal gas constant R_u through $R = R_u/\bar{M}$, where $\bar{M}$ is the mean molar mass of the gas mixture.

3.4 Numerical Solvers and Convergence Criteria

The numerical resolution of the governing equations requires their discretization, which means the conversion of the partial differential equations into a discrete algebraic form that can be solved numerically. CFD solvers are usually based on the discretization method of finite volume method (FVM). The FVM is conservative: the flux entering a given volume is identical to that leaving the adjacent volume. The integration of the differential form of the governing fluid flow equations (mass, momentum, energy) on each control volume leads to this general expression [60]:

$$\frac{\partial}{\partial t}\int_V \rho\theta \, dV + \oint_A \rho\theta V \cdot dA = \oint_A \Gamma_\theta \nabla\theta \cdot dA + \int_V S_\theta \, dV \tag{3.8}$$

Where θ is the variable within the control volume, V is the control volume and A is the boundary of the volume. The first member of the equation contains the unsteady and the advection term, while the second member contains the diffusion and the generation term.

In this way the equations are discretized, and a system of algebraic equations is obtained. All algebraic equations are solved numerically to render the solution field.

While the analytical solutions of partial differential equations are closed form expressions that depicts the continuous variations of dependent variables within a domain, on the contrary, numerical solutions can return a response only in discrete points of a domain, called nodes or grid points (in the FVM nodes are usually located in the center of the control volumes). FVM has two major advantages: firstly, as mentioned above, it enforces conservation of quantities at discretized level, i.e., mass, momentum and energy remain conserved also at a local scale,

secondly, the method can be easily employed for unstructured meshes. The CFD software used for the thesis work are based on the FVM.
Other two important CFD discretization methods are:

- Finite Element Method (FEM) is a numerical method for solving PDEs by splitting the domain into smaller parts called finite elements. Subsequently PDEs for each element are formulated and resolved by approximating the fields within each element as a simple function, most times linear or quadratic polynomial. The FEM method is usually applied for structural analysis and in electromagnetics but is also used in fluid dynamics when the Reynolds numbers are of the order of ten thousands.
- Finite Difference Method (FDM) is a method that approximates derivative of the differential equations with finite differences. Spatial domain and time interval are discretized and the solution at the discrete points is approximated by solving algebraic equations containing finite differences and values from nearby points. The FDM is typically used on regular grids.

Less widespread methods are: Spectral Element Method (SEM), Boundary Element Method (BEM) and Lattice Boltzmann Methods (LBM) [60].
One way to solve the system of the algebraic equations obtained with one of the discretization methods is by using a direct method such as the Gaussian Elimination, LU Decomposition or Tridiagonal Matrix Algorithm. Direct methods obtain an exact solution of the system in a finite number of steps. Typically, direct methods act better when elements of the matrix are arranged in diagonal bands.
On the contrary, an iterative method is a mathematical procedure that uses an initial value to generate a sequence of improving approximate solutions. In other terms, if the initial value is $x^{(0)}$, with an iterative method $\lim_{n\to\infty} x^{(n)} = x$, where n are the number of iterations and x is the exact solution of the system.
In CFD iterative methods are most commonly used because direct methods are too expensive. Furthermore, iterative methods are often the only choice for nonlinear equations. However, the condition $\lim_{n\to\infty} x^{(n)} = x$ is never met.
Indeed, given a linear system of equations, $Ax = B$, iterative methods generate a sequence of approximate solutions to the system that (hopefully) converges to the exact solution. After n iterations, an approximation of the exact solution is obtained:

$$Ax^{(n)} = B - r^{(n)} \tag{3.9}$$

Where $x^{(n)}$ and $r^{(n)}$ are respectively the approximate solution and the residual after n iterations. Defining the discretization error as the difference between the exact solution of the PDE and the numerical solution after n iteration:

$$\varepsilon^{(n)} = x - x^{(n)} \tag{3.10}$$

The replacement of the latter expression in the previous one results in:

$$A\varepsilon^{(n)} = r^{(n)} \tag{3.11}$$

The purpose of the iterations is to drive both residual and discretization error to zero. Actually, the residual will never be exactly zero and the simulation will stop only when a specific convergence criterion is met. Convergence, that is met when $x^{(n)} \to x$, is often measured by the level of residuals, that is the amount by which discretized equations are not satisfied. All commercial CFD software allow to choose the convergence criterion. There is not a fix convergence criterion to use, but its choice depends upon the requirements of the user, and the software package being used. A residual drop of at least three orders of magnitude (R_ϕ<10^{-3}) is a common threshold, but more stringent criteria (10^{-4}–10^{-6}) may be required during critical events like injection or ignition. Additionally, physical quantities such as in-cylinder pressure, heat release rate, and total energy are monitored across timesteps to verify temporal convergence.

Examples of iterative methods are Jacobi method, Gauss-Seidel method, Successive Overrelaxation method and Symmetric Successive Overrelaxation method.

Numerical methods, whether direct or iterative, are inherently affected by several types of error that can compromise solution accuracy. Among the most relevant are truncation errors, which arise when differential or integral equations are approximated by algebraic expressions, often due to the finite representation of infinite series solutions. Roundoff errors result from the repeated arithmetic operations that force the computer to approximate real numbers with finite precision, leading to cumulative inaccuracies. Discretization errors, on the other hand, stem from the difference between the exact analytical solution of the governing equations and the exact solution of the corresponding discrete numerical formulation.

In the context of CFD, ensuring the reliability of simulations requires a careful understanding and control of key numerical properties: consistency, stability, convergence, and accuracy [61].

A numerical scheme is considered consistent if its discrete operators reduce to the continuous partial differential operators as the spatial and temporal resolutions (Δx and Δt) approach zero. Stability refers to the boundedness of the numerical solution in the presence of perturbations—i.e., that discretization and roundoff errors do not amplify uncontrollably during time advancement. According to the Lax Equivalence Theorem, for linear problems, a consistent scheme will be convergent if and only if it is stable.

Convergence ensures that the numerical solution tends to the exact solution of the differential equations as the discretization becomes finer, while accuracy relates to the ability of the numerical solution to reproduce experimental or analytical reference data within acceptable error margins.

For explicit numerical schemes, stability is typically limited by the Courant–Friedrichs–Lewy (CFL) condition, expressed as:

$$C = \frac{u\Delta t}{\Delta x} \leq C_{max} \tag{3.12}$$

Where Δt is the time step, Δx is the spatial grid size, u is characteristic flow speed and C is the Courant Number. Violating the CFL condition leads to numerical divergence or spurious oscillations. Implicit schemes, frequently adopted in CFD simulations of ICEs, relax this constraint, allowing for larger time steps but requiring the solution of coupled algebraic systems at each iteration. In practical ICE simulations, pressure-based segregated solvers such as SIMPLE (Semi-Implicit Method for Pressure-Linked Equations) and PISO (Pressure-Implicit with Splitting of Operators) are often employed to resolve the strong coupling between pressure and velocity induced by piston motion and changing cylinder volume. Temporal discretization is commonly performed using second-order implicit schemes, which offer a good compromise between stability and numerical diffusion, especially in simulations involving stiff chemical kinetics.

Regarding spatial discretization, the treatment of convective terms plays a crucial role in the simulation's robustness and fidelity. High-resolution schemes, such as the second-order upwind method, are preferred to minimize artificial diffusion while avoiding non-physical oscillations near steep gradients, such as those observed at flame fronts or spray–air interfaces.

In summary, the careful integration of consistent, stable discretization schemes and rigorous convergence criteria is essential for producing accurate and reliable CFD predictions of turbulent reactive flows in ICEs.

3.5 CFD applied to ICEs

In order to accurately replicate the complex and highly transient processes that characterize ICEs, a variety of numerical models have been developed and integrated into modern CFD software over the past decades. These models are designed to capture the wide range of physical and chemical phenomena occurring during the engine cycle, including turbulent mixing, phase change, combustion and heat transfer. Given the highly coupled nature of these processes, each numerical model must strike a balance between physical fidelity and computational efficiency to ensure the feasibility of simulations within reasonable timescales.

This section provides a comprehensive overview of the primary physical phenomena taking place in ICEs and discusses their numerical representation within the CFD framework. Each subsection is dedicated to a specific aspect of engine operation, including fuel atomization and vaporization, turbulent flow behavior, combustion modeling for premixed and non-premixed regimes, and heat transfer processes involving both gas and solid boundaries. Particular attention is given to the justification for the selected modeling approaches.

3.5.1 Injection Phase

Since combustion in ICEs predominantly occurs in the gaseous phase, liquid fuels injected into the combustion chamber must undergo a sequence of physical transformations to facilitate efficient mixing and ignition. Upon entering the chamber, the high-pressure fuel jet interacts with the surrounding gas, triggering a complex breakup process known as atomization. This process transforms the initially coherent liquid jet into a spray of droplets with a broad size distribution, governed by aerodynamic forces, surface tension, and turbulent fluctuations. The subsequent vaporization of these droplets is critical to achieving a well-homogenized fuel–air mixture, which directly impacts combustion efficiency and pollutant formation.

Atomization is the physical process whereby a bulk liquid volume, such as a fuel jet, disintegrates into smaller particles (droplets) under the action of interfacial forces. These forces act at the liquid–gas interface, inducing instabilities that fragment the continuous jet into ligaments and droplets of varying diameters and velocities. The primary objective of atomization is to maximize the liquid–gas interfacial area, thereby enhancing evaporation rates and improving the efficiency of mass, momentum, and heat transfer between the two phases. Enhanced atomization, resulting in smaller droplets, also promotes more efficient combustion and contributes to lower emissions of UHC and particulates.

The breakup process can be divided into two stages: primary breakup, which occurs close to the nozzle exit where the liquid jet disintegrates into large ligaments and droplets under the

influence of aerodynamic shear and nozzle-induced effects (e.g., cavitation, turbulence); and secondary breakup, which describes the further fragmentation of these primary droplets into finer sprays, including droplet–droplet interactions such as collisions and coalescence.

The behavior of these breakup processes is governed by dimensionless numbers that quantify the relative importance of inertial, viscous, and surface tension forces. The Weber number (We) expresses the ratio of aerodynamic forces to surface tension forces:

$$We = \frac{\rho_g v_{rel}^2 D}{\Sigma} \tag{3.13}$$

Where ρ_g is the gaseous density, v_{rel} is the relative velocity between the two phases, D is the initial droplet diameter and Σ is the surface tension. The Ohnesorge number represents the ratio between the viscous forces and the inertia-surface tension forces:

$$Oh = \frac{\mu_l}{\sqrt{\rho_l D \Sigma}} \tag{3.14}$$

Where μ_l is the liquid viscosity and ρ_l is the density of the droplet.

In general, higher Weber numbers leads to higher desegregation of the liquid jet and a large number of droplets. On the contrary, higher Ohnesorge number means more droplet stability since viscous forces are dominant and they tend to dampen the oscillations of the droplet.

The modeling of the injection phase in CFD involves capturing these complex multi-phase interactions through a combination of atomization models and vaporization sub-models. Atomization models, such as the Kelvin–Helmholtz and Rayleigh–Taylor (KH-RT) breakup models, describe the primary and secondary disintegration of the fuel jet into droplets. Vaporization models, on the other hand, account for heat and mass transfer between the droplets and the surrounding gas, enabling the prediction of evaporation rates and the evolution of the spray cloud. The accuracy of these models is pivotal for correctly representing the initial conditions of combustion and, consequently, the overall engine performance in the numerical simulations.

3.5.1.1 Modeling Atomization

Different numerical models have been developed to represent the atomization process in ICEs simulations. In all atomization models, the liquid fuel jet is discretized into computational parcels, each representing a collection of droplets with homogeneous properties such as size, temperature, and velocity. These parcels are tracked individually using a Lagrangian reference frame, where their subsequent positions and thermodynamic states are functions of time only. Importantly, such models do not explicitly resolve the coherent liquid jet issuing from the injector nozzle but instead consider a set of dispersed droplets whose initial size is defined by

user-specified parameters or sub-models. Among the various atomization approaches proposed in the literature, notable examples include the Blob model, the Taylor Analogy Breakup model, and the Kelvin–Helmholtz/Rayleigh–Taylor (KH-RT) model [62]. While the Blob and TAB models offer simplicity and reduced computational cost, they are less suited to capturing the complex dynamics of high-pressure sprays in modern diesel injection systems. In contrast, the KH-RT model accounts for both primary and secondary breakup mechanisms driven by aerodynamic instabilities, making it particularly appropriate for turbulent, high-Reynolds-number jet disintegration. For these reasons, the KH-RT model was selected in this study to represent the atomization process of diesel sprays under engine-relevant conditions.

The KH-RT model [63] is one of the most widely adopted approaches in CFD for simulating spray breakup in high-pressure injection systems. It combines two fundamental instability mechanisms—KH and RT—to account for the two breakup processes (primary and secondary). This dual consideration is particularly important for modern diesel engines and gasoline direct injection systems, where aerodynamic forces and density gradients play a significant role in jet disintegration.

The KH instability arises due to aerodynamic shear at the interface between two fluids of different velocities, such as the high-speed liquid jet and the surrounding gas. This shear induces surface waves on the jet, which grow and lead to droplet formation. Conversely, RT instability occurs when a dense fluid (liquid fuel) is accelerated or decelerated relative to a lighter fluid (air), causing perturbations at the interface to amplify and trigger breakup. The KH-RT model captures the competition between these mechanisms, improving prediction accuracy over models that consider only one of them.

In the KH-RT formulation, the KH mechanism is dominant near the nozzle exit, within a characteristic breakup length, where it models the primary disintegration of the coherent liquid jet (Region A in Figure 3.4). Beyond this length, the model dynamically selects the dominant instability—either KH or RT—based on which predicts the fastest growth rate, governing the secondary breakup of droplets in the downstream spray region (Region B).

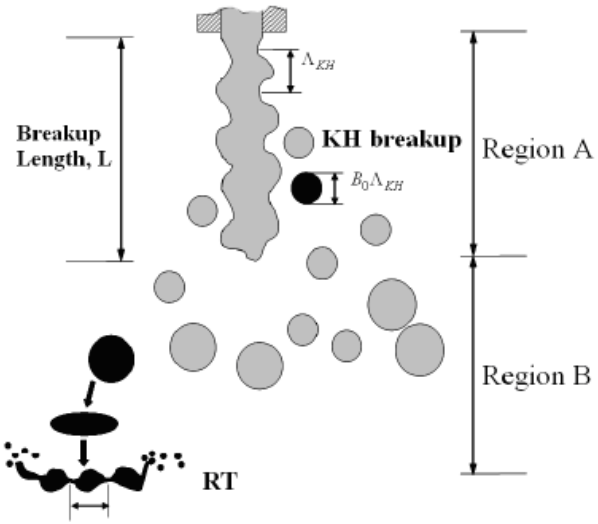

Figure 3.4: Schematic of KH-RT breakup model [63]

The KH component of the model is derived from linear stability analysis of a liquid jet, identifying the wavelength of the fastest-growing mode, Λ_{KH}, to estimate the size of child droplets as:

$$r_c = B_{KH}\Lambda_{KH} \tag{3.15}$$

Where B_{KH} is the Size Constant of the KH breakup model.

During the breakup the parent droplets r_P reduces the diameter as a result of the loss of mass. The radius change of the parent droplet is expressed by:

$$\frac{dr_P}{dt} = \frac{r_p - r_C}{\tau_{KH}} \quad \text{with} \quad \tau_{KH} = \frac{3.726 C_{KH} r_P}{\Lambda_{KH}\Omega_{KH}} \tag{3.16}$$

C_{KH} is the time constant of KH breakup and Ω_{KH} is the growth rate of the fastest wave growing on the surface of the droplet and it is a function of the Weber and Ohnesorge numbers. Finally, τ_{KH} is defined as the breakup time scale.

The RT model, used only in the KH-RT model in competition with the KH model, considers the instability generated when two fluids with different densities accelerate in a direction that is perpendicular to their interface. As well as the KH model, the fastest growing wave leads to break-up of the droplets. The main expressions for the RT model are the following:

$$r_c = B_{RT}\Lambda_{RT} \tag{3.17}$$

$$\frac{dr_P}{dt} = \frac{r_p - r_C}{\tau_{RT}} \quad \text{with} \quad \tau_{RT} = \frac{C_{RT}}{\Omega_{RT}} \tag{3.18}$$

B_{RT} and C_{RT} are the size constant and the time constant respectively. The RT model foresees the catastrophic breakup of parent droplets in child droplets.

Compared to simpler models such as the Blob model or the Taylor Analogy Breakup model, the KH-RT approach provides improved fidelity for high-pressure sprays by capturing both primary jet disintegration and secondary droplet breakup in turbulent environments. However, it assumes axisymmetric jet structures and neglects non-linear turbulence–spray interactions, which may limit its applicability in multi-hole injector configurations or under highly transient engine conditions [64]. Despite these limitations, the KH-RT model remains a robust and computationally efficient choice for engine CFD applications, providing accurate predictions of droplet size distributions and spray penetration critical for air–fuel mixing and combustion modeling.

3.3.1.2 Modeling Vaporization

The modeling of droplet vaporization in CFD is essential to accurately predict air–fuel mixing and combustion processes in ICEs. The main objective of a vaporization model is to quantify the mass loss of a liquid droplet over time due to phase change phenomena, considering the exchange of mass, momentum, and energy between the droplet and the surrounding gas. These interactions are strongly influenced by the relative motion between the two phases, as well as the droplet's internal heat transfer characteristics.

In its most simplified form, vaporization can be described by the classical D^2-law [65], which assumes a stationary droplet with no relative velocity with respect to the gas (i.e., droplet Reynolds number (Re=0). Additional simplifications include uniform temperature within the droplet, single-component liquid behavior, ideal gas properties in the surrounding phase, and constant thermophysical parameters. Under these assumptions, the time evolution of the droplet radius r_d and the droplet temperature T_d can be computed as follows:

$$4\pi r_d^2 \rho_L \frac{dr_d}{dt} = -\dot{m}_f \tag{3.19}$$

$$\frac{4}{3}\pi r_d^3 \rho_L C_{PL} \frac{dT_d}{dt} = \dot{Q}_L \tag{3.20}$$

where ρ_L is the liquid density, $\dot{m}_f$ is the vaporization rate of the droplet, C_{PL} is the liquid specific heat at constant pressure and $\dot{Q}_L$ is the thermal power entering the droplet.

By applying mass and energy conservation, and following analytical derivation, the vaporization rate of a stationary droplet is expressed as:

$$\dot{m}_f = 2\pi r_d D_f \rho_g B_M Sh \tag{3.21}$$

Where ρ_g is the density of the gas, D_f is the mass diffusivity, Sh is the Sherwood and B_M is the Spalding number, defined as:

$$B_M = \frac{Y_{F,\infty} - Y_{F,S}}{Y_{F,S} - 1} \tag{3.22}$$

Where $Y_{F,\infty}$ and $Y_{F,S}$ are the fuel mass fraction far away from the droplet surface and the fuel mass fraction at the droplet surface respectively.

However, in realistic engine conditions, droplets are subjected to significant relative motion with respect to the surrounding gas, which enhances heat and mass transfer due to convective effects. Furthermore, internal circulation within droplets can lead to more uniform internal temperature distributions. To account for these phenomena, more advanced vaporization models have been developed.

The Infinite Conductivity Model (ICM) assumes infinite thermal conductivity within the droplet, enforcing a uniform internal temperature throughout its life. While computationally efficient and suitable for small droplets, a major limitation of the ICM is that it fails to accurately capture internal temperature gradients that can arise in larger droplets or under low thermal conductivity conditions.

The Finite Conductivity Model (FCM) addresses this by solving the unsteady heat conduction equation within the droplet, capturing spatial temperature gradients and better representing physical behavior in more demanding conditions. Among the advanced models derived from FCM, the Discrete Multi-Component (DMC) model was used in this PhD thesis, due to its superior ability to model multi-species fuels under engine-relevant conditions.

In the DMC model, the droplet is treated as a multi-component system composed of various fuel species, each characterized by its own volatility [66]. In particular, with the fuel components treated as discrete species and assuming no absorption of the ambient gas into the liquid droplet, the system is a discrete system consisting of the liquid phase fuel species and a discrete mixture system of vapor phase fuel and ambient gas. The surface temperature of the droplet is determined from a heat and mass transfer balance at the interface between the droplet and the surrounding gas. Two regimes of heat transfer are considered, i.e., heat transfer occurring from the inside of the droplet to the surface, q_i, and heat transfer occurring from the outer gas to the surface, q_0. The rate of heat transfer balances the required heat for vaporization at the surface:

$$L(T_S)\dot{m} = q_i + q_0 \tag{3.23}$$

Where $L(T_S)$ is the latent heat of the fuel at the surface temperature T_S and $\dot{m}$ is the mass vaporization rate. Resolving energy equation for the gas phase and the governing equation for the change in the liquid fuel distribution the latter equation becomes:

$$L(T_S)\dot{m} = h_{i,eff}(T_d - T_s) + \frac{\kappa \bar{C}_p \dot{m}}{exp\left[\frac{2r_0 \bar{C}_p \dot{m}}{\lambda_{th} Nu} - \frac{[C_A](y_{FSur} - y_{F0})}{\lambda_{th}} \frac{Sh}{Nu}\right] - 1}(T_{sur} - T_s) \tag{3.24}$$

Where $h_{i,eff}$ is the heat transfer coefficient inside the droplet, which is determined from the thermal conductivity, λ, and the unsteady equivalent thickness of the thermal boundary layer, r_0 is the droplet radius, Nu is the Nusselt number, $\bar{C}_p$ is the average specific heat of the gas mixture including fuel vapor, κ is a correlation factor defined by Ra and Reitz [67], $[C_A]$ is the inter-diffusional difference of energy flux between fuel, y_{F0} and y_{FSur} are the mass fractions of fuel at the interface and far away, respectively, and T_{sur} is the surrounding gas temperature. The rate of mass transport at the droplet surface is calculated using the high mass transfer rate equation with Spalding's transfer number [68]:

$$\dot{m} = g_m \ln(1 + B_M) \tag{3.25}$$

Where g_m is the mass transfer coefficient determined from $g_m = (Sh\rho\bar{D}/2R)$, where $\bar{D}$ is the average diffusion species of fuel species.

In this way, the model provides a detailed framework to evaluate both the evolution of the droplet temperature field and the component-wise vaporization rate, thereby capturing the coupled thermal and compositional dynamics of multi-component fuel droplets under engine-relevant conditions. This makes the DMC model particularly well-suited for CFD simulations of realistic sprays in ICEs, where accurate prediction of evaporation behaviour strongly influences mixture formation and combustion performance.

3.5.2 Turbulence Phenomenon

Turbulence is a highly complex, three-dimensional, and unsteady phenomenon characterized by chaotic fluctuations in velocity, pressure, and other flow properties. In ICEs, the in-cylinder flow field during the engine cycle is inherently turbulent due to the high Reynolds numbers achieved. The Reynolds number is a dimensionless parameter that quantifies the ratio of inertial to viscous forces within a flow and is defined as:

$$Re = \frac{uL}{\upsilon} = \frac{\rho uL}{\mu} \tag{3.26}$$

where u is the flow speed, L is a characteristic length for a given geometry, ρ is the density of the fluid, υ and μ are respectively the kinematic and dynamic viscosity. In ICEs, the combination of high intake velocities, rapid piston motion, and small characteristic dimensions leads to Reynolds numbers on the order of 10^4–10^6, indicating fully turbulent flow regimes where inertial forces dominate over viscous damping.

Turbulent flows are inherently difficult to model and predict because of their stochastic nature and the wide range of length and time scales involved. A widely accepted conceptual framework for turbulence is Richardson's energy cascade theory [69], which describes turbulence as a hierarchy of eddies of progressively smaller sizes. Large eddies, generated by boundary interactions and flow instabilities, contain most of the TKE and are characterized by integral length scales (L_I). These large structures are unstable and break down into smaller eddies, transferring their energy without dissipation through inertial subranges. This process continues until the eddies reach a sufficiently small scale, known as the Kolmogorov microscale (η), where viscous forces become dominant, and the TKE is converted irreversibly into internal energy (heat) through viscous dissipation. This multiscale process is known as the turbulent energy cascade.

In the context of ICEs, turbulence generation and evolution are closely linked to the engine's operating phases. During the intake stroke, the flow entering the cylinder through the intake valves creates large-scale structures, energizing the mean flow field and imparting kinetic energy (K) to the system. As the piston progresses toward BDC, flow interactions with the cylinder walls and piston surfaces amplify turbulence through shear layers and flow impingements. The large-scale kinetic energy is gradually converted into TKE (k) via production mechanisms (P), representing the energy associated with both macro- and micro-vortical motions within the cylinder. Finally, as the energy cascade reaches the smallest scales, viscous dissipation (D) converts the remaining TKE into heat at the molecular level.

This process, schematically illustrated in Figure 3.5, highlights the importance of turbulence for ICE operation. Turbulence enhances air–fuel mixing, promotes flame propagation during combustion, and influences heat transfer rates to the cylinder walls. Accurately capturing the turbulence characteristics and their evolution is thus essential in CFD modeling to predict engine performance, combustion efficiency, and pollutant formation reliably.

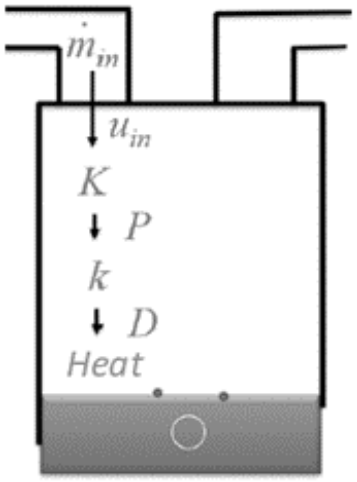

Figure 3.5: Schematic of energy transformations in an ICE

3.5.2.1 Modeling Turbulence

Turbulence modeling is a critical aspect of CFD, particularly in ICE simulations, where in-cylinder flows are characterized by high Reynolds numbers, complex geometries, and transient boundary conditions. Turbulence models can be broadly classified into three main categories based on their level of fidelity and computational cost, as illustrated in Figure 3.6. These are Direct Numerical Simulation (DNS), Large Eddy Simulation (LES), and Reynolds-Averaged Navier–Stokes (RANS) models [66].

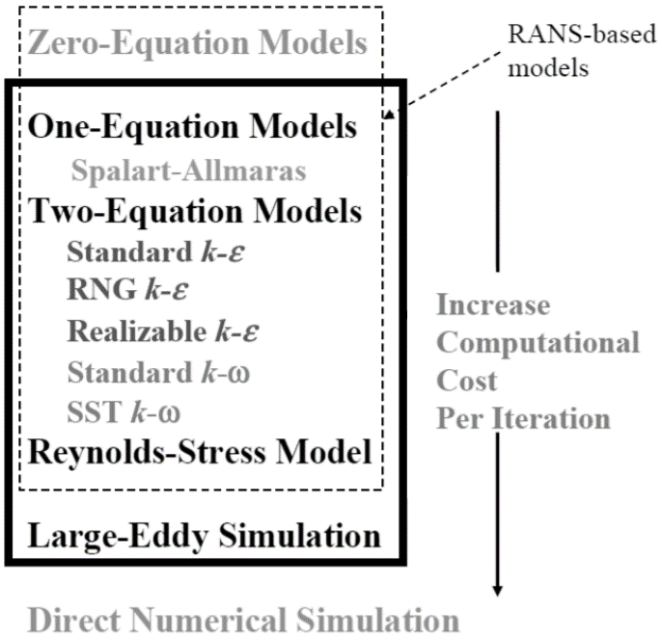

Figure 3.6: Turbulence Models in CFD [66]

- At the highest level of accuracy, DNS solves the full Navier–Stokes equations without any turbulence modeling assumptions. DNS resolves all turbulent scales, from the largest energy-containing eddies down to the smallest dissipative scales, known as the

Kolmogorov microscales (η). The mesh resolution and time steps required scale approximately with Re^3, making DNS computationally infeasible for the complex, high-Reynolds-number flows in ICEs. As a result, DNS is primarily confined to academic research on canonical flows and serves as a reference for validating lower-fidelity models.

- LES offers a compromise between accuracy and computational expense. LES directly resolves the large, energy-containing turbulent structures while modeling the effects of the smaller, subgrid-scale eddies using subgrid-scale (SGS) models. The assumption that small-scale turbulence is isotropic allows for simpler modeling of these scales. LES has proven effective for many engineering flows but remains computationally demanding for full engine simulations, particularly due to the fine spatial and temporal resolutions required to capture near-wall turbulence and cyclic variability in ICEs.

At the industrial level, RANS models are the most widely used approach. RANS relies on time-averaged formulations of the Navier–Stokes equations, achieved through Reynolds decomposition, which separates each flow variable into a mean component ($\bar{u}$) and a fluctuating component (u'):

$$u = \bar{u} + u' \tag{3.27}$$

This leads to the RANS equations, where additional terms, known as the Reynolds stresses ($\rho\overline{u_i' u_j'}$), appear due to turbulence-induced momentum transport. These terms require closure models, giving rise to a variety of turbulence models. For incompressible, Newtonian fluids, the RANS momentum equation in tensor form is:

$$\rho\overline{u}_j \frac{\partial \overline{u}_i}{\partial x_j} = \rho\overline{f}_i + \frac{\partial}{\partial x_j}\left[-\overline{p}\delta_{ij} + \mu\left(\frac{\partial \overline{u}_i}{\partial x_j} + \frac{\partial \overline{u}_j}{\partial x_i}\right) - \rho\overline{u_i' u_j'}\right] \tag{3.28}$$

The most common approach to close the system is through the Boussinesq hypothesis, which relates the Reynolds stresses to the mean velocity gradients via an eddy viscosity (υ_t):

$$-\overline{u_i' u_j'} = \upsilon_t\left(\frac{\partial \overline{u}_i}{\partial x_j} + \frac{\partial \overline{u}_j}{\partial x_i}\right) - \frac{2}{3}k\delta_{ij} \tag{3.29}$$

This closes the RANS system by reducing the number of unknowns to those which can be computed from additional equations for turbulence quantities. This approach directly links the RANS methodology to the development of turbulence models, as the eddy viscosity and TKE

are not known a priori and must be determined by solving additional transport equations. Depending on the model, one or more equations are introduced to compute these variables, leading to different classes of RANS-based turbulence models. RANS turbulence models are generally classified by the number of additional transport equations they solve:

- The standard $k-\varepsilon$ model, which solves transport equations for turbulent kinetic energy (TKE) (k) and its dissipation rate (ε). It provides a robust, general-purpose model applicable to many industrial flows.
- The RNG (Renormalized Group) $k-\varepsilon$ model improves upon the standard formulation using renormalization group theory to account for different turbulence scales and streamline curvature effects [71]. It modifies the ε-equation production term, enabling a more accurate representation of highly strained and swirling flows. This enhanced accuracy makes the RNG $k-\varepsilon$ particularly suitable for ICE simulations. It is also the default turbulence model used by ANSYS Forte and has been adopted in this study.
- The standard $k-\omega$ model uses the specific dissipation rate (ω) instead of ε for closure, improving near-wall flow predictions.
- The SST $k-\omega$ model blends $k-\omega$ near walls and $k-\varepsilon$ in the free stream, providing improved accuracy in adverse pressure gradients and separated flows.
- Reynolds Stress Models (RSM): These directly solve transport equations for each component of the Reynolds stress tensor, avoiding the isotropic eddy-viscosity assumption. While RSMs can capture anisotropic turbulence effects, their complexity and high computational cost limit their use in industrial applications.

The RNG $k-\varepsilon$ model was selected for this work due to its improved handling of turbulence in highly strained and rotational flows typical of in-cylinder processes, while maintaining computational efficiency.

Specifically, the RNG $k-\varepsilon$ model is an advanced two-equation turbulence model that extends the widely used standard $k-\varepsilon$ model formulation by incorporating statistical techniques derived from renormalization group theory. It solves transport equations for the TKE (k) and its dissipation rate (ε), which provide a measure of the turbulence intensity and its rate of decay, respectively. The transport equation for k is expressed as:

$$\frac{\partial(\bar{\rho}k)}{\partial t}+\frac{\partial\left(\bar{\rho}ku_j\right)}{\partial x_j}=\frac{\partial}{\partial x_j}\left[\left(\mu+\frac{\mu_t}{\sigma_k}\right)\frac{\partial k}{\partial x_j}\right]+G_k-\bar{\rho}\varepsilon \tag{3.30}$$

where G_k represents the production of TKE due to velocity gradients, μ_t is the turbulent (eddy) viscosity, and σ_k is the turbulent Prandtl number for k. The dissipation rate ε is governed by:

$$\frac{\partial(\bar{\rho}\varepsilon)}{\partial t} + \frac{\partial(\bar{\rho}\varepsilon u_j)}{\partial x_j} = \frac{\partial}{\partial x_j}\left[\left(\mu + \frac{\mu_t}{\sigma_\varepsilon}\right)\frac{\partial \varepsilon}{\partial x_j}\right] + C_{1\varepsilon}\frac{\varepsilon}{k}G_k - C_{2\varepsilon}\rho\frac{\varepsilon^2}{k} - R_{add} \tag{3.31}$$

where σ_ε is the turbulent Prandtl number for ε, $C_{1\varepsilon}$ and $C_{2\varepsilon}$ are model constants, and R_{add} is an additional term derived from the RNG theory to account for the interaction between dissipation and mean strain.

The turbulent viscosity μ_t is determined by using:

$$\mu_t = \rho C_\mu \frac{k^2}{\varepsilon} \tag{3.32}$$

with C_μ as a model constant. The inclusion of the R term and variable turbulent Prandtl numbers in the RNG formulation allows it to better capture turbulence in flows with strong strain rates, curvature, and recirculation—common features in ICE simulations. Furthermore, damping functions inherent to the model improve its performance near walls, enhancing its applicability to complex geometries without requiring additional wall functions.

3.5.3 Combustion Phenomenon

Combustion is defined as a chemical reaction in which a fuel reacts with an oxidant to form products, accompanied by the release of energy in the form of heat.

Two kind of combustion process and flames can occur based on the fuel/oxidizer mixing: in a premixed combustion (premixed flame) fuel and oxidant are mixed before combustion, while in a diffusion combustion (diffusion flame), or non-premixed combustion, they are separated. Both premixed and diffusion flames can be laminar or turbulent depending on the Reynolds number of the region where the flame is located as it is shown in Figure 3.7.

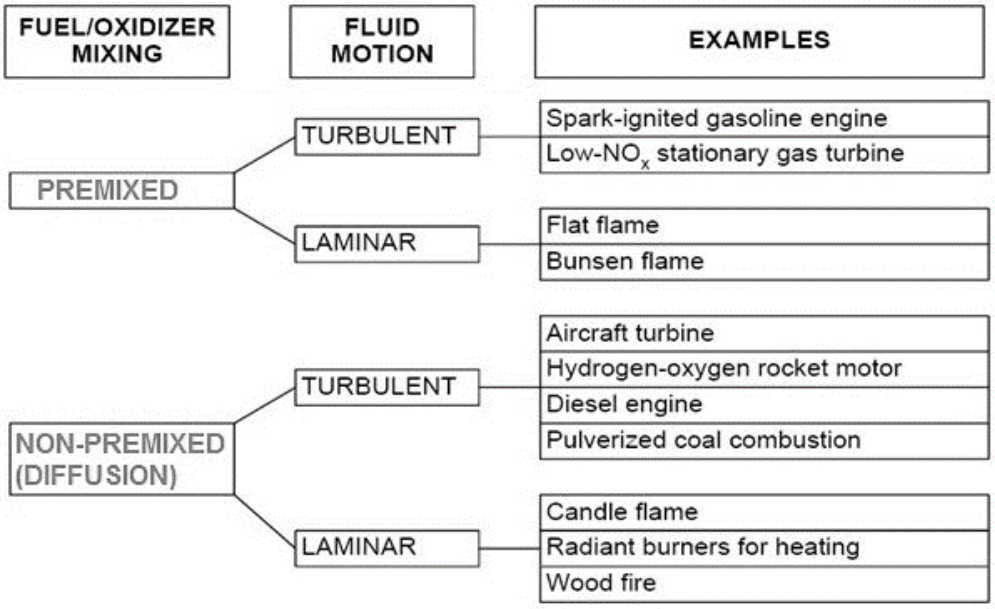

Figure 3.7: Types of flame with some examples

The science of combustion involves complex interactions between many constituent disciplines, including chemical kinetics, fluid dynamics, thermodynamics, heat and mass transfer and two-phase flow (i.e., the gas phase, and a liquid or solid fuel phase).

Each of these topics may be represented mathematically by equations, however, since all the processes are interdependent, these governing equations must be solved simultaneously to model the overall combustion process.

In practice, when combustion is activated in a CFD simulation, the model should be able to solve in addition to governing equations for fluid flow (conservation of mass, momentum and energy) and turbulence equations, also the equations of combustion chemistry and chemical kinetics.

The conservation equation for the ith chemical species can be written as:

$$\frac{\partial(\rho Y_i)}{\partial t} + \nabla \cdot (\rho \vec{v} Y_i) = -\nabla \cdot \vec{J}_i + R_i + S_i \tag{3.33}$$

Where Y_i is the mass fraction of a chemical species i, R_i is the mass rate of creation or depletion of chemical species i by chemical reaction and S_i is the rate of creation by addition from the dispersed phase. J_i is the diffusion flux of species i and in turbulent flows is given by:

$$J_i = -\left(\rho D_{im} + \frac{\mu_t}{Sc_t}\right)\nabla Y_i - D_{i,T}\frac{\nabla T}{T} \tag{3.34}$$

Where $D_{i,T}$ is the thermal diffusion coefficient and $D_{i,m}$ is the mass diffusion coefficient of species ith in the mixture, Sc_t is the turbulent Schmidt number and μ_t is the turbulent viscosity.

In multistep and multispecies reactions, the source of chemical species i due to reaction, R_i, is computed as the sum of the reaction sources over the k reactions that the species may participate in. The overall rate of production of species i is:

$$R_i = \sum_k R_{i,k} \tag{3.35}$$

The reaction rate, $R_{i,k}$ is controlled either by kinetics or mixing. Several models were formulated to describe the source term R_i. Among them there are the laminar finite-rate and the eddy-dissipation model.

3.5.3.1 Modeling Non-Premixed Combustion

Non-premixed (diffusive) combustion, where fuel and oxidizer meet and react at the interface of their respective flows, requires modeling approaches capable of capturing the complex interplay between turbulent mixing and chemical kinetics. Over the years, several models have been developed, each with varying degrees of accuracy and computational cost:

- Eddy Dissipation Model (EDM) [72]: this model assumes that chemical reactions are infinitely fast compared to turbulent mixing. The reaction rate is determined solely by the rate at which turbulent eddies bring fuel and oxidizer together, making it suitable for systems where mixing limits combustion.
- Finite-Rate Chemistry Model [73]: in this approach, only Arrhenius-type chemical kinetics are considered, without accounting for turbulence effects. It is accurate for laminar flows or regimes where turbulence has little influence on combustion.
- Finite-Rate/Eddy Dissipation Model (Finite-Rate/EDM): this hybrid approach combines the two limits above by evaluating both the finite-rate kinetics and the turbulence-controlled mixing rate, taking the lower of the two as the effective reaction rate. This makes it suitable for practical engineering applications where both mixing and chemistry play roles.
- Probability Density Function (PDF) Models: these solve transport equations for joint PDFs of species and temperature, offering a detailed statistical treatment of turbulence-chemistry interaction but at a significant computational cost.
- Eddy Dissipation Concept (EDC): this model assumes that reactions occur in small turbulent structures (fine scales) and couples turbulence and chemistry more tightly than the standard EDM [74].

In non-premixed combustion the reaction rate is influenced by the interplay between chemical kinetics and turbulent mixing. Accurate modeling of such processes in engines requires approaches capable of capturing this dual dependency. The Turbulence-Kinetics Interaction (TKI) model, originally proposed by Kong and Reitz [75], very similar to the EDC model, addresses this challenge by coupling detailed chemical kinetics with turbulent mixing effects within CFD simulations. The model was developed in response to the observation that purely kinetics-controlled simulations often predict excessively fast combustion rates, failing to account for the finite time required for turbulent eddies to mix fuel and oxidizer down to the molecular scale. Conversely, assuming infinitely fast chemistry and purely turbulence-controlled rates can also lead to inaccuracies in cases where chemical reactions are not instantaneous. The TKI model bridges these two extremes by introducing a characteristic effective time scale that modulates the species production rates. The fundamental premise of the TKI model is that the actual reaction rate for each species is governed by the relative magnitudes of the chemical and turbulent time scales. This is expressed mathematically as:

$$\omega_i = \frac{Y_{k,eq} - Y_k}{\tau_{eff}} \tag{3.36}$$

where the effective time scale is related to the chemical time scale τ_{chem} and the turbulent scalar mixing time scale τ_{mix}

$$\tau_{eff} = \tau_{chem} + \tau_{mix} \tag{3.37}$$

This scaling ensures that if turbulent mixing is extremely fast ($\tau_{mix} \to 0$), the model reduces to purely kinetics-controlled behavior. Conversely, if chemical reactions are extremely fast ($\tau_{chem} \to 0$), the reaction rate becomes mixing-controlled (or turbulence-controlled).

The chemical time scale is defined as the time required for a species to reach its equilibrium concentration under perfectly mixed conditions. It is calculated from the kinetics solver as:

$$\tau_{chem} = \frac{Y_{k,eq} - Y_k}{\Delta Y_k} dt \tag{3.38}$$

where $Y_{k,eq}$ is the equilibrium mass fraction of species, Y_k is its current mass fraction, ΔY_k is the change in species concentration over a timestep Δt. To reduce computational complexity, two key assumptions are introduced: the chemical timescale is assumed to be the same for all species and is determined based on the fuel.

This leads to a simplified expression for the chemical timescale:

$$\tau_{chem} = \frac{-Y_{fuel}}{\Delta Y_{fuel}} dt \tag{3.39}$$

The turbulent scalar mixing time scale is obtained from the local TKE and dissipation rate:

$$\tau_{mix} = C_{tki}\tau_{turb} = C_{tki}\frac{k}{\varepsilon} \tag{3.40}$$

Finally, the TKI model adjusts the species mass fractions at each timestep according to:

$$\omega_i = \frac{\tau_{chem}}{\tau_{eff}} \Delta Y_k \tag{3.41}$$

This formulation ensures that turbulence effects become significant after ignition has occurred and the reaction zones have grown to scales comparable to turbulent eddies. During ignition, which is initiated at the molecular level, the process remains dominated by chemical kinetics. The emphasis of the latter equation is the incorporation of the mixing concept in the reaction rate in addition to the chemical kinetics itself.

In general, the TKI model provides a balance between physical accuracy and computational efficiency. Unlike simpler models (e.g., EDM), it does not assume infinitely fast chemistry and can handle cases where chemical kinetics are not negligible. At the same time, it avoids the high computational cost of PDF model, making it well-suited for engine-scale simulations where both turbulence and finite-rate chemistry influence combustion behavior.

3.5.3.2 Modeling Premixed Combustion

In a premixed combustion, fuel and oxidizer are mixed at molecular level before the ignition. Combustion occurs as a flame front propagating into the unburnt reactants. Examples of premixed combustion include aspirated SI ICEs, lean-premixed gas turbine combustors, and gas-leak explosions.

In general, premixed combustion is more difficult to model compared to a non-premixed combustion. This is because the premixed combustion process occurs as a propagating thin flame, stretched and contorted by turbulence, while, as seen in the previous paragraph, a non-premixed combustion can be simplified to a mixing problem.

In particular, for subsonic flows, the burning rate is determined by both the laminar flame speed and the turbulent eddies:

$$\frac{dm_b}{dt} = \rho_u A_T S_L \tag{3.42}$$

Where ρ_u is the density of unburnt gas, A_T is the turbulent flame area and S_L is the laminar flame speed.

The laminar speed can be obtained experimentally by using a transparent tube in which air and fuel enters at a given speed. A propagating flame will be visible in the tube. Increasing the entering velocity of the mixture, the flame will slow and eventually stop inside the tube. This entering velocity is the laminar flame speed. The laminar flame speed is determined by the kinetic scheme and the rate that species and heat diffuse upstream into the reactants and burn. Its value depends on the mixture (fuel structure, stoichiometry) and, in particular, the maximum of the laminar flame speed is always around the stoichiometric conditions, as shown in Figure 3.8 for gasoline and ethanol.

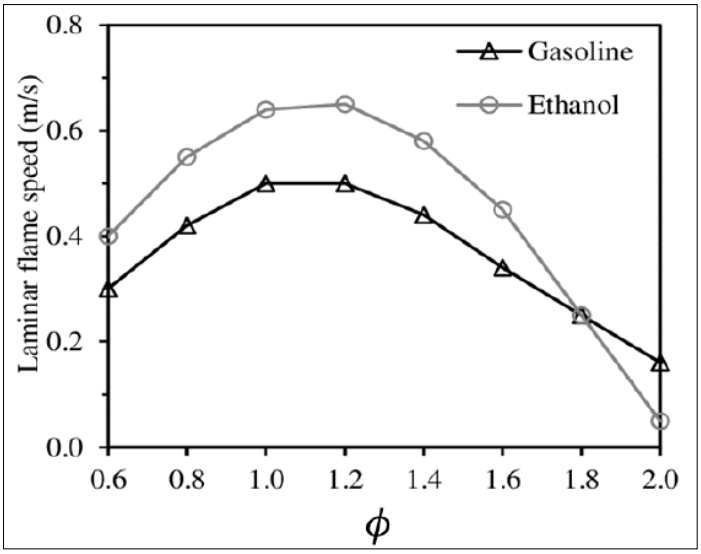

Figure 3.8: Trend of laminar flame speed of two different fuels [76]

In addition, the S_L depends on thermodynamic conditions upon mixture ignition (pressure, temperature) and on the quantity of EGR [76]:

$$S_L = S_{L0}\left(\frac{T_u}{T_0}\right)^{\alpha}\left(\frac{p_u}{p_0}\right)^{\beta}\left(1-\gamma x_r^{\delta_S}\right) \tag{3.43}$$

Where S_{L0} is the laminar flame speed at standard conditions, p_u and T_u are the pressure and temperature of unburnt gases, p_0 and T_0 are the pressure and temperature at standard conditions, α_S and β_S are parameters function of the equivalence ratio, x_r is the percentage of inert in unburned mixture, γ and δ_S are constant coefficients.

The laminar flame speed at standard conditions can be specified using the Metghalchi or Gülder formula [77]. Their expressions are reported below:

$$S_{L0} = B_m + B_\phi(\phi-\phi_m)^2 \tag{3.44}$$

$$S_{L0} = \omega\phi^{\eta}exp(-\xi(\phi-\sigma)^2) \tag{3.45}$$

Values of B_m, B_ϕ, ϕ_m and ω, η, ξ, σ are listed on tables and they depend on the selected fuel. The flame has a thickness δ described by the following relation:

$$\delta = \frac{\upsilon}{S_L} \tag{3.46}$$

Where υ is the kinematic viscosity.

Moreover, a characteristic time of chemistry time can be defined as the time that unburnt gases take to cross the flame front:

$$t_c = \frac{\delta}{S_L} \tag{3.47}$$

In addition, a stretch effect must be taken into account since the propagation of the flame is spherical [78]:

$$S_{L,streched} = S_L - L_b K \tag{3.48}$$

Where K is the stretch rate and L_b is a characteristic length, known as Markstein length. The stretched laminar flame speed can be higher or lower compared to the unstreched laminar flame speed, since $L_b < 0$ or $L_b > 0$ depending on the fuel and equivalence ratio.

The turbulence also influences the flame speed. In particular, the turbulent vortices corrugate the flame, and this leads to an increase of the reaction area that passes from laminar area, A_L to higher turbulent area, A_T. The consequence is an increase of the burning rate.

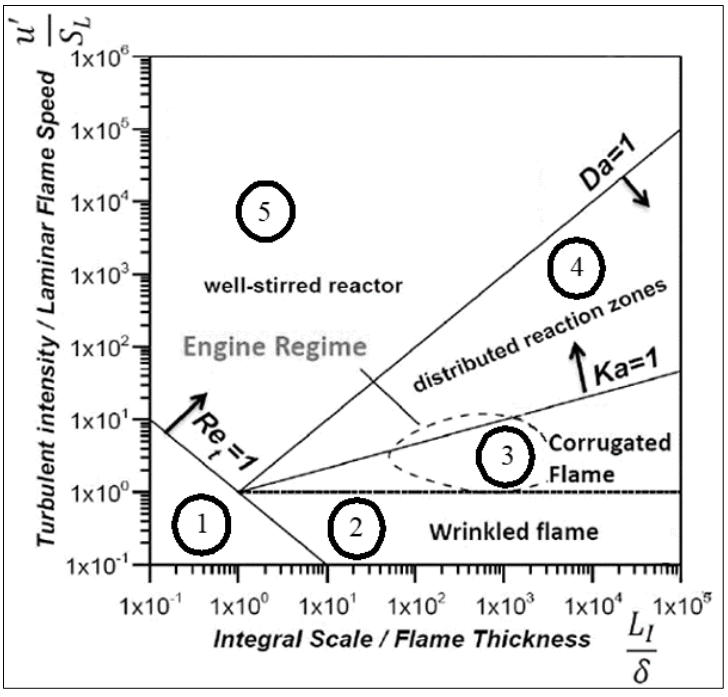

Figure 3.9: Borghi diagram [79]

To better understand how the turbulence affects the combustion it is necessary to introduce the Borghi diagram (Figure 3.9) in which different combustion regimes are represented depending on the ratio between the length scales of the turbulent flow L_I and the flame thickness δ and the ratio between the turbulent intensity u' and the laminar flame speed S_L, and on the dimensionless number of Reynolds, Damköhler and Karlovitz. These two last dimensionless numbers are defined respectively as:

$$Da = \frac{t_t}{t_c} \tag{3.49}$$

$$Ka = \frac{t_c}{t_\eta} \tag{3.50}$$

Where t_t is the characteristic time of turbulence of macro-vortices (turnover time), and t_η is the characteristic time of the micro-vortices.
A detailed description of the combustion regimes is here provided [79]:

- Region 1 ($Re < 1$): there is only laminar propagation of the flame. This is the only zone in which there is no turbulence.
- Region 2 ($Re > 1, Ka < 1, Da > 1$): in this zone $u' < S_L$. This means that there is turbulence, but it is small in intensity, and it can be negligible compared to the laminar speed of the flame front. The flame in this area is practically spherical in the case of an engine, at most slightly corrugated due to the effect of little turbulence. This area is called of the wrinkled flames.
- Region 3 ($Re > 1, Da > 1, Ka < 1$): the values of the dimensionless numbers are the same of the second region, but, in this case, $u' > S_L$. Furthermore, since $t_t > t_c$ and $t_c < t_\eta$, the result is $t_t > t_\eta > t_c$. Turbulence is slow compared to chemistry and therefore the dimension of the flame front is lower than the smallest scale of turbulence. Turbulence cannot affect chemistry. This does not mean, however, that the burning rate is laminar, but the thickness of the flame is practically a surface of discontinuity with infinitesimal thickness. The flame is subject only to the convective action of turbulence. The presence of vortices at the various scales deforms the flame front, making it no longer spherical, but with corrugations (macro-corrugations for the macro-vortices, up to micro-corrugations in the micro-vortex scale). But locally, the flame front always propagates at S_L (laminar speed) and on average the surface remains spherical and is not torn by vortices. But it is the burning rate that increases, because the reaction surface

grows a lot due to corrugations. The mechanism that allows the increase in the burning rate is the simple growth of the reaction surface.

- Region 4 ($Re > 1, Da > 1, Ka > 1$): in this zone $t_t > t_c$ and $t_c > t_\eta$ so $t_t > t_c > t_\eta$. In this occasion the turnover time of the smallest vortices is higher than chemistry, thus the Kolmogorov vortex enters the thickness of the flame front (that is the reaction zone) and can therefore affect the chemistry of the combustion process. This region is called distributed reaction zone because there are more areas where the combustion occurs. It is called also region of thick flames.
- Region 5 ($Re > 1, Da < 1, Ka > 1$): this time $t_t < t_c$ and $t_c > t_\eta$ so $t_c > t_t > t_\eta$. The chemistry is very slow, and the turbulence controls all the process. There is not a true propagation of the flame front, and this zone is called well-stirred reactor since the reaction is homogeneous.

The engine operating conditions are located in the dashed band, mainly in the corrugated flame zone. However, also the thick flames can occur, especially when the rpm increases (in this case turbulence and so u' increases) or the mixture becomes lean (in this case S_L decreases).
In 3D combustion simulation, beyond the use of correlations, the S_L could be calculated directly during the calculations. In particular, a tabulated approach is often adopted. In this method, S_L is first computed using detailed chemical mechanisms in 1D flame simulations, covering a range of pressures, temperatures, and equivalence ratios. The results are then stored in a lookup table, where S_L is expressed as a function of these parameters. During the 3D simulation, the solver accesses this table: for each computational cell, based on the local thermodynamic conditions (pressure, temperature, and equivalence ratio), the corresponding S_L is interpolated from the precomputed data. This approach allows accurate representation of flame propagation characteristics while maintaining computational efficiency.
However, since combustion and turbulence are two phenomena related, the consequence is that the effective flame speed in the engine is a turbulent flame speed, and a general expression of it can be expressed as:

$$S_T = S_L \frac{A_T}{A_L} \tag{3.51}$$

This expression means that the flame is only corrugated by the turbulence since the smallest turbulence eddies are bigger than the width of the flame speed (Region 3 of the Borghi diagram).

Several modeling strategies have been proposed to track the propagation of the flame front in a premixed combustion and use the S_L. Broadly, they can be categorized as:

- Thickened Flame Models [80]: In which the flame front is artificially broadened to be resolved on the numerical mesh.
- Level-Set and G-equation Models: Which use scalar functions to track the position of the flame front as a propagating interface.
- Flamelet-Based Approaches [81]: Where the structure of the flame is assumed to remain thin and laminar, embedded into turbulent flows.

Among these, level-set models, particularly the G-equation approach, have gained widespread application in engine CFD due to their simplicity, efficiency, and ability to represent the evolution of wrinkled premixed flame fronts under turbulent conditions and it was chosen for the simulations in the thesis. The model can be applied to the corrugated flame regime where the flame structure is totally embedded within eddies of the size of Kolmogorov scales, and to the thin reaction zone where the Kolmogorov eddies can penetrate into the flame structure.
The G-equation model consists of a set of Favre-averaged set equations [82]:

$$\frac{\partial \tilde{G}}{\partial t} + \left(\tilde{\vec{u}} - \vec{u}_{vertex}\right) \cdot \nabla \tilde{G} = \frac{\overline{\rho}_u}{\overline{\rho}_b} S_T^0 \left|\nabla \tilde{G}\right| - D_T \tilde{\kappa} \left|\nabla \tilde{G}\right| \tag{3.52}$$

$$\frac{\widetilde{\partial G''^2}}{\partial t} + \tilde{\vec{u}} \cdot \nabla \widetilde{G''^2} = \nabla_{||} \cdot \left(\frac{\overline{\rho}_u}{\overline{\rho}_b} D_T \nabla_{||} \widetilde{G''^2}\right) + 2 D_T \left(\nabla \tilde{G}\right)^2 - c_s \frac{\tilde{\varepsilon}}{\tilde{k}} \widetilde{G''^2} \tag{3.53}$$

Where $\nabla_{||}$ is the tangential gradient operator, $\vec{u}$ is the fluid velocity, $\vec{u}_{vertex}$ is the velocity of the moving vortex; ρ_u and ρ_b are the average densities of the unburned and burned mixtures, respectively, D_T is the turbulent diffusivity, $\tilde{\kappa}$ is the Favre mean flame front curvature and c_s is a model constant. Together with the RANS equations and the turbulence modeling equations, the G-equations provide a complete set of equations able to describe premixed turbulent flame-front propagation.
However, at the earliest stage of combustion, the flame front originates from a spark-initiated ignition kernel, whose size is typically much smaller than the computational cell dimensions. Under such conditions, the flame front cannot be resolved using conventional Eulerian-based formulations. To overcome this limitation, the Discrete Particle Ignition Kernel Flame (DPIK) model is employed [83]. This model treats the ignition kernel as a spherical structure whose surface is represented by Lagrangian particles; the local flame surface density is then derived from the spatial distribution of these particles across the computational mesh.

Assuming the temperature inside the kernel to be uniform, the kernel growth rate is:

$$\frac{dr_k}{dt} = \frac{\rho_u}{\rho_k}\left(S_{plasma} + S_T\right) \tag{3.54}$$

where r_k is the kernel radius, ρ_u is the density of the local unburnt region, ρ_k is the density inside the kernel region.

The plasma velocity S_{plasma} is given as:

$$S_{plasma} = \frac{\dot{Q}_{spk}\eta_{eff}}{4\pi r_k^2\left[\rho_u(u_k - h_u) + P\frac{\rho_u}{\rho_k}\right]} \tag{3.55}$$

Where ρ_u and h_u are the density and enthalpy of the unburned mixture. ρ_k and u_k are the density and internal energy of the mixture inside the kernel. $\dot{Q}_{spk}$ is the electrical energy discharge rate, η_{eff} is the electrical energy transfer efficiency due to heat loss to the spark plug and it has a typical value of 0.3.

In the G-equation model, the turbulent flame speed can be obtained as:

$$\frac{S_T}{S_L} = 1 + I_P\left\{-\frac{a_4 b_3^2}{2b_1}\frac{L_I}{\delta} + \left[\left(\frac{a_4 b_3^2}{2b_1}\frac{L_I}{\delta}\right)^2 + a_4 b_3^2\frac{u' L_I}{S_L^0 \delta}\right]^{\frac{1}{2}}\right\} \tag{3.56}$$

In which the term I_P is a progress variable, a_4, b_1 and b_3^2 are constants, L_I is the turbulence integral length scale and δ is the laminar flame thickness.

When the flame structure grows bigger than a characteristic flow length scale the calculation switches from the Kernel model to the turbulent G-equation model. The transition is controlled by a comparison of the kernel radius with a critical size that is proportional to the locally averaged turbulence integral length scale:

$$r_k \geq C_{m1} \cdot L_I = C_{m1} \cdot 0.16\frac{k^{\frac{3}{2}}}{\varepsilon} \tag{3.57}$$

Where C_{m1} is a model constant and L_I is the turbulent integral length scale.

3.5.4 Heat Transfer Phenomenon

Heat transfer in ICEs is a complex phenomenon governed by the interaction of conduction, convection, and radiation processes occurring within the combustion chamber. During engine operation, the hot gases resulting from combustion exchange energy with the cooler solid boundaries of the cylinder walls, piston crown, and cylinder head. This heat transfer affects not only the thermal loading of engine components but also the in-cylinder thermodynamic state,

which in turn influences combustion efficiency, emission formation, and overall engine performance. The heat flux through the chamber walls is mainly due to gas-phase convection, fuel-film conduction and radiation. However, under typical engine operating conditions, gas-phase convective heat transfer is the dominant factor, while the other two mechanisms are usually negligible. The convective heat transfer in the gas phase is driven by the turbulent motion of the combustion gases. Indeed, as the piston moves, complex flow structures such as swirl, tumble, and squish generate highly unsteady and three-dimensional turbulence that enhances the mixing of hot and cold gas layers near the walls. This turbulent convection leads to localized variations in the heat transfer coefficient, h, and results in spatially non-uniform wall heat fluxes. The convective heat flux at the wall is typically expressed by Newton's law of cooling:

$$q_W = h(T_g - T_w) \tag{3.58}$$

Where q_W is the wall heat flux, T_g is the gas temperature near the wall, and T_w is the wall temperature. The heat transfer coefficient h depends on the local flow velocity, turbulence intensity, and thermophysical properties of the gas such as density, viscosity, and thermal conductivity. In addition to convection, conduction within the solid engine components plays a critical role in dissipating the absorbed heat throughout the engine structure. This internal conduction determines the wall surface temperature T_w, which forms the boundary condition for the gas-side heat transfer. Radiative heat transfer is generally a minor contribution under typical engine conditions due to the relatively low temperatures of the walls and the low emissivity of the combustion gases; however, it can become significant in regions exposed to soot radiation, such as in diesel engines operating under rich combustion.

The highly transient nature of engine operation further complicates the heat transfer process. Rapid changes in pressure and temperature during the intake, compression, combustion, and expansion strokes lead to unsteady thermal boundary layers, while moving geometries such as the piston introduce additional time-dependent effects. Accurate modeling of these phenomena requires capturing both the macroscopic flow behavior and the microscopic turbulent eddies that influence heat transfer at the wall.

3.5.4.1 Modeling Heat Transfer

In engine simulations, accurate prediction of wall heat transfer is crucial to correctly estimate in-cylinder temperatures, pressure evolution, and thermal boundary conditions. Several models have been developed to describe heat transfer between the gas and the combustion chamber

walls, each with varying degrees of complexity and fidelity. Among the various wall heat transfer models, the Han and Reitz model [84] for wall heat transfer is designed to predict convective heat transfer in ICEs, accounting for the variable-density turbulent flows typically found in such environments. The model is based on a temperature wall function derived from the one-dimensional energy conservation equation in the near-wall region. Assuming ideal gas behavior, negligible pressure gradients parallel to the wall, and dominant temperature gradients normal to the wall, the governing energy equation can be written as:

$$\frac{\partial q}{\partial y} = -\rho c_p \frac{\partial T}{\partial t} + \frac{dp}{dt} - \dot{Q}_c \tag{3.59}$$

where q is the heat flux, y is the wall-normal coordinate, ρ is the gas density, c_p is the specific heat at constant pressure, T is the temperature, p is the pressure, and $\dot{Q}_c$ represents volumetric heat release due to combustion. The heat flux q is defined as:

$$q = -(k_{mol} + k_t)\frac{\partial T}{\partial y} \tag{3.60}$$

where k_{mol} is the molecular thermal conductivity and k_t is the turbulent thermal conductivity. To simplify the formulation, the quasi-steady assumption is applied, which allows neglecting the transient and pressure work terms for many practical cases. This leads to a simplified balance where the heat flux is primarily governed by the near-wall temperature gradient.
Integration of the equation (3.59) over the distance y from the wall (y=0) with consideration of the gas-density variation and the increase of the turbulent Prandtl number in the boundary layer, the temperature profile equation (wall function) is formulated as:

$$T^+ = \ln(y^+) + 2.1G^+y^+ + 33.4G^+ + 2.5 \tag{3.61}$$

Here, $y^+ = u^*y/v$ is the dimensionless wall distance, v is the kinematic viscosity, and $G^+ = \dot{Q}_c v/q_w u^*$ is a dimensionless source term accounting for heat release due to combustion. The corresponding formulation for wall heat flux is given by:

$$q_w = \frac{c_p \rho u^*(T - T_w) - (2.1\ y^+ + 33.4)Gv/u^*}{2.1\ln(y^+) + 2.5} \tag{3.62}$$

This formulation allows the model to predict local heat fluxes with better accuracy than traditional incompressible wall functions, especially under the compressible and highly turbulent conditions found in engines. The model also demonstrated grid independence in CFD simulations, showing reliable predictions even with coarse near-wall mesh resolution.

3.6 Boundary and Initial Conditions

In CFD simulations of ICEs, the accurate specification of boundary and initial conditions is fundamental to ensuring the fidelity of the numerical results [85]. These conditions define the thermodynamic and flow properties within the computational domain and govern the interaction of the domain with its surroundings. The initial conditions establish the state of the system at the start of the simulation. The initial pressure and temperature fields are derived from experimental measurements or estimated using 1D engine models, while species mass fractions are assigned based on the composition of air and any residual exhaust gases present in the cylinder. To account for turbulence at initialization, characteristic turbulence quantities such as the TKE and its dissipation rate ε are prescribed using relations based on the turbulent intensity and length scales [85].

The boundary conditions in ICE CFD simulations are inherently transient and spatially varying due to the moving piston and valve geometries. The piston is treated as a moving boundary, where the piston displacement is calculated from engine kinematics using the crank radius, connecting rod length, and crank angle. Depending on the thermal boundary condition strategy, the engine surfaces can be modeled as adiabatic or assigned fixed wall temperatures representative of engine operating conditions. Intake and exhaust processes are represented by time-varying valve openings, with pressure, temperature, and species mass fractions specified at the inlet and outlet boundaries to reflect manifold conditions. For fuel injection, the injector is treated as a transient mass flow boundary with prescribed injection profiles, including spray characteristics such as injection rate, spray angle, droplet size distribution, and initial droplet velocities.

The transport of turbulence quantities and species across these dynamic boundaries is managed to maintain numerical stability and physical realism. For multi-cycle simulations or studies involving residual gas effects, the initial and boundary conditions may also incorporate carryover information from prior engine cycles, including wall heat fluxes and trapped species concentrations. The correct definition of the initial conditions is particularly crucial for accurately capturing phenomena such as charge motion, spray-air interactions, and combustion development, and any inaccuracies in boundary or initial condition specification can propagate through the simulation, leading to significant deviations in predicted performance and emissions. A rigorous validation of these parameters against experimental data is therefore essential to ensure that the CFD results reliably reflect the physical behavior of the engine.

Chapter 4

4. STATE OF THE ART

The ongoing decarbonization of maritime systems is driving the development of advanced combustion strategies and the integration of low-carbon and carbon-neutral fuels. Among the most promising technologies are DF CI engines and SI PC engines, both of which offer potential for improved efficiency and reduced emissions when fueled with alternative energy carriers such as methane, hydrogen, ammonia, methanol, and ethanol. This chapter presents a structured review of the current state of the art in these two combustion systems, focusing on their fundamental operating principles, recent experimental and numerical investigations, and their interaction with alternative fuels.

4.1 CI DF engines

CI DF engines have emerged as one of the most promising technologies for integrating alternative fuels into the maritime sector [86]. This configuration is widely adopted in various vessel types, including LNG carriers, container ships, and Ro-Ro vessels [87]. Although DF engines are now well established in naval propulsion, ongoing research continues to focus on improving combustion efficiency, fuel flexibility, and emissions control [88]. The use of natural gas in DF mode has been extensively studied, ranging from conventional operation to advanced modes of combustion, such as reactivity-controlled compression ignition (RCCI) [89] and high-pressure direct injection (HPDI) [90].

In particular, methane for DF applications is used on LNG carriers, where boil-off gas (BOG) can be directly utilized for propulsion [91].

Overall, the effect of natural gas on brake thermal efficiency (BTE) strongly varies according to engine operational conditions, making this parameter hard to predict without proper investigation. Ignition delay (ID), on the other hand, presents a more predictable behavior: the lower reactivity of methane compared to diesel leads to a delayed start of combustion, increasing its ignition delay time [92].

The use of natural gas in DF marine engines leads to decreased CO_2 emissions, primarily due to its higher hydrogen-to-carbon ratio [93]. NO_x emissions are also generally reduced when diesel is partially replaced by natural gas, as the slower combustion of the premixed charge results in lower in-cylinder temperatures and thus reduced thermal NO_x formation [94]. PM emissions have been reported to decrease in engines operating with diesel–methyl ester blends

when natural gas is introduced [92]. On the other hand, CO emissions may either increase—due to incomplete combustion [93, 95]—or decrease, depending on the carbon content of the fuel consumed [96]. UHC emissions have shown mixed results: in some studies, an increase was observed, suggesting a less efficient combustion process [97].

The DF operation with hydrogen in diesel engines has often been associated with environmental benefits, including the reduction of PM, CO, and CO_2, and lower pilot fuel consumption [98]. In addition to lowering GHG emissions, hydrogen DF combustion has also been linked in some cases to higher BTE [99, 100]. This is mainly attributed to hydrogen's high flame speed and combustion temperature, which can enhance combustion completeness and shift the heat release closer to top dead center, improving cycle efficiency [101]. However, several studies have also reported efficiency penalties under certain conditions [102, 103, 104]. Hydrogen has shown a non-linear effect on ignition delay, which may either increase or decrease depending on load and substitution level, often peaking at intermediate concentrations [105, 106]. Combustion duration similarly varies with hydrogen addition, with both increases [107, 108] and decreases as reported in [109, 110], depending on engine characteristics and operating conditions.

In marine engines, hydrogen represents a promising solution for reducing fossil fuel dependency and lowering GHG emissions, with potential that extends beyond ICE technologies [111]. In DF operation for maritime applications, hydrogen generally exhibits similar behavior to land-based engines, with a consistent trend of reduced carbon-based pollutants, such as CO, CO_2, and HC, alongside a notable increase in NO_x emissions [98]. This rise in NO_x is largely attributed to the higher combustion temperature of hydrogen, though some studies report lower NO_x formation under low-load conditions [112]. The partial substitution of diesel with hydrogen can result in either increased [113, 114] or decreased [115] thermal efficiency, depending on engine design and operational conditions. Hydrogen addition is also associated with an increase in ignition delay under certain circumstances [114, 116]. Pollutants not directly related to hydrogen oxidation, such as CO and PM, tend to decrease; however, under unfavorable combustion conditions where efficiency drops, these emissions may unexpectedly rise [112]. Conversely, CO_2 and HC emissions consistently decrease with the introduction of hydrogen [114], confirming its potential as a clean energy vector for marine DF applications.

In recent years, ammonia has emerged as a key focus in the search for carbon-free energy vectors, given its abundant availability and anthropogenic production levels reaching approximately 150 million tons per year [117]. Its application as a LRF CI engines has shown promising results, but outcomes remain highly sensitive to engine parameters and operating

conditions. Due to its low flame speed, ammonia combustion generally promotes a premixed combustion phase with lower heat release rates [118], which, in some cases, has translated into improved thermal efficiency, particularly for low-speed marine engines [119].

Conversely, for faster engine speeds, efficiency may decline, as reported by Yousefi et al. [120], who observed reduced DF performance attributed to ammonia's combustion limitations. Nevertheless, blending ammonia with natural gas has shown advantages over diesel-natural gas DF modes, offering lower fuel consumption and reduced CO_2 and NO_x emissions [121].

However, ammonia combustion is often associated with increased emissions of NO_x, N_2O, and unburned NH_3, even under advanced combustion strategies such as RCCI [122]. This is due to both incomplete oxidation and thermal NO_x formation mechanisms. Nonetheless, effective mitigation strategies include HPDI, optimized pilot injection timing, and injector design improvements, all of which have demonstrated notable pollutant reductions [119]. For example, in a 2.44L Caterpillar 3401 diesel engine, researchers achieved minimum GHG emissions through advanced diesel pilot injection, despite increased NH_3, HC, N_2O, and CO emissions compared to single-fuel diesel operation [120].

Further studies, such as those by Shin and Park [123], confirmed that early pilot injection could compensate for ammonia's low flame speed, improving combustion completeness and reducing unburned NH_3 and N_2O, though at the expense of higher NO_x emissions. Similarly, increasing the equivalence ratio was found to enhance premixed combustion, but with a tradeoff: lower N_2O levels and higher NO_x emissions [122]. In almost all reviewed studies, ammonia slip in the exhaust was present to some extent, and N_2O emissions were consistently elevated. However, CO and CO_2 emissions generally decreased, as expected from a carbon-free fuel, except under specific operating conditions [124, 125]. In addition, ammonia's low reactivity tends to increase ignition delay in DF operation [126]. Notably, NO_x emissions vary widely, depending on combustion strategies. For instance, Rodriguez et al. [124] identified a nonlinear correlation between substitution ratio and NO_x, with the lowest NO_x observed at an intermediate ammonia concentration. The injection method also plays a decisive role with the direct injection, which tends to minimize NO_x formation [127]. Finally, thermal efficiency outcomes appear mixed: some studies reported increases [126], while others noted declines [124], with both results strongly influenced by fuel injection strategies [119].

Another important aspect to highlight is that ammonia combustion can be significantly improved by optimizing the injection strategy, especially in ammonia/diesel DF engines operating at high ammonia energy ratios. Several studies [128, 129] have used three-dimensional numerical simulations to explore the effects of varying diesel injection timings and

ammonia energy ratios on combustion and emissions. For instance, Jin et al. [130] proposed a split diesel injection strategy, which, sometimes combined with hydrogen addition, helped create more favorable in-cylinder thermal conditions for ammonia ignition and subsequent combustion. Similarly, Yang et al. [131] conducted experimental investigations on a heavy-duty DF engine, showing that increasing the ammonia fraction reduced NO, NO_2, and CO_2, but caused higher NH_3 and N_2O emissions. Their work emphasized identifying optimized operating conditions based on GHG reduction goals.

A complementary line of research has focused on the shape of the diesel injection rate, which plays a crucial role in determining the fuel–air mixing quality and the development of combustion. In particular, Ref. [132] demonstrated that non-conventional injection shapes, such as trapezoidal or triangular, facilitate a more homogeneous mixture, which results in lower unburned ammonia emissions compared to standard square-shaped injection profiles.

Experimental studies on light-duty ammonia/diesel DF engines under low-load conditions [133] further explored the effects of ammonia energy ratio, pilot injection ratio, and timing on combustion performance. It was observed that pilot injection can extend the upper limit of allowable ammonia substitution. However, an excessively high pilot injection ratio may cause temperature reduction, impairing combustion and leading to incomplete ammonia oxidation. At the same time, pilot injection showed a positive influence on the indicated mean effective pressure (IMEP), improving overall performance.

Finally, as discussed in Ref. [134], the timing of pilot injection also plays a key role in shaping combustion behavior and thermal efficiency. An earlier pre-injection was found to reduce NH_3 slip, by allowing more time for the pilot diesel to mix with the ammonia–air charge. This improved the reactivity of the premixed mixture and led to more complete ammonia oxidation, ultimately enhancing combustion quality and emissions control.

4.2 SI Conventional Engines

While DF CI engines currently represent the most widespread strategy to meet increasingly stringent marine emission regulations, SI technologies are gaining traction in maritime propulsion, especially for medium-speed engines and auxiliary units. SI engines offer the advantage of operating directly on gaseous or liquid alternative fuels without requiring pilot diesel injection, enabling the use of low- and zero-carbon fuels such as natural gas, methanol, ethanol, and hydrogen. This results in significantly reduced emissions of PM and NO_x compared to conventional diesel engines. However, the application of SI systems to marine

contexts brings unique challenges, such as ignition stability, load flexibility, and overall efficiency.

Among the different alternative fuels, ethanol stands out as a promising option, especially due to its liquid state at ambient conditions, which makes it easy to store and transport an advantage over gaseous fuels like hydrogen. As underlined in Chapter 2, ethanol is considered a biofuel, as it can be derived from a wide variety of renewable sources, including sugar cane [135], olive tree pruning [136], wheat straw [137], vine shoots [138] and cellulosic biomass [139]. Its low carbon-to-hydrogen ratio, high octane number, and broad flammability limits [56] make it well suited for SI engines, allowing for higher compression ratios (CR) without knocking [140] and resulting in lower emissions compared to gasoline. One of ethanol's key benefits is that it requires minimal modifications to existing engines [141]. Additionally, its low stoichiometric air–fuel ratio and high latent heat of vaporization contribute to enhanced charge cooling, improved volumetric efficiency, and higher power output [142]. Ethanol's high flame speed also leads to faster combustion, which further enhances thermal efficiency [143, 144].

However, ethanol is not without drawbacks. Its oxygenated molecular structure leads to a LHV compared to gasoline, reducing energy content per unit of fuel. Also, the low volatility of high ethanol blends, combined with the charge cooling effect, can cause cold start difficulties [145].

Various strategies have been explored to optimize ethanol use in SI engines. A common method involves blending ethanol with gasoline, along with additives to improve cold-start performance, prevent corrosion, and stabilize the fuel [146]. For example, Cooney et al. [147] analyzed the combustion of E20 and E84 blends at constant load and various CRs (8:1 to 16:1), reporting that burning duration decreased with E20, but further ethanol additions did not significantly impact combustion speed. Similarly, Hsieh et al. [148] evaluated E5 to E30 blends and found that ethanol increased engine torque and brake specific fuel consumption (BSFC), while reducing CO and UHC emissions due to its lean combustion effect. Pourkhesalian et al. [149] compared gasoline, hydrogen, propane, methane, ethanol, and methanol in SI engines and concluded that while ethanol reduced NO_x and CO, it also increased fuel consumption. Celik [150] tested blends from E25 to E100 across CRs from 6:1 to 10:1 and found that E50 provided the best trade-off between performance and emissions, with higher BSFC but lower CO, CO_2, and NO_x emissions. At CR 10:1 with E50, engine performance improved significantly compared to gasoline at CR 6:1, with a 29% increase in power, improved BSFC, and lower pollutant output. Al-Hasan [151] also showed that E20 increased brake power, thermal efficiency, and volumetric efficiency, while reducing CO and UHC emissions. An alternative approach is to operate engines on pure ethanol (E100). İlhak et al. [152] examined a 4-cylinder

SI engine under constant speed and partial loads using ethanol and acetylene, finding promising results for ethanol. Liu et al. [153] investigated various direct injection strategies under lean conditions and high CR (15.5), showing that ethanol prevented autoignition, especially at high concentrations, due to accelerated flame propagation. Furthermore, ethanol's high oxygen content drastically reduced particulate emissions, achieving levels two orders of magnitude lower than E15 blends. Balki and Sayin [154] demonstrated that E100 use resulted in a 5.25% increase in brake mean effective pressure (BMEP) compared to gasoline, along with reductions in UHC, CO, and NO_x emissions, and improved combustion efficiency.

4.3 SI PC Engines

A further promising solution for achieving clean combustion in ICEs is the use of PC ignition systems, especially in combination with lean mixtures to reduce pollutant emissions. Similarly, methanol is another attractive fuel for PC engines due to its excellent combustion properties, especially in SI mode. Its high-octane number, fast flame speed, and low knock tendency make it suitable for high-efficiency combustion [155], although studies have shown that auto-ignition risk in large-bore engines is not entirely avoided [156, 157]. The oxygen content of methanol (50% by mass) [158] allows for reduced air requirement for stoichiometric combustion, while its low lean flammability limit facilitates lean operations. Studies consistently report higher engine efficiency, earlier ignition, higher peak pressures, and reduced emissions of HC, NO_x, and CO when methanol is used in SI engines compared to gasoline [154, 159, 160]

Nevertheless, methanol's partial oxidation can lead to unregulated emissions, including formaldehyde [161, 162], which requires mitigation via oxidation catalysts [159]. A viable strategy to address these challenges is employing active PC systems as combustion enablers. Several numerical and experimental investigations on heavy-duty engines with PC ignition have examined alternative fuels like methanol. For instance, Hlaing et al. [164, 165] evaluated the impact of different fuels such as methane, methanol, ethane, and n-butanol on key parameters such as combustion stability, duration, knock tendency, IMEP, and emissions, finding that methanol offered the fastest and most stable combustion without knock, and with higher gross indicated efficiency at similar equivalence ratios. Liu et al. [166] carried out optical diagnostics and CFD simulations on a heavy-duty PC engine fueled with methanol, highlighting that PC operation benefits low-load conditions, where distributed jet flames allow stable ultra-lean combustion. By optimizing variables such as compression ratio, EGR rate, PC fuel injection, and chamber geometry, they achieved clean and efficient combustion with reduced throttle dependency and pumping losses. Similarly, Leng et al. [167] conducted a numerical

study on a medium-speed marine PC engine (bore 320 mm, stroke 420 mm, CR 11.5, 750 rpm) analyzing methanol combustion at varying equivalence ratios (ϕ). Their results showed peak indicated thermal efficiency of 49.2% at ϕ = 0.42, while lower ratios led to diminished combustion performance and increased emissions of HC, CO, unburned methanol, and formaldehyde. It's worth noting, however, that studies on methanol PC systems for marine engines remain limited and mostly numerical in nature.

4.4 Main Contribution of the Thesis

This thesis is focused on the analysis of combustion processes and pollutant emissions associated with the use of alternative fuels in advanced combustion systems, with particular attention to their application in the maritime sector. The research has been structured into three main areas of investigation:

1. **DF CI Engines**: the first part of the study DF CI engines operating with hydrogen and ammonia as low-and zero-carbon fuels. The analysis investigates ignition behavior, thermal efficiency, and emission trends under different substitution ratios and injection strategies.
2. **SI Systems**: the second area focuses on spark-ignition technologies. Two configurations are examined:
    - Conventional SI engines operating with ethanol blends, assessing performance, efficiency, and pollutant formation.
    - PC SI engines fueled with methanol and methane, targeting both ultra-lean combustion operating and performance.
3. **Integration of an Innovative Marine Propulsion System:** based on the insights gained from the combustion analysis, one of the most promising engine configurations was selected and integrated into a hybrid marine power system. The proposed architecture includes a methane reformer coupled with a HT-PEMFC and a PC SI engine, with the objective of reducing CO_2 emissions while maintaining high electrical efficiency. A full-system energy and emission analysis was performed, considering also the role of auxiliary loads, carbon capture, and battery storage systems.

Through this multi-scale approach—ranging from detailed in-cylinder combustion to system-level performance in a naval context—the thesis contributes to the advancement of cleaner propulsion solutions based on alternative fuels, supporting the decarbonization pathway of the maritime sector.

Chapter 5

5. COMPRESSION IGNITION DUAL FUEL ENGINE

In this chapter, the DF combustion mode, of a six-cylinder Wärtsilä 20DF CI marine engine is investigated through a comprehensive numerical study, integrating a 1D and a 3D approach. The fundamental principles and operating characteristics of the DF combustion concept have been previously introduced in Chapter 1. The study builds upon the methodology and experience developed in previous works focused on a DF research engine fueled with hydrogen [133,168]. The analysis focuses on performance, combustion behavior, and emissions when using pure methane, methane/hydrogen blends, pure ammonia, and ammonia/hydrogen blends—fuels relevant to maritime decarbonization strategies. Finally, various diesel injection strategies are tested (timing, mass, and square vs sinusoidal profiles) to optimize ammonia-based DF operation. This parametric analysis identifies injection settings that approach nominal engine performance while minimizing carbon and ammonia emissions. The results presented in this chapter are based on the works [169], [170] and [171] are framed within the context of the project "CN-MOST - Spoke 3 (Waterways)", Mission 4, Component 2, under the National Recovery and Resilience Plan (NRRP) of Italian Ministry of University and Research (MUR)".

5.1 The Wärtsilä 20DF Engine

The engine object of study is a 6-cylinder Wärtsilä 20DF (W20DF) engine (Figure 5.1).

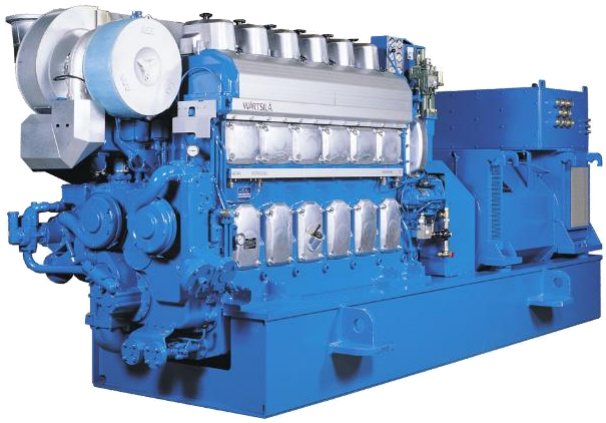

Figure 5.1: The 6-cylinder W20DF engine

The W20DF engine is a compact and proven four stroke engine with high reliability and fuel flexibility, originally designed to run with heavy fuel oil. Available in cylinder configurations

from 4L to 9L and with a power output ranging from 0.7–2.0 MW, the W20DF provides compact power as a main propulsion engine and is exceptionally flexible for auxiliary installations. The engine is available in diesel and DF versions. It can smoothly switch between different fuels during operation without power interruption. The W20 offers outstanding flexibility, enabling it to be installed and optimized for generating sets in larger vessels and as a main engine for both mechanical and electric propulsion. The multi-fuel capability makes it an ideal choice for various vessel applications including hybrid installations. Typical installation examples include car carriers and merchant vessels. The compact and lightweight W20DF is also ideal as a mechanical drive prime mover for applications such as small cargo vessels, ferries and tugboats. The W20DF is fully compliant with the IMO Tier II exhaust emission regulations in diesel mode, Option to reach IMO Tier III in diesel mode with an SCR catalyst such as the Wärtsilä NO_x Reducer (NOR) exhaust treatment solution, compliance with IMO Tier III regulations in gas mode without aftertreatment, minimized SO_x and CO_2 emissions as well as smokeless operation in gas model [172]. The geometrical characteristic of the engine and the valve timing are shown in Table 5.1, originally fueled with natural gas. Note that the intake and exhaust valve time opening and closing in the table are referred to the TDC of combustion.

Table 5.1: Engine characteristics [173]

DF, 4-stroke turbocharged, 6 cylinders, 4 valves per cylinder	
Stroke [mm]	280
Bore [mm]	200
Displacement volume [cm^3]	~52800
CR [-]	13.4:1
IVO	365° BTDC
IVC	215° BTDC
EVO	145°ATDC
EVC	350° ATDC
Valve lift [mm]	17

In the thesis, a representative case at medium load, relevant because it closely reflects cruise conditions, is analyzed, and the corresponding operating parameters are summarized in Table 5.2.

Table 5.2: Engine operating conditions at medium load [174].

Engine speed [rpm]	1000
GMEP [bar]	10
Diesel injection timing [CAD BTDC]	15
Diesel injection pressure [bar]	1700
Pressure at IVC [bar]	1.85

Finally, the fuel data of the original engine operating with natural gas are reported in Table 5.3.

Table 5.3: Fuel data of the engine [174].

Diesel mass [mg]	50
NG mass [mg]	328
Diesel LHV [MJ/kg]	43.1
NG LHV [MJ/kg]	48.1
RP [%]	88
Global ER [-]	0.5

The RP parameter reported in Table 5.3 represents the premixed ratio, which quantifies the energetic contribution of the primary fuel relative to the total fuel energy input. It is defined as:

$$RP = \frac{m_{pf} LHV_{pf}}{m_{pf} LHV_{pf} + m_{sf} LHV_{sf}} \tag{5.1}$$

where m_{pf} and m_{sf} are the mass flows of the primary and secondary fuels, respectively, and LHV denotes the lower heating value of each fuel. In the present study, used to calibrate the model, the primary fuel is the LRF, while the secondary fuel is the HRF. The global equivalence ratio value of 0.5 (Table 5.3) considers the combined contribution of both fuels. It should be noted that, compared to the fuel properties reported in the referenced experimental studies, n-dodecane and pure methane were used here as surrogate fuels, which may not perfectly replicate the exact behavior of the experimental counterparts. Despite these differences, the objective of this work is not to achieve precise reproduction of the experimental results, but rather to capture the essential features of combustion timing and development under the selected operating conditions.

5.2 1D Modeling

In order to obtain the pressure and temperature at the intake valve closure as initial conditions for 3D calculations, a single cylinder 0D/1D model of the W20DF naval engine was implemented using the commercial software Ricardo WAVE. The schematic of the engine is reported in Figure 5.2.

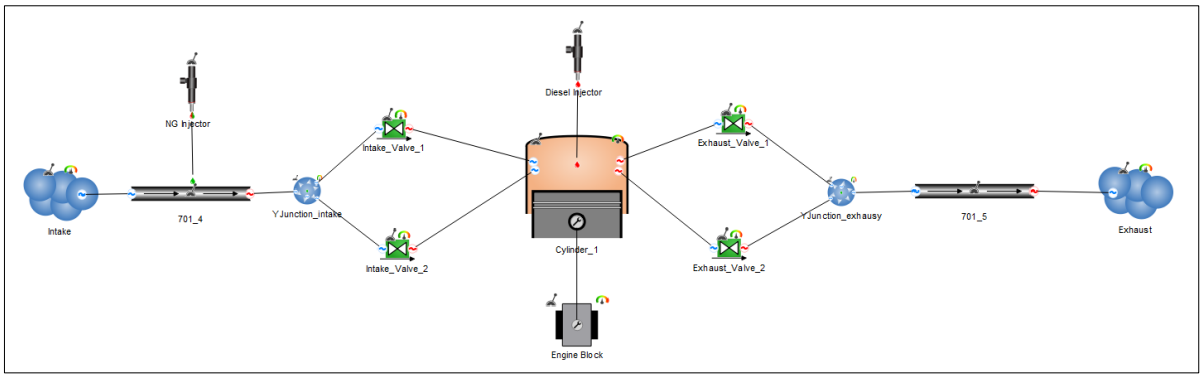

Figure 5.2: 1D schematics of one cylinder

Since the literature reference provided only the experimental ROHR data, a 1D thermodynamic model was employed to reconstruct the corresponding pressure trace by imposing the prescribed heat release profile. The 1D pressure obtained in this way will be referred to as the experimental case. The cylinder was modeled using a single-zone approach, where the entire in-cylinder mixture is represented as a homogeneous region with uniform temperature, pressure, and composition at each crank angle. In this simplified formulation, combustion is modeled through an imposed heat-release law, which results in a direct increase in average cylinder temperature and pressure. While this method does not resolve the spatial gradients between fresh and burned gases, it offers high computational efficiency. Thus, it is well-suited for evaluating global engine performance metrics and for generating initial conditions to be used in more detailed 3D CFD simulations.

The energy balance for the single-zone model is given by:

$$\frac{dU}{dt} = \sum_{i=1}^{nvalves} \dot{m}_i h_i - \dot{Q} - p\frac{dV}{dt} \tag{5.2}$$

Intake boosting was considered by setting an intake pressure of 1.85 bar, as reported in the experimental dataset (Table 5.2). The intake temperature was tuned to achieve a global equivalence ratio of 0.5. A back pressure of 2 bar was imposed at the exhaust port.

Since the original reference [174] does not provide specific data regarding duct and junction geometries, these were estimated based on prior experience with a light-duty engine (bore = 84 mm) described in [175]. Geometric scaling was applied proportionally to the bore ratio between the current engine and the reference one (200 mm / 84 mm ≈ 2.38), and a multiplicative factor of 2.5 was used for all dimensions.

Regarding fuel injection strategies, the pilot diesel was directly injected into the cylinder, whereas natural gas was injected into the intake manifold with a mass flow rate of 9.85 kg/h. The methane injection starts at 330° BTDC and lasts for 60° CA, ending at 270° BTDC. Heat transfer was modeled using the Woschni correlation [176] to calculate the heat transfer coefficient h_g.

$$h_g = 0.0128 D_{cyl}^{-0.2} p^{0.8} T^{-0.53} v_c^{0.8} \tag{5.3}$$

Where D_{cyl} is the cylinder bore, p and T are the in-cylinder pressure and temperature, respectively, and v_c is a characteristic velocity.

$$v_c = c_1 v_m + c_2 \frac{V_D T_r}{p_r V_r} (p - p_{mot}) \tag{5.4}$$

Where c_1 and c_2 are two dimensionless coefficients function of the mean piston speed and of the swirl velocity, v_m is the mean piston speed, V_D is the cylinder displacement, T_r, p_r and V_r are the reference temperature, pressure and volume, respectively, and p_{mot} is the motored in-cylinder pressure.

A modified form of the Chen-Flynn correlation was used to compute the engine friction losses. The friction mean effective pressure (FMEP) calculated through the equation is here reported:

$$FMEP = A_{cf} + \frac{1}{ncyl} \sum_{i=1}^{ncyl} \left[B_{cf} (p_{max})_i + C_{cf} \left(\frac{n \cdot s}{2} \right)_i + Q_{cf} \left(\frac{n \cdot s}{2} \right)_1^2 \right] \tag{5.5}$$

Where A_{cf}, B_{cf}, C_{cf} and Q_{cf} are user inputs, p_{max} is the maximum in-cylinder pressure, n is the engine speed in rpm and s is the engine stroke.

At the same time, the ducts take into account of the friction losses through a friction coefficient described in the following formulas:

$$\frac{C_f}{2} = \frac{4}{Re} \text{ for laminar flows} \tag{5.6}$$

$$\frac{C_f}{2} = 0.027Re^{-0.25} \text{ for turbulent flows} \tag{5.7}$$

Through the 1D model described above, the experimental ROHR reported in Figure 5.3a was used to derive the experimental pressure showed in Figure 5.3b and the initial conditions for the 3D calculations, namely a pressure of 1.65 bar and a temperature of 362.5 K.

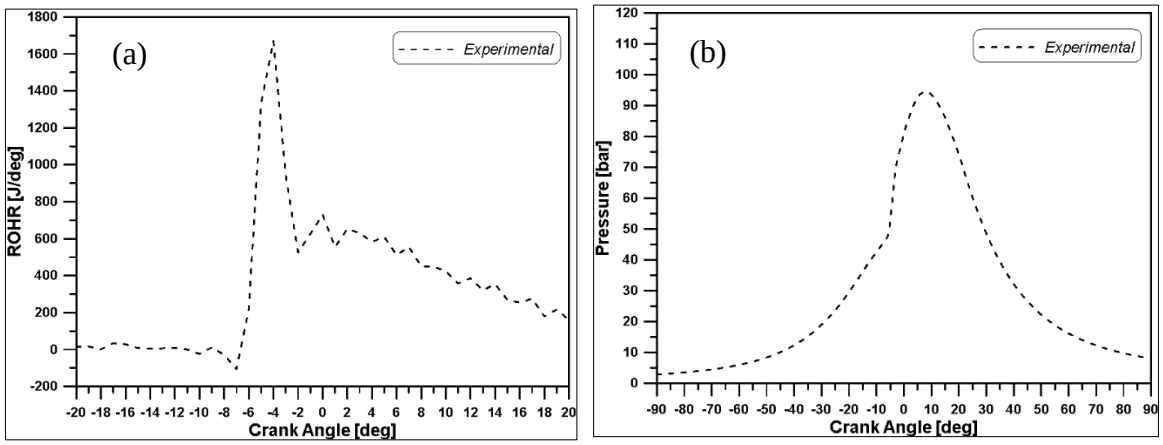

Figure 5.3: Experimental ROHR (a) and experimental pressure derived with 1D through the imposition of the experimental ROHR (b).

5.3 3D CFD

The numerical simulations were carried out using ANSYS FORTE®, applied to a computational domain representing the Wärtsilä W20DF marine engine. To optimize computational efficiency, a 40-degree sector of the combustion chamber was modeled, leveraging the engine's nine-hole diesel injector and the assumption of axisymmetry. Further details regarding the bowl configuration are provided in Section 5.3.2. The simulations were limited to the closed-valve period, specifically from −215° ATDC (Inlet Valve Closing, IVC) to 145° ATDC (Exhaust Valve Opening, EVO). The flow field was modeled using the unsteady Reynolds-Averaged Navier–Stokes (URANS) equations, solved with a modified SIMPLE iterative algorithm [177]. A two-step iterative process was adopted to resolve the flow variables. Turbulence was simulated via the RNG k–ε model [178], which enhances the conventional k–ε model by introducing correction terms in the dissipation rate equation, improving accuracy in highly strained and swirling flows. To capture the interaction between turbulence and chemistry, a kinetics–turbulence interaction model was employed, solving detailed chemical mechanisms in conjunction with the turbulent flow field. The combustion modeling was conducted by coupling ANSYS FORTE® with the ANSYS Chemkin-Pro solver, as detailed in Section 5.3.3. This allows for the direct solution of detailed chemical kinetic mechanisms,

essential in DF configurations where fuel reactivity and mixture composition significantly influence ignition behavior.

Wall heat transfer was modeled using the Han and Reitz model [84], with all engine walls maintained at a constant temperature of 450 K. Initial conditions, including pressure, temperature, and fuel–air composition, were derived from the corresponding 1D engine simulation, depending on the fuel blend.

Spray vaporization was modeled using the DMC model [66], which accounts for multi-component fuel evaporation and heat/mass exchange. One of the most critical aspects of DF combustion is the description of spray breakup and fuel–air mixing, which strongly affects ignition delay and combustion development. Given the influence of gaseous fuel presence in the bulk mixture, a sensitivity analysis on spray parameters was conducted to identify optimal spray settings for accurate prediction of IMEP; this analysis is presented in Section 5.3.4. Note that the IMEP reported in the text refers exclusively to the indicated mean effective pressure of the high-pressure cycle (compression and expansion phases only).

Spray atomization and droplet breakup were modeled using the KH-RT hybrid model [63], which simulates primary and secondary breakup of diesel sprays in high-pressure environments. A detailed description of the models is provided in Chapter 3.

5.3.1 Mesh Sensitivity Analysis

A mesh sensitivity analysis was conducted to balance computational efficiency with result accuracy. To minimize simulation time, a sector mesh of 40° was adopted, consistent with the nine-hole diesel injector configuration of the W20DF engine and the assumption of axial symmetry of the domain. Three mesh configurations were generated, with the key parameters for each reported in Table 5.4.

Table 5.4: Mesh dimensions

Mesh n°	Min. number of cells	Peak pressure [bar]	Max. average T [K]
Mesh 1	4702	66.6	1535
Mesh 2	11760	101.4	2101
Mesh 3	28224	102.6	2113

A comparative analysis of critical combustion indicators, including in-cylinder pressure, ROHR, and temperature, is illustrated in Figure 5.4. The comparison reveals that Meshes 2 and 3 yielded very similar results, both in terms of thermodynamic profiles and IMEP, with

differences of less than 1%. In contrast, Mesh 1 produced notably divergent outcomes, suggesting insufficient resolution to capture the combustion phenomena reliably.

Based on this analysis, Mesh 2, was selected as the optimal configuration, offering a good trade-off between computational cost and model accuracy, while keeping consistency with the results of the finer Mesh 3.

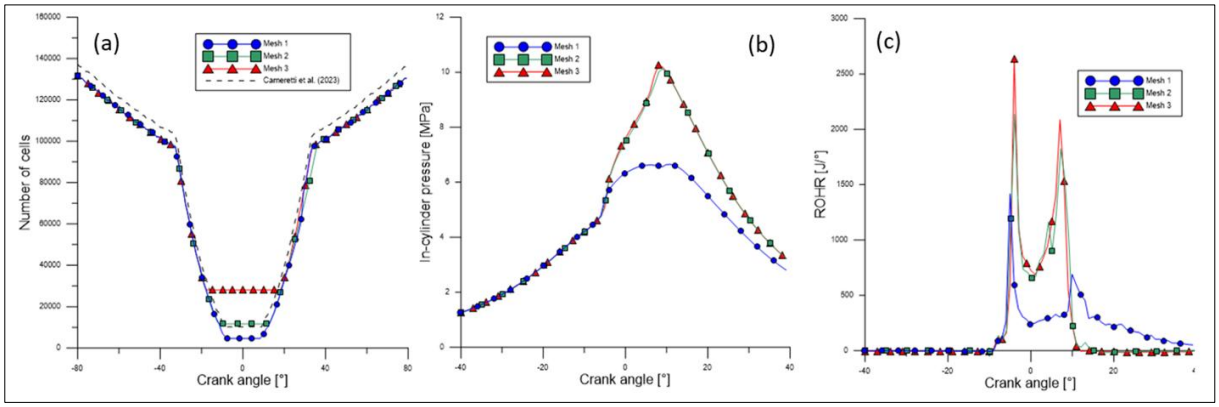

Figure 5.4: Mesh sensitivity analysis including: (a) number of cells, (b) in-cylinder pressure, (c) ROHR.

5.3.2 Bowl Profile Comparison

Due to the lack of specific information on the bowl geometry of the W20DF engine, and with only the bowl profile of the Wärtsilä 46 (W46) engine available from literature [179], a scaling approach was adopted. The W46 bowl (ω-shaped) was geometrically scaled to match the dimensional characteristics of the W20DF engine. To evaluate the influence of this approach and the suitability of the ω-shaped bowl, a comparative study was carried out between the ω-shaped geometry and a simplified square bowl design, which was defined by considering a simple rectangular profile for the bowl. The configurations of the two bowl profiles and the corresponding computational grids are illustrated in Figure 5.5.

RECTANGULAR BOWL (TDC)	**ω-SHAPED BOWL (TDC)**
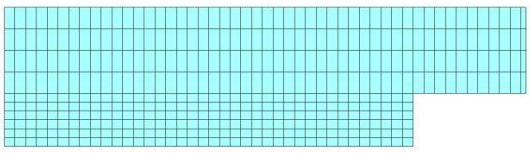	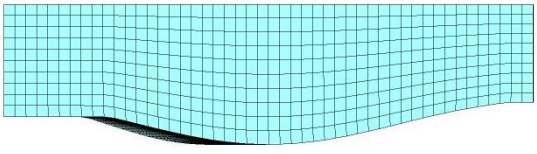

Figure 5.5: Comparison of the two mesh grids at TDC

At TDC, the mesh based on the scaled geometry exhibits more uniform cell distribution across the domain, both in terms of shape and size, thanks to the treatment of bowl and squish regions as a unified layered zone. In contrast, the old mesh presents elongated and irregular cells in the

squish area due to reduced layering, whereas in the bowl region, the cell count remains constant throughout the simulation. Importantly, both geometries maintain identical displacement volumes and compression ratios, and the mesh densities are comparable.

The motivation for adopting the ω shaped bowl design becomes clear when analyzing the in-cylinder flow field, particularly the streamlines shown in Figure 5.6. At 10° BTDC, shortly after the injection event, the flow is dominated by the momentum of the fuel jet. As is typical in marine engine combustion chambers, which are often referred to as "quiescent chambers", the fuel–air mixing is primarily driven by the injector-induced jet velocity, rather than by swirl or tumble motion. The radial propagation of vortices, strongly affected by the geometry of the bowl, becomes particularly evident at TDC.

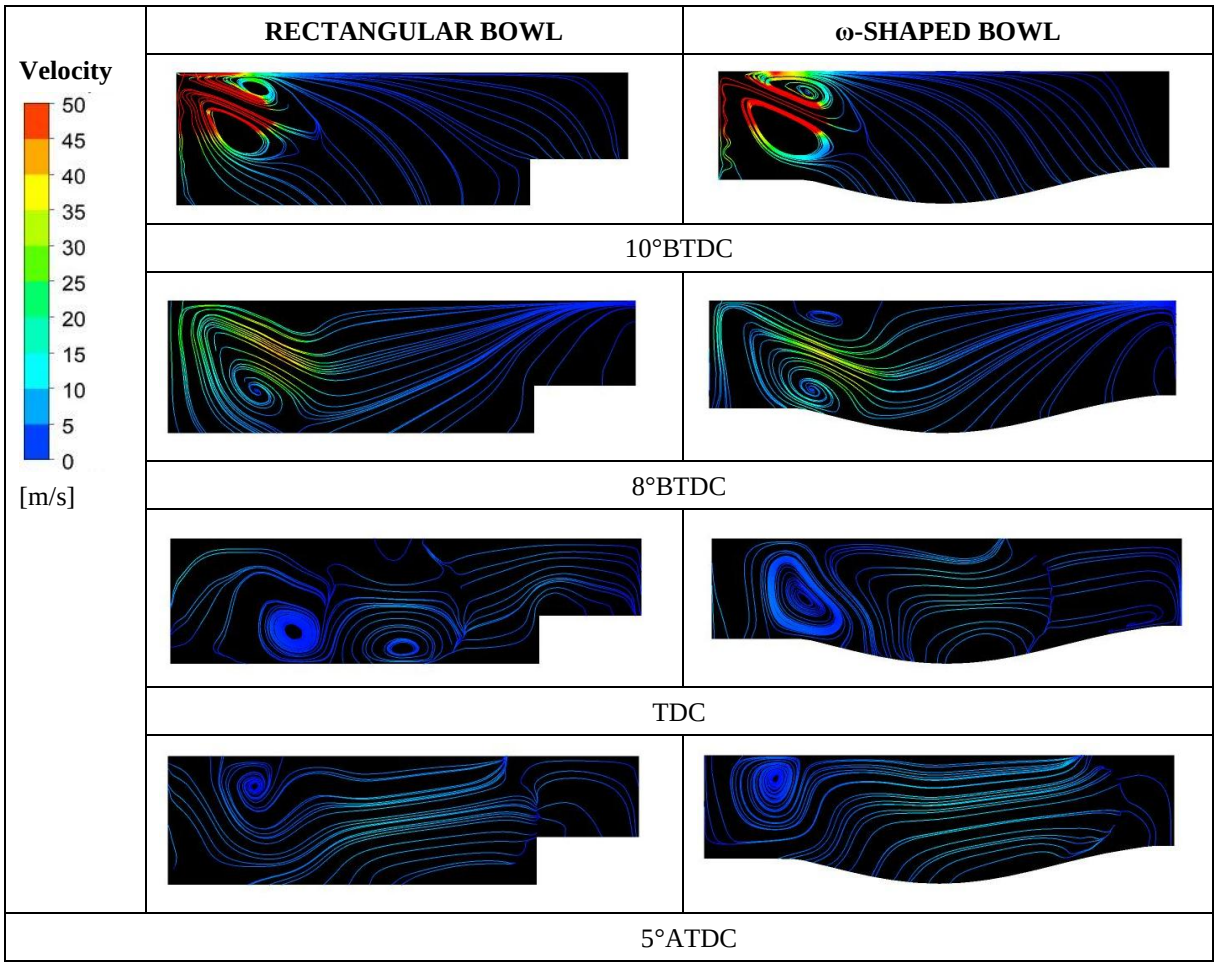

Figure 5.6: Streamlines for the two bowl geometries

Further evidence of the bowl's influence is provided in Figure 5.7, which displays the n-dodecane vapor concentration contours. The simulation using the ω-shaped bowl geometry shows a more realistic vapor fuel distribution, with the absence of unrealistic fuel accumulation near the cylinder head. This improved behavior confirmed the suitability of the ω-shaped bowl geometry, which was consequently adopted for all subsequent numerical investigations.

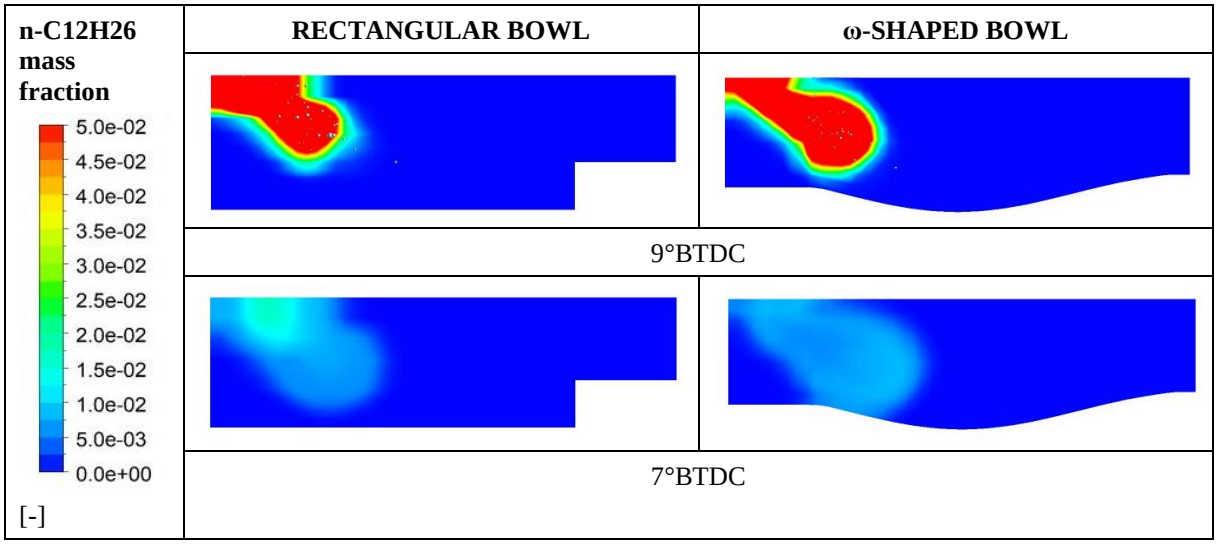

Figure 5.7: N-dodecane distributions for the two bowl geometries

The 40° sector computational domain with the chosen bowl design (ω-shaped) geometry is reported in Figure 5.8.

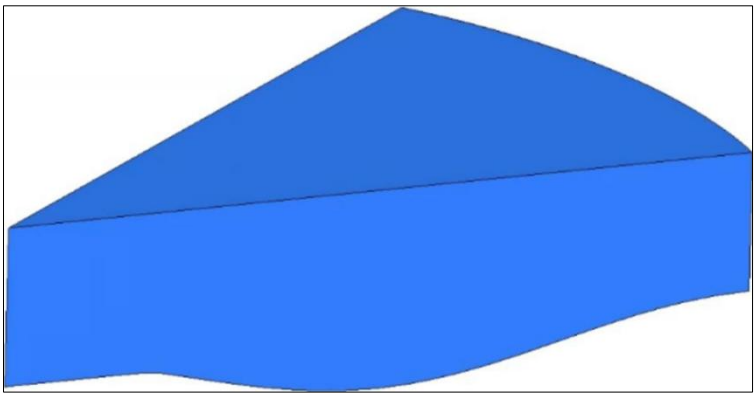

Figure 5.8: Sector used for the calculations

5.3.3 Kinetic Model Tuning

In the present study, n-dodecane (n-$C_{12}H_{26}$) was selected as a surrogate for diesel fuel, while pure methane (CH_4) was used to represent natural gas. To accurately simulate the DF combustion process, starting from diesel ignition and extending to the oxidation of methane, hydrogen, and ammonia, the kinetic mechanism must include detailed reaction pathways for all these fuels. Initially, the Ra&Reitz mechanism [180] for n-dodecane was combined with the GRI-MECH 3.0 mechanism, a well-established model for methane oxidation, yielding a mechanism comprising 124 species and 660 reactions. However, given that auto-ignition chemistry, particularly at low temperatures, is critical to DF combustion, a more advanced mechanism was adopted. Specifically, a reduced mechanism for n-dodecane, explicitly optimized for low-temperature auto-ignition and reported in [181], developed by the CRECK

Modeling Group, was merged with the GRI-MECH 3.0 using ANSYS Chemkin-Pro. The resulting detailed kinetic mechanism featured 151 species and 2570 reactions and provided a more accurate description of the ignition delay and combustion phasing.

As illustrated in Figure 5.9, the comparison between the Ra&Reitz + GRI-MECH 3.0 and the CRECK + GRI-MECH 3.0 kinetic mechanism highlights a significant improvement: the latter mechanism captures earlier and more realistic ignition timing, emphasizing the importance of including low-temperature chemistry for diesel auto-ignition in DF systems.

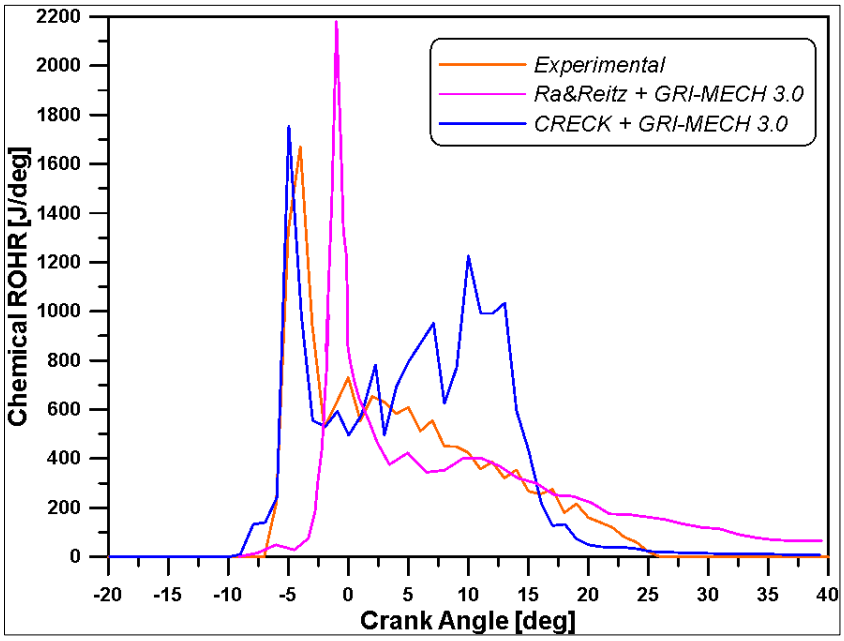

Figure 5.9: Chemical heat release. Comparison between the two kinetic mechanisms

To accurately model ammonia combustion when used as the LRF in DF mode, the Otomo kinetic mechanism [182], specifically developed for NH_3 oxidation, was merged with the CRECK Group mechanism for n-dodecane. The Otomo mechanism has been validated against experimental data and is capable of accurately reproducing both the laminar flame speed and the ignition delay of ammonia, as demonstrated in Otomo's original study.

The final merged mechanism, used for simulations involving ammonia and ammonia/hydrogen blends, consisted of 152 species and 2593 reactions. This comprehensive kinetic model allowed for the accurate simulation of ignition behavior and flame development across a wide range of DF fuel blends and operating conditions, making it a key contribution to this work.

5.3.4 Atomization Model Tuning

The diesel spray atomization and droplet breakup were modeled using the well-established KH-RT hybrid breakup model, previously introduced in Chapter 3. This model is widely recognized as the most reliable approach for simulating the atomization process in conventional diesel and

DF combustion, as it captures the interplay between aerodynamic shear forces and instabilities caused by droplet acceleration. Among the several parameters in the KH-RT model, the simulations revealed a notable sensitivity to the KH breakup time constant (τ), specifically controlled by the empirical coefficient C_{KH}, as discussed in the theoretical section of this thesis. To investigate its impact, C_{KH} was varied, while all other model constants were kept at their default values. As demonstrated in previous works by Reitz [63] and Brulatout [183], increasing C_{KH} prolongs the primary breakup time, leading to greater spray tip penetration and altering the resulting vapor distribution. In particular, a lower C_{KH} value (e.g., C_{KH} = 5) leads to excessively rapid breakup, resulting in a complete absence of droplets at 9° BTDC, while higher C_{KH} values extend penetration and delay atomization. The breakup dynamics have a direct influence on ignition delay, and thus on the peak in-cylinder pressure and chemical ROHR, as shown in Figure 5.10. The most accurate match with the 1D model in terms of start of combustion and pressure development was obtained with C_{KH} = 7.5.

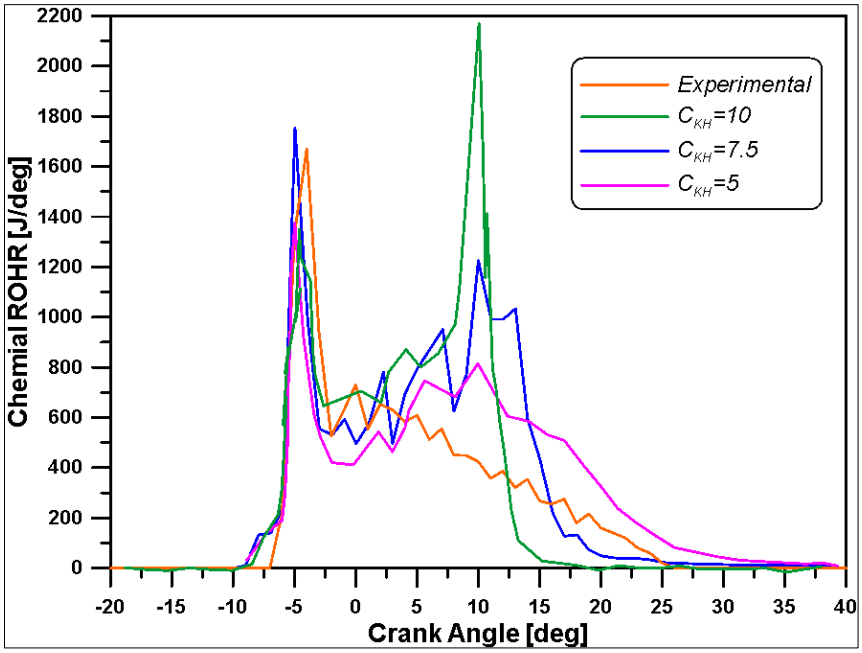

Figure 5.10: In-cylinder pressures and ROHRs by the varying time constant of the KH model.

This tuning yielded an IMEP of 10 bar, and a peak pressure of 86.68 bar, closely aligning with the results from the experimental results (see Table 5.5). The use of this calibrated C_{KH} value, combined with the updated chemical kinetic mechanism described earlier, enabled a reliable reproduction of the ignition behavior in DF operation.

Table 5.5: Values of IMEP and peak pressure for the different cases.

	IMEP [bar]	Pressure peak [bar]
Experimental	10	86.5
C_{KH} = 5	9.67	77.28
C_{KH} = 7.5	10	86.69
C_{KH} = 10	9.91	95.07

5.3.5 Model Validation

In Figure 5.11 the curves of the ROHR are plotted by comparing the numerical result with the experimental data for the test case with methane/air. As mentioned, although the used fuels do not coincide exactly, the numerical trend obtained is similar to the experimental one. Indeed, the timing of the combustion development was fairly reproduced. A two-stage shape of the curve was detected in the numerical simulation as well. The first peak, due to the pilot ignition, and especially the equal rise rate, mean that the spray evolution and ignition were adequately reproduced. The second phase, due to methane oxidation can be considered globally acceptable since the order of magnitude of the numerical ROHR is close to experimental one for all the oxidation duration. Moreover, the IMEP of both curves is equal to 10 bar.

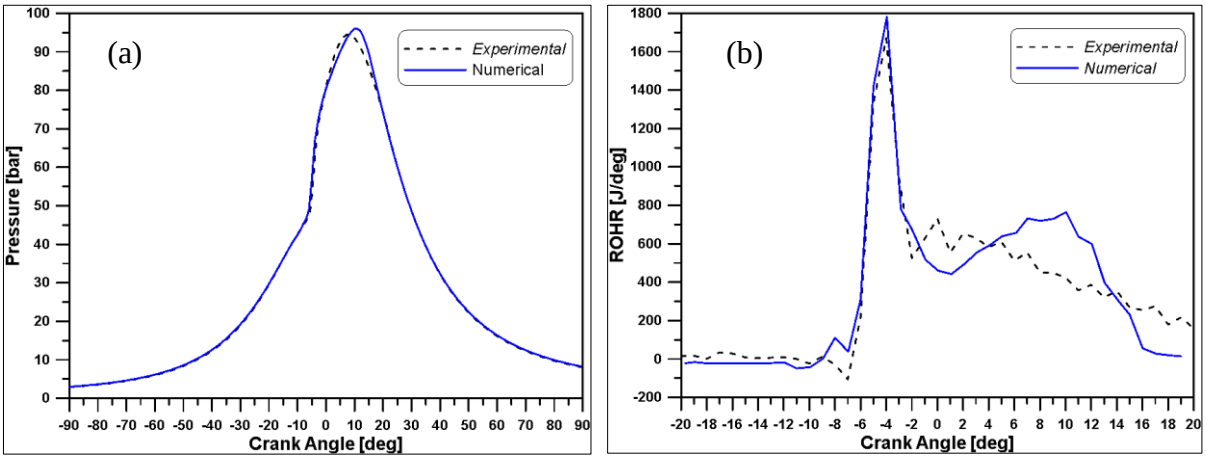

Figure 5.11: Experimental vs numerical pressure (a) and ROHR (b).

5.3.6 CH_4 and CH_4/H_2 Blends

5.3.6.1 Test cases

Different methane–hydrogen blends were tested keeping the same energy input, as shown in Table 5.6. The diesel is injected at 15°BTDC and the diesel mass is equal to 50 mg for all cases. Note that the global equivalence ratio lowers from 0.5 (full methane) to 0.473 (full hydrogen).

Table 5.6: Input data for the different cases simulated.

3D Simulations					
H_2 [%]	0	25	50	75	100
CH_4 [%]	100	75	50	25	0
Mass H_2 [mg]	0	34.2	68.3	102.5	136.6
Mass CH_4 [mg]	328	246	164	82	0
Energy from H_2 [J]	0	4100	8200	12300	16400
Energy from CH_4 [J]	16400	12300	8200	4100	0
Global phi	0.5	0.494	0.487	0.48	0.473

5.3.6.2 Results

Figure 5.12 shows that the addition of hydrogen leads to a progressive increase in both the peak values and the rise rates of pressure and temperature, due to the higher reactivity of hydrogen. A particularly pronounced step is observed between the pure methane case and the mixture with 25% hydrogen, where the pressure peak rises to just above 110 bar. Further hydrogen enrichment continues to increase the peak pressure; however, at 75% hydrogen a plateau effect becomes evident, as the difference in peak pressure between 75% and 100% hydrogen is minimal.

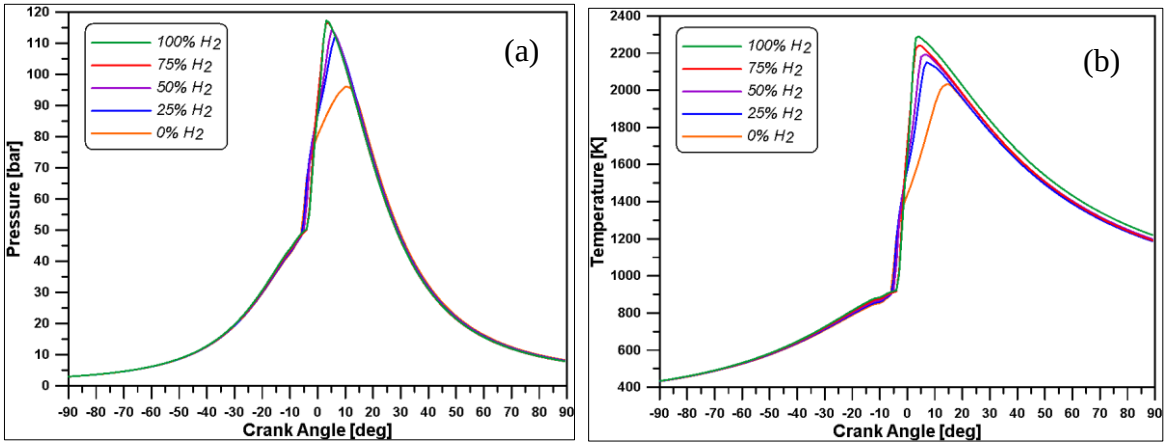

Figure 5.12: In-cylinder pressure (a) and temperature (b).

In the following analysis, three cases are considered: the two extreme cases of 100% hydrogen and 100% methane, and the intermediate case with a 50/50 mixture of hydrogen and methane. By looking at the ROHR trends in Figure 5.13, it is possible to observe that the increase the percentage of hydrogen leads to a decrease of the combustion duration mainly due to the higher reactivity of this fuel including high burning velocity and LHV. Especially, hydrogen significantly affects the ignition phase and hence the consequent heat release. Moreover, it is

evident that a delay occurs the more the hydrogen is inside the combustion chamber. Another important aspect to highlight is the progressive enhancement of the secondary diffusive peak with increasing hydrogen fraction which can be explained by the combined influence of hydrogen chemistry and transport properties. Hydrogen addition increases flame reactivity and promotes an earlier and more vigorous premixed combustion stage, thereby advancing the consumption of the readily mixed charge. Owing to its high diffusivity, hydrogen also intensifies local mixture inhomogeneities, allowing intermediate-species pockets to persist after the passage of the flame front. The subsequent oxidation of these pockets, together with enhanced post-flame CO oxidation driven by the elevated radical pool, manifests as a strengthened secondary peak in the diffusive heat-release phase.

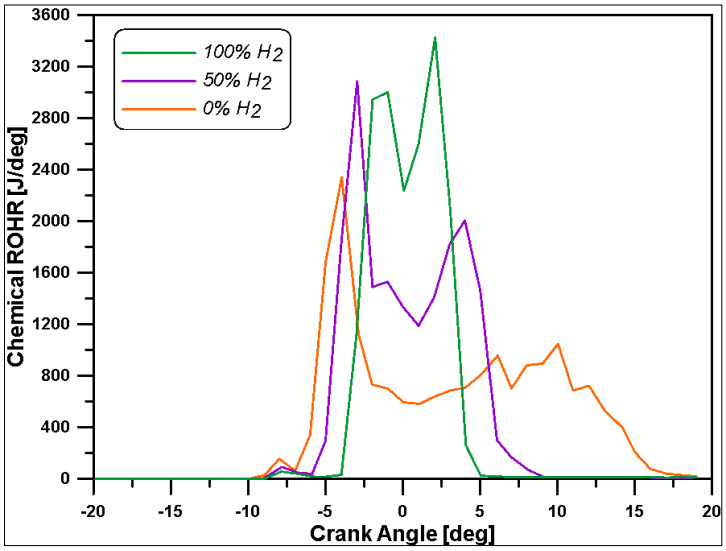

Figure 5.13: Chemical heat release for three cases

To better understand the combustion development of the low and high reactivity fuels, the images in Figure 5.14 show the dispersion of diesel vapor in the cylinder: in the case with air/hydrogen mixture, the vapor amount occupies a greater volume with higher penetration. Specifically, the case with only H_2 shows red zones persisting up to 5° BTDC. This suggests the pilot hasn't effectively ignited until that point, whereas with methane, the pilot is already being consumed by 7.5° BTDC. This later start of combustion with hydrogen can be explained by the higher effective heat capacity, and—because H_2 diffuses extremely fast—strong dilution and stretching of the nascent pilot flame. These effects cool and destabilize the first ignition kernels and lengthen the pilot ignition delay compared with CH_4, which perturbs the pilot less and allows earlier stabilization. Once ignition finally establishes in the H_2 case, the chemistry is very fast and the premixed charge is already well mixed; the burn then accelerates sharply, so the H_2 case shows shorter combustion duration than methane.

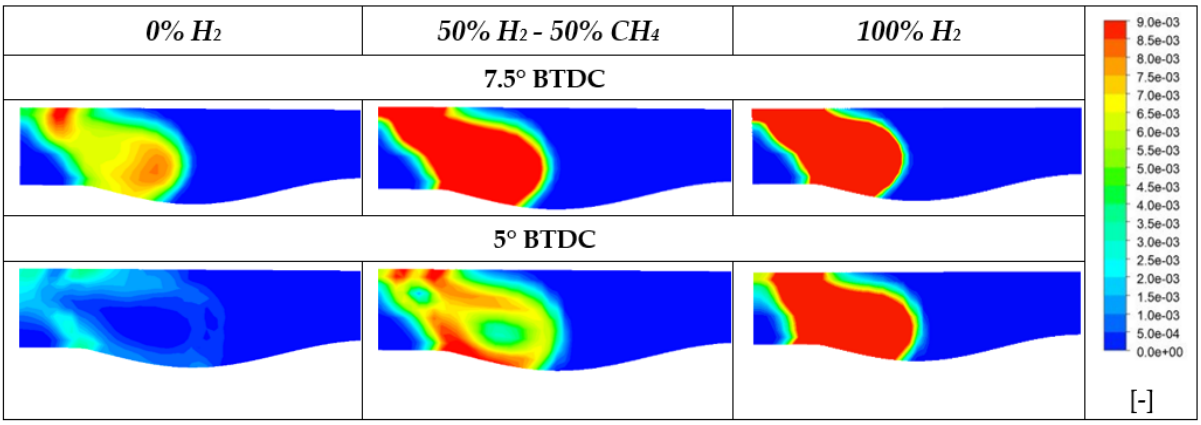

Figure 5.14: Diesel mass fraction distributions for three cases

The temperature distributions obtained for the three fuel cases in Figure 5.15 clearly highlight the influence of hydrogen addition on combustion development. For pure methane (0% H_2), the flame propagation is relatively slow and produces highly localized hot regions near the ignition point at TDC, while large parts of the chamber remain comparatively cool. As the crank angle advances, the flame front gradually spreads, and only at later stages such as 10°–20° ATDC does the combustion zone fill most of the chamber, with noticeable temperature stratification persisting. When hydrogen is introduced in a 50% blend with methane, the combustion process accelerates significantly. Already at TDC and especially by 2.5° ATDC, the high-temperature region expands more quickly across the chamber, and temperature distribution becomes more uniform compared to the methane case. At 10° ATDC, most of the volume is already involved in combustion, while by 20° ATDC the chamber shows more homogeneous medium-high temperatures, indicating that the heat release has largely concluded earlier than with methane. With 100% hydrogen, the combustion process is extremely rapid and highly reactive: at TDC the chamber already exhibits widespread high temperatures, and by 2.5° ATDC, the majority of the chamber's temperature exceeds 1500–2000 K. By 10° ATDC, the chamber is almost uniformly hot, while at 20° ATDC the temperature has already decreased due to the expansion stroke, indicating that the combustion process ended much earlier in the cycle. This behavior demonstrates that hydrogen not only shortens combustion duration and shifts peak temperatures closer to TDC but also reduces spatial temperature gradients compared to methane. While these characteristics ensure more complete combustion, they also imply a higher propensity for NO_x formation due to the higher and earlier temperature peaks. In contrast, methane combustion shows lower NO_x potential. The blended case represents an intermediate scenario, improving combustion speed and uniformity compared to pure methane, while moderating the excessive peak temperatures observed with pure hydrogen.

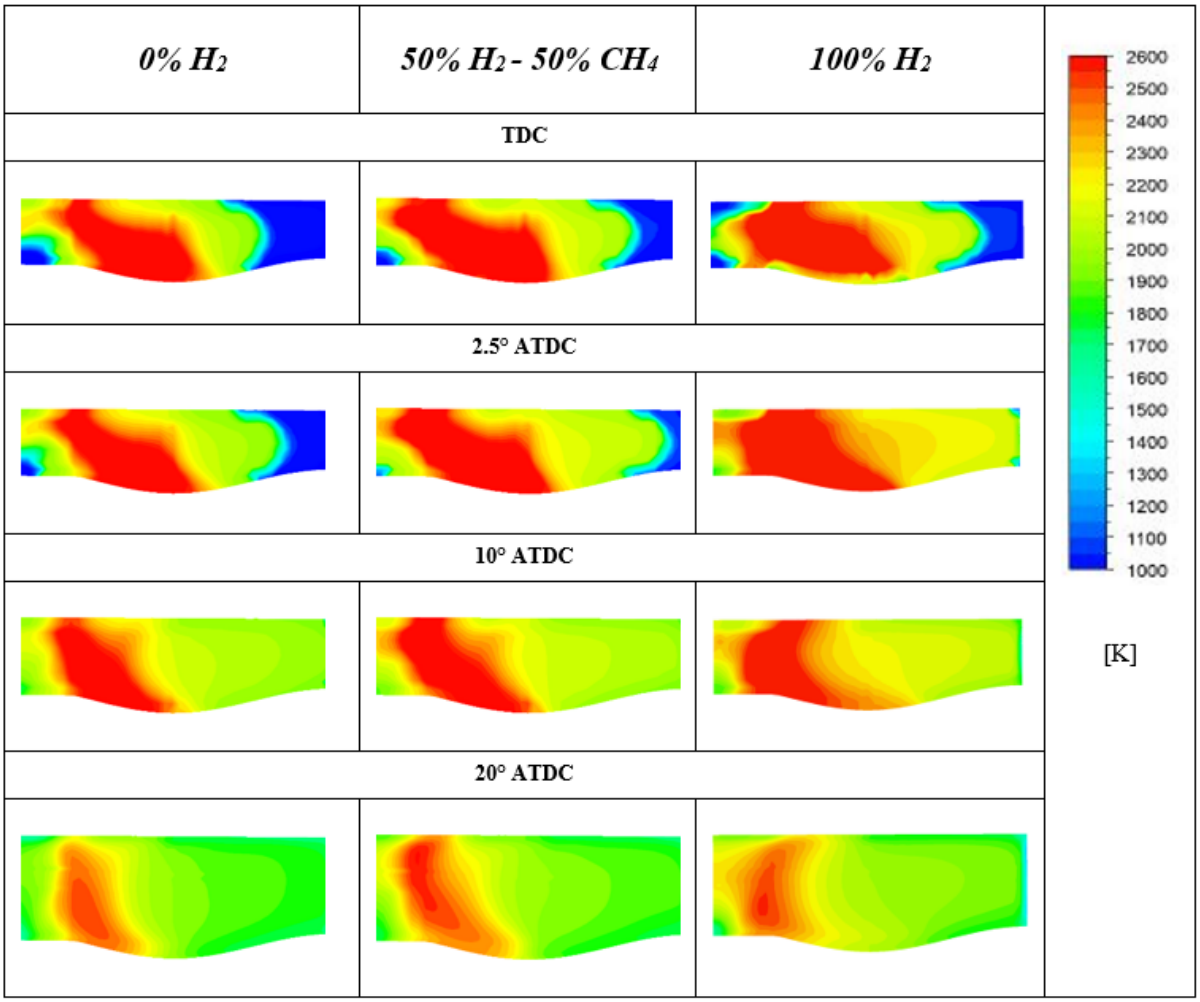

Figure 5.15: Temperature distributions for three cases

Regarding pollutant emissions, under the examined operating conditions, combustion is completed even for methane, resulting in negligible CO and UHC emissions, respectively 0.049 g/kWh and 0.0333 g/kWh. In contrast, NO_x emissions are considerably high, and they increase with the hydrogen fraction, due to the elevated in-cylinder temperatures promoted by hydrogen's higher reactivity.

As shown by the red curve in Figure 5.16, NO_x emissions range from 15 g/kWh (pure methane) to 25.7 g/kWh (pure hydrogen).

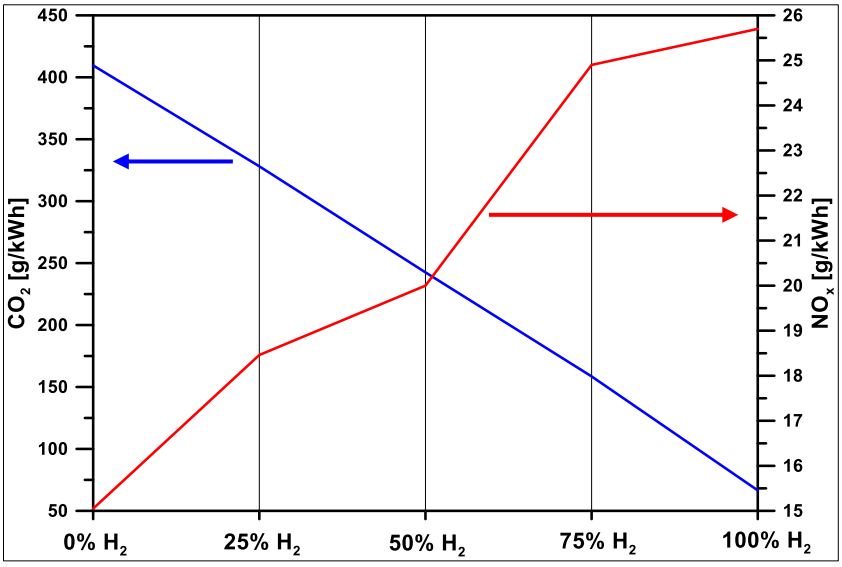

Figure 5.16: CO_2 and NO_x emissions

These values exceed even the IMO Tier I regulatory limit of 12 g/kWh, indicating that the engine configuration fails to comply with even the least stringent marine emission standards under the tested conditions. The evolution of Tier limits as a function of engine speed is shown in Figure 5.17. This outcome clearly highlights the necessity of implementing NO_x mitigation strategies, such as EGR or after-treatment systems, in order to bring emissions within regulatory thresholds.

Conversely, CO_2 emissions display an opposite trend, as illustrated by the blue line in Figure 5.17, with carbon emissions increasing linearly with the methane content in the fuel blend, due to its higher carbon-to-hydrogen ratio.

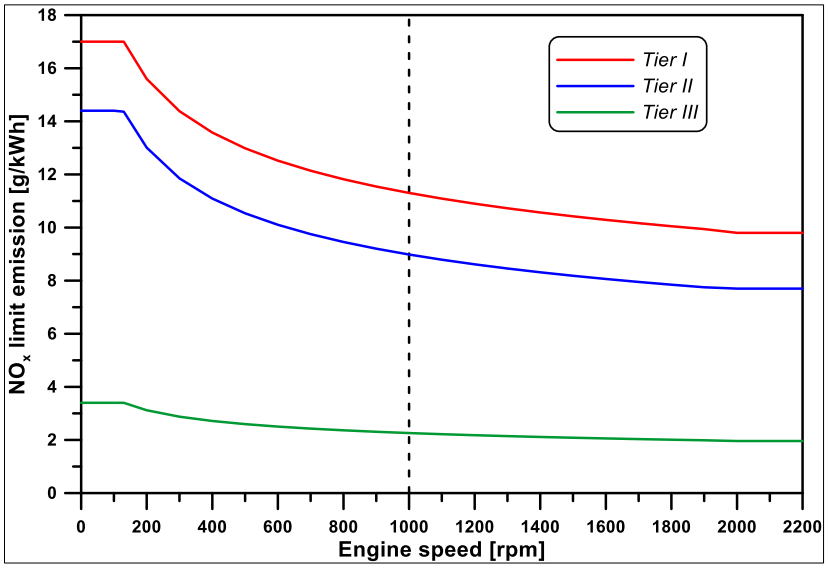

Figure 5.17: Tier limit emissions [184]

Finally, it is interesting to note that, assuming the same energy input, although hydrogen leads to faster combustion and higher peak in-cylinder pressures, this does not result in an increase in engine performance. On the contrary, with the progressive addition of hydrogen to the fuel blend, the IMEP decreases from 10 bar (pure methane case) to 9.42 bar, as reported in Table 5.7.

Table 5.7: IMEP values for the different test cases

IMEP [bar]				
0% H_2	**25% H_2**	**50% H_2**	**75% H_2**	**100% H_2**
10	9.85	9.68	9.39	9.42

This can be mainly to the phasing of the combustion. Due to hydrogen's higher ignition delay and much faster flame speed, the combustion process tends to occur more rapidly and closer to TDC. As a result, a larger portion of the heat release takes place when the piston is near TDC, where the swept volume is minimal and thus less effective expansion work can be extracted. Despite the higher peak pressure values, this unfavorable combustion phasing reduces the integrated pressure-volume area, leading to a lower IMEP.

5.3.7 NH_3 and NH_3/H_2 Blends

5.3.7.1 Test cases

Switching to the DF configurations employing ammonia, Table 5.8 summarizes the test cases investigated in this study. The parameters ER_{prem} and ER_g refer to the equivalence ratios of the premixed charge and the overall mixture, respectively, while DOI denotes the diesel injection duration. The first configuration listed in the table, referred to as the "base case," corresponds to 100% methane as premixed fuel. As previously discussed, this case serves both as the model validation benchmark and as a reference point for evaluating the performance of the subsequent configurations.

Table 5.8: Test cases

Case	Premixed blend	Energy Input [kJ]	RP [%]	Fuel mass [mg/cycle]			ER_{premix}	ER_{global}	DOI	Diesel mass [mg]
				CH_4	H_2	NH_3				
Base	CH_4	18.5	88	328	0	0	0.43	0.5	1.5° CA	50
1	NH_3	18.7	88	0	0	887	0.44	0.5	1.5° CA	50
2	NH_3	21.3	77	0	0	887	0.44	0.57	3.2° CA	110
3	NH_3	24.4	67	0	0	887	0.44	0.65	5.4° CA	180
4	NH_3/H_2	18.7	88	0	7	842	0.44	0.5	1.5° CA	50
5	NH_3/H_2	18.7	88	0	14	798	0.44	0.5	1.5° CA	50
6	NH_3/H_2	18.7	88	0	28	709	0.43	0.49	1.5° CA	50

Cases 1 through 3 explore the use of pure ammonia as the premixed fuel, while Cases 4 through 6 introduce ammonia/hydrogen blends. The rationale behind this simulation strategy is aligned with the analysis presented in the results section, and it is based on exploring two different approaches aimed at reducing carbon-based fuel dependency while preserving satisfactory engine performance.

- Case 1 maintains the same amount of diesel fuel, similar energy input, and the same premixed equivalence ratio as the base case, in order to assess the engine's behavior when ammonia is used as the sole premixed fuel.
- In Cases 2 and 3, while keeping the premixed equivalence ratio constant with respect to Case 1, the amount of diesel is progressively increased (from 50 to 110 and 180 mg/cycle, respectively) to enhance flame propagation efficiency. Accordingly, the injection duration is extended to maintain the injection pressure at 1700 bar, as specified in Table 5.2. It should be noted that this approach is pursued strictly for analytical purposes, to investigate combustion development. The associated increase in carbon-based fuel clearly limits its viability as a long-term decarbonization strategy.
- To promote the combustion of ammonia while maintaining a low carbon footprint, Cases 4, 5, and 6 investigate the use of hydrogen–ammonia blends as premixed fuels, with hydrogen proportions of 5%, 10%, and 20%, respectively. Given its high reactivity, hydrogen is expected to play a synergistic role in facilitating the ignition and propagation of ammonia flames.

5.3.7.2 Results

In Figure 5.18, the simulation results for Case #1 (ammonia as the sole premixed fuel) are compared against the Baseline Case (methane as premixed fuel) and the experimental data.

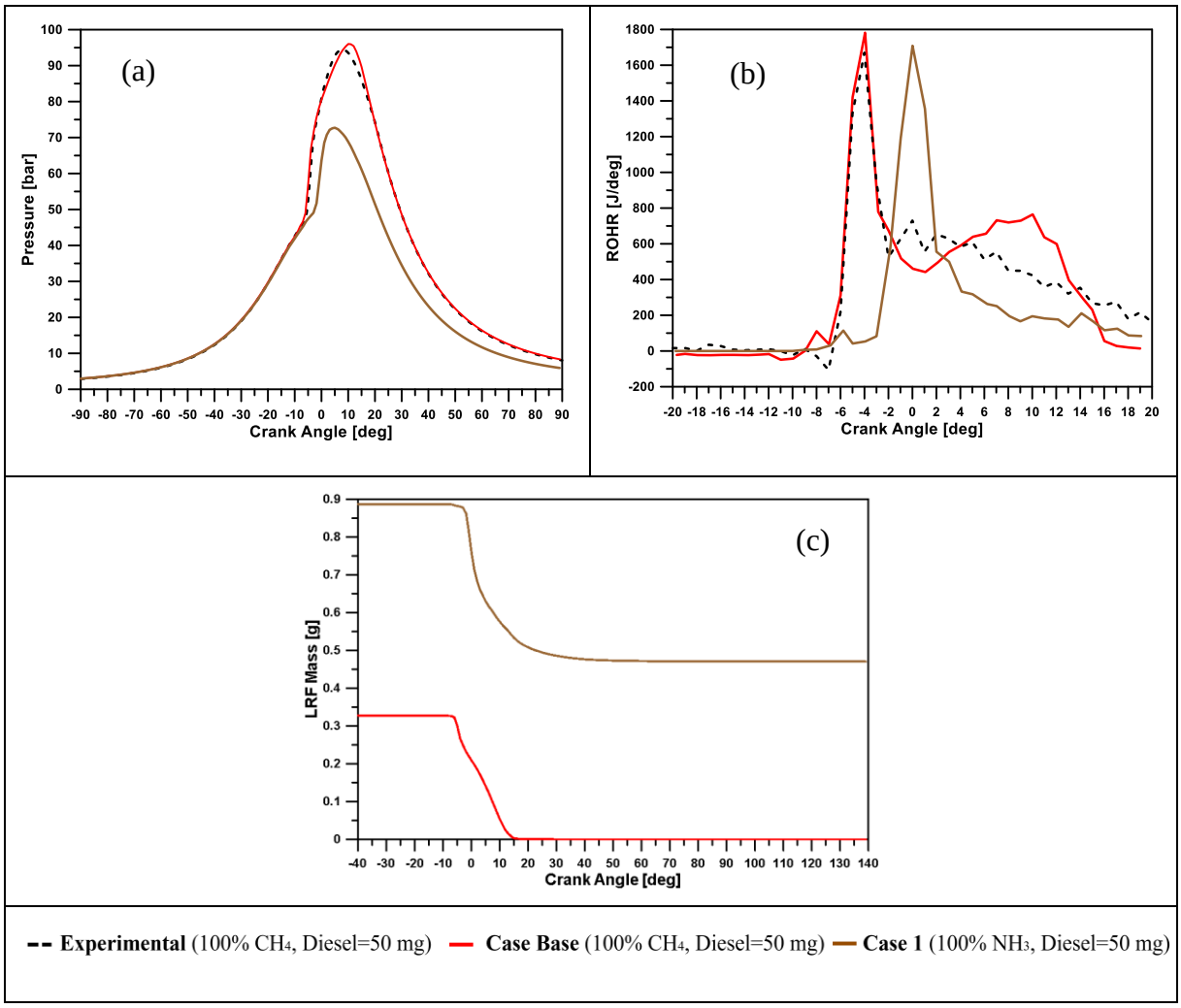

Figure 5.18: In-cylinder pressure (a), ROHR (b) and LRF consumption (c) for experimental, Case Base and Case 1

Case #1 clearly shows a significantly lower in-cylinder pressure compared to the methane-based reference, highlighting the inadequate performance of the engine when ammonia is used as the only premixed fuel. Moreover, the combustion is delayed. The ROHR curve for Case #1 exhibits only a single peak, likely corresponding to the initial combustion phase driven primarily by the pilot diesel injection, indicating limited reactivity of the ammonia–air mixture. In contrast, the Baseline Case displays a second ROHR peak shortly after TDC, which denotes a more complete and sustained combustion process, facilitated by the higher flammability of methane.

Figure 5.19c illustrates the consumption of the primary fuels for the different simulated cases, namely pure methane for the Baseline and pure ammonia for Case 1. While the Baseline Case shows complete oxidation of the premixed fuel, Case 1, despite having a slightly higher premixed equivalence ratio (ER_{prem}) and a greater fuel mass, results in incomplete oxidation. This leads to a significant amount of unburned ammonia in the exhaust.

The presence of residual ammonia at the exhaust must be strictly avoided due to its corrosive nature and potential environmental harm. Therefore, to enhance ammonia combustion reactivity and achieve more complete oxidation, two alternative strategies are proposed:

- Increasing the amount of injected diesel fuel, to support the ignition;
- Introducing hydrogen as an additive to the ammonia–air mixture, taking advantage of its high reactivity and flame speed to assist the combustion process.

Increase of pilot fuel amount

The enhancement of the pilot fuel amount was explored as a strategy to improve the oxidation efficiency of ammonia. As previously demonstrated in Ref. [175], the pilot diesel injection not only initiates the ignition process, but can also contribute to sustaining the combustion, particularly in low-reactivity mixtures. To assess the impact of this strategy, Cases 1, 2, and 3 are analyzed, wherein only the mass of injected diesel fuel is progressively increased, while the energy input from ammonia is kept constant, as indicated by the unchanged premixed equivalence ratio (ER_{prem}). This approach inevitably leads to an increase in the global equivalence ratio, thereby improving the combustion process. However, this comes at the expense of reducing the RP value, i.e., the energy contribution from the carbon-free fuel (ammonia). As already discussed, such a solution is not viable in the current context, where stringent carbon emission reductions are mandated. Nevertheless, it remains important to investigate this case study, as pilot fuel enhancement is a commonly adopted strategy in real-world applications to mitigate performance losses at low engine loads [95]. In Figure 5.19, a comparison is provided between these three ammonia-based DF cases and the Baseline Case (with methane as premixed fuel), with the objective of evaluating differences in performance and combustion behavior. The effects of increased diesel injection are clearly observable: both in-cylinder pressure and temperature (Figure 5.19a and Figure 5.19b) show a monotonic increase as more diesel is supplied, owing to the higher total energy input. Furthermore, ignition delay is progressively reduced, as seen in Figure 5.19c, which aligns with expectations given the enhanced reactivity of the mixture.

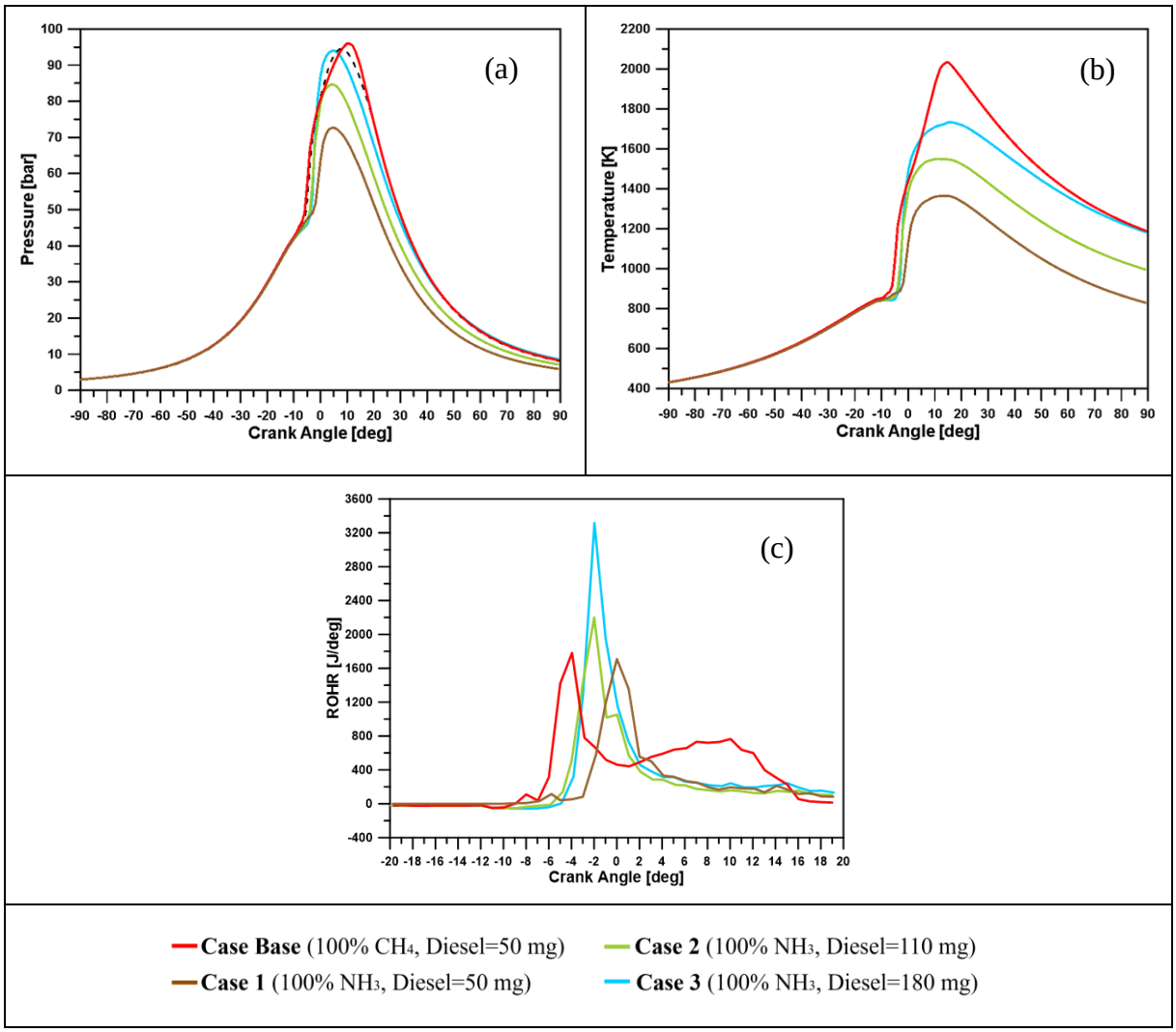

Figure 5.19: In-cylinder pressure (a), ROHR (b) and LRF consumption (c) for Case Base, Case 1, 2 and 3

By increasing the injected mass of n-dodecane by a factor of two to three (or more), a clear reduction in ignition delay is observed. Although the rail pressure is held constant and the additional fuel is delivered by extending the injection duration, the larger pilot increases spray momentum and entrainment, enriches local equivalence ratio near the jet, and strengthens low-temperature chemistry, thereby accelerating auto-ignition kinetics in the vicinity of the spray. Consistent with this, Figure 5.20 (spray and vapor distributions at 8° BTDC) shows that vaporization is complete in Case 2, whereas in Cases 3 and 4 it is still ongoing; the larger pilot masses thus produce a greater total vapor mass at that crank angle even though some liquid persists. Once ignition occurs, oxidation proceeds faster in Cases 3 and 4, as indicated by the steeper ROHR peak in Figure 5.19c. Notably, the secondary heat-release bump typically seen in staged DF operation is suppressed (or merges with the main peak), consistent with a shorter delay and a more synchronized, largely premixed heat-release event.

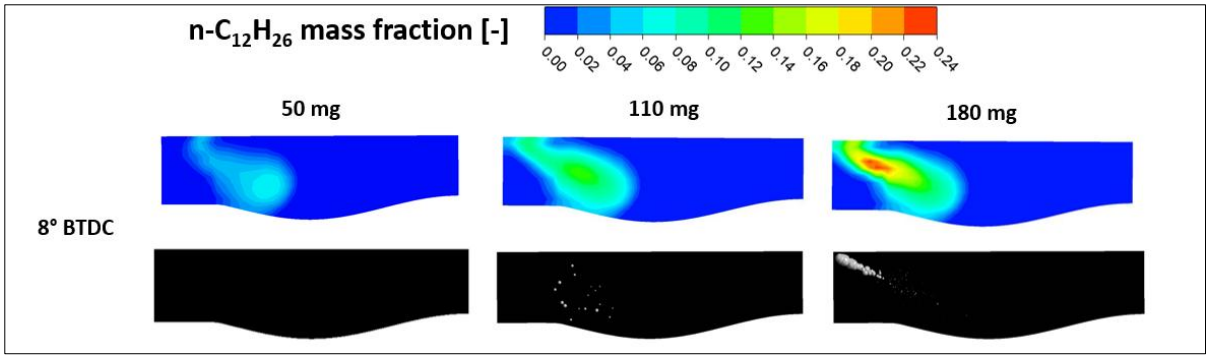

Figure 5.20: Distributions of spray and n-dodecane for Cases 1, 2 and 3 at 8°BTDC

Further insight is provided in Figure 5.21, which presents the mass evolution of key species inside the cylinder across the different cases. The ammonia consumption trend (Figure 5.21a) reveals that increasing the amount of pilot fuel does indeed enhance the oxidation of the premixed ammonia. However, even with more than three times the base diesel amount, complete combustion is not achieved. This may be explained by the diesel vapor distribution shown in Fig. 5.20, which remains concentrated near the spray axis. As a result, the oxidation of ammonia is effectively sustained only in the regions close to the pilot jet, while in peripheral zones, far from the jet, the low reactivity of ammonia hinders complete oxidation. The carbon dioxide mass fraction (Figure 5.21b) increases, as expected, with the growing diesel amount, while carbon monoxide emissions (Figure 5.21c) suggest incomplete oxidation of the pilot fuel in Cases 2 and 3. This could indicate that excessive diesel quantities may actually inhibit their own complete combustion, likely due to local over-rich regions or insufficient mixing. Nonetheless, when comparing the Base Case and Case 1, which feature the same diesel mass (Table 5.8), it becomes evident that CO_2 emissions are significantly reduced in Case #1. This result aligns with expectations, given that ammonia, being a carbon-free fuel, does not contribute to CO_2 formation. Regarding NO_x emissions (Figure 5.21d), a decreasing trend is observed with higher diesel supply. Although more pilot fuel enhances ammonia combustion, the temperature distribution becomes more localized, which may limit the formation of thermal NO_x. Furthermore, a comparison with the Base Case, which shows higher peak temperatures (Figure 5.19b), confirms that NO_x emissions can be reduced with this strategy.

In summary, the pilot fuel enhancement strategy is able to sustain localized combustion in the vicinity of the spray, improving ignition and flame development. However, this approach fails to meet carbon emission reduction targets, as the increased carbon input leads to higher CO_2 and CO emissions. Therefore, a second strategy is investigated to improve the flammability of

the premixed charge without increasing carbon emissions. This involves the use of a carbon-free, highly reactive fuel: hydrogen.

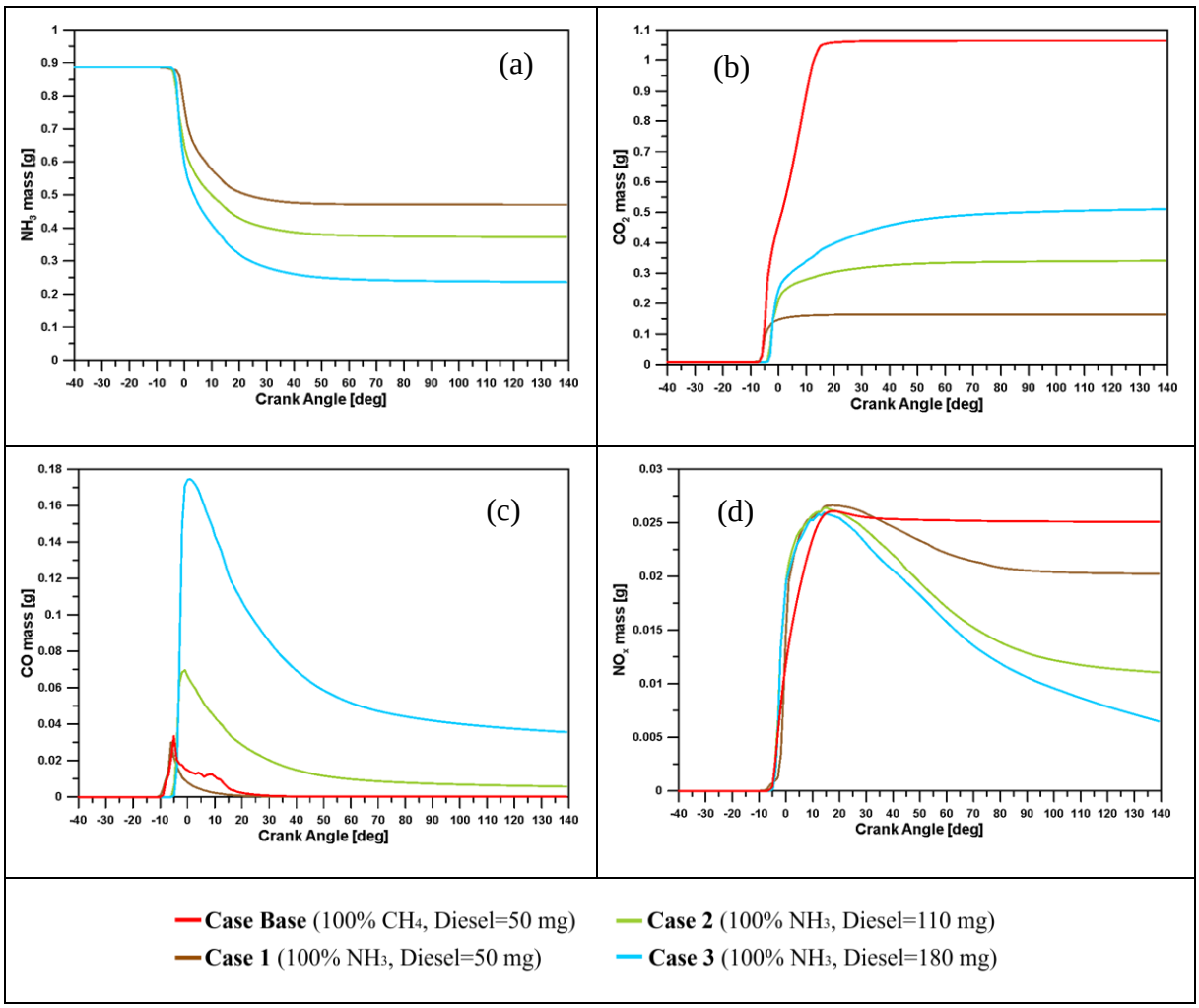

Figure 5.21: NH_3 mass (a), CO_2 mass (b), CO mass and NO_x mass (c) for Case Base, Case 1, 2 and 3

Addition of hydrogen

As a second strategy, hydrogen was introduced into the premixed charge by replacing a portion of ammonia, while maintaining the diesel pilot amount constant at 50 mg. Figure 5.22 compares the in-cylinder pressure, temperature, and ROHR for Cases 4, 5, and 6, featuring increasing hydrogen content, with the Base Case (pure methane) and Case 1 (pure ammonia).

As shown in Figure 5.22a and Figure 5.22b, the addition of hydrogen has a nonlinear effect on performance. In Case #4 (5% H_2), the engine performs even worse than with pure ammonia. This counterintuitive outcome suggests that a small amount of hydrogen may act more as a diluent than as a reactive species, possibly inhibiting mixture reactivity. However, starting from a 10% hydrogen content (Case #5), a significant improvement in pressure and temperature is

observed. At 20% H_2 (Case #6), performance even exceeds that of the methane-fueled Base Case.

The ROHR curves in Figure 5.22c also reflect this trend. Although the ignition delay of the diesel pilot appears slightly prolonged across all hydrogen cases—possibly due to hydrogen's high diffusivity interfering with pilot ignition—the second heat release peak becomes more pronounced with increased hydrogen content. Notably, in Case #5, the combustion event begins slightly later than in Case #6, suggesting a maximum ignition delay around 10% hydrogen. In contrast, Case #6 exhibits a rapid and complete combustion of the premixed charge, with the second ROHR peak exceeding the first.

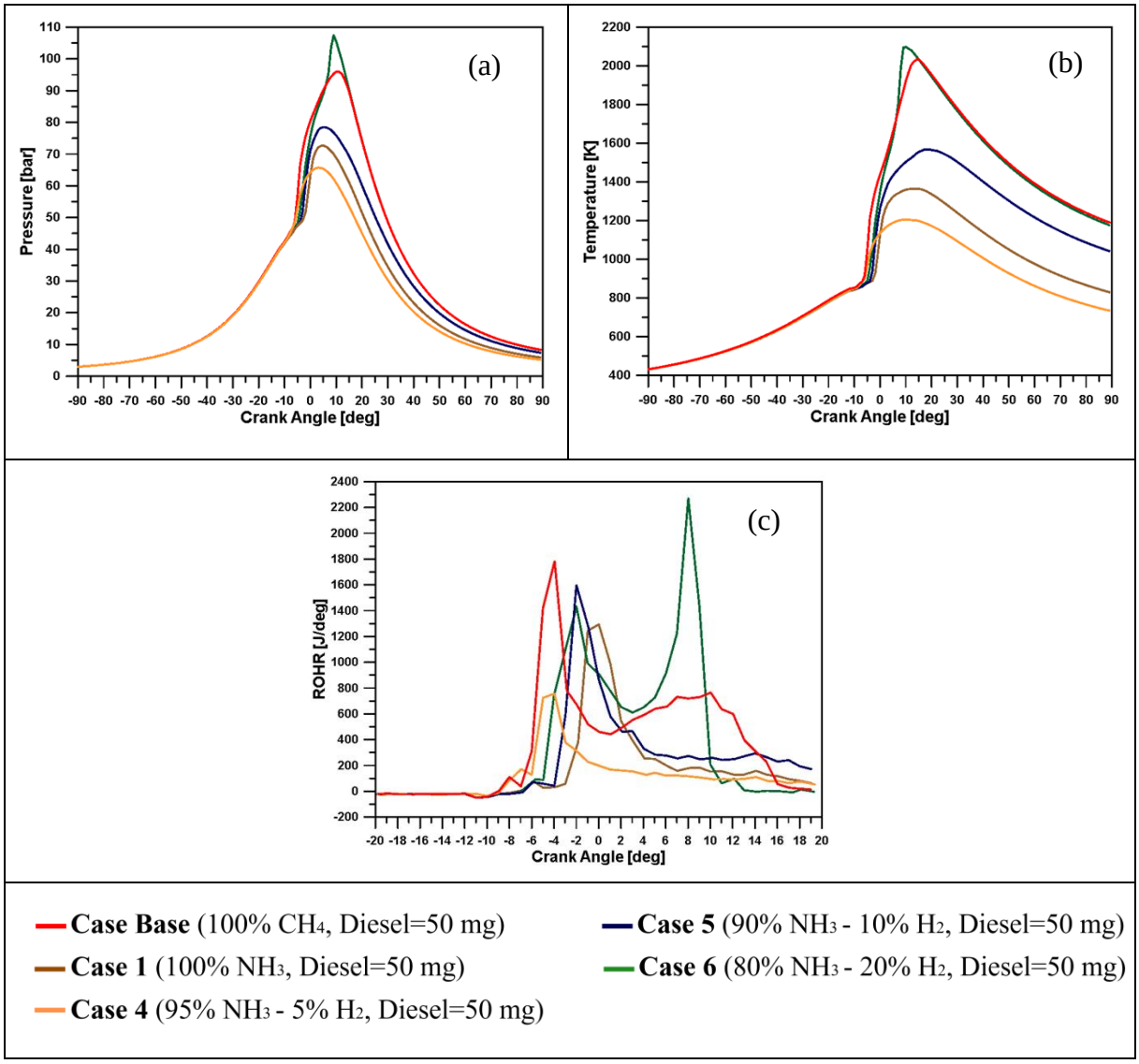

Figure 5.22: In-cylinder pressure (a), Temperature (b) and ROHR (c) for Case Base, Case 1, 4, 5 and 6

These combustion dynamics directly influence emissions, as reported in Figure 5.23. The oxidation of ammonia remains incomplete in Cases 4 and 5 (Figure 5.23a), although partial

improvement is noted as hydrogen content increases. In Case #6, where hydrogen constitutes 20% of the premixed fuel, complete ammonia consumption is finally achieved. This confirms the beneficial role of hydrogen in promoting ammonia reactivity, especially at higher concentrations. It is also important to consider the oxidation of hydrogen itself. Figure 5.23b shows that in Case #1 (no hydrogen in the mixture), hydrogen is nonetheless produced during the first combustion stage due to the decomposition of ammonia and n-dodecane. However, this internally generated hydrogen is fully oxidized. Conversely, in Case 4, a noticeable peak of unburned hydrogen appears, likely due to incomplete diesel oxidation and poor flame propagation. As hydrogen content increases in Cases 5 and 6, hydrogen oxidation improves, aligning with the rise in cylinder temperature and as confirmed by the temperature contours in Figure 5.24. The carbon emissions (Figure 5.23c and Figure 5.23d) reveal a key result: except for Case 4, hydrogen addition—especially above 10%—substantially reduces CO_2 emissions compared to the baseline, while ensuring complete diesel oxidation, as evidenced by the absence of carbon monoxide. This highlights the GHG mitigation potential of ammonia/hydrogen DF strategies in marine engines. However, NO_x emissions remain a concern (Figure 5.23e). Although hydrogen enhances performance and reduces CO_2, it also raises peak temperatures, leading to higher NO_x formation compared to the Base Case. It should be noted that after-treatment systems, commonly adopted in marine applications, are not considered in this study.

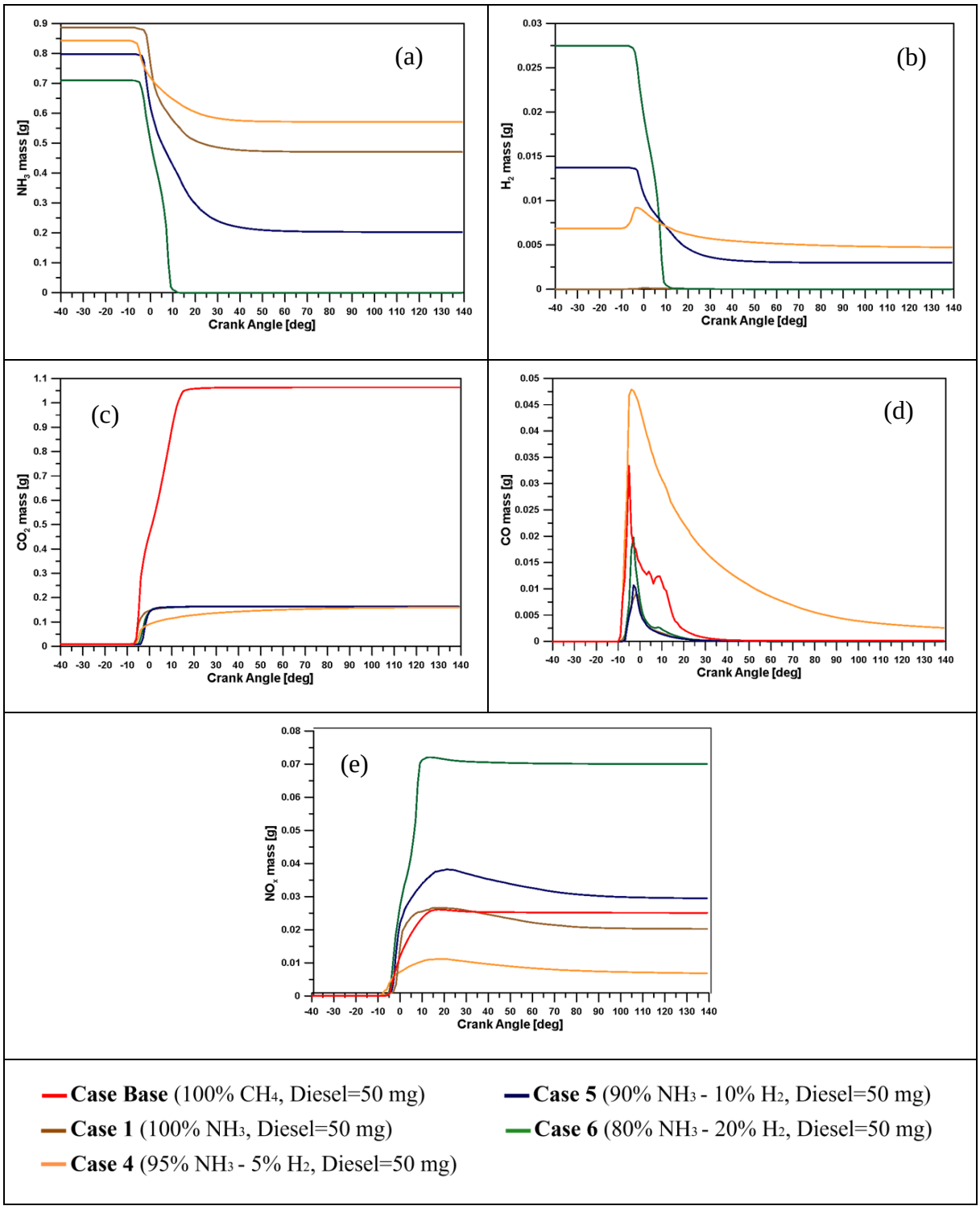

Figure 5.23: NH_3 mass (a), H_2 mass (b), CO_2 mass (c), CO mass (d) and NO_x mass (e) for Case Base, Case 1, 4, 5 and 6

Figure 5.24 confirms that the temperature rise is delayed with hydrogen addition, consistent with the ROHR curves. All cases reach peak temperatures above 2500 K, but NO_x formation also depends on the volume and duration of high-temperature regions. In Case 4, combustion is limited to zones near the diesel spray, while in Case 6, a more uniform and complete flame propagation is achieved, extending even to near-wall regions. This is corroborated by the

species contours in Figure 5.25 and Figure 5.26, where residual NH_3 and H_2 are found mostly in non-reacted near-wall zones.

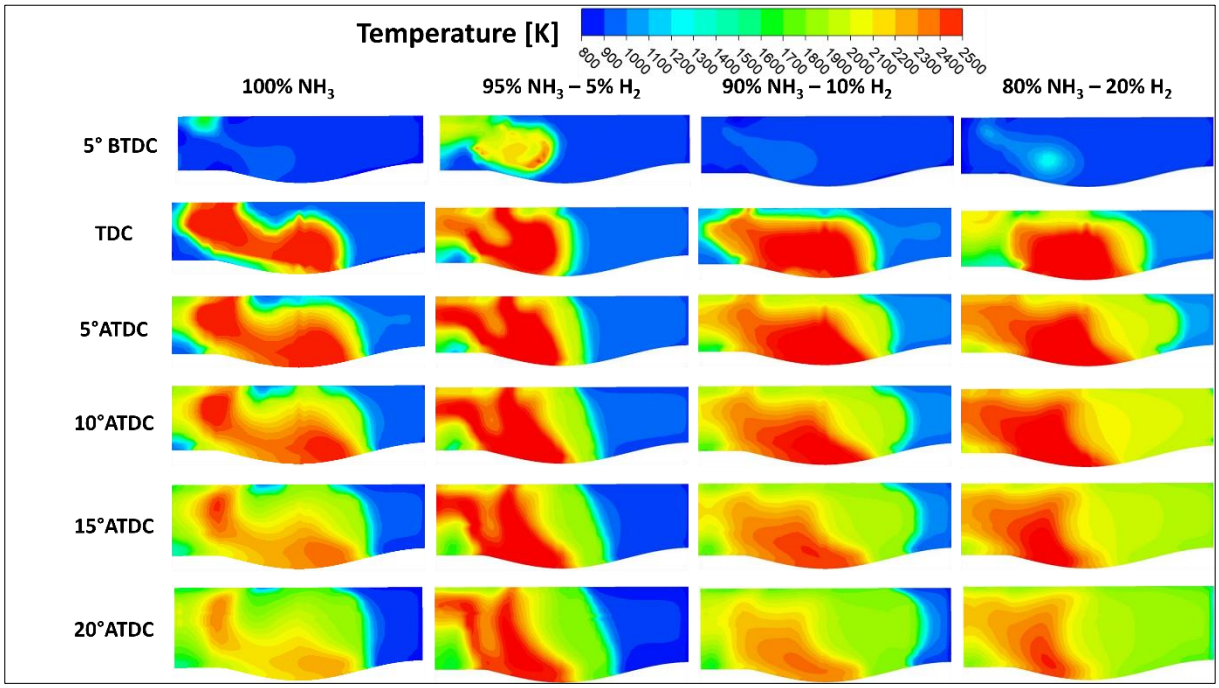

Figure 5.24: Temperature distributions at different crank angles for Cases 1, 4, 5 and 6

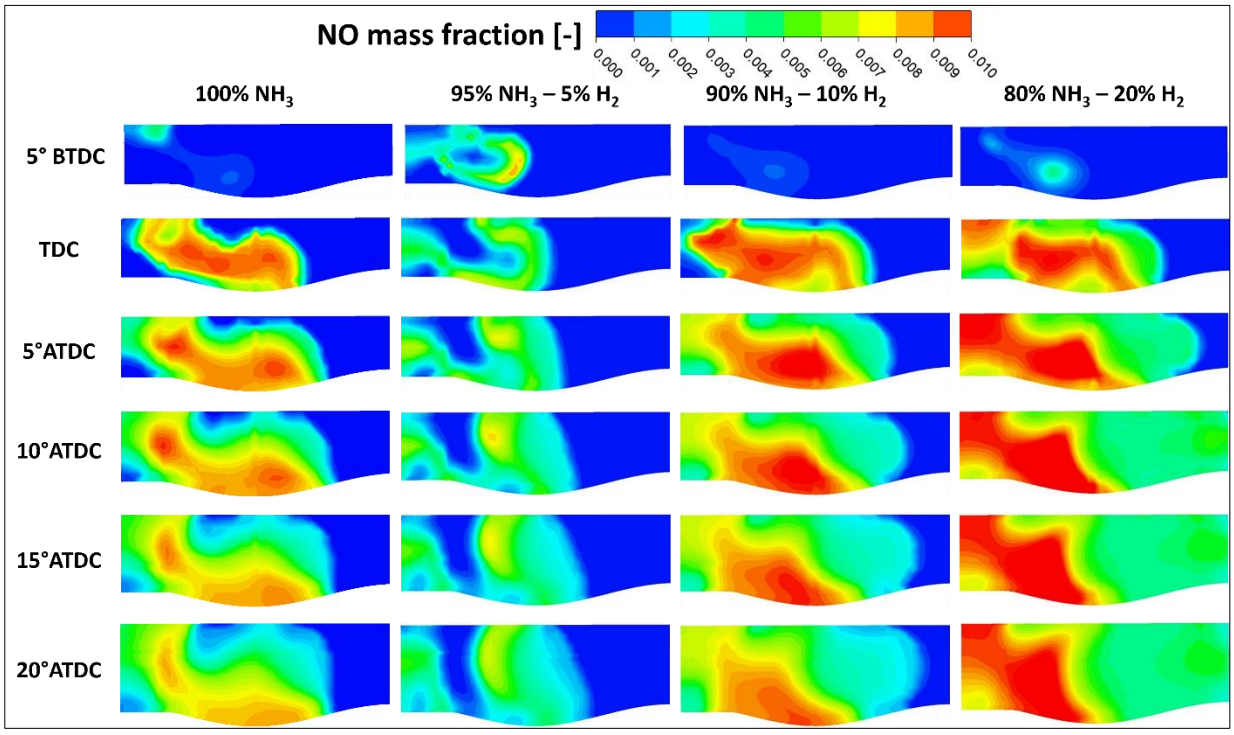

Figure 5.25: NO distributions at different crank angles for Cases 1, 4, 5 and 6

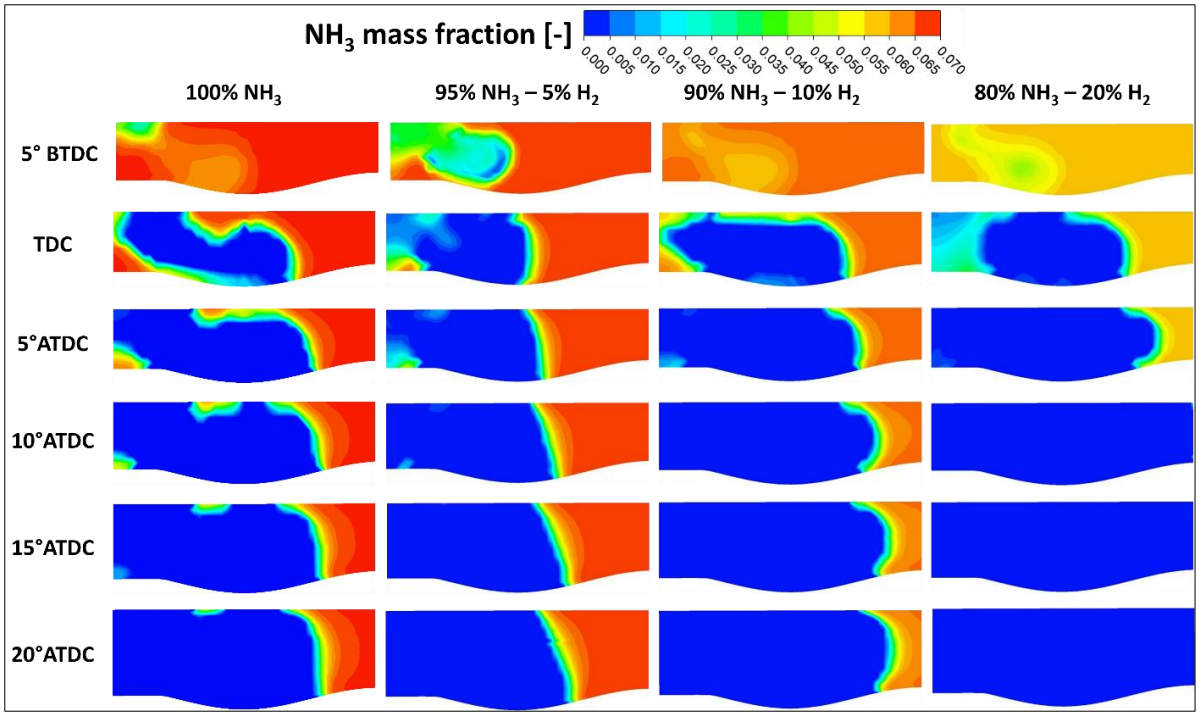

Figure 5.26: Ammonia distributions at different crank angles for Cases 1, 4, 5 and 6

Finally, Figure 5.27 illustrates hydrogen accumulation along the spray axis in Case 4, likely due to the incomplete oxidation of diesel fuel. Although Cases 1 and 5 also exhibit limited NH_3 conversion, only Case 4 displays a distinct, high-concentration H_2 region, reinforcing the hypothesis that poor combustion of the pilot fuel compromises the oxidation of both ammonia and hydrogen.

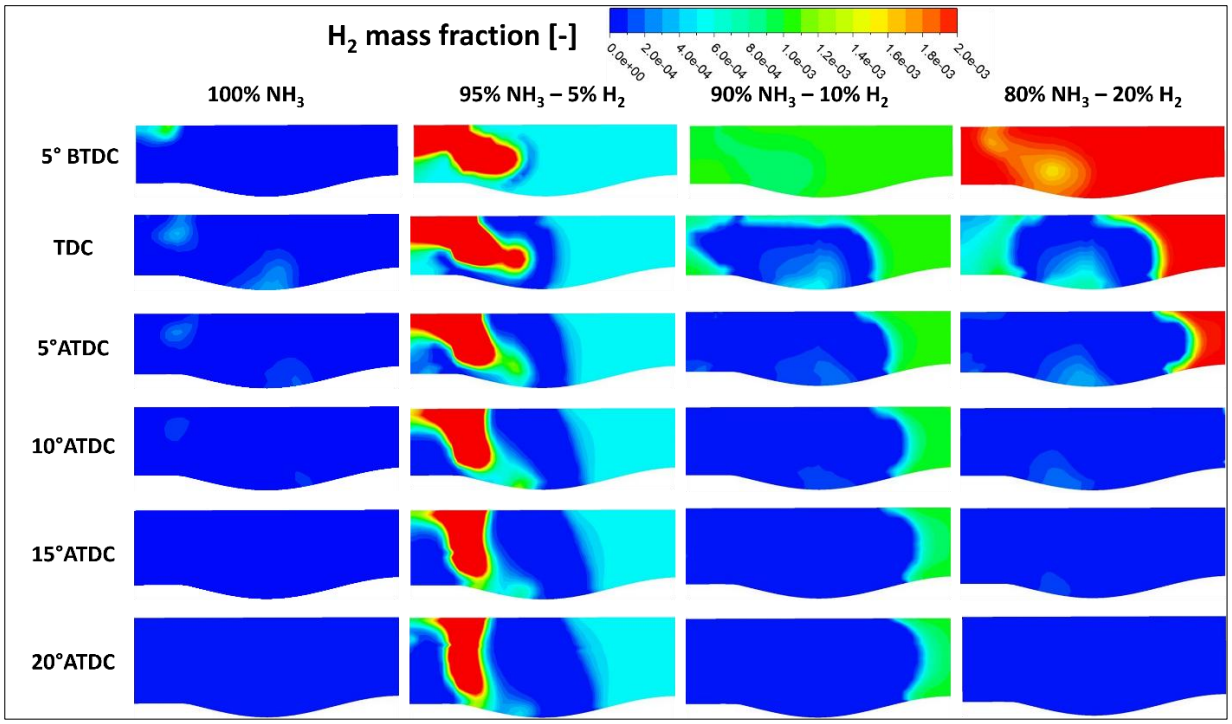

Figure 5.27: Hydrogen distributions at different crank angles for Cases 1, 4, 5 and 6

Discussion

Table 5.9 and Table 5.10 summarize the performance and emission results for all the test cases analyzed. The columns reporting ammonia and hydrogen slips refer to the percentage of unburned species with respect to the total mass of that species introduced during the cycle.

The Baseline Case, calibrated to match not only the combustion phasing but also the performance of the experimental reference point (IMEP ≈ 10 bar, as reported in [174]), serves as a benchmark for comparison. The primary objective of fuel reformulation is to reduce emissions while preserving similar performance levels. This goal is effectively met in Case 6 with a quantity of 20% of hydrogen: an IMEP of 10.1 bar is achieved, CO_2 emissions are significantly reduced, but NO_x emissions are high. Conversely, Case 1, involving complete substitution of the premixed fuel with pure ammonia, leads to drastically deteriorated engine performance: IMEP, combustion efficiency, and thermal efficiency are all roughly halved compared to the baseline. For Case 1, the emissions reduction is essentially confined to CO_2. More critically, over 50% of the ammonia remains unburned, indicating severe deficiencies in combustion stability and completeness; consequently, fuel-NO_x formation is increased. In Cases 2 and 3, the diesel pilot quantity is progressively increased in an attempt to enhance ammonia oxidation. This strategy allows for a recovery of IMEP to near-original levels. However, the increased mass of carbon-based fuel results in higher carbon input, and a rise in CO_2 emissions. Instead, the combustion remains globally inefficient, leading to orders of magnitude increases in CO emissions, which is a clear indicator of incomplete oxidation of the pilot fuel. NO_x emissions reduces due to the lower ammonia slip in Case 2 and 3. Despite the initial deterioration observed in Case 4 (5% H_2), the progressive addition of hydrogen up to 20% (Case 6) leads to comprehensive improvements:

- IMEP, combustion efficiency, and thermal efficiency are restored to levels comparable with the original engine.
- Ammonia and hydrogen slips are eliminated, ensuring complete oxidation of both species.
- CO_2 emissions are drastically reduced, reflecting the lowering in carbon content in the fuel.
- The low concentration of CO in the exhaust confirms the complete combustion of the diesel pilot, contrary to the inefficiencies seen in Cases 2 and 3.

Finally, although NO_x emissions are very high for various cases, it is essential to highlight that aftertreatment systems, such as SCR or EGR, commonly adopted in marine applications, are

not considered. Therefore, the emissions reported represent raw values, and further reductions are expected when real-world exhaust treatment is applied.

Table 5.9: Emissions values for all cases.

Case	Premixed blend	IMEP [bar]	CO [g/kWh]	CO_2 [g/kWh]	NO_x [g/kWh]	NH_3 slip [%]	H_2 Slip [%]
Base	CH_4	10	0.049	409	15	-	-
1	NH_3	4.7	0.12	118	23	56	-
2	NH_3	9.6	2.85	177	9.05	42	-
3	NH_3	9.78	13.8	201	3.87	27	-
4	NH_3/H_2 (95%-5%)	3.5	2.45	159	11.04	68	68
5	NH_3/H_2 (90%-10%)	7.63	0.007	81	23.45	25	22
6	NH_3/H_2 (80%-20%)	10.1	0.0002	62	41.76	0	0

Table 5.10: Combustion and thermal efficiency for all cases.

Case	Premixed blend	Combustion efficiency [%]	Thermal efficiency [%]
Base	CH_4	99	51
1	NH_3	50	25
2	NH_3	67	32
3	NH_3	82	37
4	NH_3/H_2 (95%-5%)	40	19
5	NH_3/H_2 (90%-10%)	78	39
6	NH_3/H_2 (80%-20%)	99	50

5.3.8 Injection Strategies

Given the crucial role of injection timing in shaping the combustion process and its direct influence on pollutant formation, this section presents a detailed analysis of different injection strategies in a DF configuration using ammonia as the primary gaseous fuel. This choice aligns with the current research focus on low-carbon and carbon-free alternatives for marine propulsion systems. The objective is to demonstrate that the limited performance observed in Case 1 of the previous section can be significantly improved through optimization of the diesel injection process, while maintaining the same mass of ammonia.

The main goal is to achieve the nominal IMEP under these conditions, while minimizing CO_2, unburned ammonia, NO_x, and N_2O emissions at the exhaust. To this end, several numerical simulations are carried out by varying the injected diesel mass, the start of injection (SOI), and the injection rate shaping.

Table 5.11 summarizes the test matrix considered for this analysis. In this section, the Base Case corresponds to Case 1 discussed previously and serves as the reference configuration. Initially, square-rate injections are analyzed. In Case #1, the diesel mass is doubled, and, in order to preserve the injection pressure level, the duration of injection (DOI) is increased from 1.5°CA to 3°CA. Subsequently, the effect of split injections, dividing the diesel delivery into a pilot and main injection event, is investigated (Case #2). However, a significant increase in diesel quantity is not a viable long-term solution for decarbonization; thus, the following cases explore the reduction of diesel mass while modifying the split ratio between pilot and main injections, as well as testing variations in their respective timing.

To further enhance fuel-air mixing and combustion efficiency, the injection rate profile is also modified. Specifically, a sinusoidal (sine-shaped) rate is implemented to compare its effects with the conventional square profile. This alternative profile enables a more gradual and controlled fuel delivery, potentially improving the premixed combustion process and limiting pollutant formation, as discussed in [185].

Finally, a parametric sweep of pilot SOI is performed, ranging from 18° BTDC to 27° BTDC, to assess the sensitivity of ignition delay and heat release phasing to early diesel injection timing. The results presented in this section aim to identify the optimal injection strategy capable of approaching the rated IMEP value while simultaneously minimizing emissions and ensuring complete combustion of the premixed ammonia-air mixture.

Table 5.11: Test cases examined

	RP%	Pilot SOI timing [deg]	Main SOI timing [deg]	Pilot Diesel injected [mg]	Main Diesel injected [mg]	Injection rate shape
Base	88	-	12° BTDC	-	50	*square*
Case#1	79	-	12° BTDC	-	100	*square*
Case#2	79	20° BTDC	12° BTDC	50	50	*square*
Case#3	82	20° BTDC	12° BTDC	40	40	*square*
Case#4	85	20° BTDC	12° BTDC	40	25	*square*
Case#5	85	20° BTDC	12° BTDC	25	40	*square*
Case#6	84	20° BTDC	12° BTDC	30	40	*square*
Case#7	85	25° BTDC	12° BTDC	25	40	*square*
Case#8	84	25° BTDC	12° BTDC	30	40	*square*
Case#9	85	20° BTDC	12° BTDC	25	40	*sine*
Case#10	85	25° BTDC	12° BTDC	25	40	*sine*
Case#11	85	27° BTDC	12° BTDC	25	40	*sine*
Case#12	85	18° BTDC	12° BTDC	25	40	*sine*
Case#13	84	25° BTDC	12° BTDC	30	40	*sine*
Case#14	82	20° BTDC	12° BTDC	40	40	*sine*

Effects of different diesel mass on combustion and emission

A split injection strategy was adopted in all test cases discussed in this section, except for the Base Case and Case #1, which operated with a single injection event. As a first step in the sensitivity analysis, the injected diesel mass was increased to assess its impact on performance and combustion development. In particular, a higher IMEP and reduced ammonia slip are expected due to improved ignition and flame propagation. However, diesel fuel tends to oxidize almost completely, resulting in increased CO_2 emissions. For this reason, in the present work, the diesel quantity increase was kept limited, and the influence of other injection parameters was evaluated. The injected diesel mass per cycle was varied from 50 mg (baseline) up to 100 mg in either single or split configurations. In Case #1, a single injection of 100 mg at 12° BTDC was used, maintaining the same injection pressure as the Base Case, and therefore requiring a doubled injection duration. Starting from Case #2, all configurations used a split injection, with the pilot SOI set at 20° BTDC and the main injection fixed at 12° BTDC, both featuring a square-shaped injection rate.

The in-cylinder pressure and ROHR (Figure 5.28a and Figure 5.28b) show a strong dependence on the injected diesel mass, with notable variations in start of combustion and pressure peak values. Diesel fuel not only acts as an ignition source but also contributes to sustaining flame propagation, thereby influencing the oxidation process.

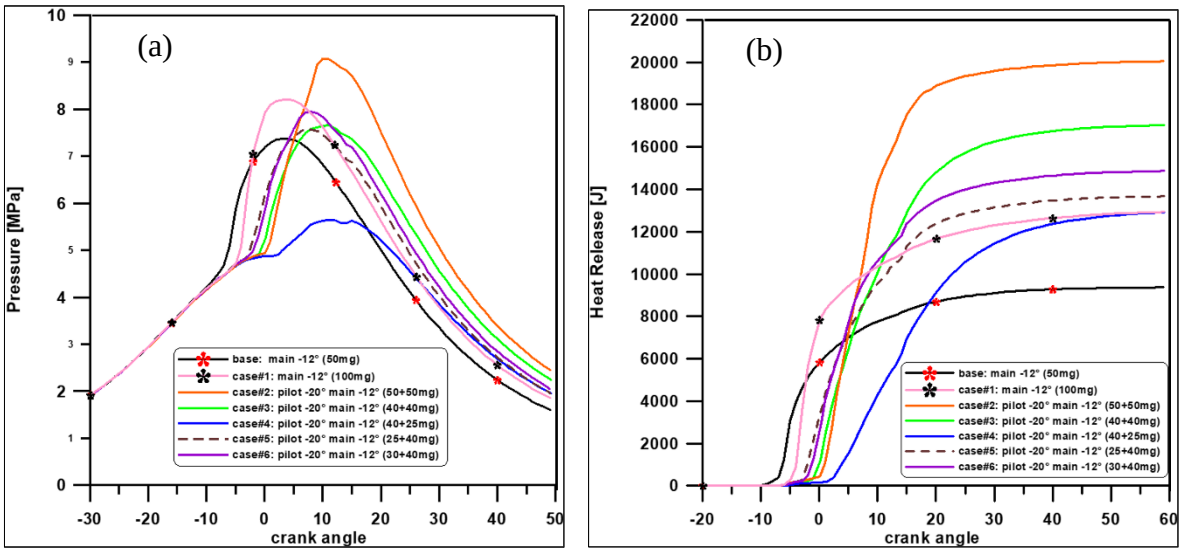

Figure 5.28: In-cylinder pressure and accumulated ROHR by varying diesel injected mass (split inj.: pilot 20°BTDC; main 12°BTDC). Square profile

Interestingly, even when the total diesel mass is the same (100 mg in both Case #1 and Case #2), the presence of a pilot injection significantly affects results in terms of both IMEP and ammonia slip (Figure 5.29 and Figure 5.30). In particular, the start of combustion is delayed in Case #2 (split injection) compared to Case #1 (single injection).

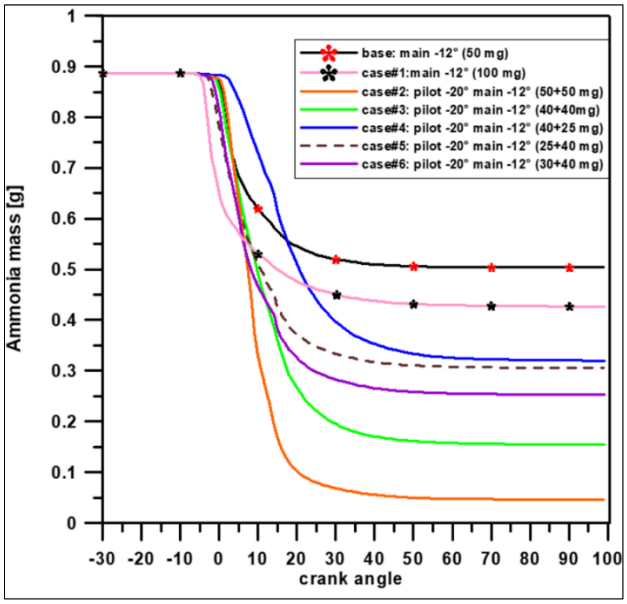

Figure 5.29: Ammonia mass fraction by varying diesel injected mass (split inj.: pilot 20°BTDC; main 12°BTDC). Square profile.

This delay is attributed to two main factors:

- A reduction in injection pressure—resulting from maintaining the same DOI across both events—lowers spray velocity.
- The evaporation of the pilot fuel, which cools the surrounding mixture and delays ignition.

Further insights emerge from comparing Case #4 and Case #5, which feature the same total diesel mass, but a different mass distribution between pilot and main injections. In Case #4, most of the diesel is delivered during the pilot phase, which may not be in optimal thermodynamic conditions for ignition. The remaining fuel during the main injection is insufficient to sustain combustion effectively. Conversely, Case #5 shows a faster energy release, resulting in better pressure development and higher IMEP values, despite comparable heat release and ammonia consumption in both cases. These findings indicate that the distribution of diesel mass between pilot and main injections is critical, with a greater influence from the main injection phase. Moreover, split injection strategies consistently improve ammonia combustion, as reflected by lower NH_3 slip and higher IMEP values (Figure 5.30a), especially in Cases #5 through #8. These cases reach performance levels equal to or exceeding Case #1 but with reduced diesel consumption. However, this improved performance and better ammonia conversion come at the cost of higher CO_2 emissions compared to the Base Case (Figure 5.30b), which utilized only 50 mg of diesel. This trade-off highlights the need for further optimization, possibly involving alternative injection profiles, timing, or pilot-to-main ratios to achieve the best compromise between performance and carbon-neutrality.

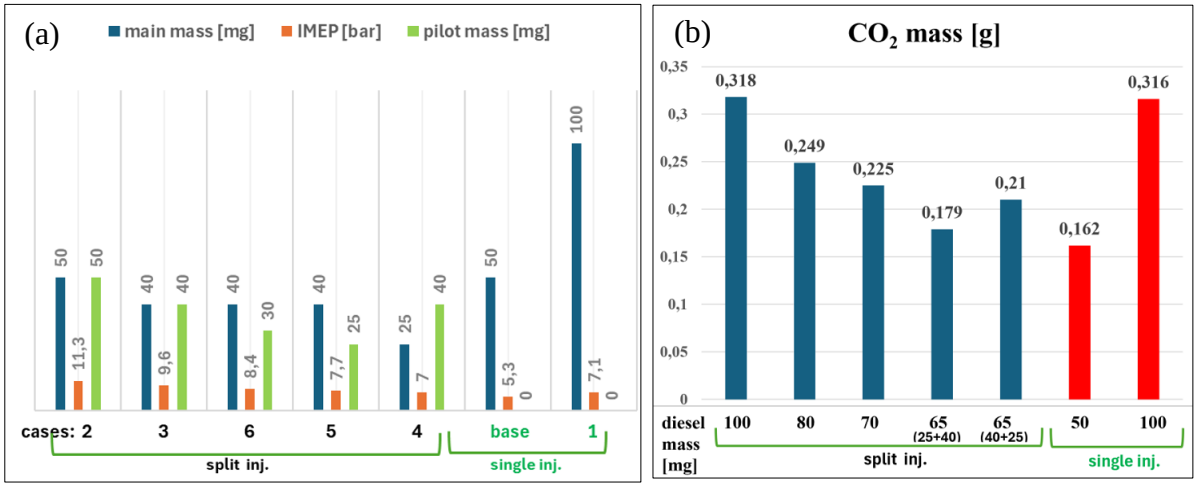

Figure 5.30: IMEP (a) and CO_2 mass (b) for different diesel injection mass (split inj.: pilot 20°BTDC; main 12°BTDC). Square profile.

At −11.5 °CA, a higher concentration of diesel vapor is observed near the injector for the 25 mg pilot injection (Case #5) compared to the 40 mg pilot (Case #4), despite both cases being operated at the same injection pressure (Figure 5.31). This behavior is primarily attributed to the reduced evaporative cooling and improved atomization associated with the smaller pilot quantity, which promote faster and more localized fuel vaporization. Conversely, the larger pilot injection induces stronger local cooling and longer liquid penetration, thereby limiting vapor formation in that region at this timing, as evidenced by the temperature distributions shown in Figure 5.32.

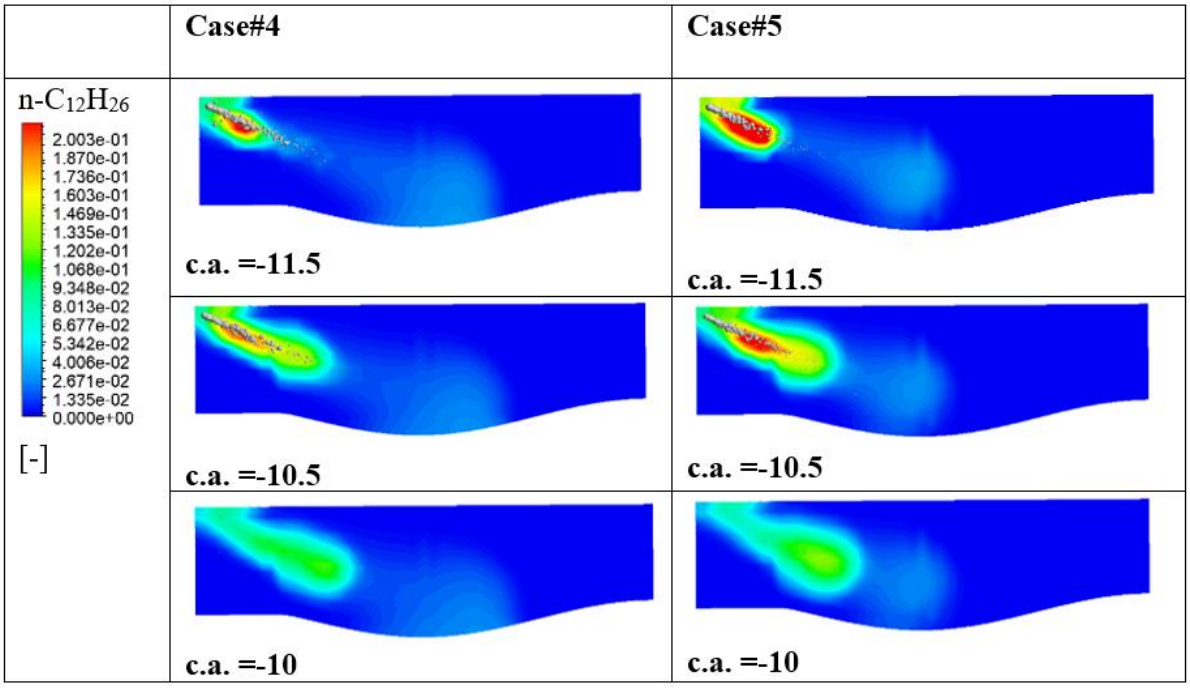

Figure 5.31: n-$C_{12}H_{26}$ distributions for Case#4 and Case#5

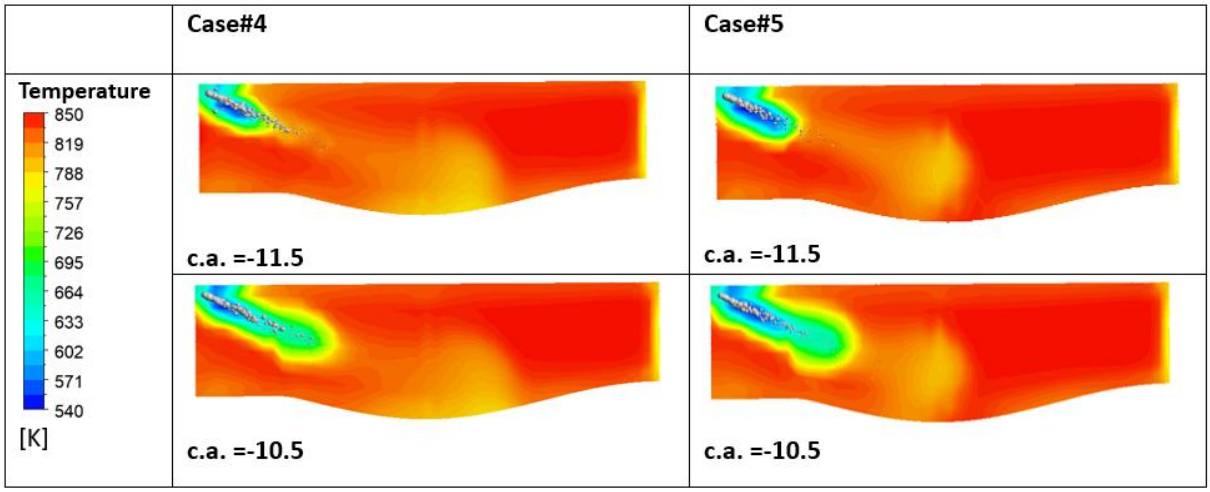

Figure 5.32: Temperature distributions for Case#4 and Case#5

Effects of different injection rate shapes on combustion and emission

The second optimization strategy involves modifying the injection rate profile from a square to a sinusoidal shape for both the pilot and main injections. The shape of the injection profile significantly affects the air–fuel mixing and combustion development. This section presents a comparative analysis of three sets of simulations where only one parameter is varied at a time, in order to isolate the influence of the injection rate shape, injection timing (SOI), and diesel mass. Building upon the findings of the previous section, Case #5, featuring a split square injection, was identified as the best configuration in terms of CO_2 reduction. In the present analysis, Case #5 is compared to Case #9, in which only the injection profile is modified to a sinusoidal shape, while maintaining the same diesel mass (65 mg) and SOI (20° BTDC). As shown in Figure 5.33a, the adoption of the sinusoidal profile significantly reduces ammonia slip, indicating enhanced oxidation of the premixed gaseous fuel. To further validate this trend, a second comparison is made between Case #7 and Case #10, both featuring the same diesel mass (65 mg) but with a more advanced pilot SOI of 25° BTDC. In this comparison, Figure 5.33b reveals an even more pronounced reduction in unburned ammonia mass fraction with the sinusoidal profile, confirming not only the benefit of smoother injection but also the critical role of injection timing. In both comparisons, the advanced SOI leads to lower NH_3 slip, suggesting that earlier diesel delivery improves fuel-air mixing and ignition quality.

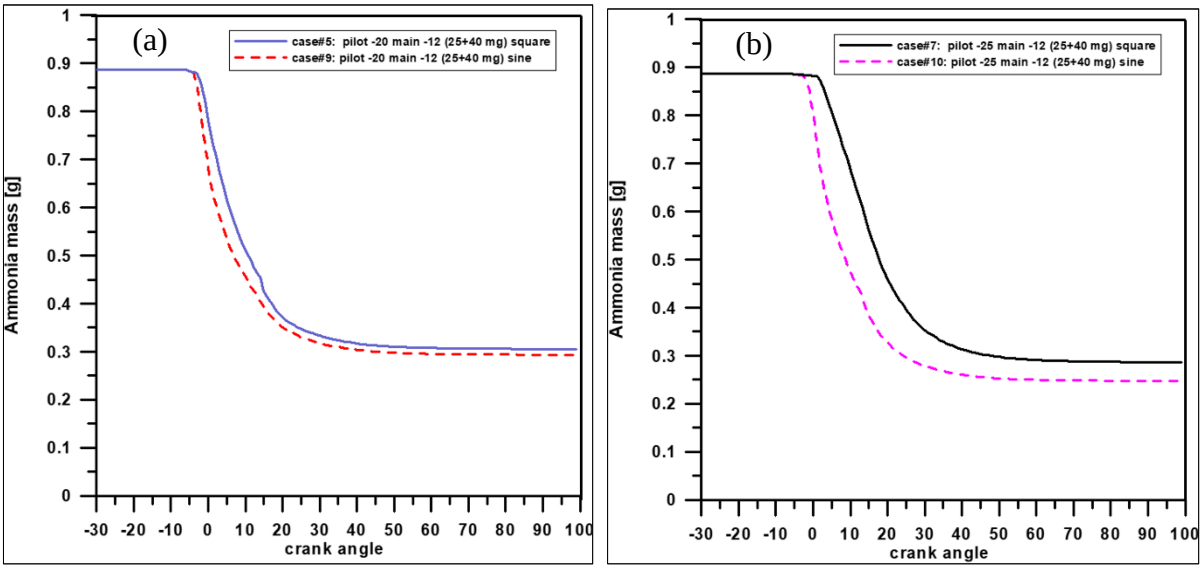

Figure 5.33: Ammonia mass fraction. Comparison between sine and square profile at fixed mass (65 mg). Pilot SOI = 20°BTDC (a); Pilot SOI = 25°BTDC (b)

The IMEP values for these four configurations (Cases #5, #7, #9, and #10) are presented in Figure 5.34. The results indicate that the use of a sinusoidal profile consistently improves engine performance, with a noticeable increase in IMEP for both injection timings. The improvement

is particularly enhanced with the advanced SOI, further reinforcing the synergistic effect of injection shape and timing.

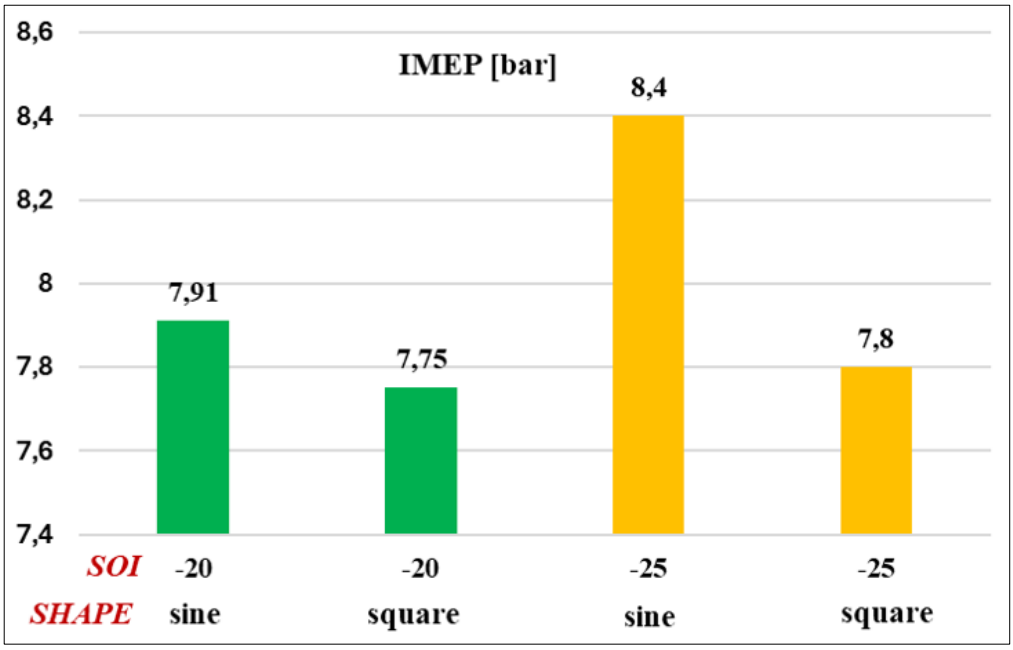

Figure 5.34: IMEP for two SOI and injection shapes at fixed total injected mass (65 mg)

Given the promising outcomes with advanced injection timing, a third comparison is carried out between Case #8 and Case #13, both using an SOI of 25° BTDC, but with diesel mass increased from 65 mg to 70 mg in Case #13. Once again, the sinusoidal profile outperforms the square one, as illustrated in Figure 5.35a, resulting in a further reduction in ammonia slip and a significant improvement in IMEP. Specifically, Case #13 achieves an IMEP increase of approximately 1 bar, attributable to enhanced peak pressure, as shown in Figure 5.35b.

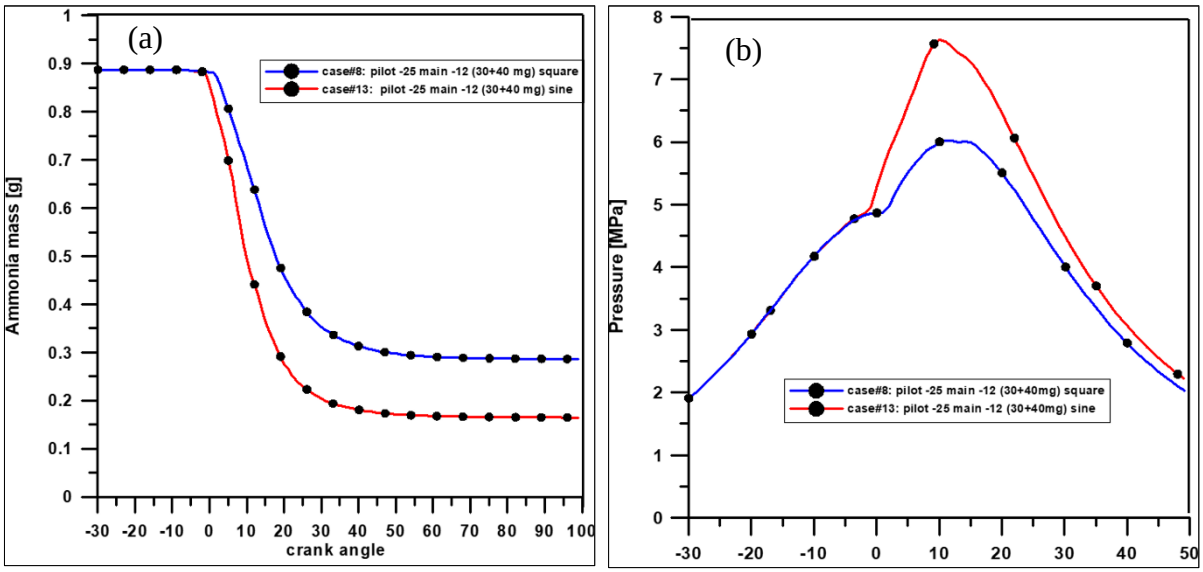

Figure 5.35: Ammonia mass fraction (a) and in-cylinder pressure (b). Comparison between sine and square profile. Diesel mass = 70 mg and SOI = 25°BTDC.

To better understand the underlying mechanisms, Figure 5.36 presents the in-cylinder temperature evolution for Cases #8 and #13. The sinusoidal injection results in earlier ignition and higher peak temperatures, reflecting more favorable combustion conditions.

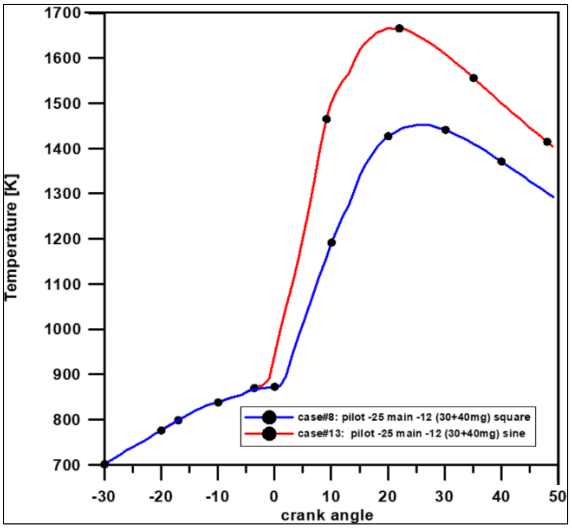

Figure 5.36:In-cylinder temperature. Comparison between sine and square profile. Diesel mass = 70 mg and SOI = 25°BTDC.

This is attributed to the altered spray and fuel vapor distributions, which are depicted in Figure 5.37. The smoother rate of fuel delivery allows for more gradual and controlled injection, facilitating improved atomization, vaporization, and air–fuel mixing. The sinusoidal shape, characterized by a gradual rise and fall in injection rate, promotes the formation of rich ignition kernels and enhances diesel–air preconditioning, which ultimately supports the initiation and propagation of combustion.

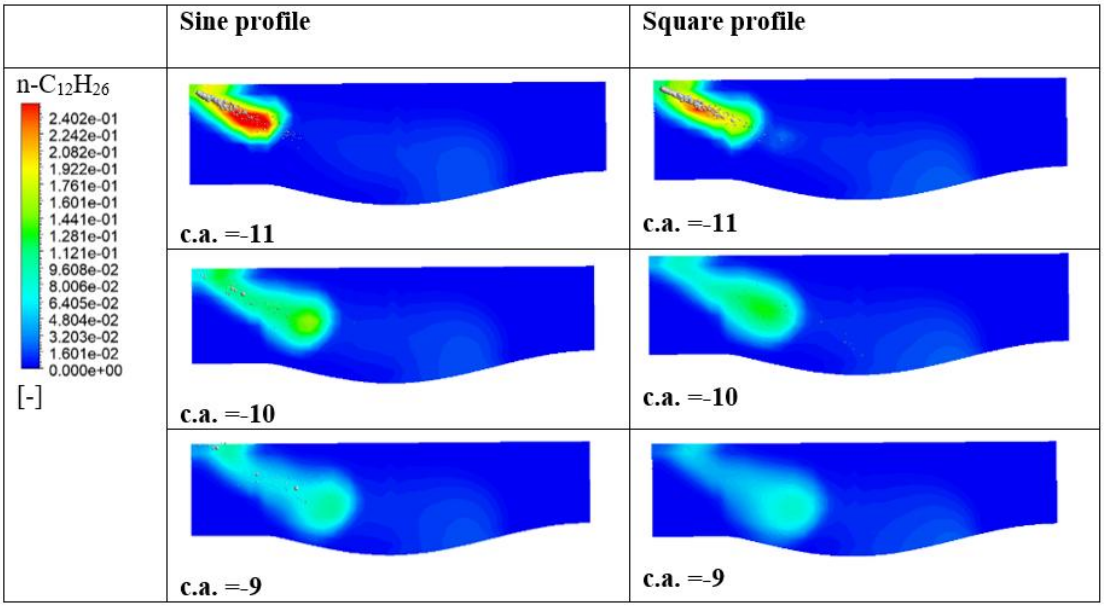

Figure 5.37: Diesel vapour distribution for two injection rate shapes. Cases #8 and #13 (70 mg; pilot -25°; main -12°).

These effects are further confirmed by the temperature contours in Figure 5.38, which reveal wider and more uniformly distributed high-temperature regions, especially along the spray direction. Finally, the ammonia distribution maps in Figure 5.39 show faster and more complete consumption of ammonia with the sinusoidal profile, corroborating the reductions observed in Figure 5.35a. This accelerated oxidation significantly contributes to more efficient flame propagation within the chamber.

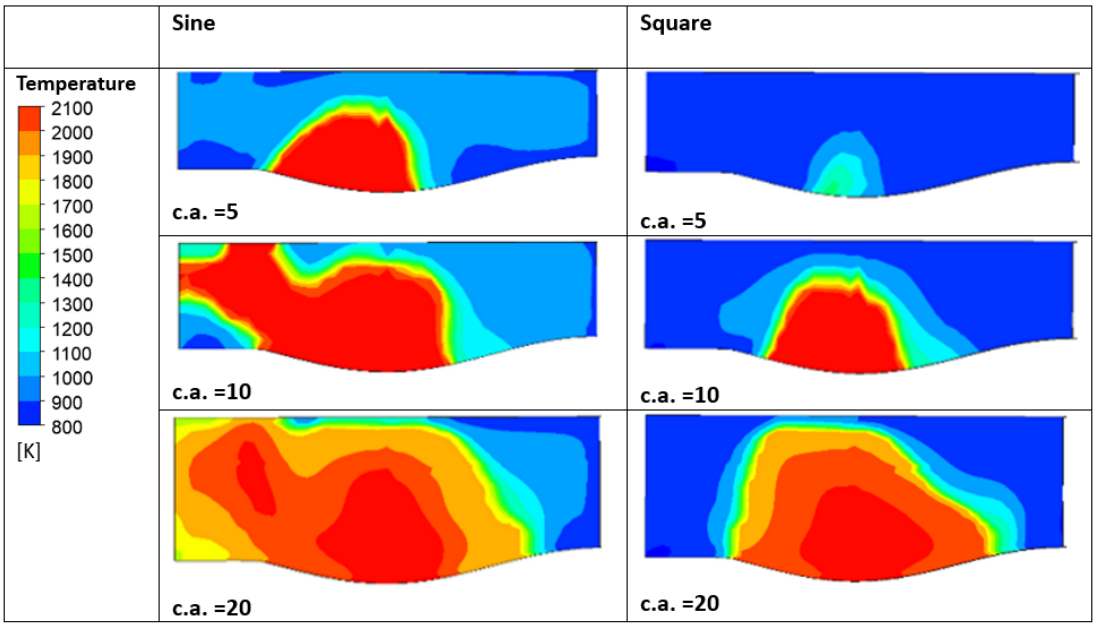

Figure 5.38: Temperature distribution for two injection rate shapes. Cases #8 and #13 (70 mg; pilot -25°; main -12°).

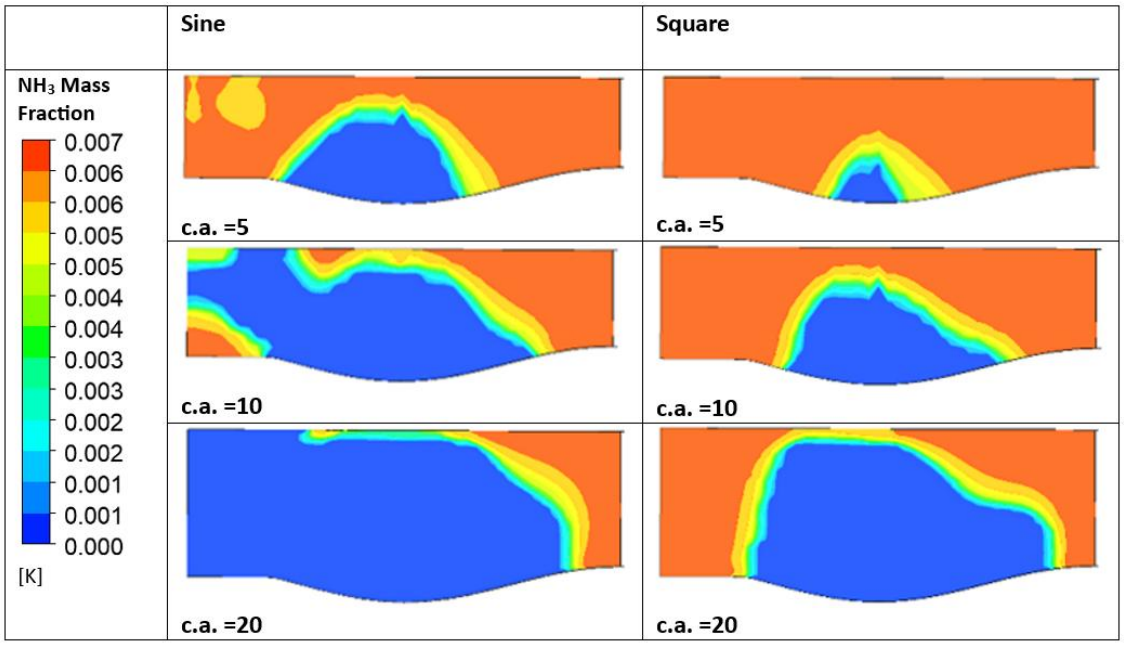

Figure 5.39: Ammonia mass fraction under different injection rate shapes analysed in a longitudinal section. Cases #8 and #13 (70 mg; pilot -25°; main -12°).

Overall, the results demonstrate that the sinusoidal injection profile, particularly when combined with an advanced SOI and slightly increased diesel mass, can substantially enhance ammonia combustion, boost engine performance, and reduce pollutant emissions, making it a promising strategy for future low-carbon DF marine engines.

Effect of different pilot SOI on combustion and emissions

As previously discussed, all the test cases in this section adopt a split injection strategy, which significantly influences the combustion behavior of ammonia. The next series of simulations (Cases #9 to #12) investigate the effect of pilot SOI variation on engine performance and emissions, while keeping the total diesel mass constant at 65 mg and employing a sinusoidal injection profile for both pilot and main injections. As shown earlier, the injection rate shape plays a key role in enhancing combustion. However, pilot injection timing is equally critical in optimizing the ignition and oxidation phases. To this end, Figure 5.40 reports the combustion duration and IMEP for the four examined SOI values (18°, 20°, 25°, and 27° BTDC). Among these, Case #10 (SOI = 25° BTDC) achieves the highest IMEP of 8.4 bar, indicating that under the given conditions, a moderately advanced pilot promotes the most effective energy release.

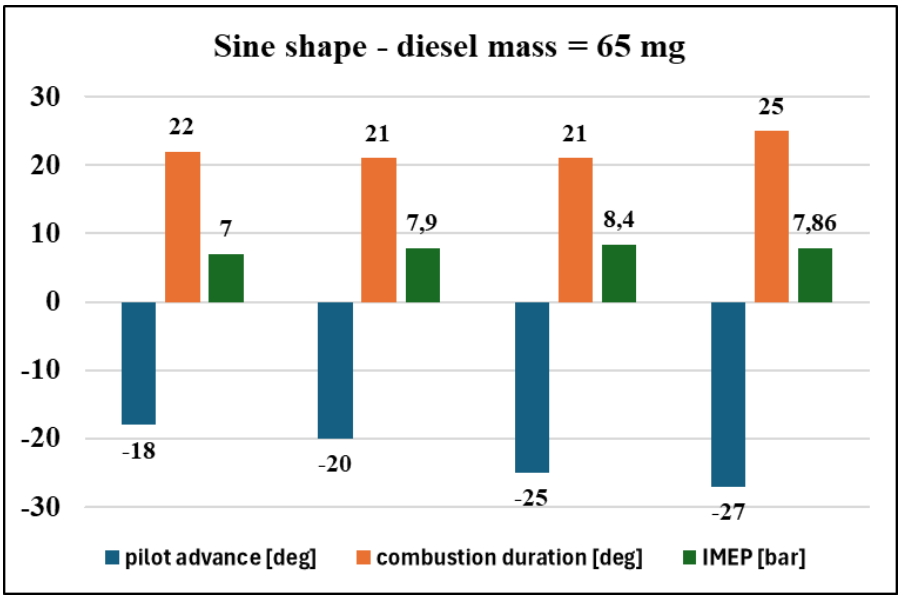

Figure 5.40: 10%-90% Heat release duration and IMEP by varying pilot advance at fixed total injected mass. Sine profile.

On the other hand, Figure 5.41a and Figure 5.41b present the results for ammonia slip and $EINO_x$. A trade-off between performance and emissions is evident: while advanced pilot injection improves combustion efficiency and IMEP, it also increases NO_x formation due to higher in-cylinder temperatures. Conversely, the lowest NO_x emissions are obtained for SOI = 18° BTDC; however, this case also shows the highest ammonia slip and lowest IMEP,

indicating poor combustion efficiency. These findings are consistent with previous studies [189], which observed a similar inverse relationship between NO_x and unburned species for ammonia-fueled DF engines.

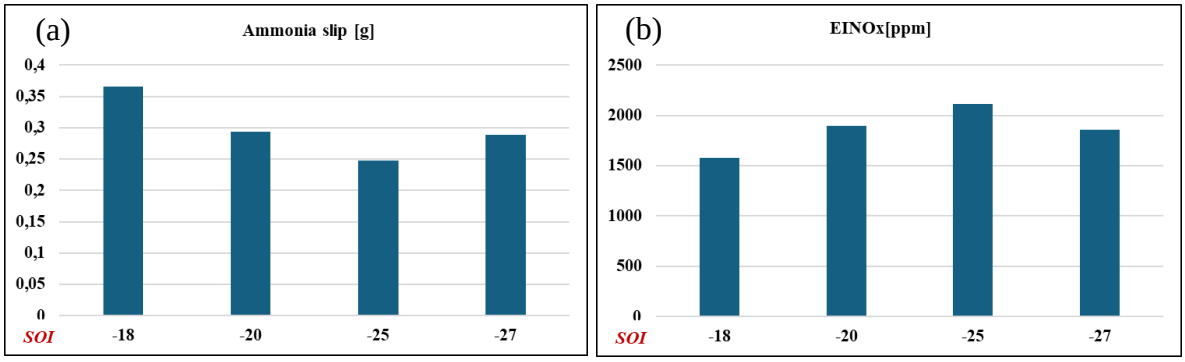

Figure 5.41: Ammonia mass (a) and EINO$_x$ in ppm (b) at exhaust at fixed total injected mass (65 mg) for different SOI. Sine profile.

Furthermore, as the SOI is progressively advanced, IMEP initially increases (from 18° to 25° BTDC), but then slightly declines for SOI = 27° BTDC, likely due to excessive ignition delay and reduced thermal efficiency. This trend confirms that SOI = 25° BTDC represents the optimal compromise for this setup, balancing high IMEP with acceptable ammonia slip and manageable NO_x levels. To provide deeper insight, Figure 5.42a and Figure 5.42b compare the in-cylinder pressure and ROHR for all cases. It is observed that earlier pilot injections (e.g., Cases #10 and #11) delay the start of combustion due to reduced injection pressure and greater vaporization cooling. As a result, these configurations exhibit smoother heat release profiles, with broader and lower ROHR peaks, which may be advantageous in mitigating combustion noise and mechanical stress.

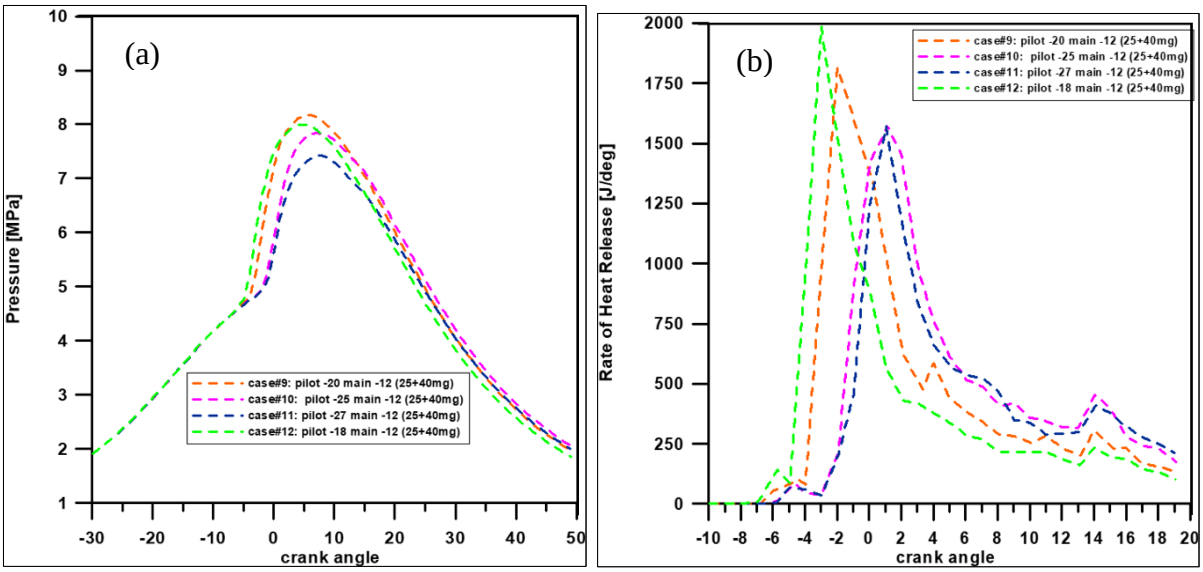

Figure 5.42: In-cylinder pressure (a) and ROHR (b) at different SOI and diesel injected mass. Sine injection rate shape.

Figure 5.43 show the mass fractions of CO_2, CO, NO, and N_2O. The case with the most delayed SOI (18° BTDC) shows the highest CO and CO_2 emissions, which reflects incomplete combustion and inefficient oxidation of the diesel and ammonia mixture. In contrast, NO and N_2O emissions are minimized in this case due to the lower combustion temperatures. Nevertheless, the overall poor combustion quality, as evidenced by low IMEP and high ammonia slip, makes this strategy suboptimal.

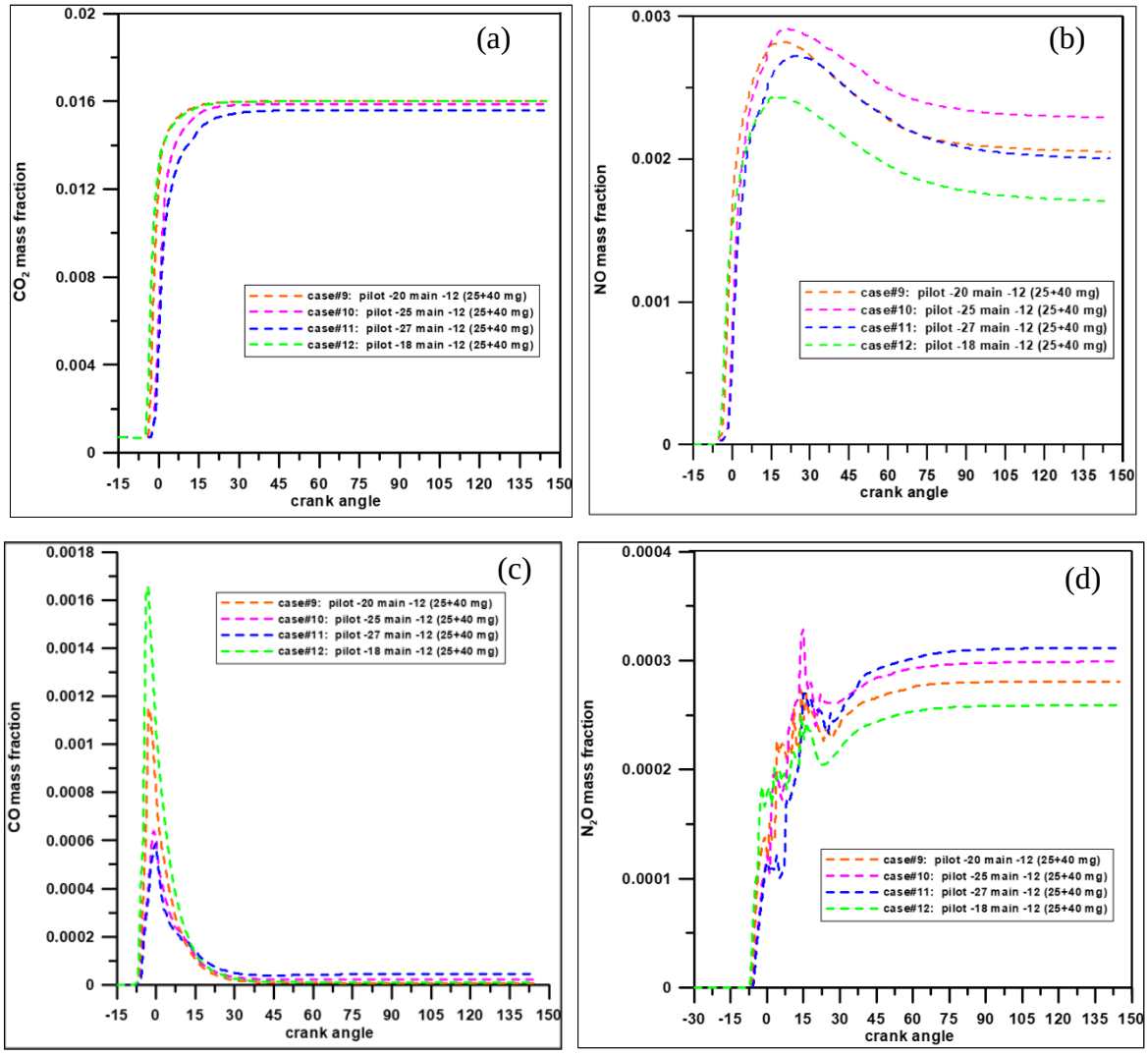

Figure 5.43: CO_2 (a), NO (b), CO (c) and N_2O (d) mass fraction at different SOI and diesel injected mass. Injection rate shape: sine profile.

For a more detailed analysis, Figure 5.44 shows the spatial distributions of diesel vapor at different crank angles for two operating cases, corresponding to pilot injection timings of −25° (Case #10) and −18° (Case #12). It is clearly observed that the delayed pilot start of injection (−18°) leads to a faster disappearance of diesel vapor and to a more intense and concentrated heat release. The shorter ignition delay reduces the premixing time, causing the pilot fuel to burn rapidly after injection. Although the heat release rate is higher and more abrupt, the overall

in-cylinder temperature remains lower compared to the −25° case, as visible in Figure 5.45. This can be attributed to the less favorable thermodynamic conditions at the later injection timing, which limit the total energy converted into thermal load within the combustion chamber. As a result, the peak temperatures are reduced, despite the stronger instantaneous combustion event.

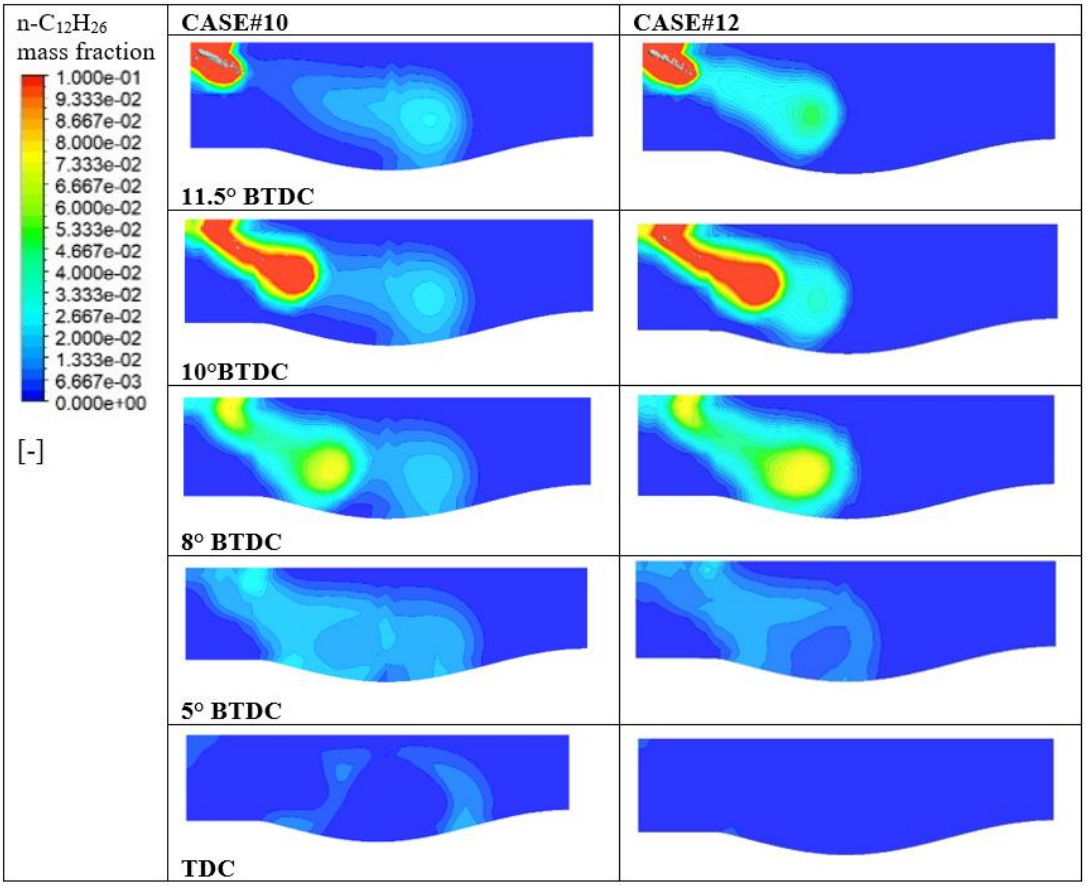

Figure 5.44: N-dodecane mass fraction distributions for Case#10 and Case#12

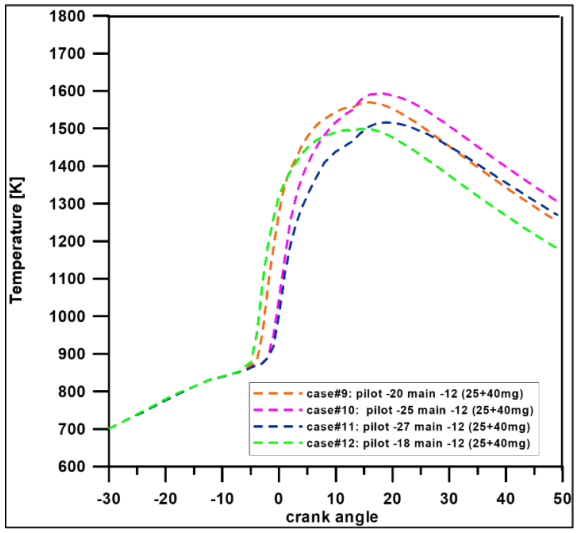

Figure 5.45: In-cylinder temperature at different SOI and diesel injected mass. Injection rate shape: sine profile.

From the temperature distribution in Figure 5.46, it is evident that combustion starts earlier for Case #12, while it is less evident that the high-temperature region is more extended in Case #10.

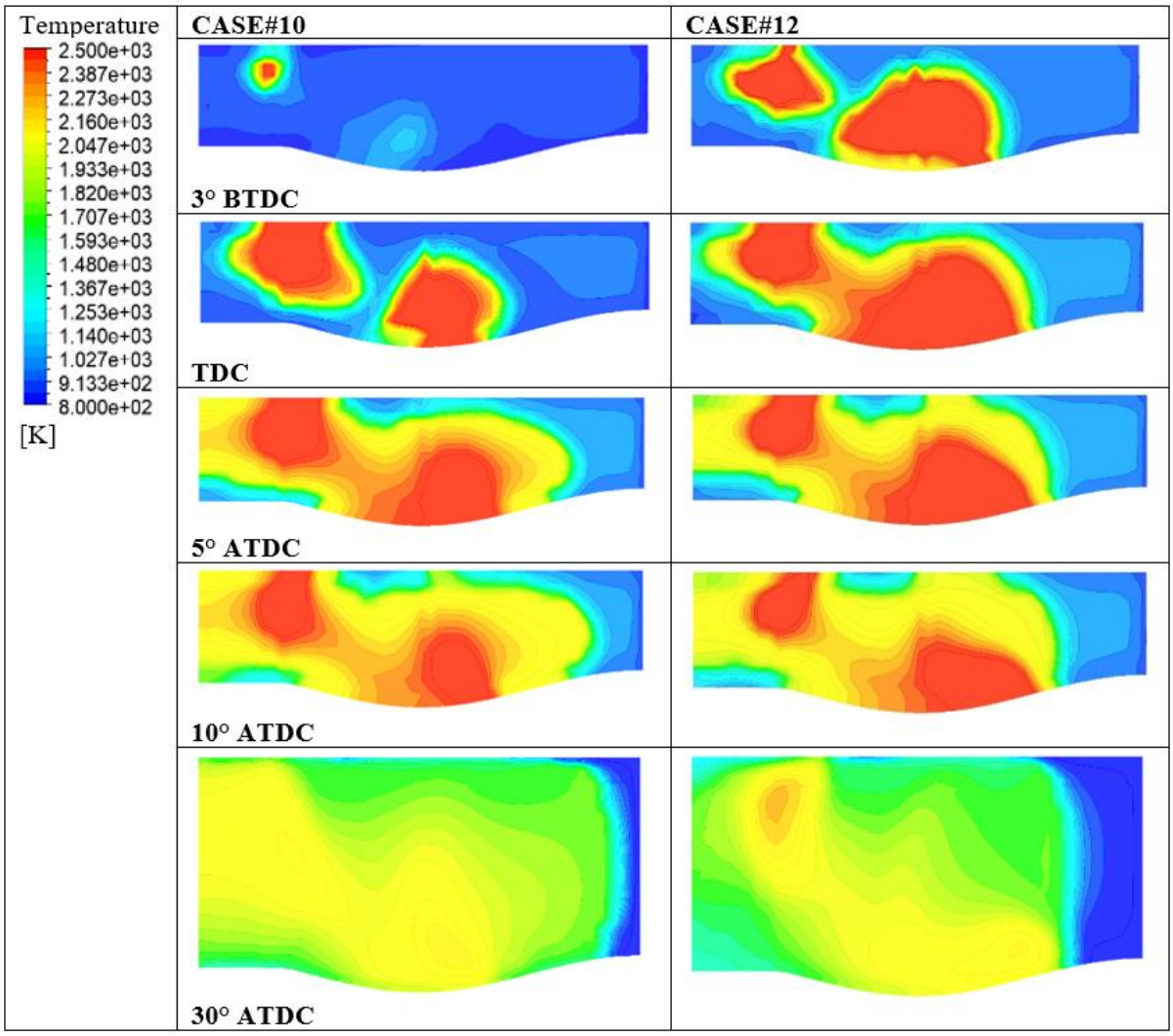

Figure 5.46: Temperature distributions for Case#10 and Case#12

In summary, although none of the examined configurations reach the nominal target of 10 bar IMEP, the sensitivity analysis of pilot SOI confirms that SOI = 20° BTDC offers the best compromise between ammonia oxidation, IMEP, and pollutant formation. This injection timing achieves relatively high performance while maintaining ammonia slip and NO_x emissions at acceptable levels. However, to fully meet the desired engine load, an increase in diesel mass or further optimization of the injection strategy might still be required.

Optimized Case

Based on the findings from the sensitivity analyses conducted in the previous sections, a final test case (Case #14) is introduced to validate the effectiveness of the proposed injection strategy. This case was specifically designed to achieve the target value of 10 bar IMEP, while simultaneously minimizing ammonia slip and CO_2 emissions. From prior evaluations, Case #3, featuring a pilot SOI of 20° BTDC and a diesel mass of 80 mg with a square injection rate, emerged as the best-performing configuration among the previously analyzed setups. Building upon this, Case #14 replicates the same SOI and diesel mass, but adopts a sinusoidal injection profile, which has been shown to significantly improve combustion development and fuel-air mixing efficiency.

In the pressure trace in Figure 5.47a, the Case#14 (black line) exhibits a slightly higher peak compared to Case#3 (magenta line). This indicates a more efficient energy conversion and a faster combustion phasing, likely due to a smoother and more progressive fuel injection that enhances air–fuel mixing in the early stage of combustion. Similarly, the heat release rate plot in Figure 5.47b shows a steeper and earlier increase for the Case#14, confirming that combustion starts earlier and develops more rapidly. The smoother injection promotes a more homogeneous mixture formation, which results in a shorter combustion duration and a slightly higher total released energy. The temperature evolution in Figure 5.47c follows the same trend: Case#14 leads to higher peak temperatures (approximately 100–150 K higher) and an earlier temperature rise. This behavior is consistent with the earlier and more intense heat release observed previously. Finally, the NO formation trends in Figure 5.47d clearly reflects this temperature effect. The Case#14 produces higher NO emissions, consistent with the higher in-cylinder temperatures and more advanced combustion phasing, which favor thermal NO formation via the Zeldovich' mechanism. Conversely, Case#3, characterized by a slower heat release and lower peak temperature, results in reduced NO levels.

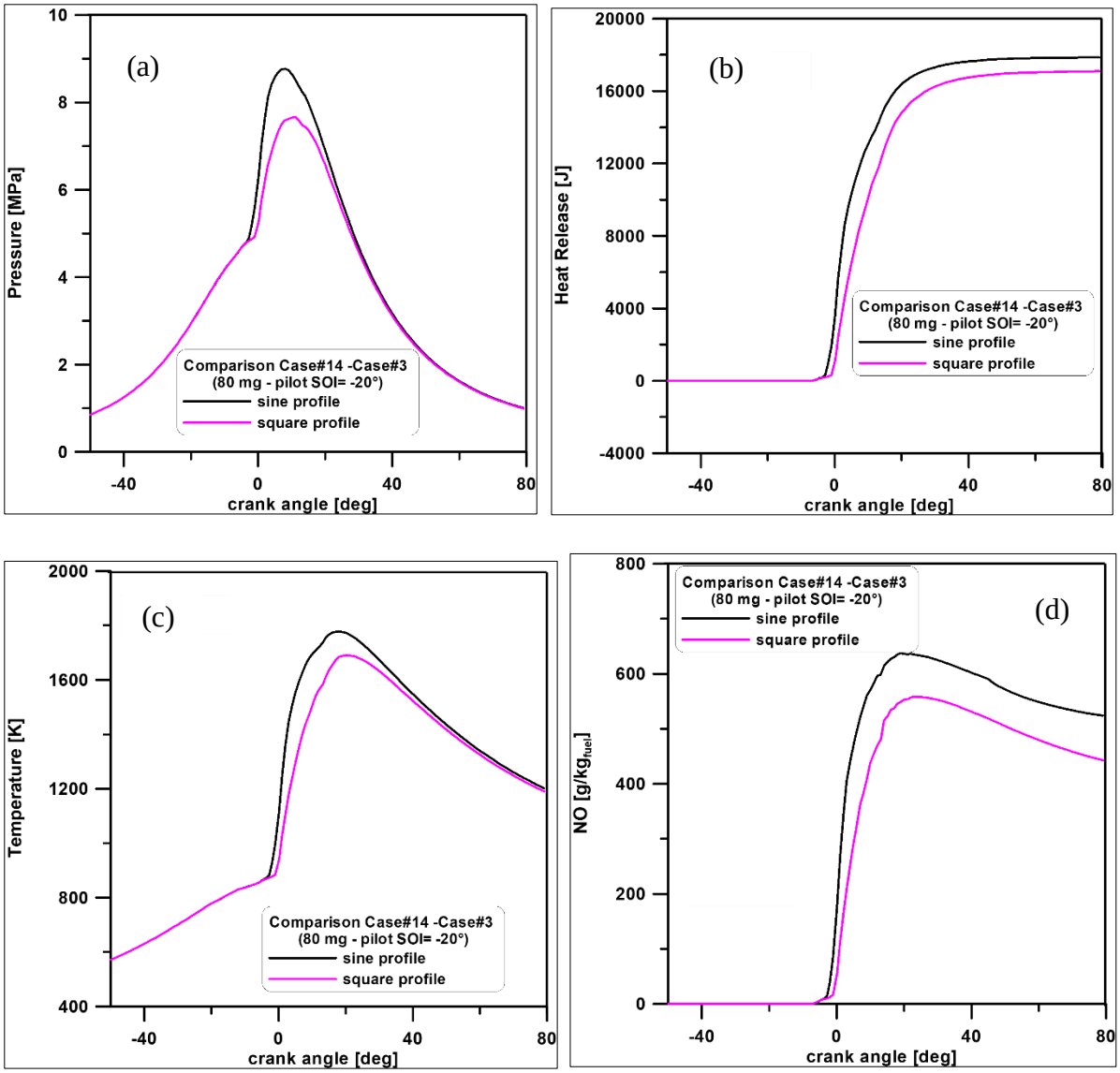

Figure 5.47: In-cylinder pressure (a), heat release (b), temperature (c) and NO trends (d) for Case#3 and Case#14.

The sinusoidal injection profile promotes a more gradual and continuous fuel delivery, as previously discussed and illustrated in Figure 5.48. In particular, at 9.5° BTDC, the liquid diesel jet is almost completely absent in the equivalent case using a square injection profile, whereas it remains visible with the sinusoidal profile. This sustained injection leads to a different vapor distribution, allowing the diesel vapor to penetrate more effectively into the surrounding air–ammonia mixture during the compression stroke.

	Case#14 (Sine profile)	Case#3 (Square profile)
11.5° BTDC	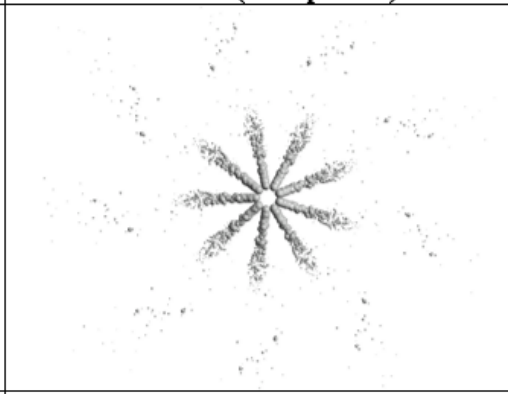	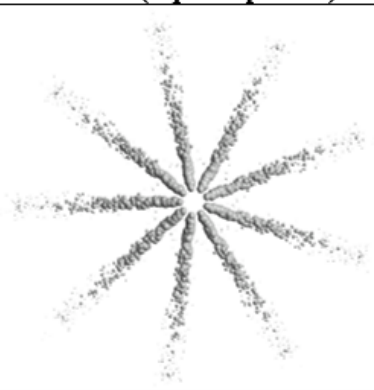
10.5° BTDC	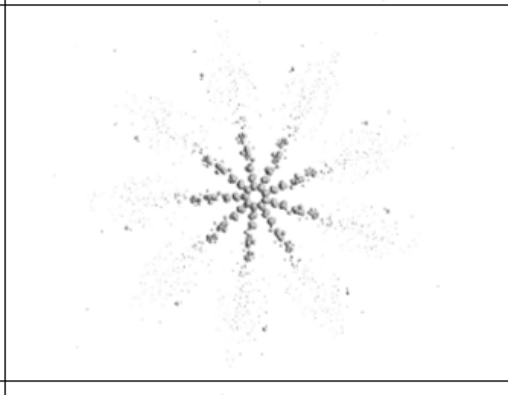	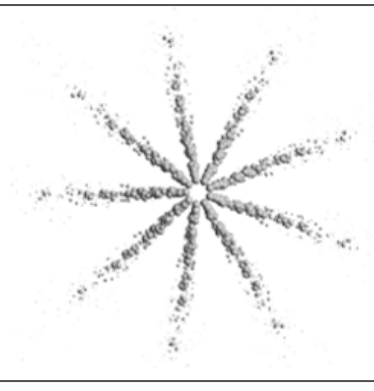
9.5° BTDC	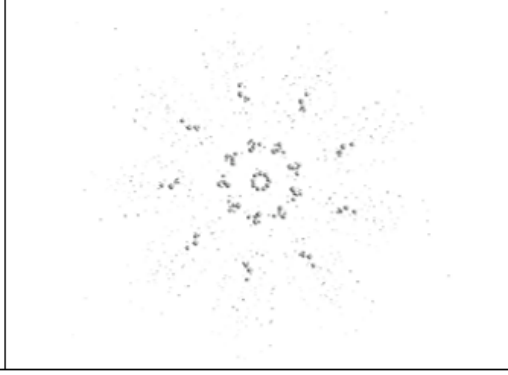	

Figure 5.48: Spray distribution. Comparison between Case#14 and Case#3

This behavior is further supported by Figure 5.49, which shows the evolution of OH concentration—a crucial indicator of flame front development and chemical reactivity. The higher OH levels observed with the sinusoidal injection confirm a more homogeneous and active combustion process. In contrast, for Case #3 with the square injection profile, combustion appears less uniform starting from TDC, as also evidenced by the temperature distributions reported in Figure 5.50.

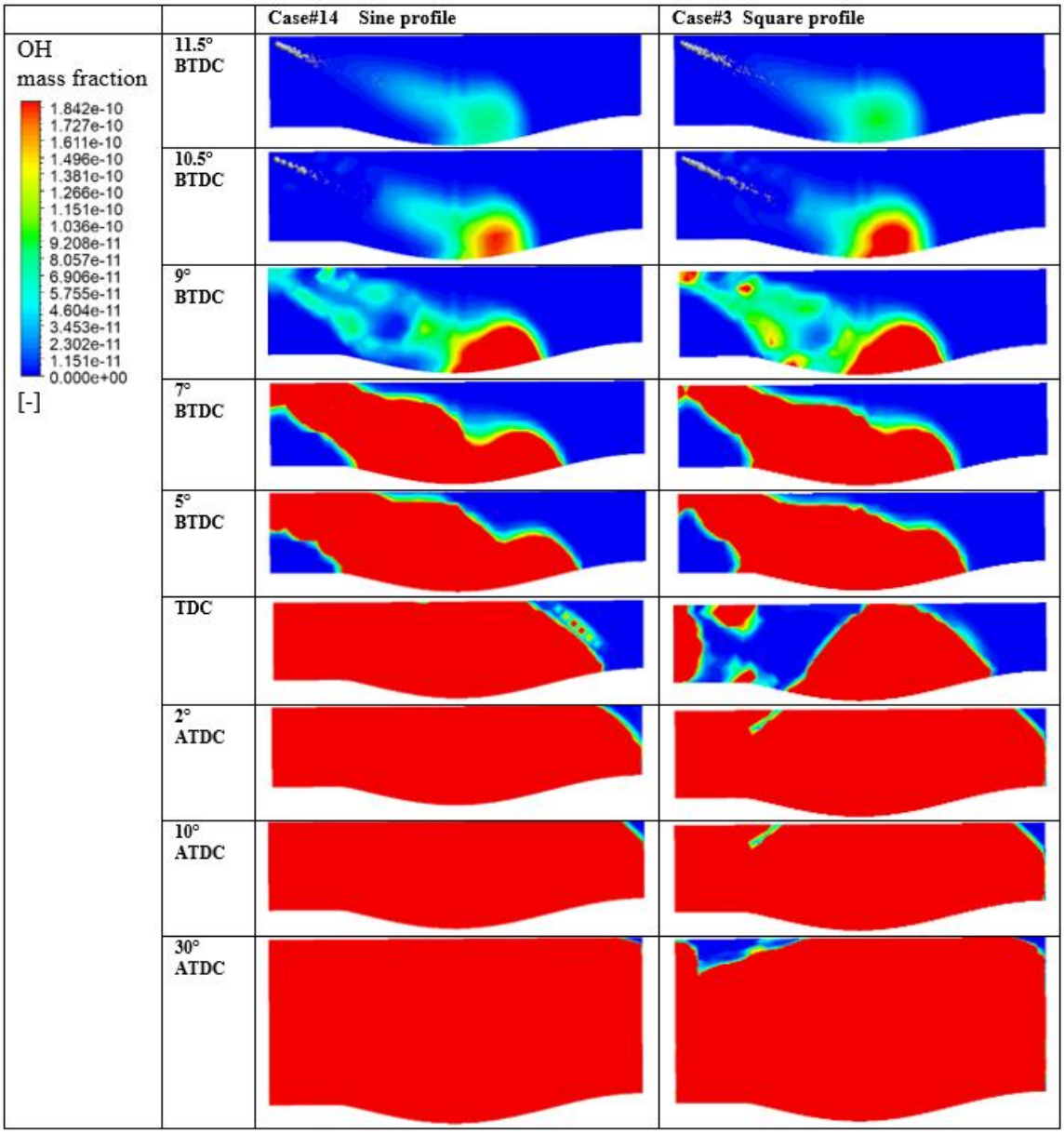

Figure 5.49: OH mass fractions distribution. Comparison between Case#14 and Case#3

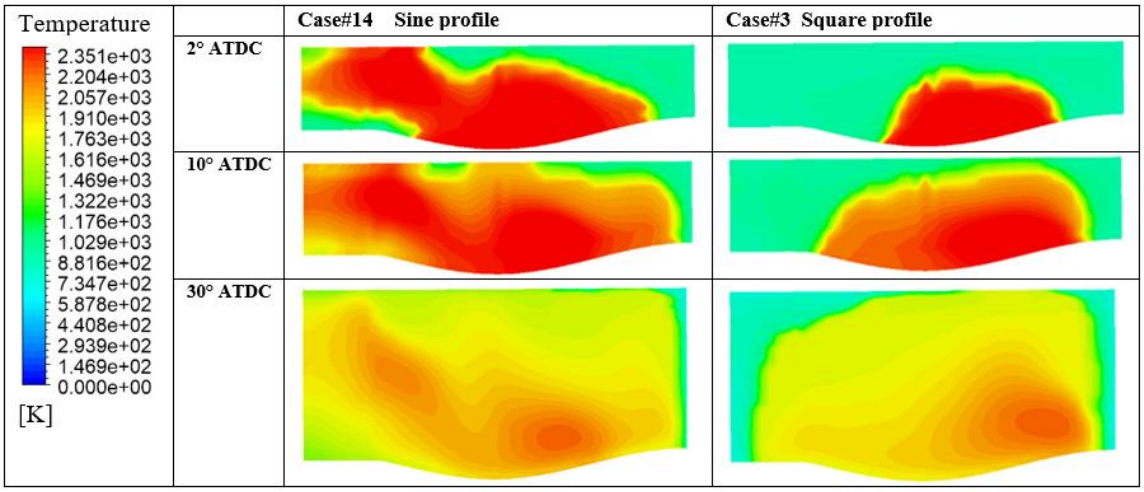

Figure 5.50: Temperature distribution. Comparison between Case#14 and Case#3

Finally, Table 5.12 provides a summary of performance and emission results for all simulated cases. Most configurations fall short of achieving the desired IMEP, particularly when operating with reduced diesel quantities or suboptimal injection timings. As expected, CO_2 emissions show a slight increasing trend with IMEP, since diesel is the sole carbonaceous contributor in the fuel blend. In contrast, ammonia slip decreases with increasing diesel mass, reflecting enhanced flame propagation and more complete oxidation of the premixed charge. Among the cases with IMEP values close to the target, the comparison between Case #3 and Case #14 is particularly insightful. Both share the same SOI and diesel quantity; however, the smoother fuel delivery offered by the sinusoidal injection profile in Case #14 yields superior performance. It reaches the nominal IMEP, ensures more complete ammonia combustion, and maintains CO_2 emissions per unit of energy at levels comparable to lower-diesel cases—demonstrating improved thermal and combustion efficiencies without additional carbon penalties.

Table 5.12: IMEP values for the different test cases.

Case	Pilot timing [deg BTDC]	Pilot Diesel injected [mg]	Main Diesel injected [mg]	Injection rate shape	IMEP [bar]
Baseline	-	-	50	*square*	4.66
Case#1	-	-	100	*square*	6.5
Case#2	20°	50	50	*square*	10.7
Case#3	20°	40	40	*square*	9.0
Case#4	20°	40	25	*square*	6.46
Case#5	20°	25	40	*square*	7.15
Case#6	20°	30	40	*square*	7.8
Case#7	25°	25	40	*square*	7.2
Case#8	25°	30	40	*square*	7.02
Case#9	20°	25	40	*sine*	7.31
Case#10	25°	25	40	*sine*	7.8
Case#11	27°	25	40	*sine*	7.26
Case#12	18°	25	40	*sine*	6.5
Case#13	25°	30	40	*sine*	8.72
Case#14	20°	40	40	*sine*	9.53
NG	-	-	50	*square*	10

	η_{comb}	Ammonia @ EVO [ppm]	CO_2 @ EVO [ppm]	CO_2 @ EVO [g/kWh]	EINOx @ EVO [ppm]
Baseline	0.50	38.4e3	12.4e3	126	1.23e3
Case#1	0.62	32.3e3	24.1e3	183	0.844e3
Case#2	0.96	3.45e3	24.3e3	115	3.54e3
Case#3	0.85	11.64e3	18.9e3	106	2.3e3
Case#4	0.77	24.3e3	13.6e3	95	1.45e3
Case#5	0.86	23.2e3	16e3	122	1.82e3
Case#6	0.66	19.2e3	17e3	109	2.07e3
Case#7	0.707	21e3	15.2e3	105	1.82e3
Case#8	0.708	21.8e3	15e3	106	1.77e3
Case#9	0.72	22.3e3	16e3	109	1.9e3
Case#10	0.76	18.8e3	15.9e3	101	2.11e3
Case#11	0.72	21.8e3	15.6e3	107	1.86e3
Case#12	0.65	27.8e3	16e3	121	1.58e3
Case#13	0.84	12.5e3	17e3	98	2.34e3
Case#14	0.89	8.9e3	19.5e3	103	2.82e3
NG	0.99	-	78.9e3	410	1.78e3

Figure 5.51 displays the $EINO_x$ trends for all test cases. The lowest NO_x levels are recorded in Cases #1, #4, and #12, where incomplete combustion leads to lower in-cylinder temperatures and poor performance (IMEP ≈ 7 bar), along with significant ammonia slip.

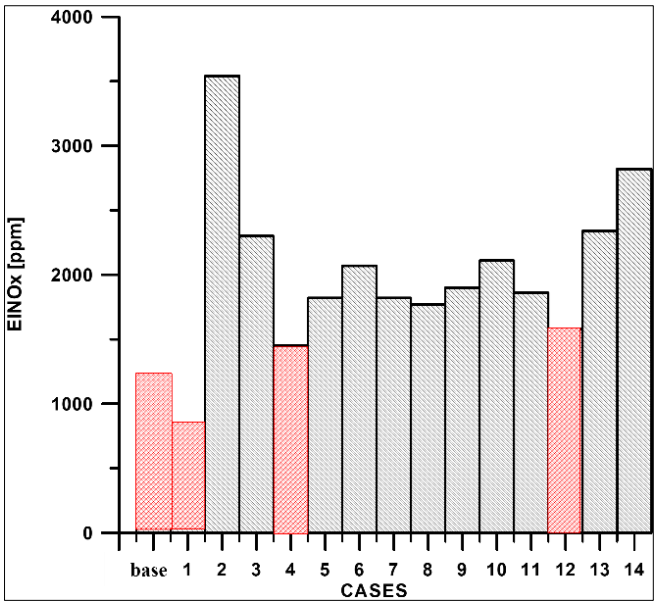

Figure 5.51: $EINO_x$ for all test cases

Although these configurations minimize NO_x emissions, they are not viable due to their inefficiency and inability to meet performance targets.

In contrast, Case #14 proves to be one of the most promising configurations among all those studied. When compared to the reference NG case, previously studied, it achieves a CO_2 concentration (in ppm) approximately four times lower, with a comparable IMEP. Although an increase in NO_x emissions is observed, this is partly attributable to the use of ammonia, whose oxidation contributes not only to thermal NO formation but also to fuel-NO pathways. Nonetheless, it must be emphasized that all NO_x values in the thesis are reported at the EVO, and aftertreatment systems, commonly employed in marine applications, can further mitigate these emissions.

Finally, for reference and benchmarking, the last row of Table 5.12 includes the results obtained from the natural gas-fuelled configuration, serving as the baseline case for performance and emissions comparison.

Chapter 6

6. SPARK IGNITION ENGINES

In this chapter, the traditional SI and the SI PC combustion modes are investigated focusing on the application for marine propulsion. The analysis considers different alternative fuels, especially ethanol and methanol, to explore their potential in decarbonizing the maritime sector while maintaining high thermal efficiency and combustion stability. The study is structured in two main parts, each addressing a specific engine configuration and fuel set.

In the first part, the attention is devoted to a modified FPT Cursor 9 SI engine, operated with 100% ethanol. This section presents the experimental setup and test campaign, which provide the basis for numerical investigation. 3D CFD simulations are performed using a full geometry (ducts included) to reproduce the in-cylinder flow, mixture formation, and combustion processes. The ethanol-related results presented in this chapter are based on the work [188] and are framed within the context of the project PRIN2022 "Bio-FIRed IC Engines for off-grid Electric Vehicles ChaRging Stations".

In the second part of the chapter, the focus shifts to a Rolls-Royce C26:33 marine engine equipped with a PC and supplied with methanol. In particular, the characteristics of an active and a passive PC combustion mode through 3D CFD simulations are investigated, building on previous experience reported in [189].

6.1 The FPT Cursor 9 engine

The first spark ignition engine studied is a SI version of the 6-cylinder FPT Cursor 9, originally developed for natural gas operation [187]. Due to its size, it is suitable for marine applications in small vessels [22]. To enable its operation with 100% ethanol, several modifications were carried out. A schematic of the engine test bench is shown in Figure 6.1 reported in [187], while the main technical specifications are summarized in Table 6.1.

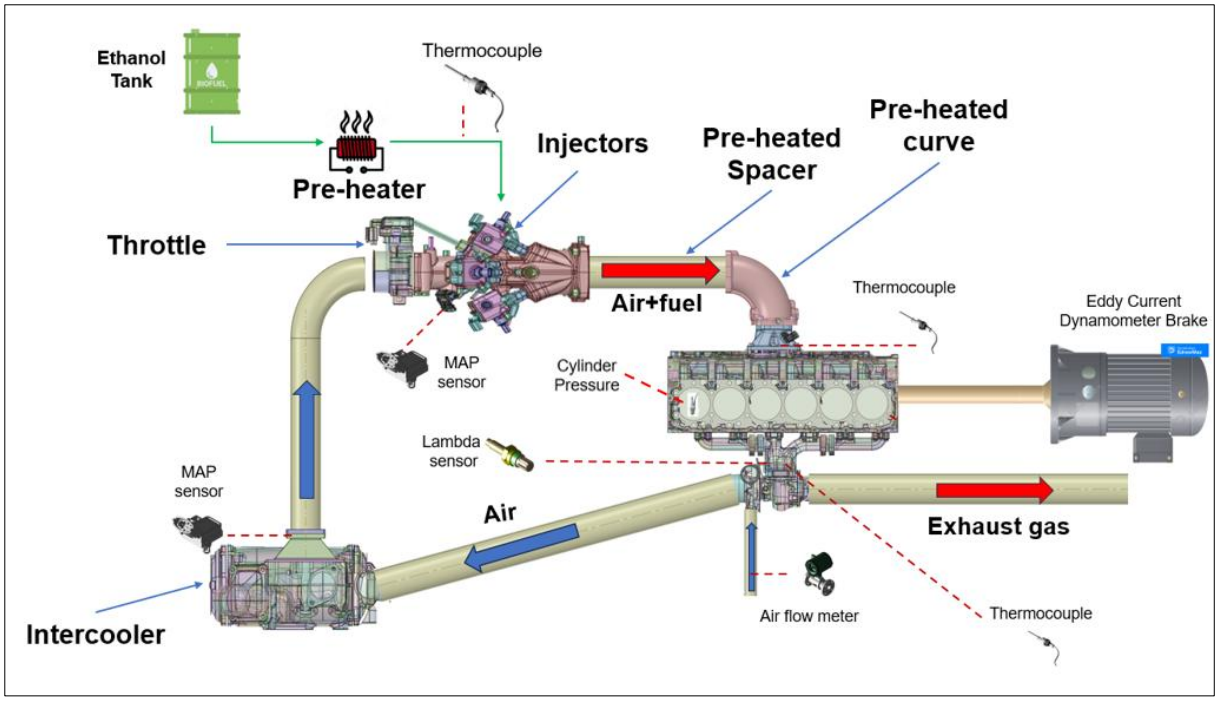

Figure 6.1: Schematic layout of the engine test bench [187]

Table 6.1: Engine characteristics

4-stroke, 6 cylinders, 4 valves per cylinder	
Stroke [mm]	135
Bore [mm]	117
Connecting rod [mm]	216
Displacement volume [cm^3]	~8700
CR [-]	12:1
IVO	343° ATDC
IVC	149° BTDC
EVO	132°ATDC
EVC	351° BTDC

12 injectors, grouped in sets of three along the circumference of the intake duct, are positioned upstream of the intake manifold, with the primary aim of promoting thorough fuel-air mixing. The experimental setup, as well as the modifications made, is described in the paper [187] where the authors report the experimental values obtained on 4 cylinders in terms of lambda and pressure in the cylinder. The global AFR is evaluated via a lambda sensor located in the exhaust duct upstream of the turbine. The experimental tests provided the initial conditions and validation data for the numerical simulations presented in the following section. The key engine

operating parameters for test conditions are summarized in Table 6.2 for a load of 161 kW. The resulting power output and thermal efficiency are significantly lower than the target value. This is attributed to the insufficient air flow rate, which yields a low lambda value and consequently prevents the full utilization of the injected fuel amount. These findings are evident from the data presented in Table 6.3.

Table 6.2: Experimental operating conditions

Engine speed [rpm]	1500
Air flow rate [kg/h]	681.8
Fuel flow rate [kg/h]	91
Spark timing [°BTDC]	5
Boost pressure [bar]	1.9
Fuel temperature [°C]	75.2
Ambient temperature [°C]	22.1
Coolant temperature [°C]	86.8

Table 6.3: Measured parameters

Brake power [kW]	161.1
Brake torque [Nm]	1025.9
BMEP [bar]	14.8
BTE [%]	25.2
Air index λ	0.89
Peak pressure, p_{max} [bar]	82.5
CA @ p_{max}, θp_{max} [°ATDC]	25.0
Pressure at IVC [bar]	1.86

Finally, it should be emphasized that considerable discrepancies in the λ values of the different cylinders were experimentally observed [187].

6.1.1 3D CFD – Closed Valves Geometry: Background

The numerical activity of the ethanol-fueled engine was initiated by adopting a closed-valve computational domain, as reported in [187]. This approach is commonly employed in preliminary CFD studies to isolate the combustion phase and facilitate the selection and validation of an appropriate chemical kinetic mechanism capable of accurately reproducing the

combustion behavior of ethanol. The in-cylinder pressure was directly retrieved from experimental measurements, while the initial temperature was calculated to match the measured trapped mass, based on the air mass flow rate reported in Table 6.2.

The computational results were obtained by using the commercial 3D CFD code ANSYS Forte®, and the simulation setup was aligned with the experimental test cases described in Table 6.2 and Table 6.3. The domain geometry was derived from the drawings provided by the engine manufacturer and corresponds to a 30° sector of the combustion chamber, comprising the piston bowl, cylinder head, and liner. The representation of the computational domain is shown in Figure 6.2. After a mesh sensitivity analysis, a 30° sector grid consisting of approximately 170,000 cells at IVC and 50,000 cells at TDC was chosen.

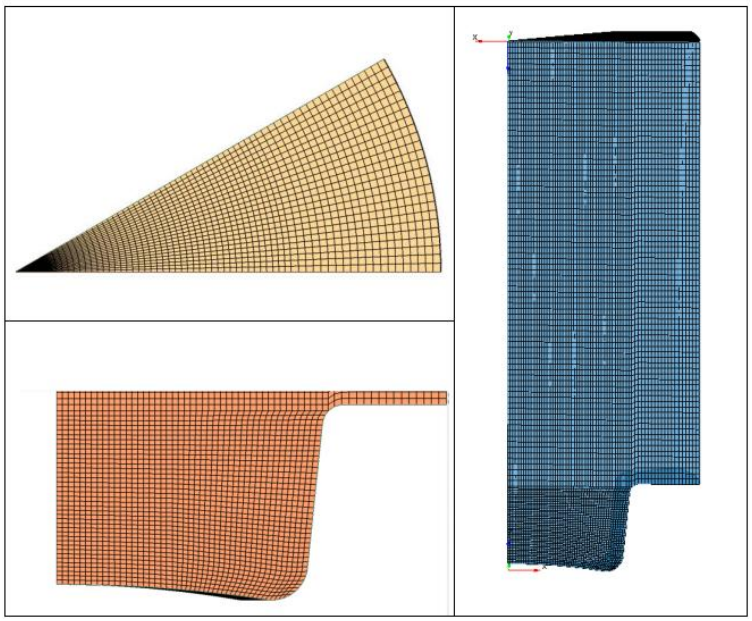

Figure 6.2: Representation of the mesh used for the calculations [187]

The preliminary simulations were instrumental in selecting the ethanol kinetic mechanism. Five chemical kinetic mechanisms for ethanol oxidation were evaluated. From this analysis, it was observed by the authors [187] that two of the evaluated mechanisms (WVU [190], composed by 39 species and 590 reactions and NUIG [191], composed by 928 species and 5965 reactions) yield similar results, despite considerable variation in their computational costs.

Based on the computational costs and the outcomes of this preliminary analysis, the WVU mechanism appears suitable for faster simulations. Meanwhile, the NUIG mechanism, which includes a sub-mechanism for C_2H_5OH validated at high pressures [192], offers the best compromise between accuracy and computational cost [193]. Additionally, this mechanism accounts for NO and NO_2 formation reactions.

6.1.2 3D CFD – Full Geometry

A closed-valve geometry, whose methodology was detailed in the previous section and used in [187], simplifies the computational domain and reduces overall simulation cost. However, this approach introduces approximations that may compromise the accurate representation of physical phenomena, especially during the early stages of the compression stroke. In contrast, using an open-valve geometry provides a more realistic description of the in-cylinder flow development. This configuration captures the actual effects of valve operation, including the evolution of turbulent structures and the non-uniform mixture distribution, which are crucial for the subsequent combustion process. For this reason, a detailed open-valve geometry replicating the FPT Cursor 9 engine was created via CAD and adopted for the CFD simulations involving ethanol fueling.

The computational domain reconstructs the geometry of the Cursor 9 engine (Table 6.1), including the in-cylinder volume, valves, intake and exhaust ducts, as shown in Figure 6.3.

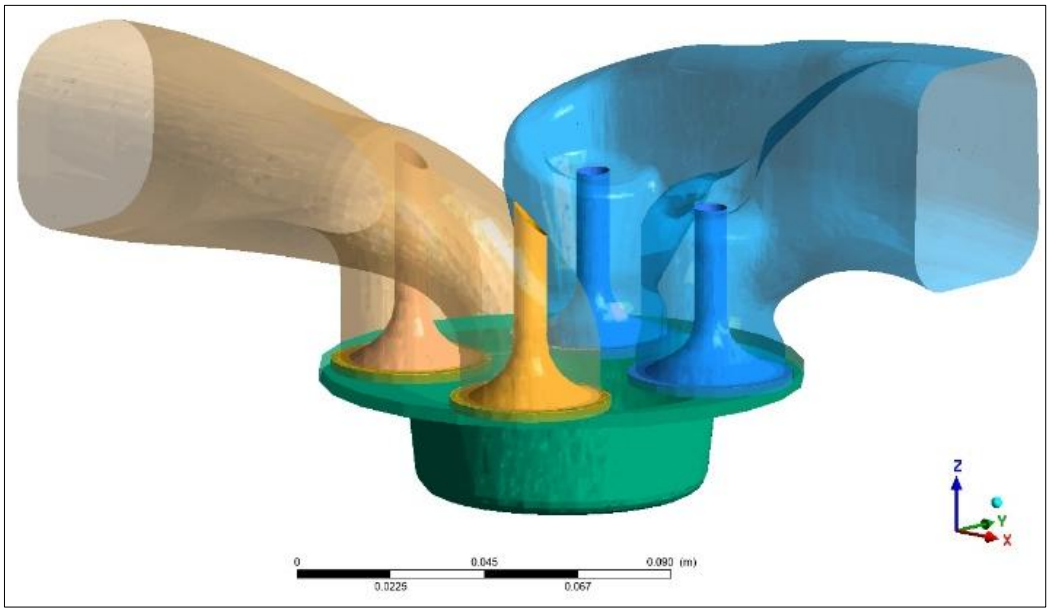

Figure 6.3: Open valve computational domain

In particular, the intake and exhaust valve lift profiles are reported in Figure 6.4, respectively, following the timing displayed in Table 6.1; hence, the simulations include the gas exchange phases.

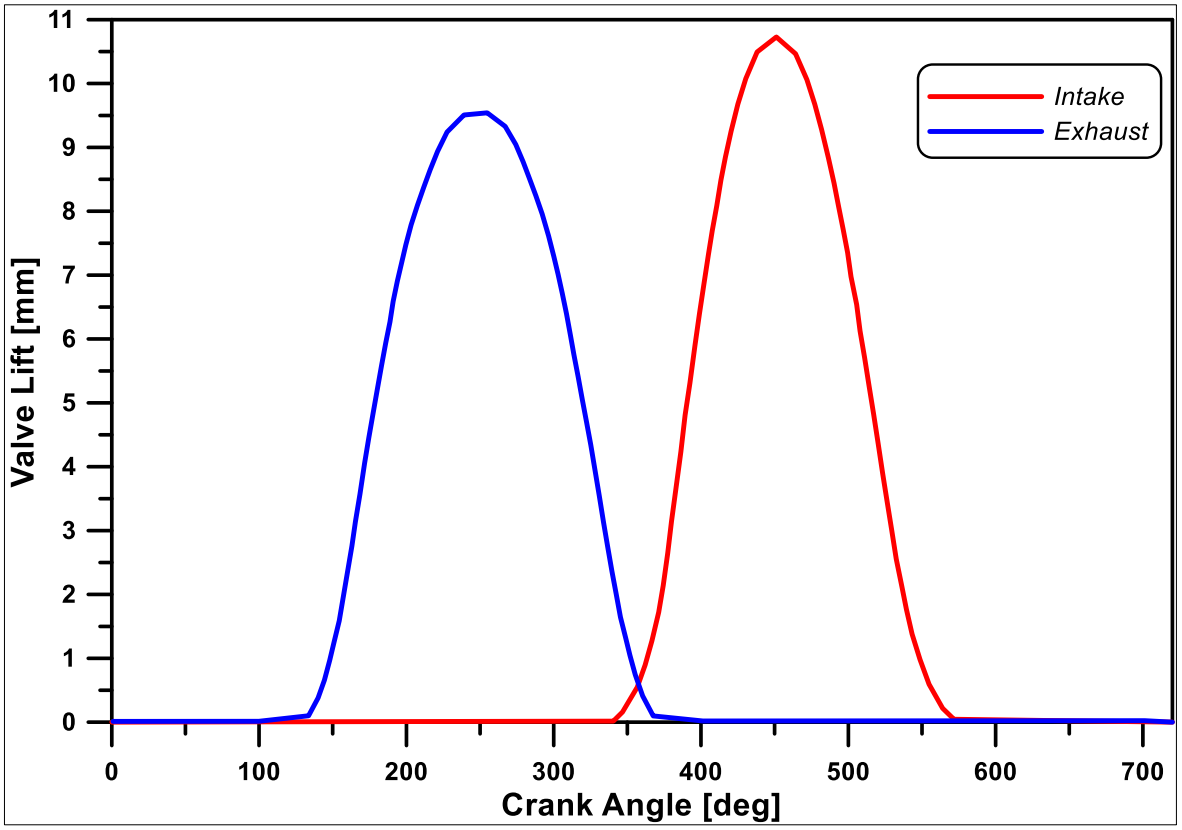

Figure 6.4: Valve lift profiles

However, Table 6.3 reveals that the ethanol-fueled engine exhibits poor performance in terms of both BTE and mechanical output. This is primarily attributed to the oxygen deficiency in the mixture and to the non-uniform fuel-air distribution among the cylinders. This justifies a thorough analysis of the in-cylinder processes, aiming to evaluate combustion efficiency and CO formation under such challenging conditions. To this end, an accurate prediction of flow behavior during both closed and open valve periods is necessary.

6.1.2.1 Mesh Sensitivity Analysis

The created geometry is imported into ANSYS Forte®, and the automatic mesh generation is configured using various global mesh sizes, as reported in Table 6.4. Starting from the recommended baseline of 2 mm, progressively finer grids are tested. For each mesh configuration, Table 6.4 lists the number of cells at TDC and the maximum number of cells reached during the simulations. This is essential to ensure sufficient discretization during the combustion phase, centered around TDC, while keeping the total number of cells manageable during the rest of the engine cycle, thereby maintaining reasonable computational times.

Table 6.4: Mesh characteristics

Mesh	Average cell size	Number of cells at TDC	Maximum number of cells
1	2 mm	82 285	267 754
2	1.6 mm	158 143	517 849
3	1.3 mm	298 972	963 285
4	1 mm	653 688	2 088 595
5	0.7 mm	1 910 902	6 099 722

Figure 6.5 presents the key combustion parameters across the tested grids. Meshes #1 and #2 produce generally unsatisfactory results, while mesh independence is clearly achieved with a cell size of 1 mm. Nonetheless, mesh sensitivity analyses are crucial to balance result accuracy with computational efficiency. As shown in Figure 6.5d, adopting mesh #4 (1 mm) results in a computational time of approximately two days to complete a single engine cycle (720 CAD).

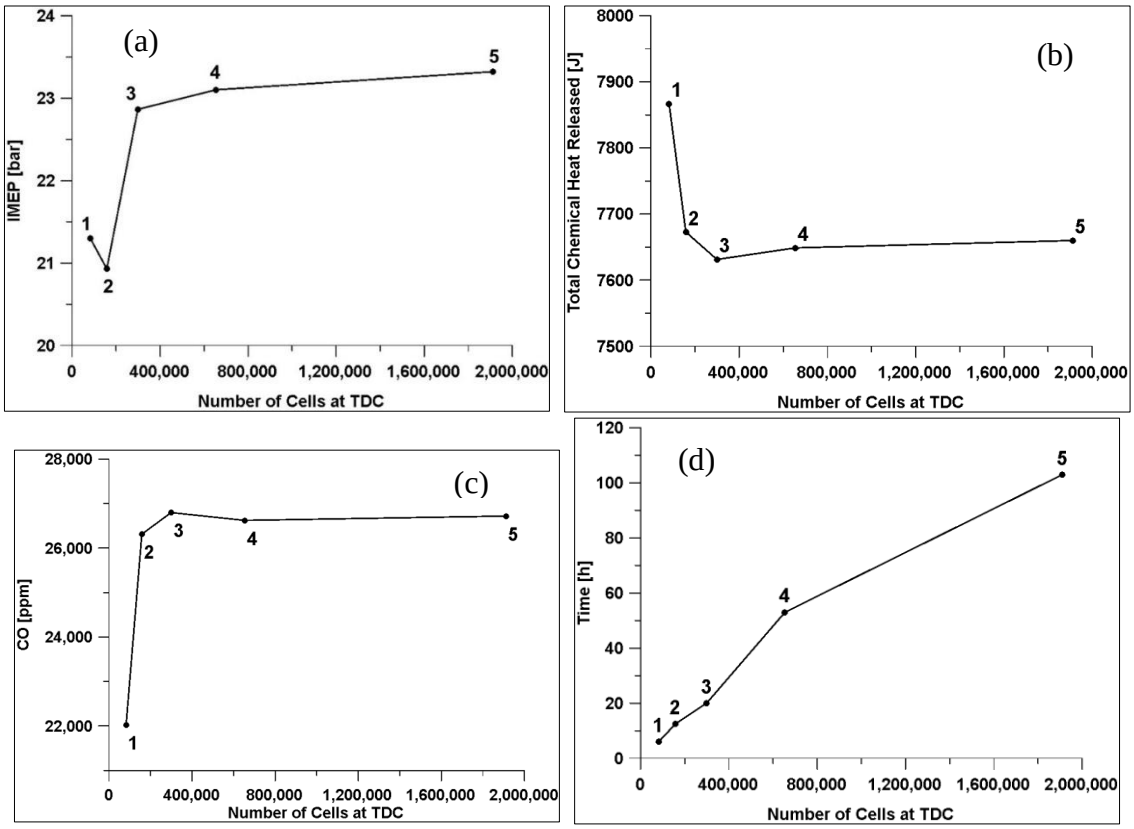

Figure 6.5: IMEP (a), total chemical heat release (b), CO emissions at EVO (c) and time of simulation of one cycle (720) (d) vs number of cells

Therefore, given that the deviations observed with mesh #3 are minimal and this configuration still ensures accurate cylinder filling (as demonstrated in Figure 6.6), mesh #3 is selected for

subsequent simulations. This choice effectively halves the computational time compared to mesh #4, while maintaining acceptable accuracy.

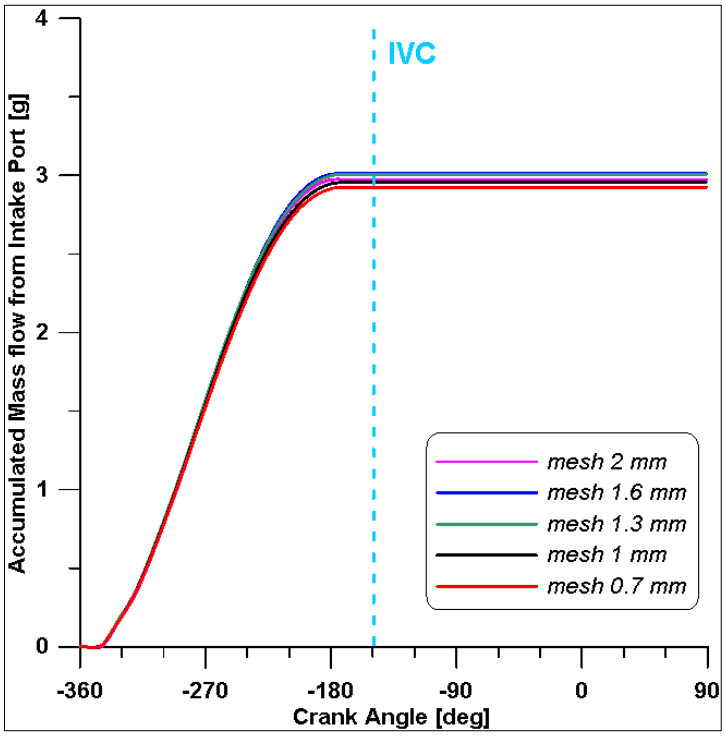

Figure 6.6: Trapped mass vs number of cells

The final adopted mesh is shown in Figure 6.7.

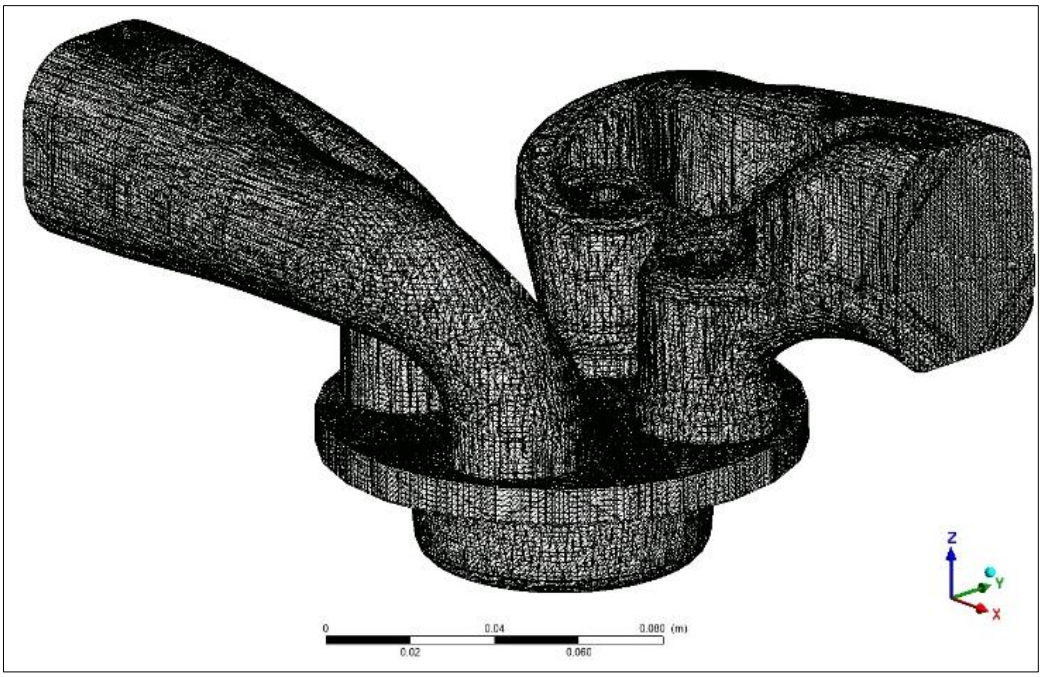

Figure 6.7: Computational mesh (#3 – 1.3 mm)

It should be noted that the mesh sensitivity analysis is performed under the assumption of a perfectly premixed fuel in the intake duct. Simulations involving liquid fuel injection are

expected to require longer runtimes due to the inclusion of additional processes such as injection, atomization, evaporation, and wall impingement. Moreover, in order to achieve convergence and cyclic stability, multiple consecutive engine cycles (at least five) must be simulated. For this reason, computational time was a critical factor in the selection of the final mesh size.

6.1.2.2 Analysis of In-Cylinder Flow Dynamics and Turbulence

As a preliminary remark, it is necessary to specify that, in the results presented in this paragraph (and in the following one), ethanol is assumed to be fully evaporated for open and closed valves geometries. The analysis of the in-cylinder flow field, reveals a purposeful design aimed at inducing specific aerodynamic structures. As shown in Figure 6.8, the velocity streamlines are directed to enter the combustion chamber perpendicularly with respect to the inlet area, before being forced to rotate around the valve stems. This is a direct consequence of the intake duct geometry, which is intentionally shaped to impart a swirling motion to the incoming flow.

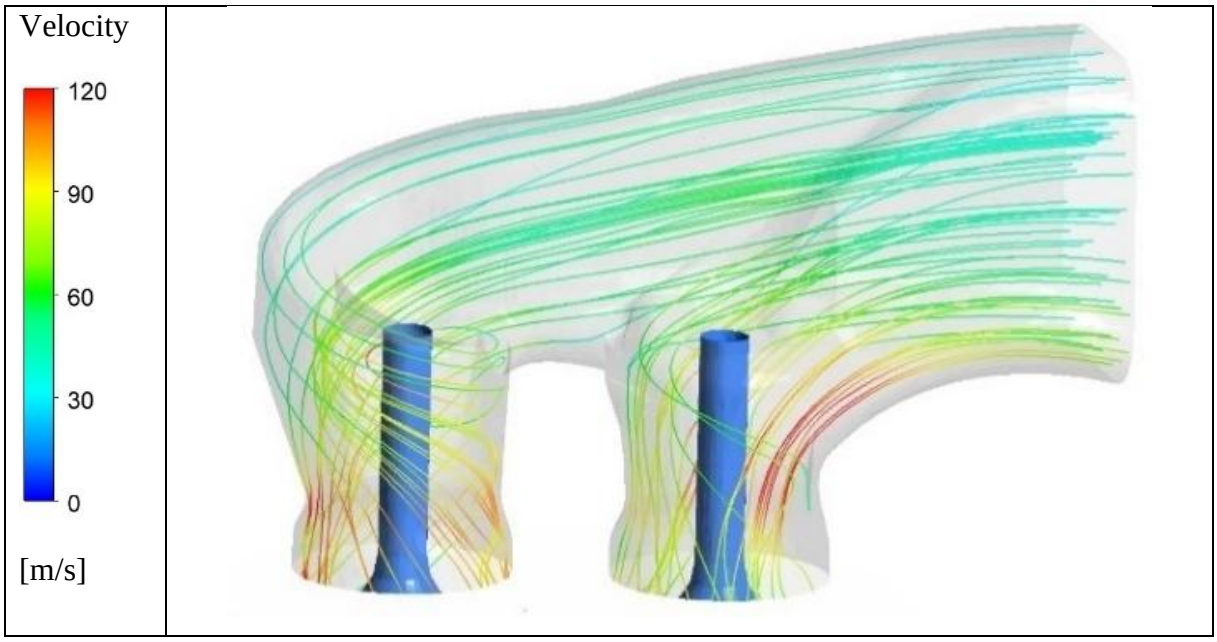

Figure 6.8: Velocity streamlines within the inlet duct

To further investigate the airflow patterns originating from the intake system, streamlines are visualized on several cut planes. These include planes intersecting both intake valves, as well as a plane crossing one intake and one exhaust valve—represented by the blue and red planes in Figure 6.9, respectively. Additionally, swirl motion is analyzed on a transverse plane orthogonal to the cylinder axis, highlighted in green in the same figure.

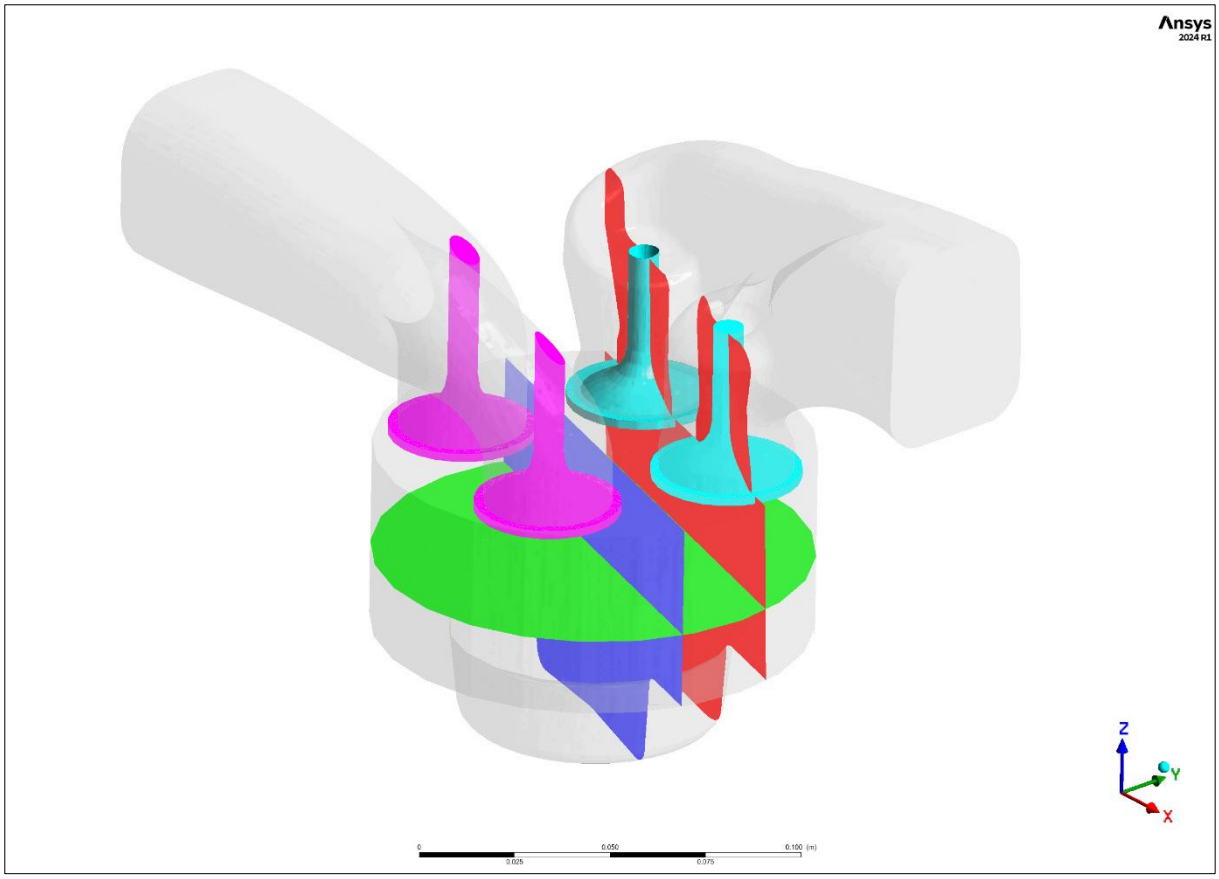

Figure 6.9: Cutplanes

Figure 6.10 illustrates the flow field during the intake stroke at 290° BTDC for the premixed case. At this point, the intake valves are fully open, and the mixture enters the cylinder, generating an intense tumble motion between the two valves. In the horizontal plane located 0.5 cm below the cylinder head, a prominent swirling vortex is clearly visible in the top-left quadrant of the image, resulting from the specific design of the intake duct. Notably, this vortex persists deeper into the combustion chamber, remaining detectable even at 5 cm from the head.

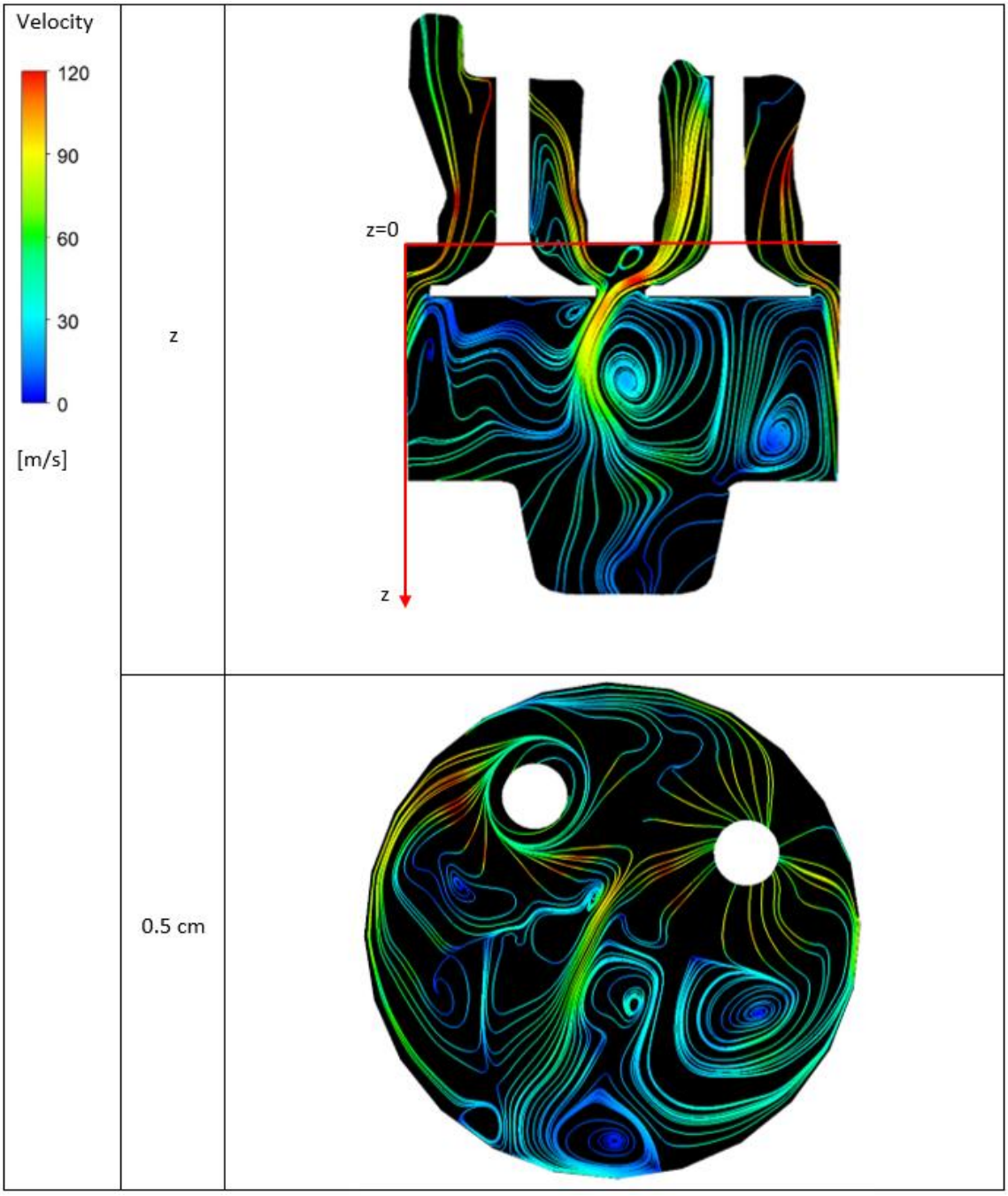
Velocity
120
90
60
30
0
[m/s]
z
z=0
z
0.5 cm

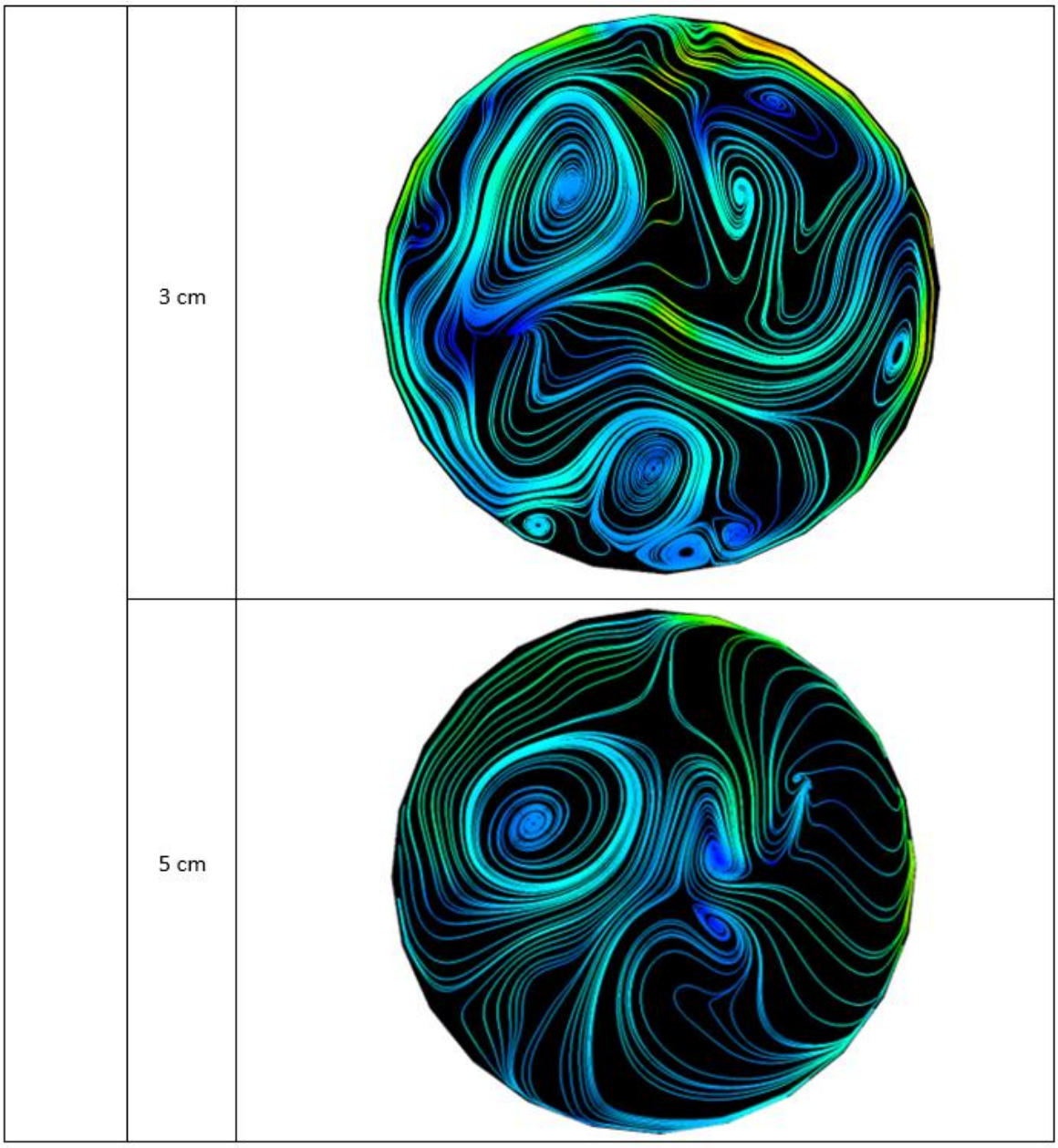

Figure 6.10: Velocity streamlines at 290°BTDC in a longitudinal cut plane crossing intake valve and at three transversal planes at different distances from the head.

Conversely, Figure 6.11 presents the flow streamlines at 5° BTDC, corresponding to the final compression phase. At this stage, the previously observed tumble motion has dissipated, while the swirling motion becomes dominant throughout the entire in-cylinder volume. However, the overall flow velocity is significantly lower than that observed during the intake phase.

For comparison, the flow field at the same crank angle is also shown for simulations conducted using the closed-valve geometry. As previously discussed, the presence of intake ports and valves in the open-valve configuration facilitates the swirl development, which is readily apparent in the horizontal cross-sections of the cylinder. Furthermore, the axial symmetry assumed in the closed-valve calculation is clearly not present in the full-geometry case. The

distinctions between the results from the two geometries will be addressed more thoroughly in the subsequent paragraph.

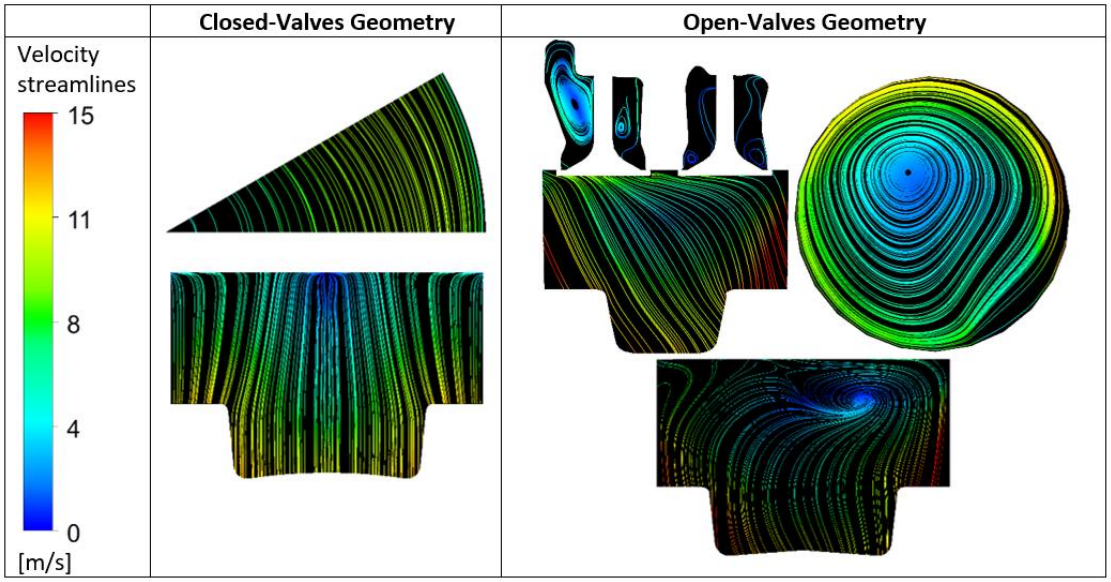

Figure 6.11: Velocity streamlines at 65°BTDC in the longitudinal cutplane crossing intake valves and in transversal plane (closed valves vs open valves)

Lastly, Figure 6.12 displays the distribution of TKE at two crank angles: 20° and 5° BTDC, the latter corresponding to the ST. A pronounced concentration of TKE is observed in the central region of the combustion chamber. However, as the piston nears TDC, this energy begins to decay, indicating a reduction in turbulence intensity just before ignition.

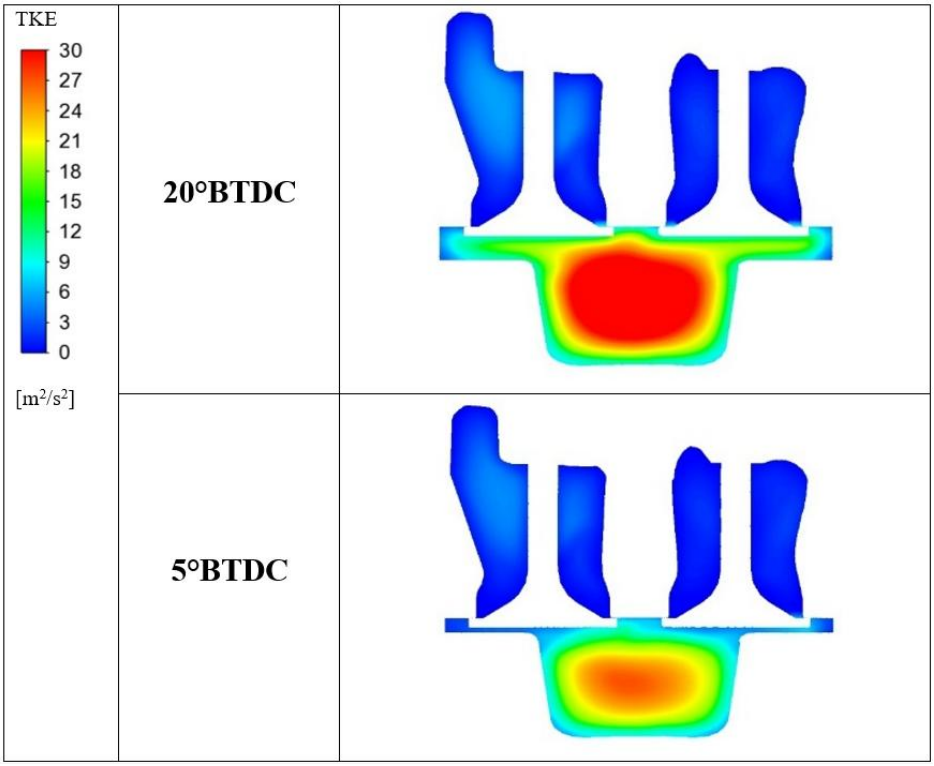

Figure 6.12: TKE in the cutplane crossing the intake valves at two different CADs

6.1.2.3 Comparison between Closed Valve Cylinder and Full Geometry (Ports Included)

As mentioned in Section 6.1.2 and observed in Figure 6.11, the importance of performing CFD calculation for an engine cylinder with ports and open valves compared with closed valves lies primarily in the ability to accurately simulate and understand the actual fluid dynamics during the gas exchange process (intake and exhaust).

The results of a CFD calculation in an engine cylinder could be different when performed with ports and open valves versus with closed valves because the two scenarios simulate fundamentally different physical processes and flow regimes. Within a closed-valve configuration, particularly following IVC, a comprehensive representation of the instantaneous flow field is generally not feasible, notwithstanding the prescription of initial conditions for turbulence kinetic energy and swirl ratio. In addition, in full geometry (ports included), the flow simulation accurately models the scavenging process and the amount of hot residual exhaust gas that remains in the cylinder, which is crucial for predicting ignition.

Specifically, in this engine, valve closing occurs at 132° BTDC, and thus the flow motion determined during the intake phase significantly influences combustion development. This effect is less significant in engines with an earlier IVC and at low engine speed, such as the DF engine described in the previous chapter, where the closed-valve calculation did not represent a significant limitation. In other words, the fine-scale accuracy of the predicted flow field during the intake stroke becomes less critical for determining the final combustion state, and a lower degree of precision in the flow-field prediction can be acceptable for such simulations.

The results obtained for the geometries are presented below, following calculations performed with identical models and utilizing the values at IVC derived from the full geometry calculation at fifth engine cycle as initial conditions for the closed-valve simulation. The physical models employed for the CFD simulations are summarized in Table 6.5, along with the NUIG chemical kinetic mechanism. For laminar flame propagation modeling, the laminar flame speed library available within the ANSYS Forte® package was utilized.

Table 6.5: CFD Models

Kinetic mechanism	NUIG
Turbulence model	RANS-RNG k-ε
Chemical kinetics solver	ANSYS Chemkin-Pro solver
Flame propagation model	G-equation
Wall heat transfer model	Han and Reitz

It is interesting to note that differences are observed in both the mean quantities and the distributions. A detailed examination reveals that the in-cylinder pressure and temperature exhibit discrepancies in the two scenarios, despite the identical operating conditions and models utilized (Figure 6.13). The only exception lies in the choice of the constant b_1 in the turbulent flame speed correlation (Eq. 3.56) which is higher in the closed-valve case to facilitate ignition.

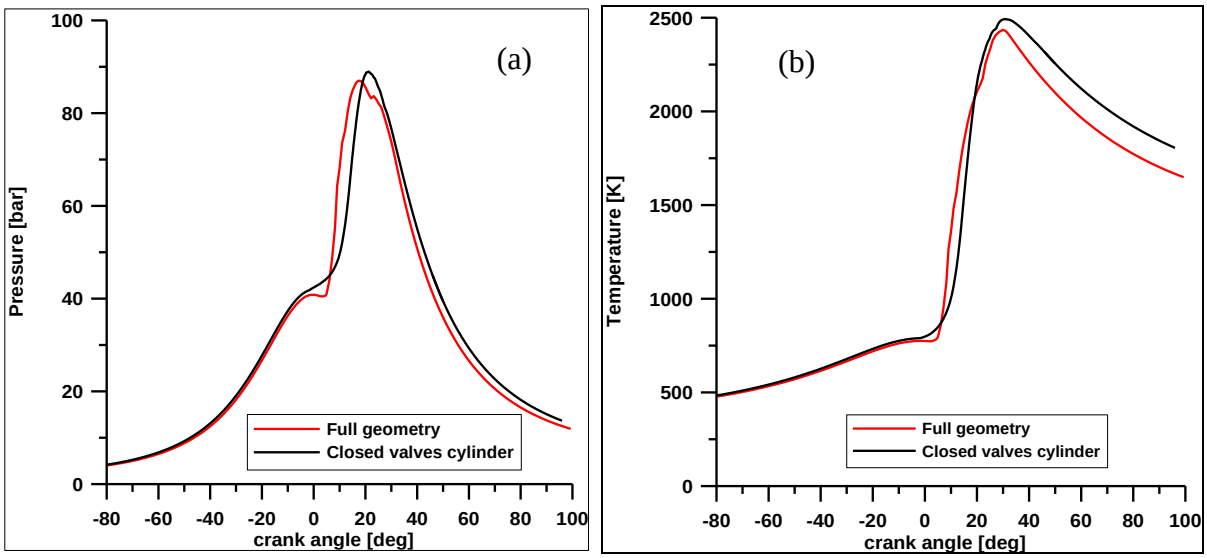

Figure 6.13: In-cylinder pressure (a) and temperature (b) for the closed valves and full geometry

This can be attributed to differences in the in-cylinder flow field and turbulent kinetic energy, both of which influence flame development and propagation. Figure 6.14 presents the TKE values for the two cases. Although starting from an identical value at IVC, the time-averaged TKE values are lower in the closed-valve case. Correspondingly, the ROHR is smoother and more sustained.

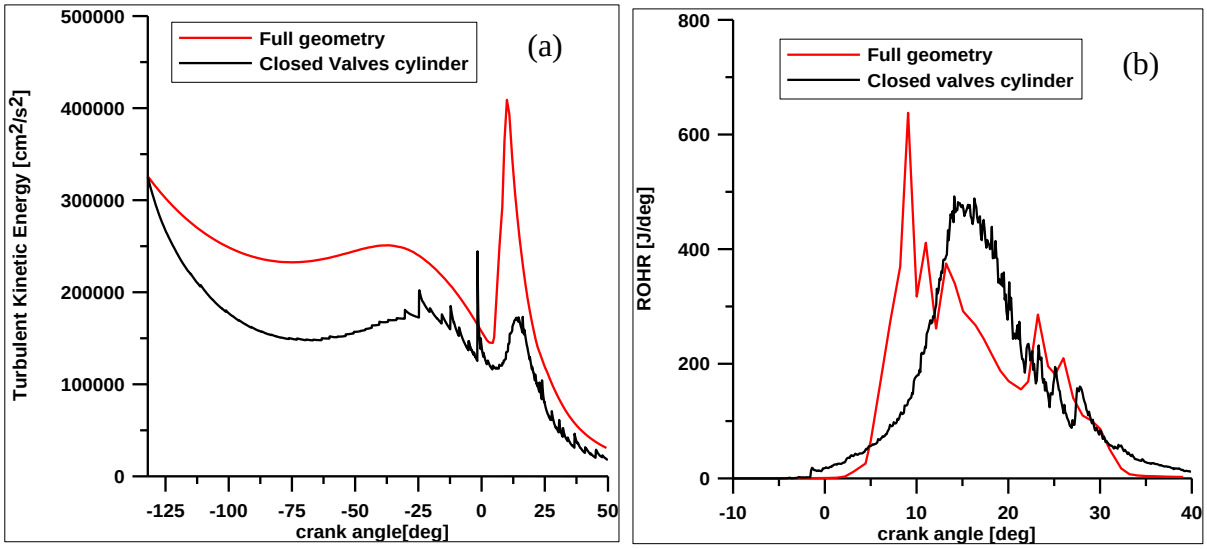

Figure 6.14: TKE (a) and ROHR (b) for the closed valves and full geometry

The comparative analysis between the Closed-Valves and Open-Valves geometries highlights significant differences in the in-cylinder flow field, turbulence evolution, and combustion development. In the case with closed valves, the distributions were obtained by multiplying the 30° angular sector by 12 (obtaining a 360° geometry) and considering a plane passing through the midsection. In the case with open valves, a plane passing through the spark plug was chosen. As shown in Figure 6.15, the velocity streamlines indicate that the closed-valves configuration promotes a symmetric and stable squish-driven flow centered along the bowl's axis of symmetry, while the open-valves case produces a more asymmetric velocity field with stronger gradients near the intake side due to residual valve flow. This altered flow structure leads to a more complex vortex pattern and a longer persistence of small-scale turbulence.

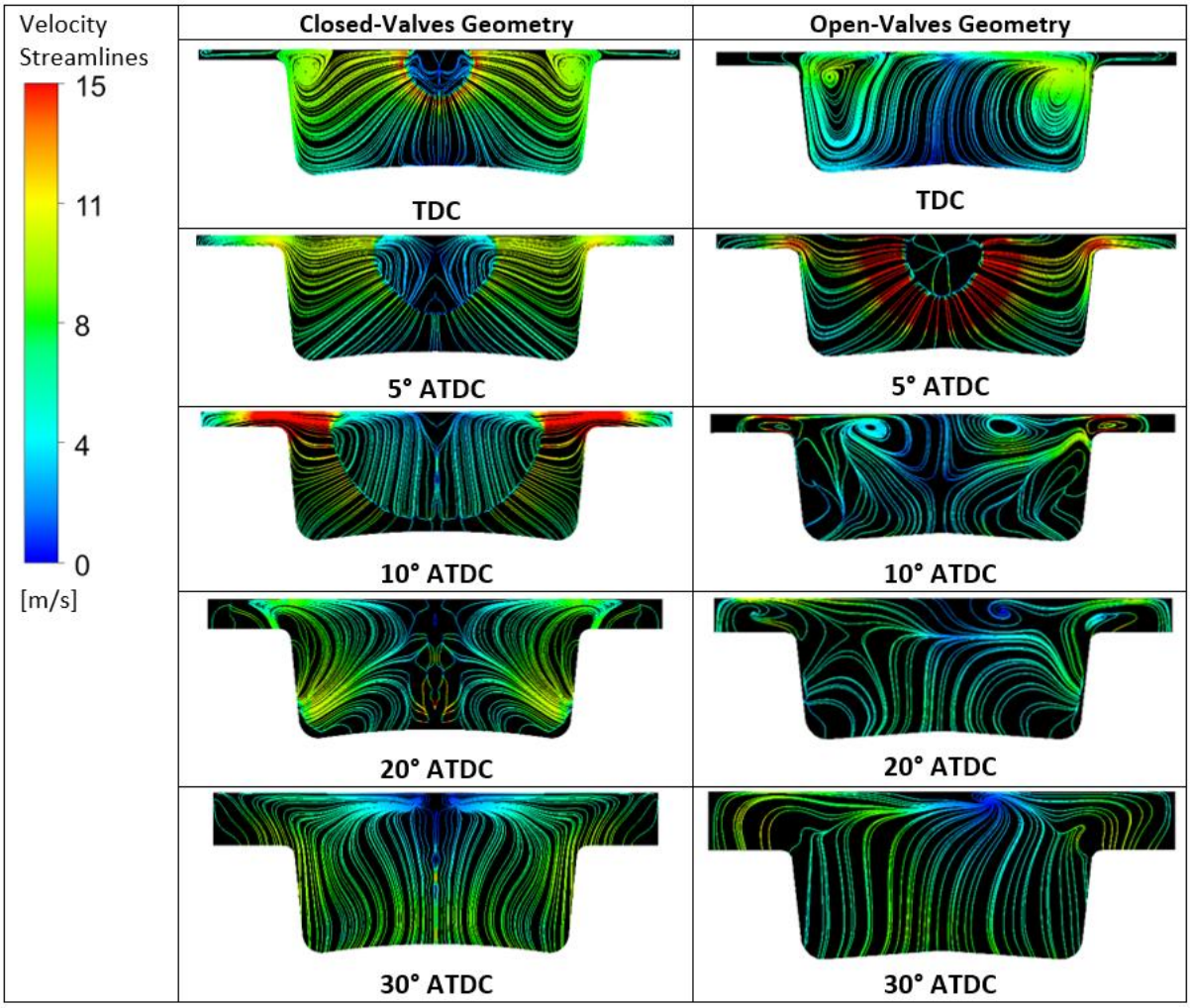

Figure 6.15: Velocity streamlines for closed and open-valves geometry

The TKE distribution, reported in Figure 6.16, confirms this behavior. High TKE levels are observed near TDC in the closed-valves configuration as a result of the compression-induced squish motion. Moreover, the highest TKE values are observed near the central axis of the

combustion chamber. In contrast, the open-valves geometry initially exhibits lower turbulence, which increases during the early expansion phase as the residual intake flow energizes the in-cylinder motion. Consequently, turbulence in the open-valves case persists longer but with greater asymmetry.

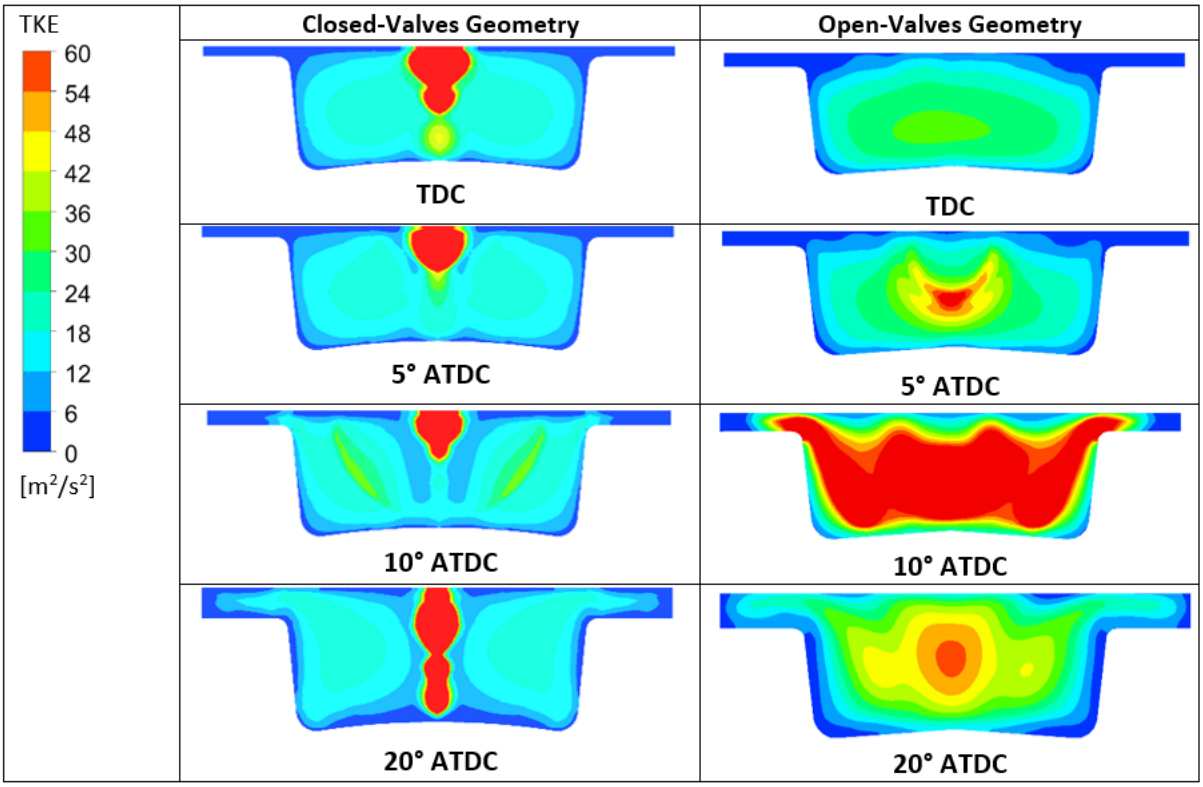

Figure 6.16: TKE for closed and open-valves geometry

The temperature fields shown in Figure 6.17 reveal that combustion initiates earlier and more symmetrically in the closed-valves geometry, forming a compact and centered high-temperature region. Conversely, in the open-valves configuration, ignition and flame growth are delayed but spread more rapidly and asymmetrically once initiated, driven by the enhanced local turbulence and flow motion.

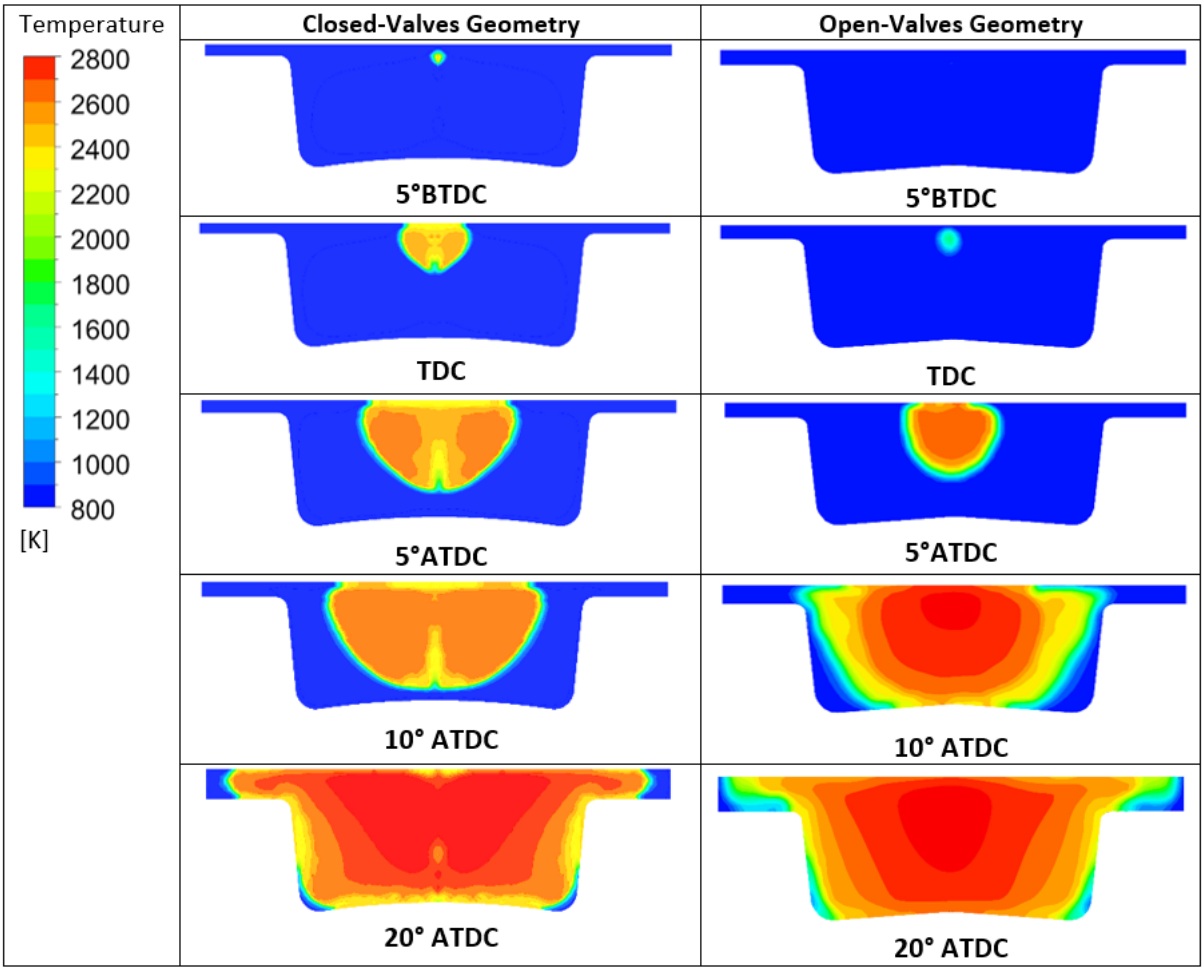

Figure 6.17: Temperature distributions for closed and open-valves geometry

Finally, the turbulent flame speed (TFS) evolution, illustrated in Figure 6.18, supports these findings. The closed-valves case maintains a uniform and symmetric flame front with moderate TFS values, while the open-valves geometry exhibits higher but more irregular TFS, characterized by an higher thickness. This behavior reflects stronger turbulence–flame interaction but also higher variability in flame propagation.

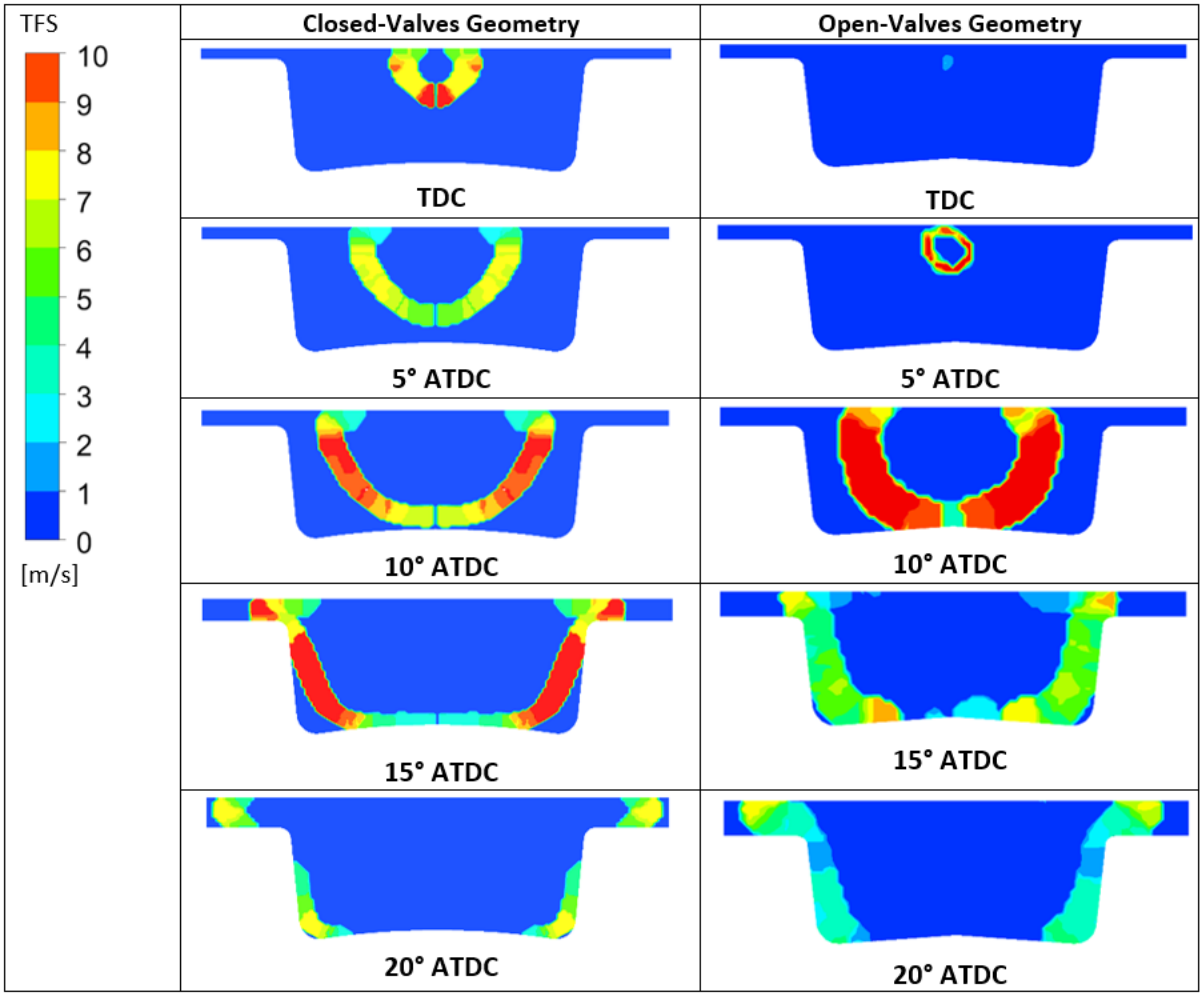

Figure 6.18: TFS distributions for closed and open-valves geometry

In synthesis, the closed-valves configuration favors a more controlled and symmetric combustion process dominated by squish-induced turbulence, whereas the open-valves configuration enhances turbulence intensity and accelerates flame propagation, though at the expense of increased flow asymmetry. Accurately predicting the evolution of the flow field is therefore essential, as it directly affects mixture formation, turbulence levels, and ultimately the combustion process.

6.1.2.4 Methodology and Numerical Test Cases

CFD calculations discussed in the following are conducted on the complete computational domain that includes the external intake and exhaust ducts. Additionally, to explore potential improvements in air and fuel supply strategies, the CFD methodology is integrated with a 1D system-level powertrain analysis.

The integration of 1D and 3D simulations is carried out with two main objectives:

- To reproduce operating conditions for which experimental data are not available, allowing the engine behavior to be predicted via the 1D model. With suitable modeling

of intake/exhaust flows, combustion, turbocharging, and control systems, the 1D tool can simulate various operating points. These simulations can then provide in-cylinder boundary conditions for detailed CFD calculations.

- Since the 1D approach lacks a predictive combustion model, the ROHR profile obtained from CFD is imposed within the 1D model to simulate engine performance under different conditions.

As for the 1D powertrain simulation, it is mainly used to estimate global engine performance under the same conditions considered in the CFD model. The iterative solution identifies the appropriate boost pressure level needed to ensure a desired air-fuel mixture quality. In this regard, turbocharger-engine matching and compressor operation within the surge-free region play a crucial role. As stated, in addition to providing boundary conditions to CFD, the system-level simulation can reach a satisfactory level of accuracy if a realistic combustion heat release profile is employed. This is where CFD helps to overcome the predictive limitations of the 1D model. Figure 6.19 shows a schematic overview of the integrated methodology.

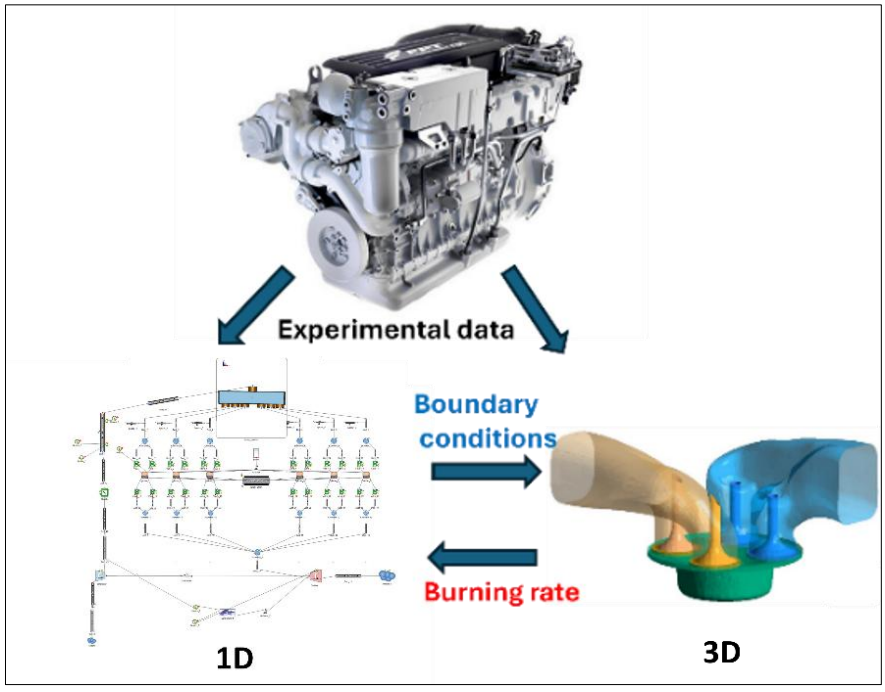

Figure 6.19: Simplified representation of the integrated procedure

The CFD simulations are performed using the ANSYS Forte® flow solver. Boundary conditions are defined in terms of total pressure and temperature at the inlet surface and static pressure at the outlet. Inlet gas composition (air or fuel/air mixture) is also specified. Wall conditions include piston motion profiles and the intake/exhaust valve lifts. Pseudo-arbitrary initial conditions are set in both the cylinder and the external ducts. As a result, the simulation must run over several engine cycles to achieve solution periodicity. The models used are the

same as those adopted for the closed-valve case and are listed in Table 6.5. Notably, species formation is calculated using a chemical kinetic mechanism specifically developed for ethanol oxidation, validated for the closed-valve geometry [187] (WVU mechanism, with 39 species and 369 reactions). Although it does not predict NO_x formation, this mechanism provides reliable CO predictions, which is essential under fuel-rich conditions. For liquid-fuel simulations, the KH-RT breakup model is applied, with additional models handling droplet collisions, wall impingement, and evaporation. Importantly, resolving the extended domain flow field provides a more accurate description of in-cylinder motion. Thus, flow features like tumble, swirl, and vortex breakdown are predicted directly, without relying on arbitrary assumptions—this is vital for accurately modeling turbulent combustion.

The numerical work begins by basing on the experimental data in Table 6.2 and Table 6.3. As observed, the engine operates with a rich mixture (overall $\lambda = 0.84$), and the mixture is unevenly distributed across the six cylinders [187]. In this thesis, an in-cylinder λ value of 0.89, matching one of the measured cylinders, was used for the CFD calculations. To address these issues, five computational test cases are explored:

- First, a model calibration is conducted using the experimental case with two setups aiming to match the same in-cylinder λ: one assumes the entire fuel mass is vaporized and premixed in the intake duct; the other adopts a more realistic scenario where 30% of the fuel remains in liquid phase.
- Second, an improvement in the mixture's equivalence ratio is attempted by increasing only the air mass (with fixed fuel mass) until $\lambda = 1$ is reached. This air increase requires a higher boost pressure level, derived from the 1D simulation.
- Finally, for a target of the in-cylinder $\lambda = 0.89$, a multipoint injection strategy is examined using two different configurations (pressure levels, nozzle diameters, jet orientation).

The test cases are summarized in Table 6.6. The first two numerical cases aim to replicate the experimental pressure profiles, by imposing at boundary conditions an air-to-fuel ratio of ~0.84. In cases where the fuel is partially injected in liquid form, the total injected mass is slightly increased to account for expected wall-film accumulation and vaporization challenges typical of ethanol. To reduce computational time, the WVU kinetic model was employed in these calculations.

Table 6.6: Input data for simulations

Case	m_{fuel} [g]	p_{inlet} [bar]	T_{inlet} [K]
Premixed λ<1	0.314	1.75	313
Liquid 30% λ<1	0.324	1.7	323
Premixed λ=1	0.319	2.16	341
Injection High Pressure	0.323	1.75	323
Injection Low Pressure	0.323	1.77	323

As previously discussed, two fuel delivery strategies are considered: in the first scenario, ethanol is assumed to be fully vaporized and premixed within the intake duct, whereas in the second, 30% of the fuel mass is still in the liquid phase. To simulate this condition, a Rosin-Rammler statistical droplet size distribution is imposed at the inlet, with droplets assigned the same velocity as the incoming mass flow. Figure 6.20 compares the in-cylinder pressure profiles from the simulations with the experimental data across the entire engine cycle, with valve events also indicated. It is evident that the inlet pressure values defined in Table 6.6 allow for a close match of the in-cylinder pressure at the point of IVC, enabling an accurate reproduction of the compression phase. This level of agreement is also attributed to the high-quality mesh, which faithfully reconstructs the engine geometry.

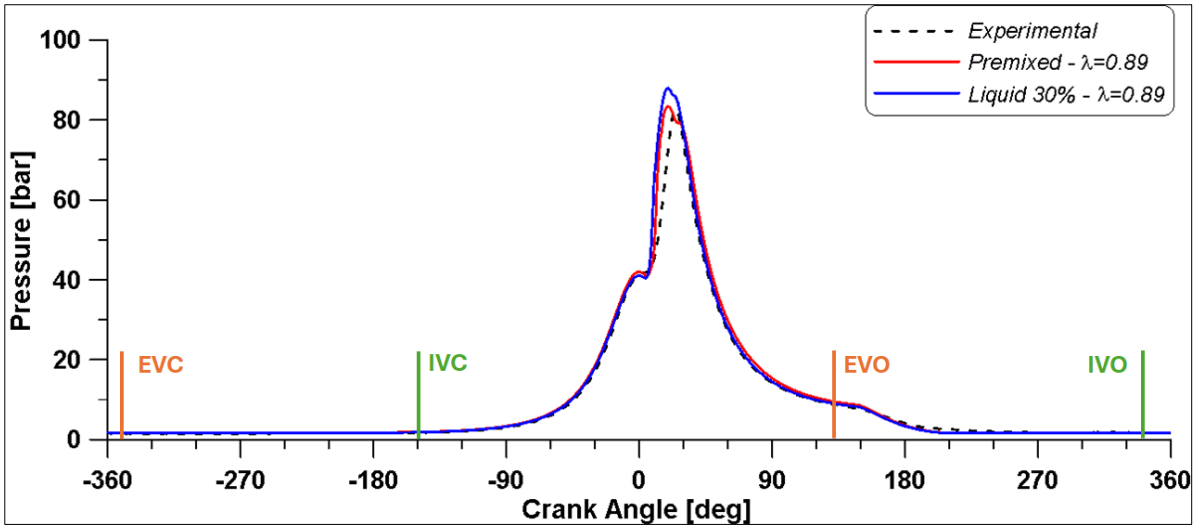

Figure 6.20: In-cylinder pressure comparison

Although the spark is triggered at 5° BTDC, the pressure rise becomes significant only after 10° ATDC, as confirmed by the cumulative heat release profile shown in Figure 6.21.

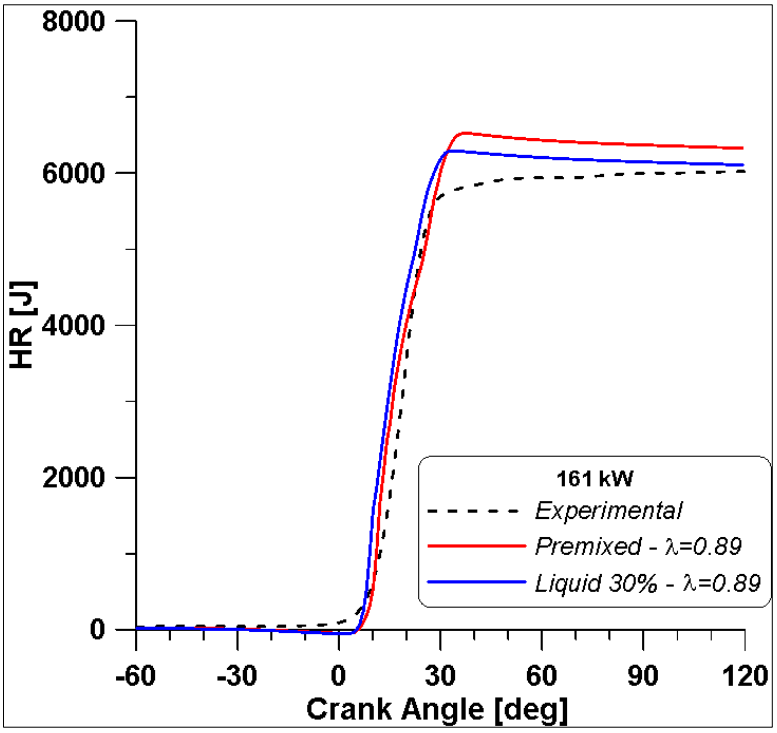

Figure 6.21: Cumulative heat release during combustion

The simulations predict a faster oxidation process and slightly higher peak pressure values, despite the use of an optimized value for the b_1 parameter, which governs the turbulent-to-laminar flame speed ratio. Further details regarding this parameter are provided in Section 3.5.3.2. Nonetheless, the expansion stroke is accurately captured. It is also worth noting that the pressure drop begins approximately 10 crank angle degrees after EVO, which can be attributed to the shape of the valve lift profile, initial lift values are low, delaying the full evacuation of the exhaust gases.

Overall, Figure 6.20 demonstrates a combustion process that is qualitatively similar to the experimental one, with nearly identical total energy release. However, in the fully premixed case, the start of combustion appears to occur slightly later, though it results in a more complete oxidation of the fuel. The discrepancies observed between the two numerical cases are likely due to the different spatial distribution of fuel within the combustion chamber. As will be discussed in a later section, in the case where a portion of the fuel remains in liquid form, some droplets may reach the cylinder without fully evaporating.

6.1.3.5 Numerical Performance Improvement

As previously noted, the reference test is conducted with a $\lambda < 1$, indicating a rich combustion condition. This condition arises from inefficient mixture formation, which is likely due to insufficient boost pressure. In this section, the engine operation is analyzed under stoichiometric conditions ($\lambda = 1$), while maintaining the assumption of fully vaporized ethanol

uniformly premixed with the intake air. The fuel mass is held constant, and the inlet pressure is increased to allow for greater air intake. The immediate result is a steeper compression curve (Figure 6.22a), and consequently, the in-cylinder pressure levels are higher throughout the cycle compared to the previous λ <1 cases. Further insight is provided by the chemical heat release profiles in Figure 6.22b. As previously anticipated, among the cases with λ <1, the premixed configuration exhibits a slightly slower oxidation rate. However, the increase in air-to-fuel ratio and intake pressure leads to an earlier onset of combustion in the stoichiometric case, as evident in Figure 6.22b.

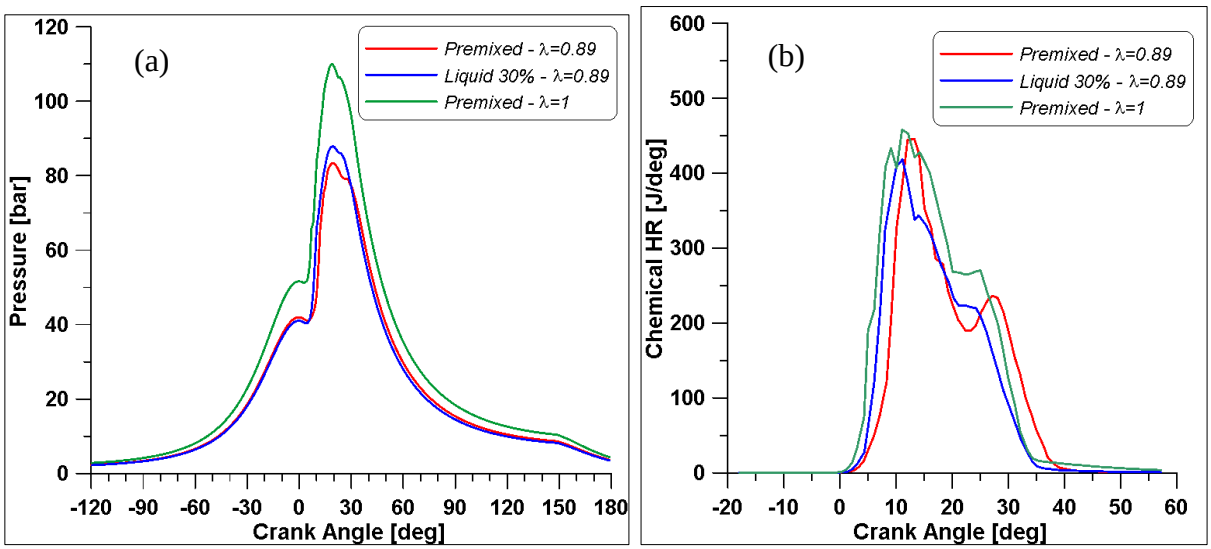

Figure 6.22: Pressure (a) and ROHR (b) for the three cases considered

The cumulative heat release fractions plotted in Figure 6.23 support these observations and provide additional insights. This parameter quantifies the fraction of energy released from combustion relative to the total chemical energy input. It is clearly shown that with a stoichiometric mixture, complete oxidation of the fuel is achieved, as the cumulative HR reaches unity.

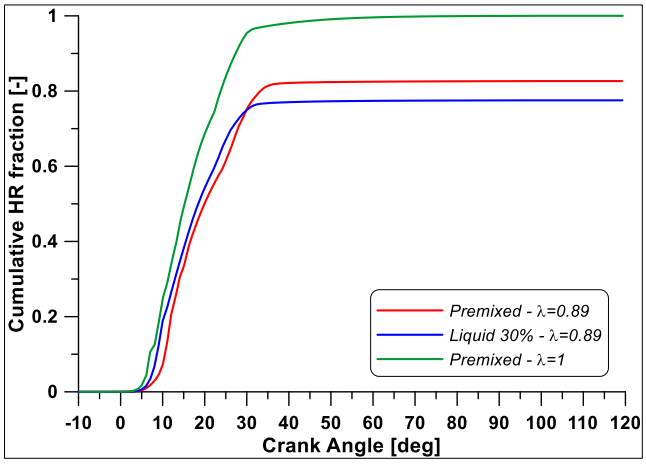

Figure 6.23: Cumulative heat release for the three cases considered

When comparing the two λ <1 cases, a higher fraction of energy is released in the fully premixed configuration, as previously noted in Figure 6.21, despite a slightly lower fuel mass being introduced. This outcome can be interpreted by analyzing Figure 6.24a and Figure 6.24b. Although ethanol is completely consumed in both cases, the rich mixture lacks sufficient oxygen to fully oxidize the CO generated during combustion. As a result, the CO retains chemical energy that remains unreleased, thus lowering the integral HR fraction observed in 6.23 for the premixed λ <1 case. This condition corresponds to the highest CO emissions. In contrast, in the case with 30% liquid ethanol at λ <1, although a greater quantity of fuel is injected (see Table 6.6: Input data for simulations), Figure 6.24a indicates that less C_2H_5OH is present in the vapor phase prior to ignition. This implies that the reduced cumulative HR fraction in this case stems not only from elevated CO emissions (as confirmed by Figure 6.24b) but also from an inadequate vapor-phase fuel supply within the cylinder. As will be further discussed in the following section, a portion of the injected liquid fuel impinges on the intake duct walls. Moreover, Figure 6.24a reveals a moderate presence of ethanol in liquid form within the combustion chamber, as indicated by the slight increase in C_2H_5OH mass fraction near TDC, suggesting that droplet vaporization is still occurring at this stage.

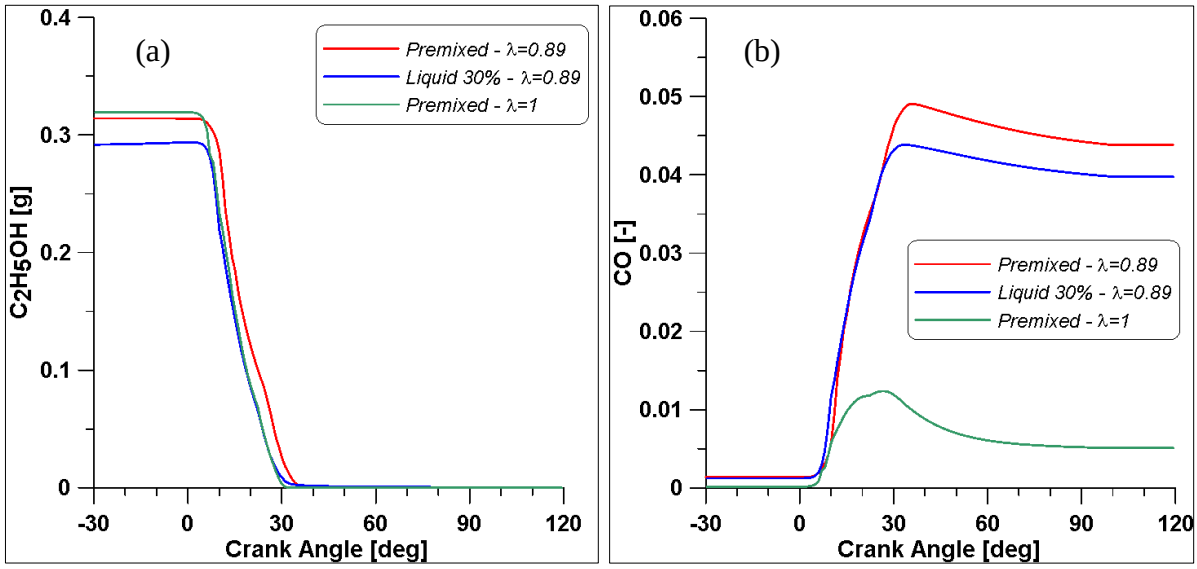

Figure 6.24: Ethanol mass consumption (a) and CO mass fraction (b) for the three cases considered

Finally, the turbulent flame speed (TFS), illustrated in Figure 6.25, begins to increase at the ST (5° BTDC), with a sharp rise occurring after TDC and peaking at approximately 10° ATDC. This behavior corresponds with the pressure rise observed in Figure 6.22a. As highlighted in the introductory section, ethanol is characterized by a high laminar flame speed, and the intense in-cylinder flow dynamics further enhance the turbulent flame propagation.

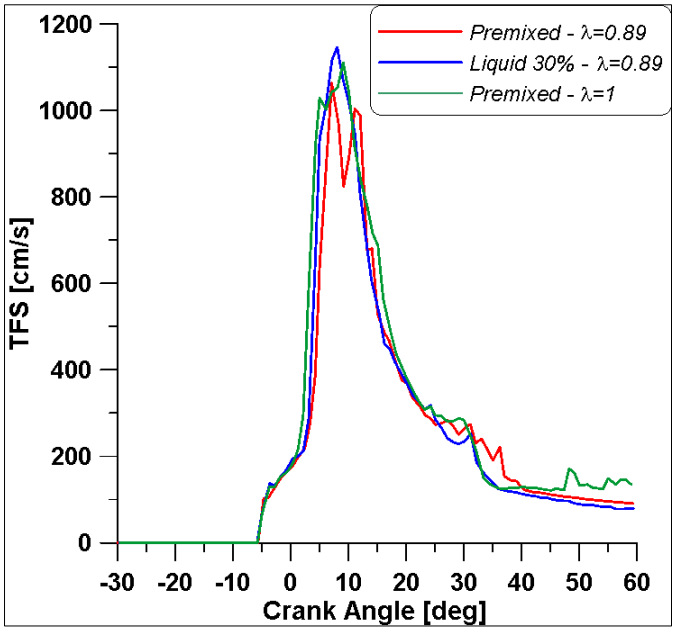

Figure 6.25: Turbulent flame speed for the three cases considered

6.1.3.6 Multipoint Injection

To address the challenges and inconsistencies associated with fuel distribution among the six cylinders, a multipoint injection strategy was implemented by evaluating two distinct injection setups, differing in terms of injection pressure, nozzle hole diameter, and spray orientation (as summarized in Table 6.7). The injector operates with a single-plume spray pattern. Considering the presence of two intake valves per cylinder, the PFI strategy employs injection during the intake valve opening, enabling air-assisted mixture preparation within the intake port. Within the ANSYS Forte® environment, higher injection pressures can be effectively achieved by reducing the nozzle diameter, thereby increasing droplet velocity. Realistic injection pressures were selected based on values reported in the literature [194]. The spray direction in each configuration is defined according to the coordinate system depicted in Figure 6.9.

Table 6.7: Injection setups

	Injection High Pressure	**Injection Low Pressure**
Injection pressure [bar]	50	3
Nozzle diameter [mm]	1	2
Droplet velocity [cm/s]	70	17.5
Spray direction (with respect to x axis)	26°	60°
Start of Injection [°BTDC]	330	330
Injection duration [CAD]	60	60

The in-cylinder pressure curves presented in Figure 6.26a demonstrate a pressure increase attributable to improved fuel delivery. Accordingly, Figure 6.26b reveals an earlier onset of combustion in the multipoint injection cases.

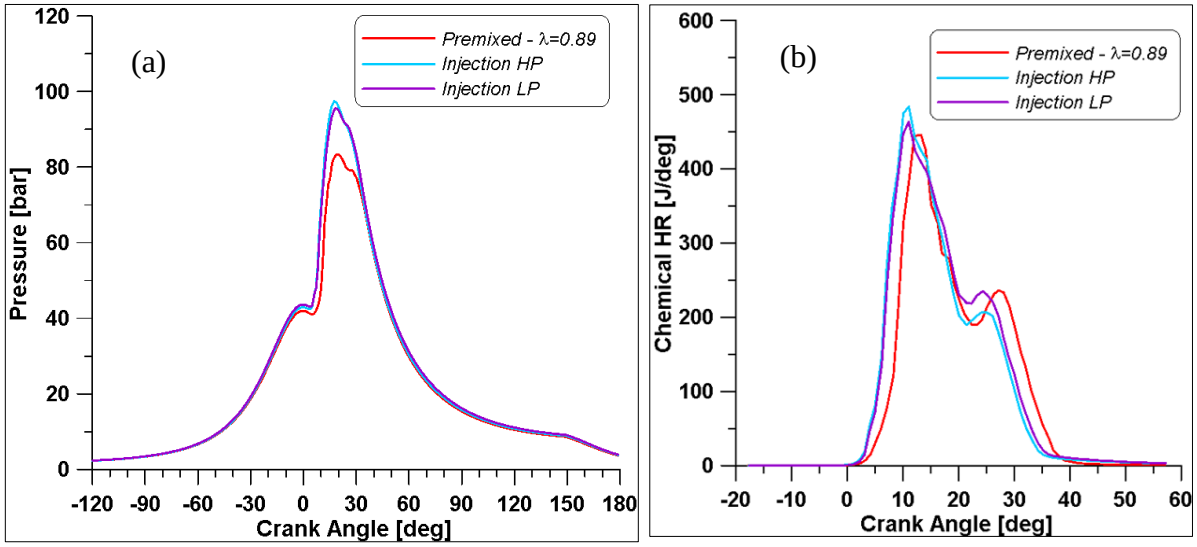

Figure 6.26: In-cylinder pressure (a) and ROHR (b) for high and low injection pressure

Furthermore, the cumulative heat release (HR) fractions in Figure 6.27 indicate a higher energy release from the configuration involving lower injection pressure.

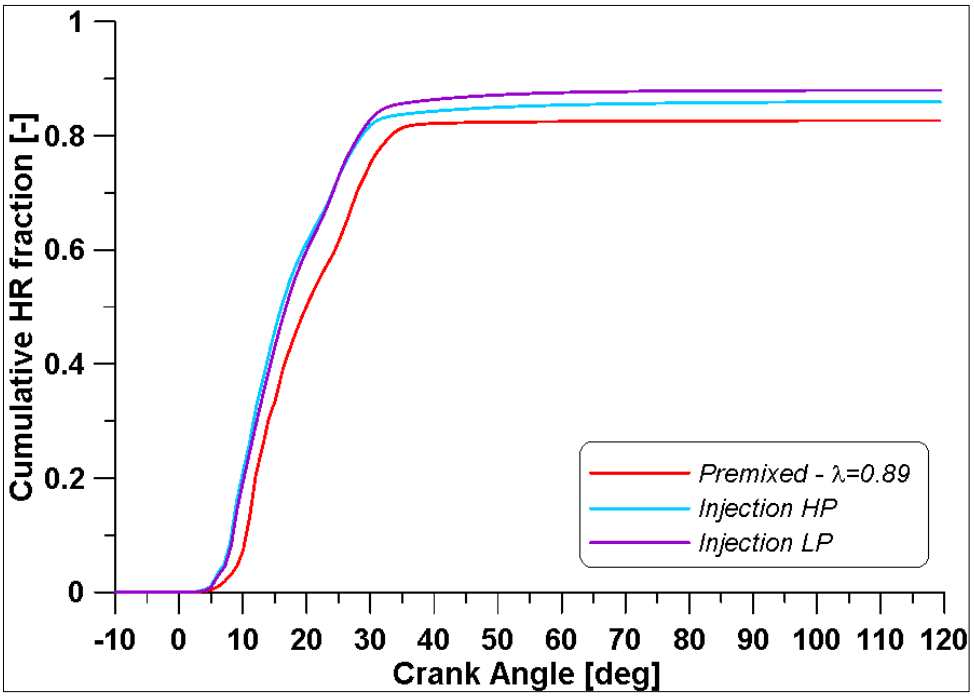

Figure 6.27: Cumulative heat release fraction for high and low injection pressure

As shown in Figure 6.28a, ethanol undergoes complete oxidation in all cases. However, Figure 6.28b confirms the presence of incomplete CO oxidation. The difference in CO emissions originates from the fact that the effective in-cylinder λ differs between the cases. However, it is

necessary to highlight that, as shown in Table 6.9, the injection boundary conditions were defined to match the target λ as closely as possible. Nonetheless, the effective in-cylinder λ is governed by the fuel evaporation process and by the wall-film mass formed within the intake ducts, and therefore it must be regarded as an outcome of the 3D simulation rather than a directly imposed parameter. When compared to the previous scenario, where 30% of the fuel was introduced in liquid form and only a slight increase in ethanol was observed prior to TDC (refer also to Figure 6.24a), the multipoint injection configurations exhibit more pronounced vaporization behavior. This is expected, as the entire fuel quantity is injected in liquid form. In the high-pressure and low-pressure injection cases, 9.8% and 13.9% of the liquid fuel, respectively, reach the combustion chamber and fully vaporize before ignition.

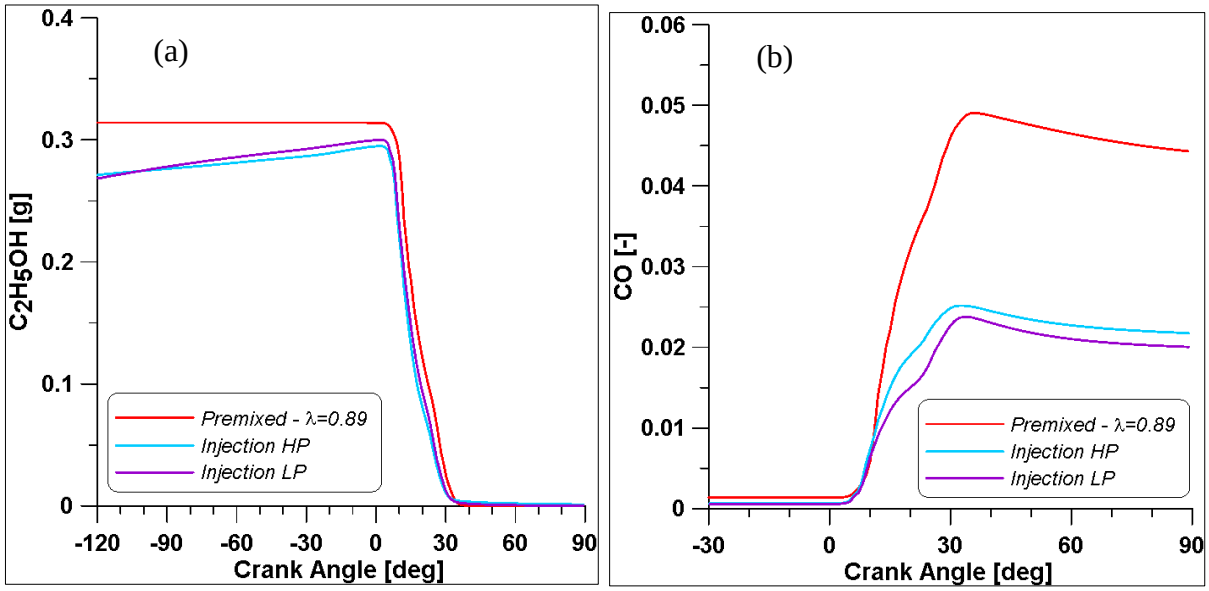

Figure 6.28: Ethanol mass consumption (a) and CO mass fraction (b) for high and low injection pressure

To gain deeper insight into mixture formation prior to combustion onset, the spatial distributions of both liquid fuel and vapor are analyzed. Figure 6.29 illustrates the spray and vapor contours 40 crank angle degrees after the start of injection. The high-pressure injection case exhibits broader droplet dispersion compared to the low-pressure scenario, despite the latter featuring a spray direction nearly perpendicular to the inlet flow.

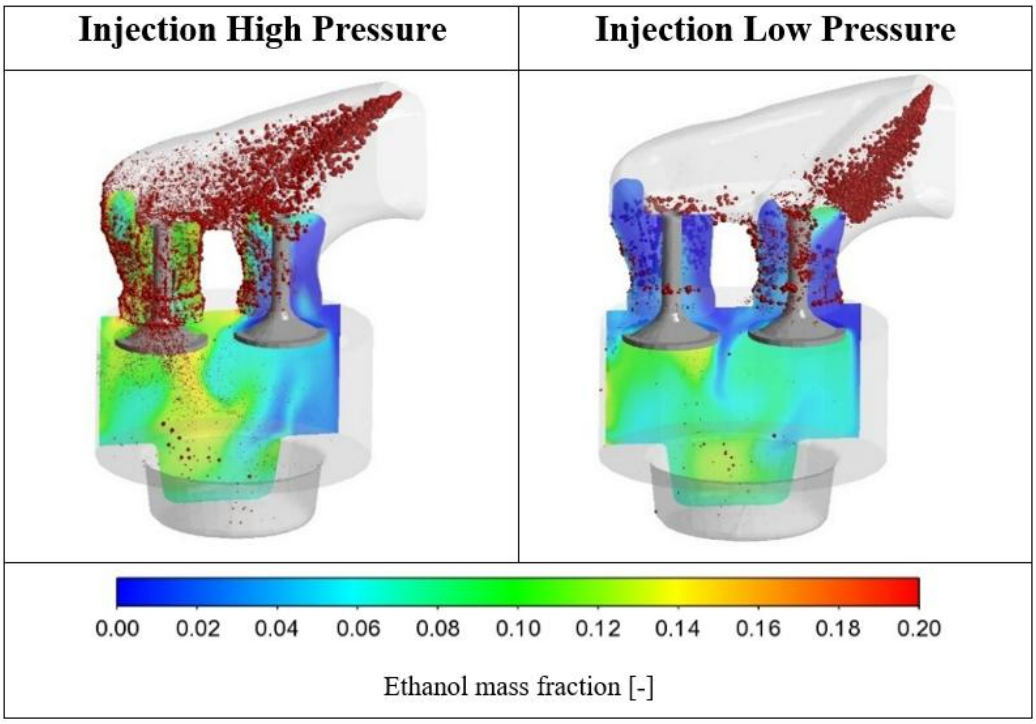

Figure 6.29: Spray and C_2H_5OH vapor distribution at 290°BTDC

Figure 6.30 compares these results with the 30% liquid ethanol case at 20° BTDC. While it is evident that in all configurations in-cylinder droplets are fully vaporized before ignition, liquid fuel is still visible on the intake duct walls [195]. This residual fuel, in conjunction with incomplete CO oxidation, contributes to the cumulative HR fraction falling below unity (see Figure 6.27). In the multipoint injection cases, the droplets appear more widely dispersed due to the higher injection velocity, whereas in the 30% liquid case, the droplets are passively transported by the incoming flow. Higher injection pressures cause the spray to concentrate predominantly on one valve, whereas lower pressure, combined with a different spray orientation, results in a more balanced distribution between the two intake valves. Simulation results quantify the amount of fuel deposition on the wall as 29 mg for the high-pressure case, and approximately 24 mg for the lower-pressure, perpendicularly directed injection. In contrast, in the 30% liquid – $\lambda < 1$ configuration, although 70% of the fuel is ideally premixed and yields a uniform ethanol distribution within the cylinder, approximately 30 mg of fuel remains in the liquid phase within the intake duct, due to ethanol's high latent heat of vaporization.

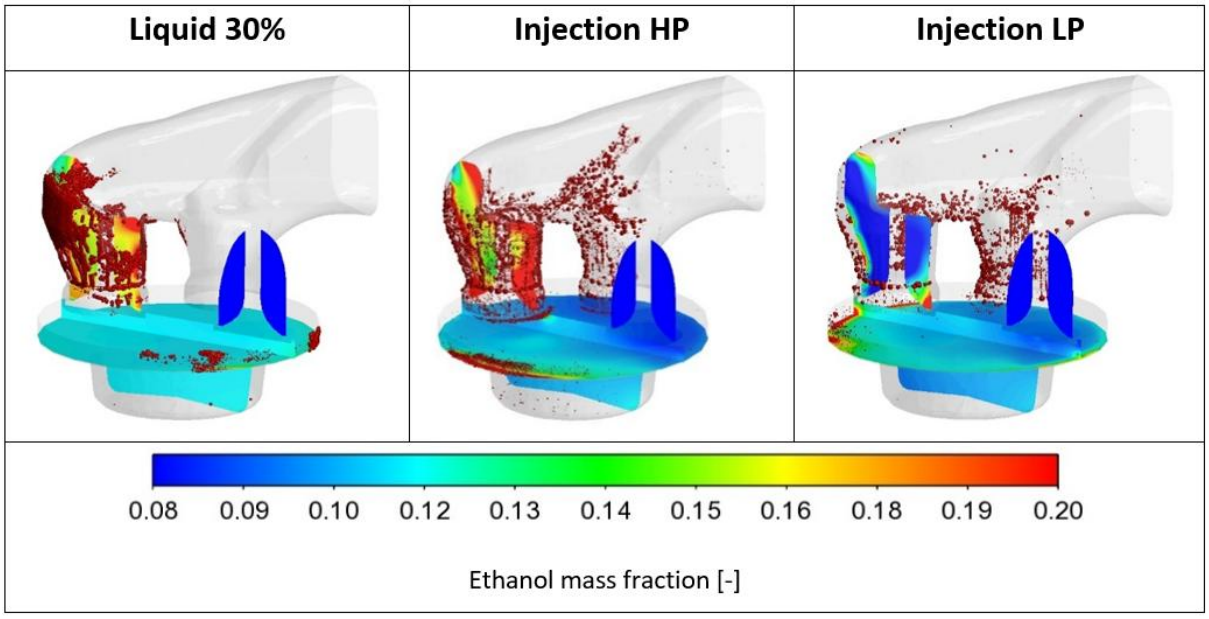

Figure 6.30: Spray and C_2H_5OH vapor distribution at 20°BTDC

6.1.3.7 Discussion and Comparison

This section provides a final comparison of the CFD results across all cases, with a comprehensive summary reported in Table 6.8. The reported λ values refer to the inlet boundary conditions and in-cylinder mixture calculated in the last engine cycle. The first three rows list: (i) the inlet fuel mass, i.e., the amount set as input in the simulations; (ii) the mass of fuel that reaches the cylinder in vapor phase at the IVC; and (iii) the vapor mass present at the SI timing. As previously noted, in cases where fuel is injected in liquid form, either partially or entirely, the values in the second and third rows are lower than the initial inlet mass, due to droplet impingement and accumulation on the intake duct walls, preventing full entry into the combustion chamber. Additionally, a portion of the liquid fuel does reach the cylinder and subsequently vaporizes before combustion begins. The difference between the SI and IVC vapor mass quantifies this vaporized fraction. Consequently, the difference between the inlet and SI vapor masses corresponds to the wall film mass, as detailed in the preceding section. The fourth row of the table expresses this wall-deposited fuel as a percentage of the inlet mass, clearly showing that multipoint injection, particularly at lower pressure and with optimized jet orientation, effectively minimizes wall film formation. Naturally, these mass quantities are identical only when the fuel is fully vaporized and premixed before intake.

Table 6.8: Summary CFD results

	Exp.	Prem. λ <1	Liquid 30% λ <1	Prem. λ = 1	Injection HP	Injection LP
Inlet fuel mass [g]	0.317	0.314	0.324	0.319	0.323	0.323
In-cylinder vapor mass at IVC [g]	0.317	0.314	0.289	0.319	0.266	0.261
In-cylinder vapor mass at SI [g]	0.317	0.314	0.294	0.319	0.294	0.299
Wall film mass in the intake ducts [%]	0	0	9.4	0	9.0	6.5
In-cylinder air mass [g]	2.525	2.449	2.342	2.888	2.524	2.554
Inlet air index (λ) [-]	0.84*	0.84	0.81	1.01	0.87	0.88
In-cylinder air index (λ) [-]	-	0.87	0.89	1.01	0.96	0.95
IMEP [bar]	18.35	20.32	19.75	25.20	20.23	21.08
Indicated efficiency [%]	31.17	34.50	32.43	42.05	33.34	34.74
CO @ EVO [-]	--	0.0438	0.040	0.0051	0.0216	0.020
Chemical HR [J]	--	6974.8	6763.8	8637.6	7465.9	7641.9
Final fuel burned fraction [%]	--	82.6	77.5	100	85.9	88.00
In-cylinder fuel burned fraction [%]	--	82.6	85.5	100	94.4	94.1

**the value refers to the λ relative to the measured cylinder*

Two air–fuel ratios are then computed: the first based on the vaporized fuel at IVC, and the second considering the vapor at SI. The first two cases yield in-cylinder λ values close to the experimental reference. Moreover, results indicate that introducing 30% of the fuel in liquid form yields performance indicators, such as IMEP and thermal efficiency, more closely aligned with the experimental data. The two multipoint injection cases exhibit λ values near stoichiometric. The fuel accumulation on the walls prevents the formation of localized rich zones, which contributes to modest IMEP gains. Thermal efficiency appears relatively insensitive to the change in injection strategy; however, CO emissions are markedly reduced, indicating a more complete oxidation process. As noted earlier, the case with lower injection pressure benefits from better fuel vaporization, which improves performance metrics.

These observations are supported by the last three rows in Table 6.8. Cases with air–fuel ratios closer to stoichiometric show higher cumulative chemical heat release, confirming more efficient fuel energy conversion. The final fuel burned fraction represents the proportion of heat released relative to the total energy input (as shown in Figure 6.23 and Figure 6.27), accounting

for energy losses due to wall film formation and incomplete CO oxidation. In contrast, the in-cylinder fuel burned fraction is calculated based on the fuel mass that effectively enters the cylinder and reflects the intrinsic combustion efficiency.

Lastly, Figure 6.31 illustrates temperature distributions across all simulated cases. While high temperatures are observed in each case, the spatial extent and symmetry of these regions vary depending on the λ value and the method of fuel delivery.

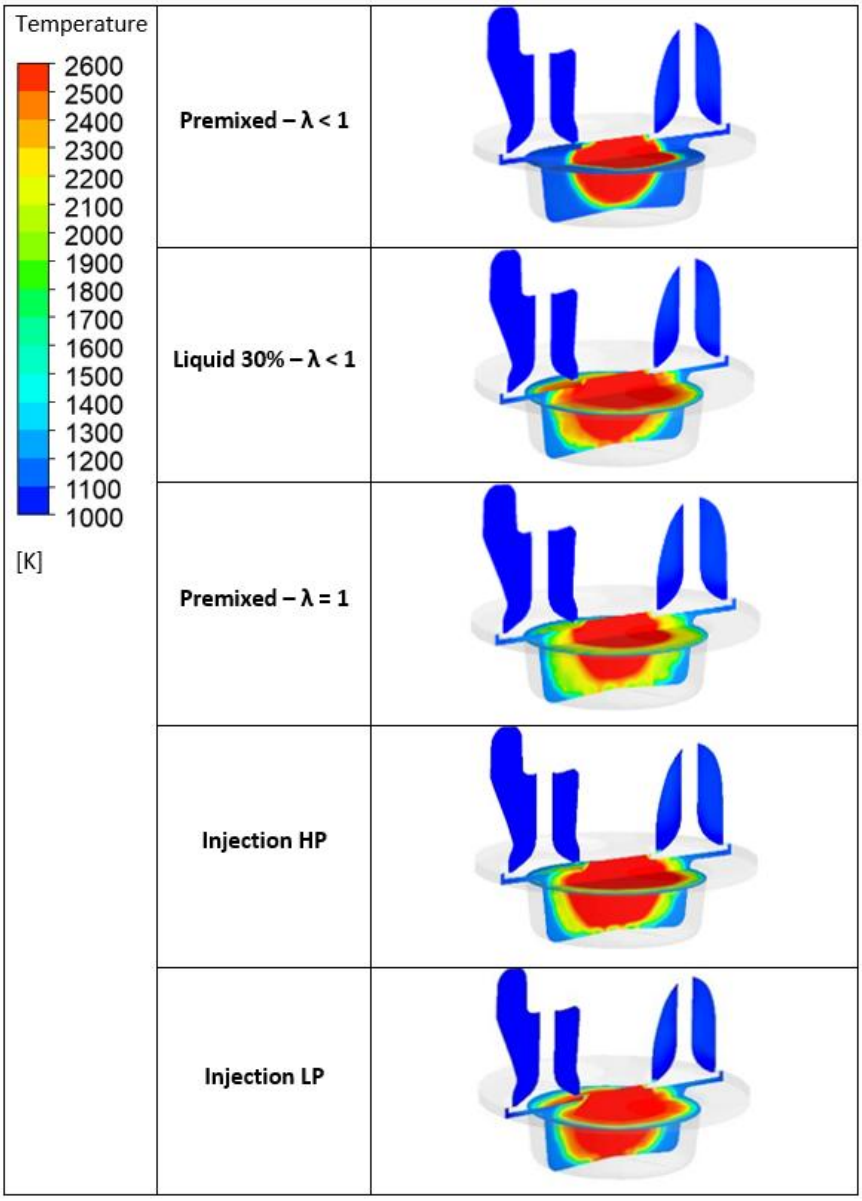

Figure 6.31: Temperature distributions at 10°ATDC on a plane crossing an intake and an exhaust valve

The first notable difference arises in the premixed λ <1 case, where peak temperatures are confined to a smaller region, consistent with the slower combustion development discussed earlier (Figure 6.22b and Figure 6.23). In the second case, also with λ <1 but with 30% liquid fuel, a more irregular temperature front is evident, likely caused by in-cylinder droplets

disturbing the fuel distribution. In the premixed stoichiometric case, temperature levels vary more extensively, likely due to increased mass flow enhancing mixing and heat diffusion during oxidation. Finally, the injection cases show a more axisymmetric temperature profile, which aligns with the more asymmetric fuel distribution previously observed in Figure 6.30.

6.1.4 CFD – 1D Integration

In this final section, engine performance across various configurations is analyzed using a 1D model of the complete engine system. As previously discussed, integrating CFD results with the simulation of the entire turbocharged, intercooled engine initially enabled the definition of appropriate boundary conditions for the intake and exhaust ducts. Following a preliminary calibration using the baseline experimental data, a suitable operating condition with a stoichiometric ethanol–air mixture was established by determining the necessary boost pressure to achieve the desired air mass flow rate. Focusing on the details of the 1D model, the six-cylinder turbocharged engine is reproduced with the schematic shown in Figure 6.32.

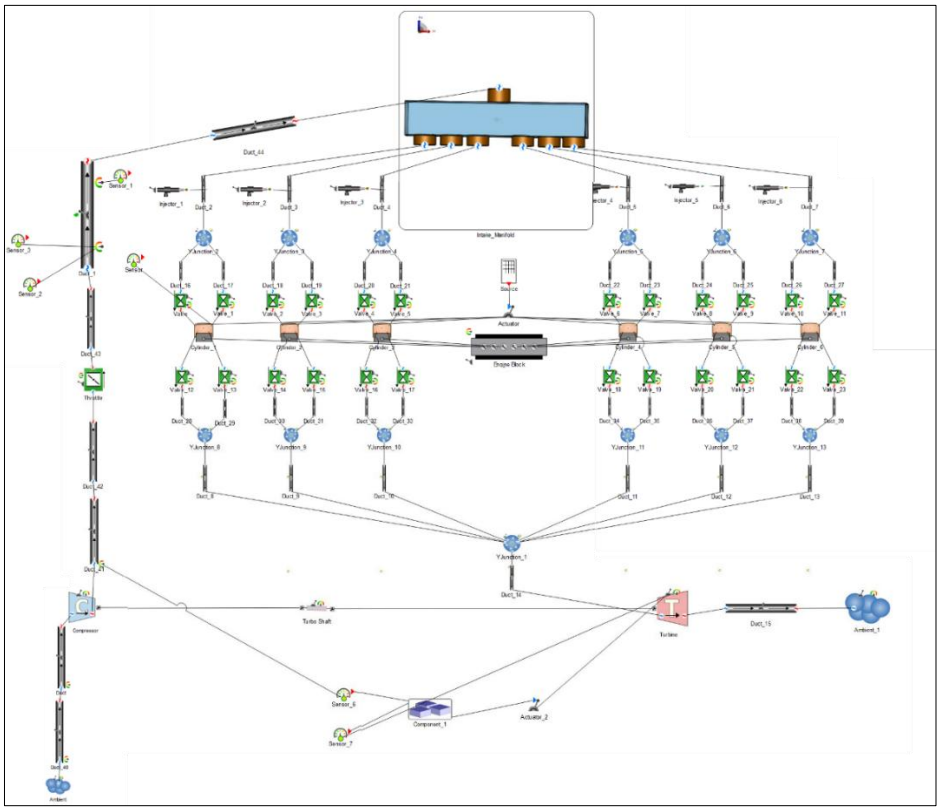

Figure 6.32:1D schematics

The boost pressure control is implemented through a proportional–integral–derivative (PID) controller that acts on the wastegate position to ensure that the desired boost pressure is achieved under different operating conditions. The controller continuously compares the actual boost pressure, calculated within the model, to a predefined target value derived from the

engine's operating strategy. Based on the control error, the PID algorithm determines the appropriate actuation signal for the wastegate, effectively regulating the proportion of exhaust gases that bypass the turbine. This adjustment modifies the turbine power and consequently the compressor speed, which directly influences the intake manifold pressure. The control action is embedded within the thermodynamic and fluid-dynamic framework of the model, where both compressor and turbine characteristics are represented by their respective performance maps, reported in Figure 6.33 and Figure 6.34, respectively. By taking these maps into account, the PID controller operates within physically realistic boundaries, ensuring that the commanded wastegate position leads to a feasible pressure ratio and mass flow through the turbocharger. The equations of the 1D model was previously introduced in section 5.2 of the thesis.

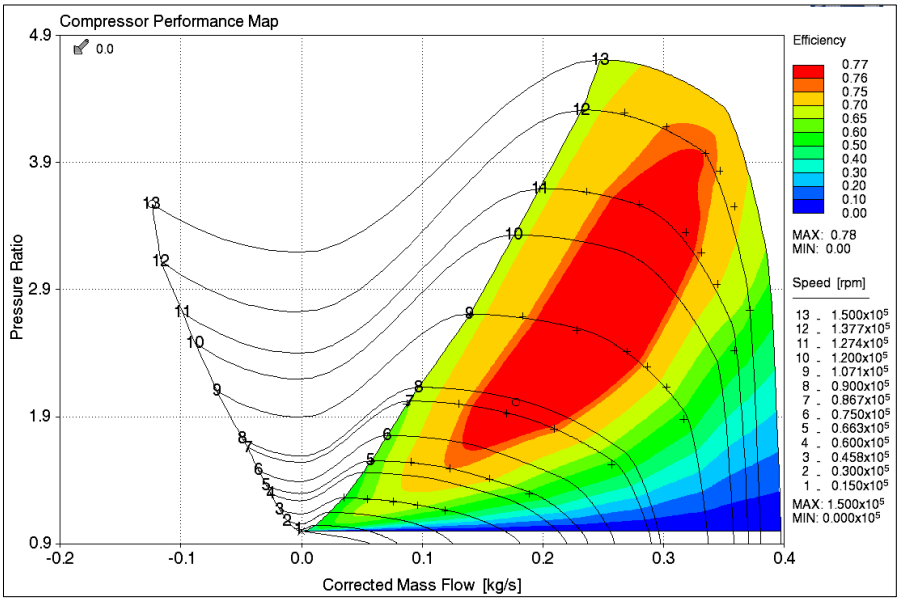

Figure 6.33: Compressor map

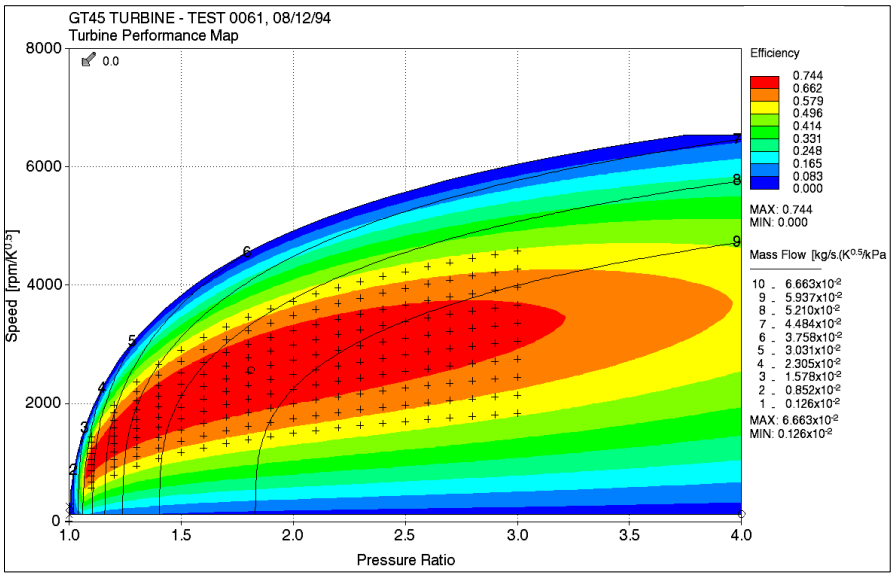

Figure 6.34: Turbine map

Particularly significant is the second stage of CFD–1D coupling, which aims to estimate overall engine performance after the design modifications assessed through the multi-dimensional CFD analyses. Consequently, the final 1D calculations are performed for the following cases: a stoichiometric mixture (λ=1) and the two multipoint injection configurations (3 bar and 50 bar), both operating at λ <1, as discussed in the previous section. The final coupling of CFD and 1D models involves the transfer of critical data into the 1D framework, namely:

- The boost pressure level required to match boundary conditions across both modeling approaches. This value also serves as the setpoint for the PID controller managing the wastegate actuation;
- The heat release rate profile derived from CFD simulations;
- The cumulative heat release level as estimated by the CFD model.

Figure 6.35, Figure 6.36 and Figure 6.37 confirm that the proposed methodology enables the 1D model to accurately replicate the in-cylinder pressure trends observed in the CFD simulations.

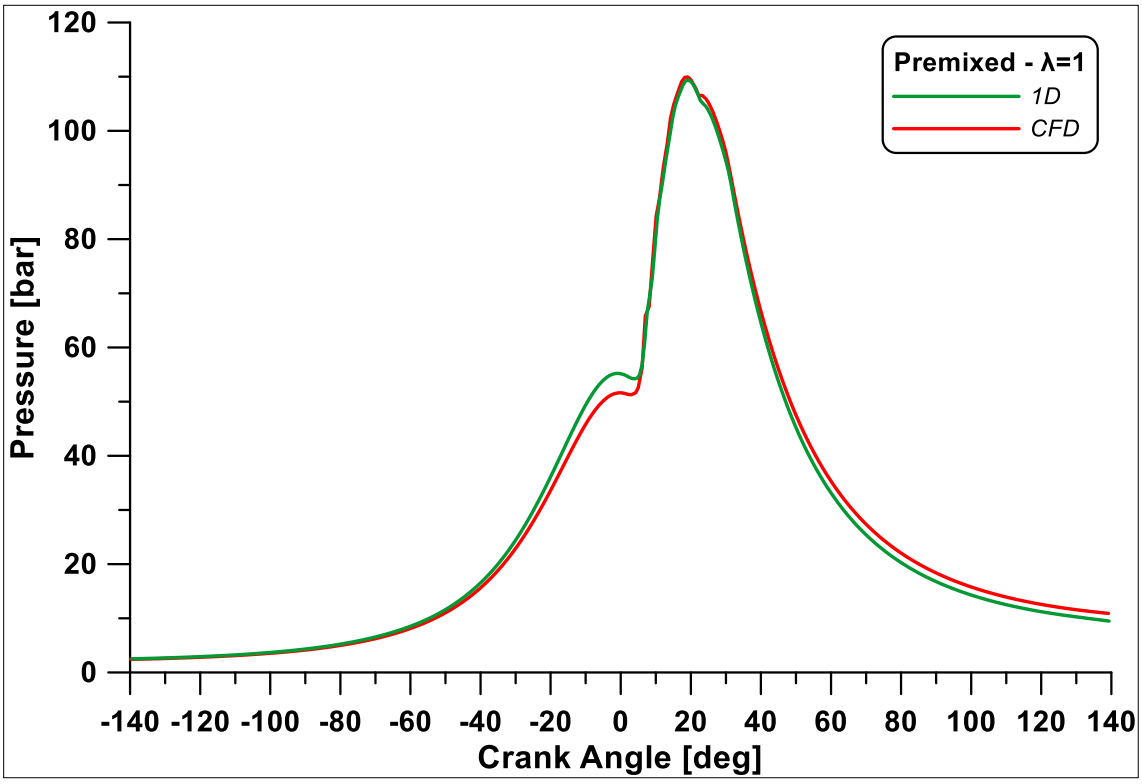

Figure 6.35: Comparison between 1D and 3D pressure. Stoichiometric mixture

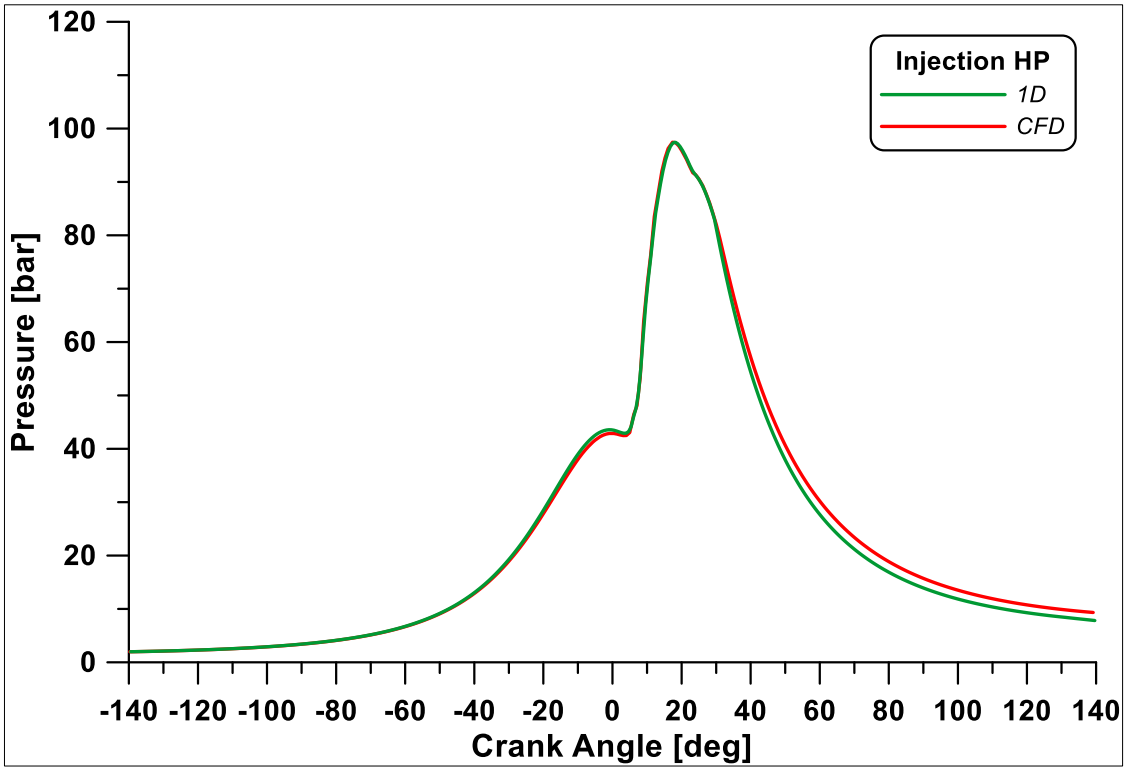

Figure 6.36: Comparison between 1D and 3D pressure. P_{inj}=50 bar

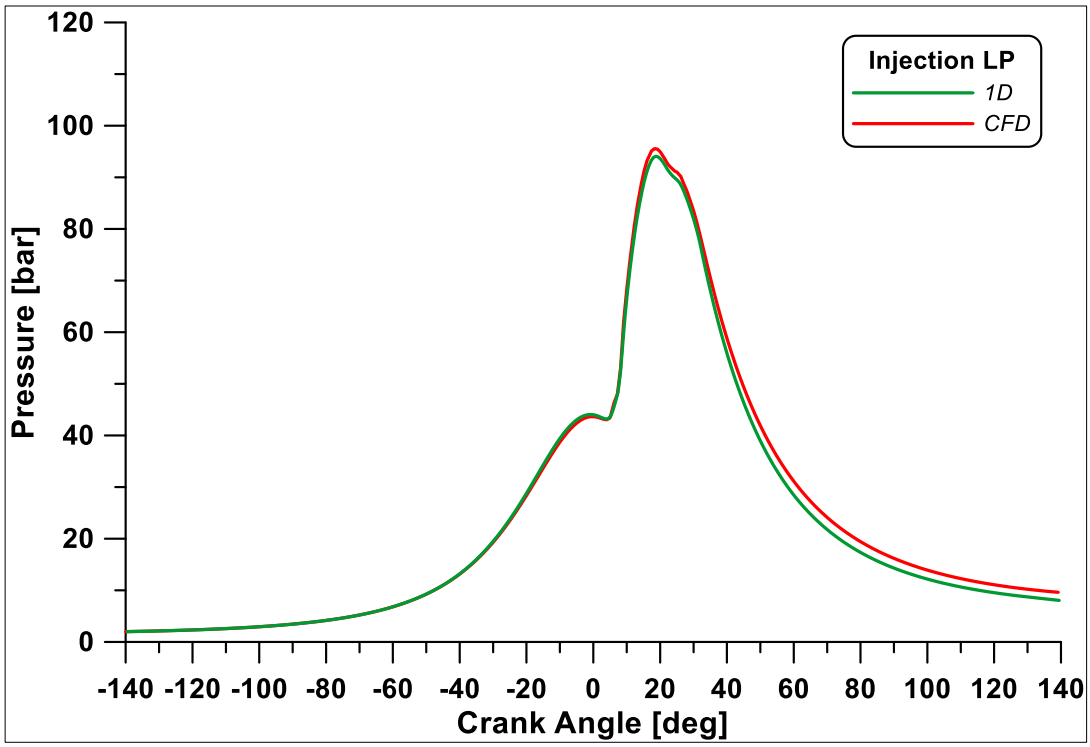

Figure 6.37: Comparison between 1D and 3D pressure. P_{inj}=3 bar

Table 6.9 summarizes the key results from the powertrain-level simulations and highlights the performance benefits arising from the different fuel–air configurations. In particular, adopting a single-point injection system in combination with a stoichiometric mixture (λ = 1) leads to

improvements not only in combustion characteristics but also in mechanical performance. A significant increase in brake power is achieved. On the other hand, with multipoint injection systems, slight gains in IMEP and indicated thermal efficiency are observed.

Table 6.9: Overall powertrain simulation results

	Experimental	Prem. λ <1	Prem. λ = 1	Injection High Pressure	Injection Low Pressure
Inlet fuel mass [g]	0.316	0.314	0.319	0.323	0.323
In-cylinder air mass [g]	2.525	2.616	3.106	2.613	2.640
Air excess (λ) [-]	0.89	0.888	1.03	0.865	0.872
IMEP [bar]	18.35	17.79	22.21	19.55	19.83
Indicated efficiency [-]	31.17	30.66	38.34	32.74	33.22
Chemical HR [J]	--	6836	8727	7443	7611
BMEP [bar]	14.8	14.83	19.50	16.39	16.72
BTE [%]	25.2	25.56	33.14	27.45	28.01
Brake power [kW] [-]	161.1	161.5	212.33	178.4	182.1
BSFC [kg/kWh]	0.529	0.525	0.405	0.489	0.479
Boost pressure [bar]	--	1.74	2.18	1.76	1.78

6.2 The Rolls Royce C26:33 Engine

As previously emphasized in this thesis, recent years have witnessed growing interest in advanced ignition systems as a means to enhance combustion efficiency and reduce pollutant emissions. Conventional SI systems often encounter significant limitations in large-bore engines or under lean-burn conditions, where flame propagation tends to be slower and less stable. This causes a reduction in thermal efficiency and increased cycle-to-cycle variability. PC ignition has emerged as a promising solution to address these challenges. This technology initiates combustion in a small, dedicated PC, producing high-energy turbulent jets that penetrate the MC. These jets serve as multiple ignition sites, substantially accelerating combustion and promoting greater stability even under lean or highly diluted conditions.

Given these advantages, and following the assessment of a conventional SI configuration, the analysis in this thesis is extended to include a PC system to evaluate its potential benefits in terms of combustion development, efficiency, and emissions when operating with methanol. Methanol has been selected due to its close similarity to ethanol in terms of molecular structure,

physical properties, and combustion behavior, making it a suitable alternative fuel for this comparative investigation. The engine selected for this study is the Rolls-Royce C26:33 L9PG marine engine (Figure 6.38) [196].

Figure 6.38: The RR C26:33 SI gas marine engine

It is a 9-cylinder, SI, turbocharged gas engine originally designed to operate with natural gas (NG). The main engine specifications are summarized in Table 6.10. At full load, the engine delivers a BMEP of 18.5 bar with a boost pressure of 3.8 bar (Table 6.11), operating at 1000 rpm. The engine is designed to run with a global equivalence ratio (ϕ) of 0.5 in the main combustion chamber, while the mixture inside the PC remains stoichiometric to ensure reliable ignition.

Table 6.10: Engine characteristics

PC, 4-stroke turbocharged, 9 cylinders, 4 valves	
Stroke [mm]	330
Bore [mm]	260
Displacement volume [cm^3]	~158000
CR [-]	11:1
IVC	135° BTDC
EVO	131°ATDC

Table 6.11: Full load data

BMEP [bar]	18.5
Rated speed [rpm]	1000
Charge air pressure [bar]	3.8
Charge air temperature [°C]	55
Air flow rate [kg/h]	1.85
Fuel flow rate [kg/h]	400
Temperature after turbine [°C]	365

Key geometrical and operational parameters of the PC system are provided in Table 6.12.

Table 6.12: PC geometrical characteristics

PC volume [cm^3]	38.13
Nozzle diameter [mm]	4
Number of nozzles [-]	6
Total nozzle cross-section area [cm^2]	0.125
V_{PC}/V_{MC} [%]	2.2

A cross-sectional view of the engine, highlighting both the main and PCs, is shown in Figure 6.39. The jets from the PC are oriented with a cone angle of 120°, ensuring adequate penetration and turbulence generation in the MC. The spark offset is 9 mm with respect to the PC's axis of symmetry.

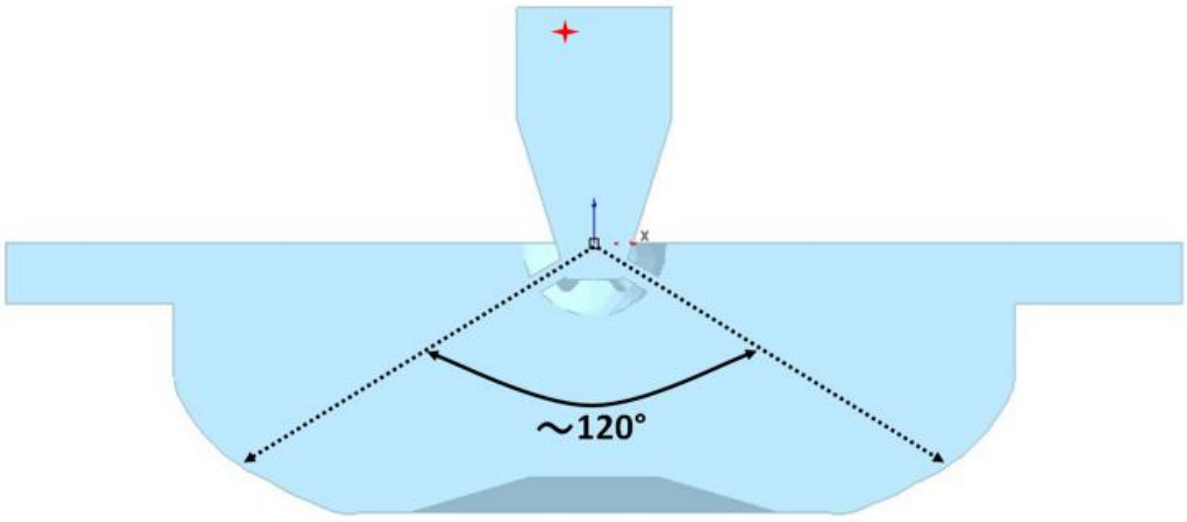

Figure 6.39: A cross-sectional view of combustion chamber and PC

6.2.1 Methodology

The adopted computational methodology integrates both 1D and three-dimensional 3D modeling approaches, as illustrated in Figure 6.40.

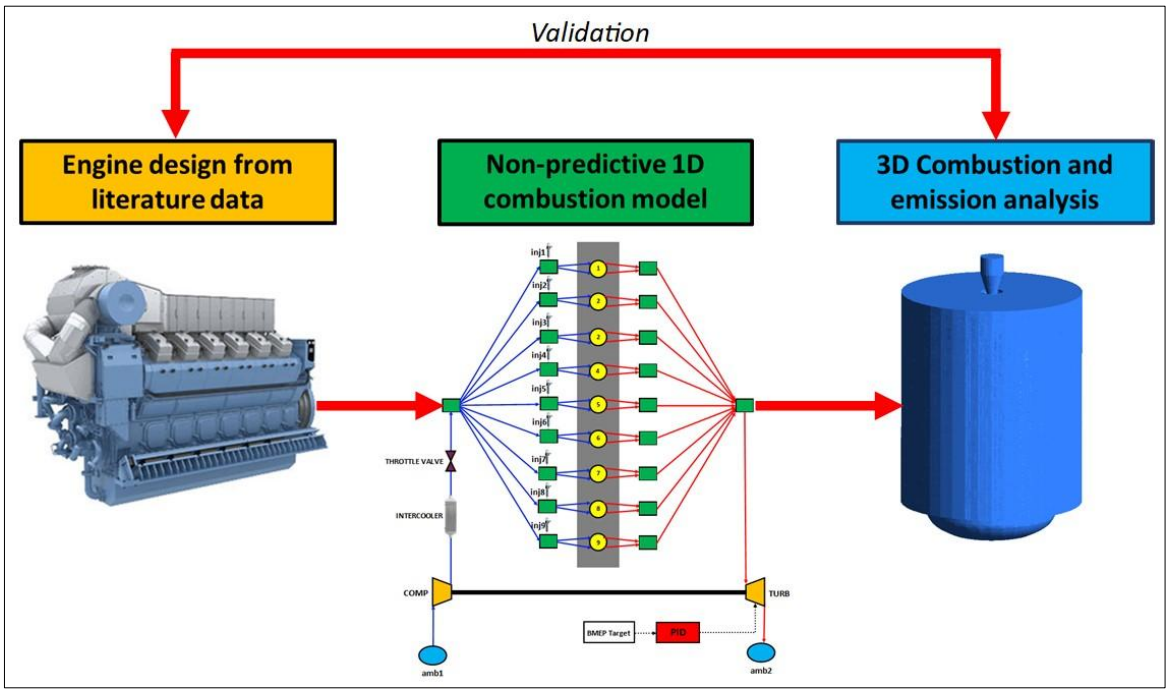

Figure 6.40: Schematic representation of the combined procedure

Engine data are sourced from the literature, enabling the development of a comprehensive 1D model that includes all nine cylinders, intake and exhaust valves, the turbocharging system, wastegate, and intercoolers, following a similar approach as previously described in this thesis. The 1D model is employed primarily to establish the boundary and initial conditions required by the 3D CFD model. The 3D model, in turn, allows for a detailed analysis of the combustion process and pollutant formation. Due to the lack of available experimental pressure traces for this engine—neither for natural gas nor alternative fuels, a coupled 1D–3D simulation strategy is implemented. In practice, the process begins with a 1D simulation to generate the initial boundary conditions for the 3D CFD model. After completing the 3D simulation, the resulting ROHR curve is exported and fed back into the 1D model. This update refines the initial conditions, which are then re-applied in a subsequent 3D simulation. This iterative loop is repeated until convergence is reached between the pressure traces predicted by the 1D and 3D models. The results presented in the following sections correspond to this final, converged state, in which the pressure curves have been validated through the 3D model.

Three engine operating conditions are considered: full load (100%), cruising load (80%), and low load (20%). These are simulated using both 1D and 3D models for two different fuels,

methane (used as a surrogate for natural gas) and methanol. The initial 3D simulations are performed using an active PC configuration to replicate the real engine operation with methane. Subsequent simulations with methanol are conducted using both active and passive PC configurations, in order to evaluate the potential advantages and drawbacks associated with each layout. All 3D simulations are conducted in closed-valve conditions using ANSYS Forte®, meaning that only the compression, combustion, and expansion strokes are modeled.

6.2.2 3D CFD

The turbulence modeling is carried out using the RNG RANS approach. For the combustion process, the G-equation-based model is adopted. A detailed description of this model is provided below. The G-equation combustion model relies on the turbulent premixed flamelet theory originally proposed by Peters, as previously discussed in Chapter 3. To overcome the limitations imposed by grid resolution and temporal discretization, particularly in capturing ignition processes and the early stages of flame kernel development, a Discrete Particle Ignition Kernel model is employed. This model tracks the evolution of ignition through Lagrangian particles, offering a more accurate depiction of kernel formation and propagation near the spark plug region. For chemical kinetics, two mechanisms are considered: the GRI-Mech 3.0 mechanism, which includes 53 species and 325 reactions and is applied for methane simulations, and the reduced Pichler mechanism [197], consisting of 18 species and 55 reactions, which is used for methanol. To account for nitrogen oxide formation during methanol combustion, the Pichler mechanism is further extended by incorporating NO_x-related reactions derived from GRI-Mech 3.0.

6.2.2.1 Model Validation

As highlighted earlier, there is a lack of experimental data specifically related to marine engines operating with a PC configuration. Therefore, model validation is performed using experimental results from a heavy-duty Scania engine equipped with an active PC and fueled by natural gas [198]. This engine has been the subject of several previous investigations [199] [200]. Although the geometric characteristics of the marine engine differ from those of the heavy-duty engine, the underlying physical phenomena, such as flame front propagation, jet penetration, and premixed combustion behavior, are sufficiently similar to ensure the validity of the modeling approach. Moreover, this methodology has already demonstrated its effectiveness for simulating premixed combustion in PC systems [167]. The simulation setup and model parameters are summarized in Table 6.13.

Table 6.13: Calculation parameters for the heavy-duty engine simulation

λ_{MC} at ST	1.9
λ_{PC} at ST	1
P_{IVC} [bar]	1.8
T_{IVC} [K]	348
m_{fuel} [mg]	109

Figure 6.41 illustrates the comparison between the computed and experimental in-cylinder pressure traces for lean operation ($\lambda = 1.9$) in the MC. The good agreement observed confirms the suitability of the employed numerical models for simulating combustion in PC engines.

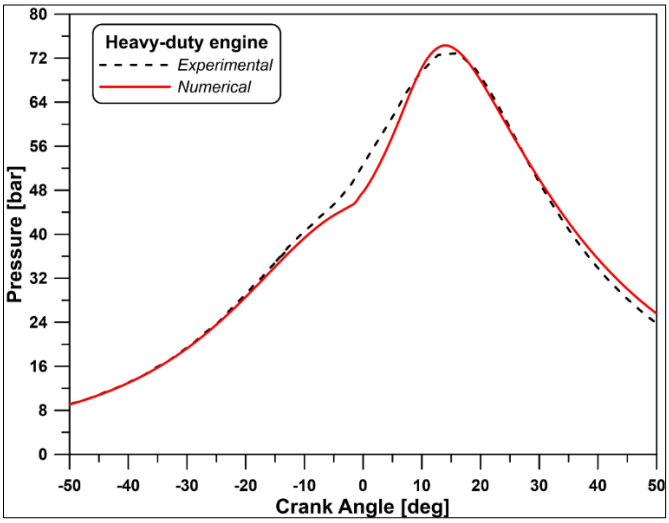

Figure 6.41:Comparison of experimental [198] and calculated in-cylinder pressure

6.2.2.2 Mesh Sensitivity Analysis

The computational domain for the simulations consists of a full 360° model of the Rolls-Royce engine cylinder and PC. This approach is necessary due to the spark plug's offset relative to the symmetry axis of the PC. As a preliminary step, a mesh sensitivity analysis was conducted to evaluate the influence of mesh resolution on the accuracy of the results.

Seven mesh grids were generated, with average cell sizes ranging from 2.0 mm to 3.2 mm. A Solution Adaptive Mesh (SAM) refinement was applied to the scalar G field within the PC volume, as shown in Figure 4. In particular, within the scalar G range of –0.3 to 0.3, the mesh was locally refined to one-quarter of the global cell size, resulting in a minimum cell size of 0.5 mm in the ignition zone.

The simulations were performed under full-load conditions (100%) using methane as fuel, with equivalence ratios of 0.5 in the MC and 1.0 in the PC. Ignition was set at 15° BTDC. Based on the comparison of pressure curves (Figure 6.42) and key performance indicators, such as IMEP,

peak pressure, the crank angle at 50% heat release (HR CA50), and average maximum temperature (Figure 6.43), the mesh with an average cell size of 2.05 mm was selected. This configuration comprises approximately 2 million cells and offers the best compromise between accuracy and computational cost. Moreover, this mesh enabled the simulation to reproduce the target BMEP of 18.5 bar, consistent with the engine specifications reported in Table 6.11.

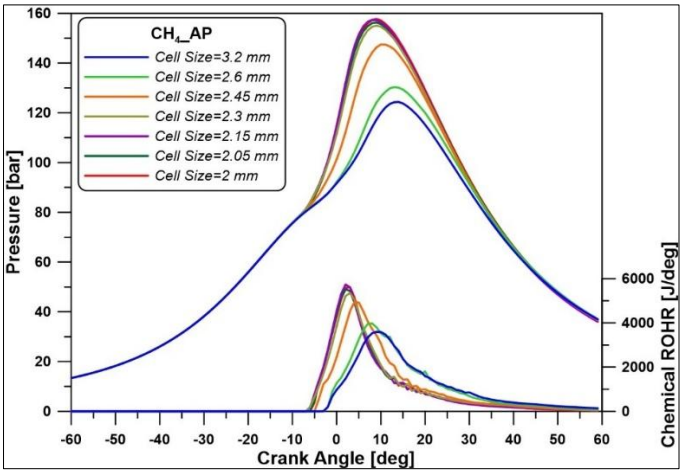

Figure 6.42: In-cylinder pressure and ROHR trends for the different mesh considered

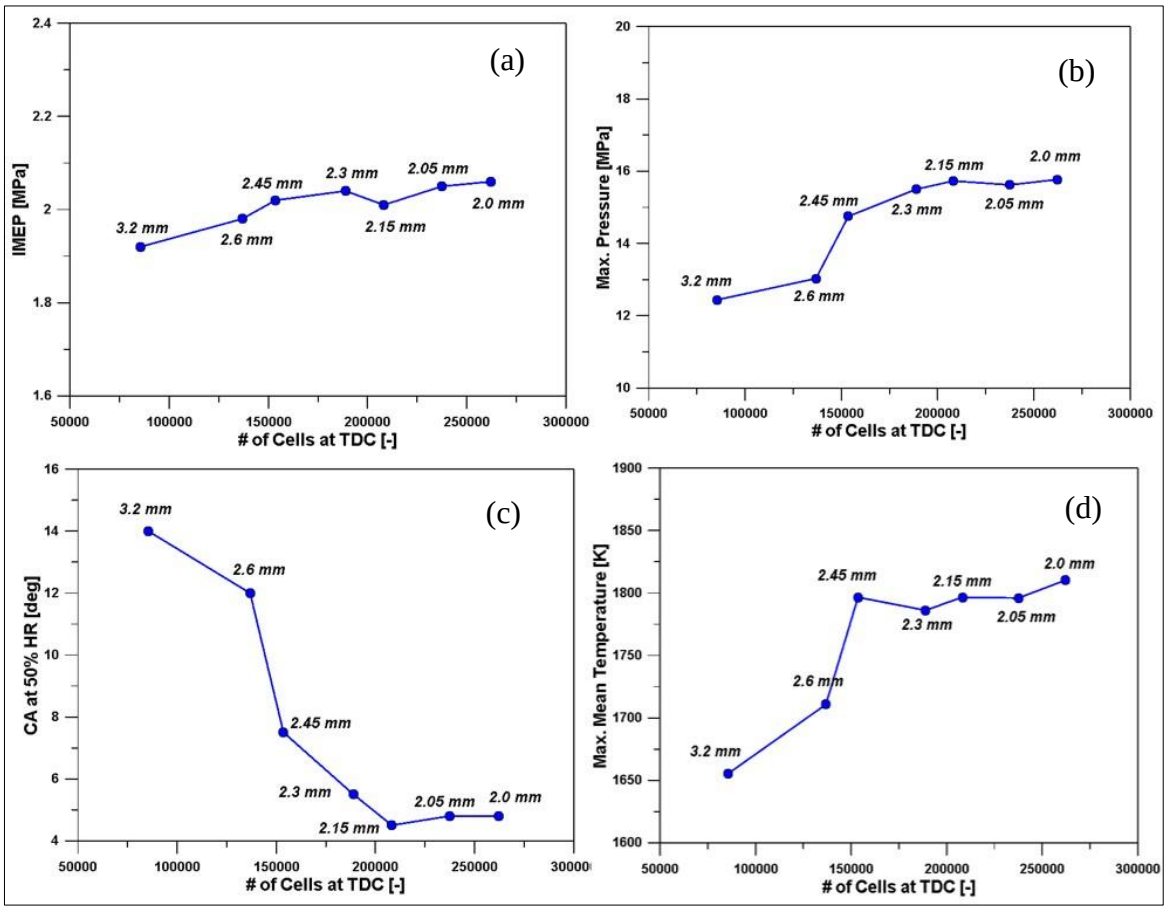

Figure 6.43: IMEP (a), maximum pressure (b), HR_CA50 (c) and maximum mean temperature (d) trends

6.2.2.3 Test cases

It is important to first highlight that, as the focus of this study is a marine propulsion engine, the engine is assumed to be coupled with a propeller. Consequently, the engine's operating behavior must be aligned with the propeller's load curve, which follows the cubic law. This law assumes a constant nominal pitch propeller capable of absorbing the rated power at 100% of the nominal rotational speed [204]. Figure 6.44 illustrates this relationship by plotting the propeller curve as a function of rotational speed against engine power. The corresponding BMEP is also reported in the same figure.

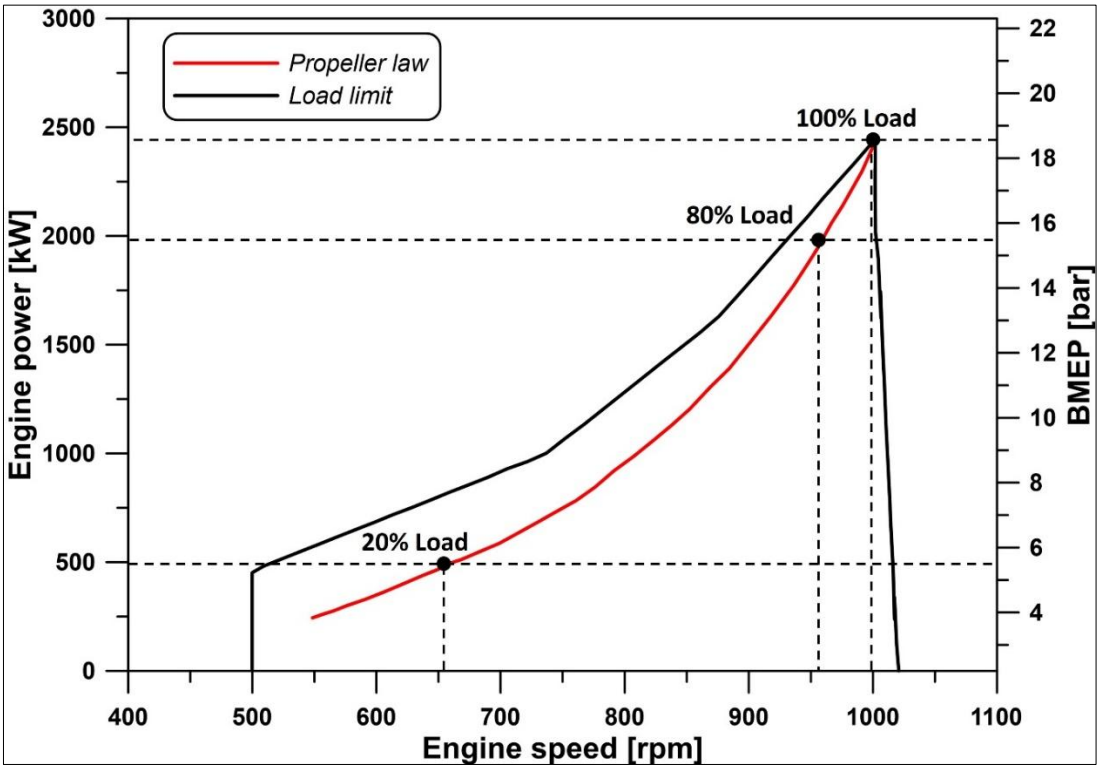

Figure 6.44: Engine load limit and the propeller law chosen

Three representative operating points, full load (100%), cruising load (80%), and low load (20%), are initially simulated using the 1D model with methane, and subsequently with methanol, to provide boundary conditions for the 3D CFD simulations. The CFD calculations are first performed using an active PC configuration fueled with methane at the three load conditions. These cases are labeled CH_4_100L_AP, CH_4_80L_AP, and CH_4_20L_AP. In each case, the λ in the MC is adjusted to match the required power output. The same operating points are then analyzed using methanol, also assumed to be in fully gaseous form. These cases are denoted as CH_3OH_100L_AP, CH_3OH_80L_AP, and CH_3OH_20L_AP. In all simulations, the MC operates under lean conditions, with λ values ranging from 2.3 to 2.5.

Since, in the experimental setup, natural gas is supplied to the PC through a check valve during the intake stroke, and because the intake phase was not simulated, the active PC configuration was reproduced by introducing a rich mixture into the PC at IVC. During the subsequent compression stroke, the pressure difference between the MC and the PC drives air from the MC into the PC, progressively leaning out the initially rich mixture. This process is illustrated in Figure 6.45, where the pressure distribution clearly shows that the higher pressure in the MC induces a flow from the MC to the PC. By appropriately calibrating the initial mixture composition, it is possible to achieve a stoichiometric mixture inside the PC at ST, thus replicating the behavior observed in an active PC engine.

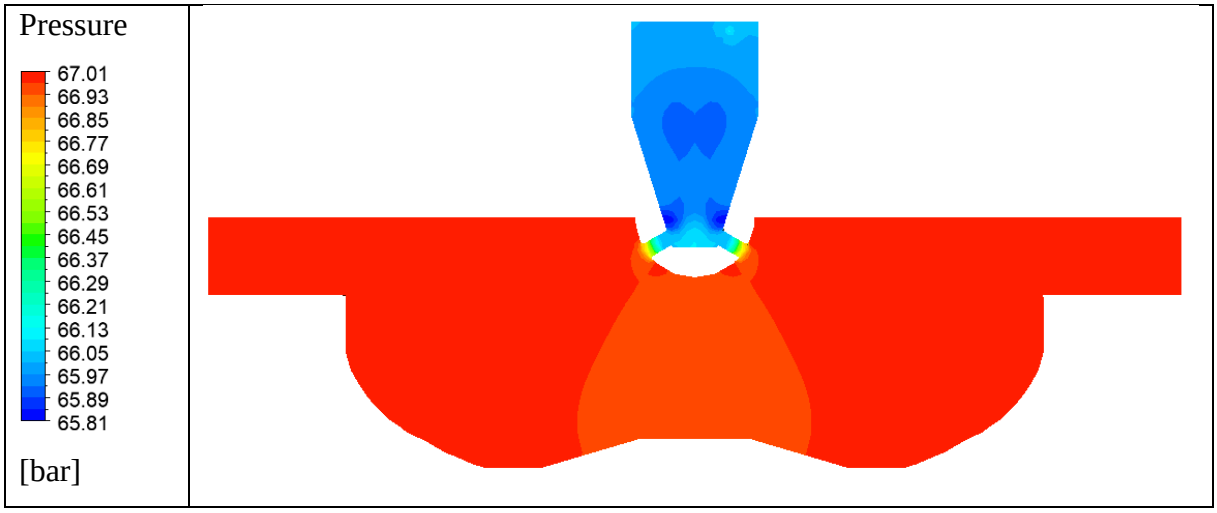

Figure 6.45: Pressure distribution for the active PC configuration at 17°BTDC

Subsequently, the passive PC configuration is analyzed under two key operating points: high load (80%) and low load (20%). These simulations are labeled CH_3OH_80L_PP and CH_3OH_20L_PP. While the active configuration allows independent control of λ in the MC and PC, the passive layout enforces the same λ in both chambers, necessitating a slightly richer global mixture to maintain stable combustion. Table 6.14 summarizes the initial CFD boundary conditions obtained from the 1D model at IVC, as well as the λ values in the MC and PC at the time of ignition.

Table 6.14: Calculation parameters for all cases simulated

Cases	λ_{MC} at ST	λ_{PC} at ST	P_{IVC} [bar]	T_{IVC} [K]	m_{fuel} [mg]	E_{input} [kJ]
CH_4_100L_AP	2.1	1	3.96	391	1582	79.09
CH_4_80L_AP	2.1	1	3.21	380	1351	67.56
CH_4_20L_AP	2.1	1	1.51	393	607	30.37
CH_3OH_100L_AP	2.5	1	3.95	337	3497	74.14
CH_3OH_80L_AP	2.3	1	3.08	334	3001	63.61
CH_3OH_20L_AP	2.4	1	1.39	320	1370	29.04
CH_3OH_80L_PP	2.2	2.2	3.08	337	3009	63.79
CH_3OH_20L_PP	2.2	2.3	1.39	320	1383	29.32

6.2.2.4 Results

To evaluate the feasibility of the proposed approach, the first simulation using methanol with an active PC (AP) configuration was conducted under full-load conditions (100%), referred to as CH_3OH_100L_AP. The results were compared with the previously validated methane case (CH_4_100L_AP). As shown in Figure 6.46, both configurations achieve the same BMEP, thereby confirming the reliability of the numerical model. Differences in in-cylinder pressure and ROHR between the two fuels are also highlighted in the figure.

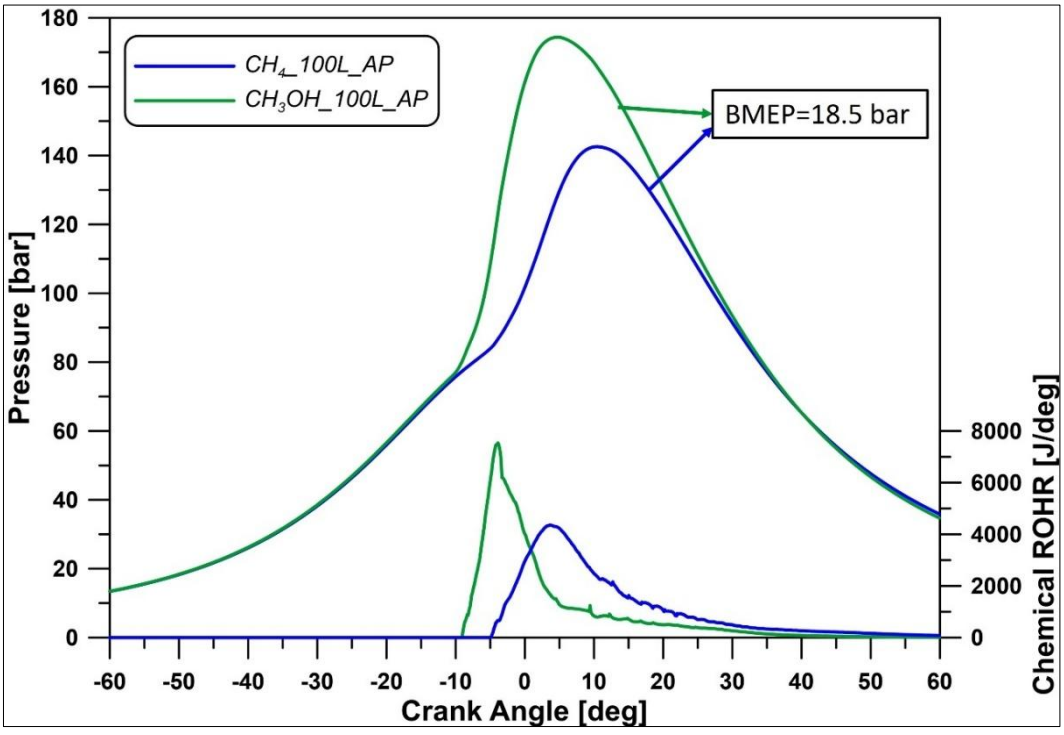

Figure 6.46: Pressure and ROHR for the cases CH_4_100L_AP and CH_3OH_100L_AP

A more comprehensive analysis is then performed at partial loads, focusing on 80% and 20% engine load conditions, which are representative of typical maritime operations such as cruising and port maneuvering, respectively. The analysis begins with the high-load cases (80%), comparing CH_4_80L_AP, CH_3OH_80L_AP, and CH_3OH_80L_PP. This is followed by the evaluation of the low-load cases (20%), including CH_4_20L_AP, CH_3OH_20L_AP, and CH_3OH_20L_PP. Finally, a comparative overview of key combustion and emission parameters is presented for all simulated cases, including the full-load scenarios (CH_4_100L_AP and CH_3OH_100L_AP), providing a complete understanding of engine behavior under various fuels and PC configurations.

High load

The 80% engine load represents typical cruising conditions for maritime applications, making it ideal for standard open-sea navigation under moderate weather and sea states. Figure 6.47 compares the combustion characteristics of three different configurations operating at this load. In Figure 6.47a, the pressure evolution in the MC is represented by solid lines, while dashed lines indicate the pressure in the PC. The CH_3OH_80L_AP configuration exhibits a higher peak pressure in the MC, occurring close to TDC. This earlier pressure rise is attributed to the inherently higher flame speed of methanol and the optimized ignition conditions provided by the active PC configuration, where a stoichiometric or slightly rich mixture enhances rapid and stable flame development in the MC. The pressure rise in the PC (dashed line) just before TDC indicates effective ignition within the PC and the generation of energetic turbulent jets that ignite the lean MC mixture. These jets act as distributed ignition sources, promoting enhanced turbulence and faster combustion. Conversely, the CH_4_80L_AP case shows a delayed and lower peak pressure due to methane's slower flame speed, though combustion remains stable owing to the turbulence induced by the active PC. The CH_3OH_80L_PP case, using a passive PC configuration with no direct fuel enrichment, shows the slowest and lowest pressure rise. Here, combustion is delayed due to the overall lean mixture in the PC, resulting in reduced reactivity and weaker ignition. Nevertheless, because methanol has a higher laminar flame speed than methane, the chemical heat release rate is higher than in the methane case, even though the combustion is shifted towards the expansion stroke, leading to lower peak pressures. Figure 6.47b illustrates the temperature trends. Methanol cases reach lower maximum temperatures due to lower initial temperatures at IVC, as reported in Table 5. This is caused by methanol's high latent heat of vaporization, which cools the charge during the intake process. The CH_3OH_80L_AP configuration again shows the earliest temperature rise, consistent with the pressure data. The CH_3OH_80L_PP case, by contrast, has the slowest and lowest

temperature increase, reflecting its weaker ignition and delayed combustion. Figure 6.47c shows the cumulative heat release. The green curve, representing CH_3OH_80L_AP, displays the steepest initial slope, indicating rapid chemical-to-thermal energy conversion, corresponding to the high pressure and temperature peaks seen previously. Interestingly, the final HR value is higher for the methane case, implying a greater energy input is required to reach the same BMEP, as confirmed in Table 5. This suggests a lower thermal efficiency for methane compared to methanol.

The evolution of TKE is depicted in Figure 6.47d. The CH_3OH_80L_AP case exhibits a sharp TKE peak just before TDC, corresponding to enhanced turbulence and accelerated flame propagation in the MC. In contrast, the CH_3OH_80L_PP case shows significantly lower TKE levels due to the lack of enriched jets from the PC, reducing the turbulence-enhancing effect in the MC.

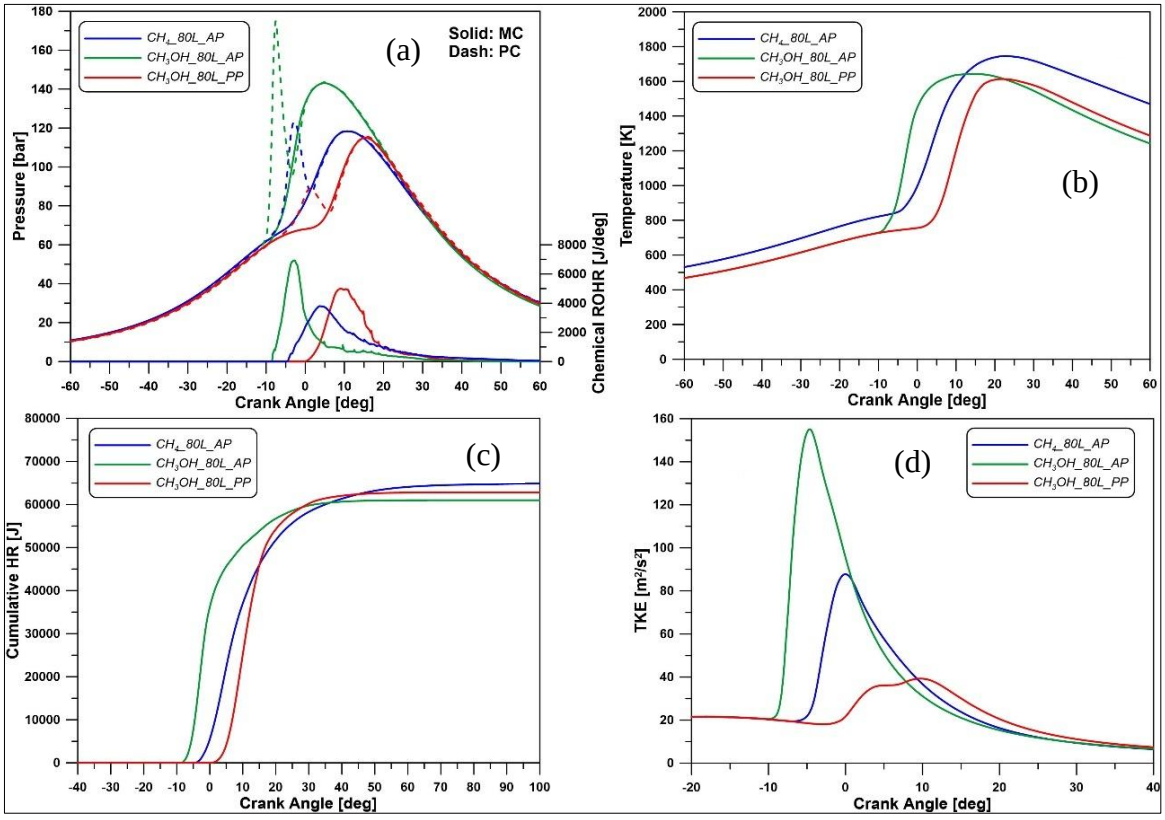

Figure 6.47: Comparison between 1D and 3D pressure (a), temperature (b), cumulative heat release (c), TKE (d). P_{inj}=3 bar

To further analyze the combustion behavior, spatial distributions of combustion-related parameters are investigated. Figure 6.48 presents the selected computational slices: a longitudinal section capturing both MC and PC (including two of the six connecting orifices) and a cross-sectional view of the piston bowl.

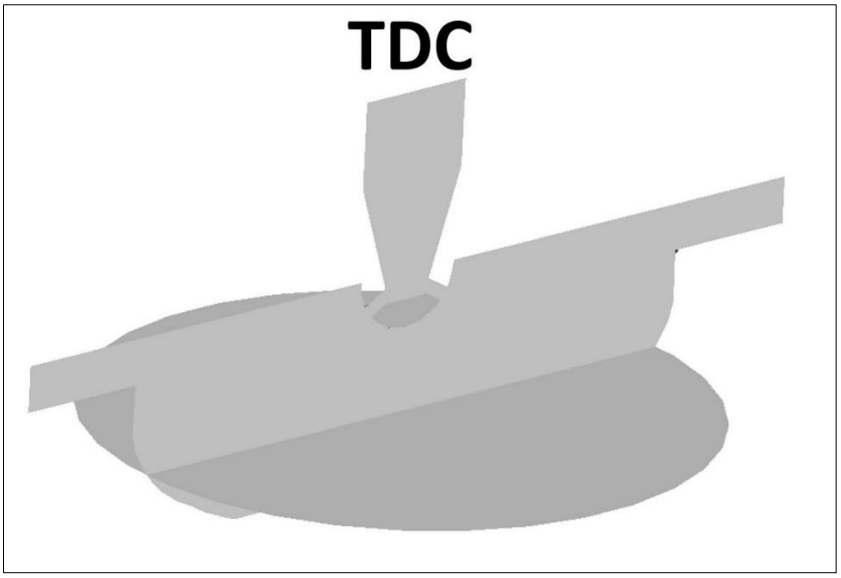

Figure 6.48: View of the cross-section and longitudinal section at TDC used for the distributions.

The G-equation distributions shown in Figure 6.49 track flame front propagation. Here, G = 0 identifies the flame front, G < 0 denotes unburned regions, and G > 0 indicates burned gases. The CH_3OH_80L_AP configuration shows flame initiation in the MC as early as 7° BTDC, while in CH_4_80L_AP the flame front appears at 3° BTDC. In CH_3OH_80L_PP, combustion begins only after TDC. The early flame development in the active PC cases aligns with the more energetic turbulent jets emerging from the spark-side orifice. These jets are more symmetrical in the active configuration, while in the passive one, where the PC mixture is leaner, jet symmetry deteriorates, particularly between 2° and 4° ATDC, leading to asymmetric and delayed flame propagation.

This asymmetry persists at later crank angles and is accompanied by a slower flame front advance. The visual transition from blue (unburned gases) to red (burned gases) clearly shows this: flame propagation takes approximately 15 CAD in CH_3OH_80L_AP, versus 27 CAD in CH_3OH_80L_PP, underscoring the role of turbulence in flame speed and combustion efficiency.

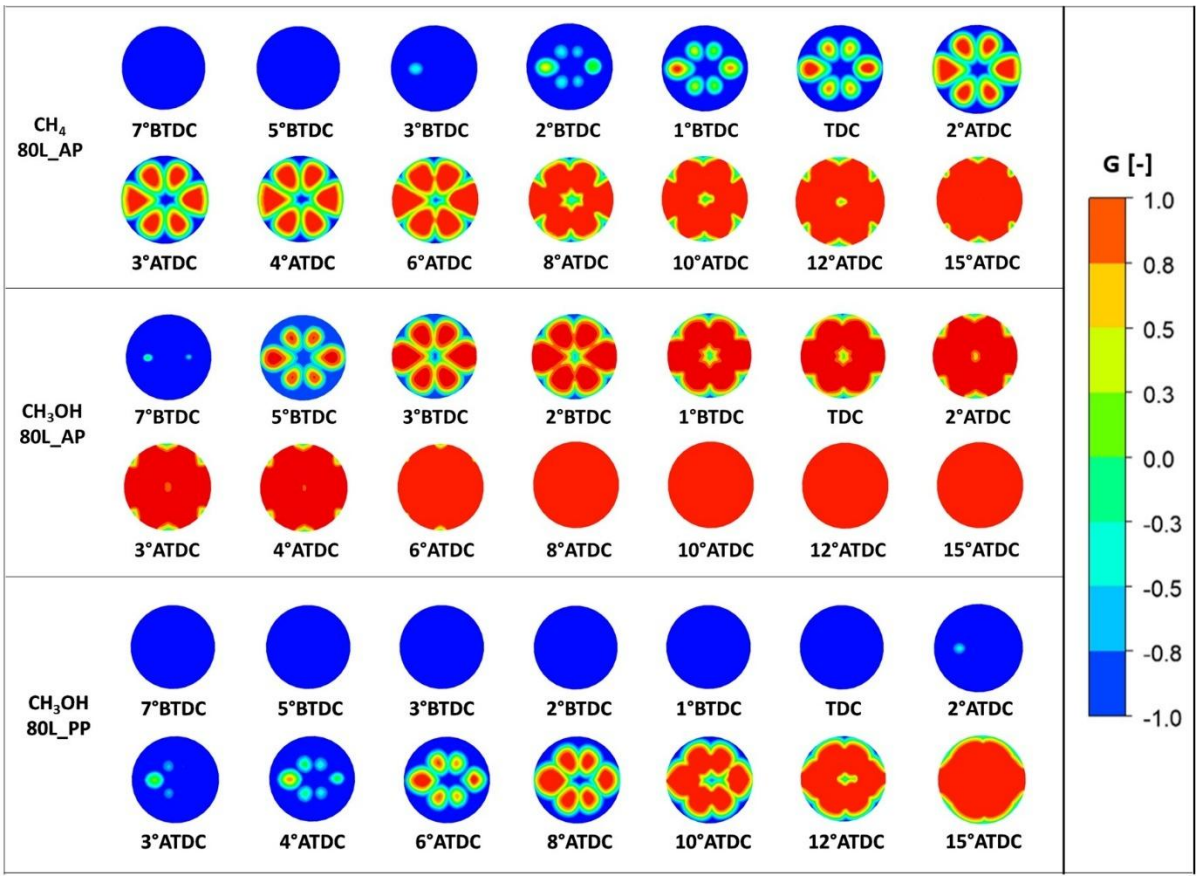

Figure 6.49: G-equation distributions at different CAs for the high load cases in a crosssection

Temperature fields in Figure 6.50, extracted from the same longitudinal section, confirm previous observations. Combustion initiates at the spark location and spreads through the PC, jets, and finally across the MC. Notable differences are observed in temperature magnitudes and distribution uniformity. In the active PC configurations, peak PC temperatures are significantly higher for both fuels. In fact, a ΔT of approximately 800 K between the PC and MC is observed in CH_3OH_80L_AP. In contrast, CH_3OH_80L_PP displays a more uniform temperature distribution at 30° ATDC, with both PC and MC reaching approximately 1600 K. This uniformity results from the less intense, leaner combustion in the passive configuration, which produces smoother and more stable thermal profiles compared to the hotter, more aggressive combustion in the active PC case.

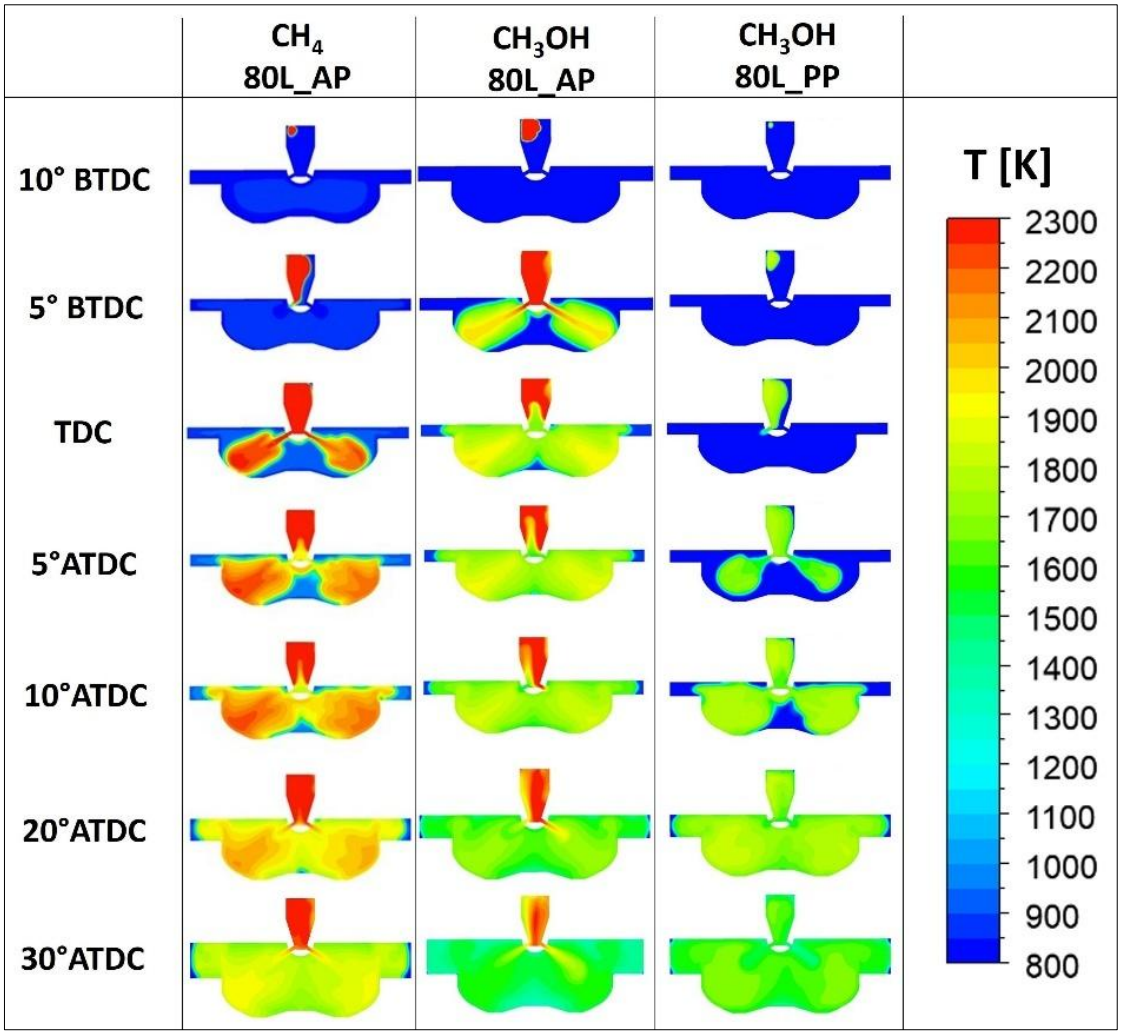

Figure 6.50: Temperature distributions at different CAs for the high load cases in a longitudinal section.

Figure 6.51a compares NO distributions for the two cases operating at 80% load, both employing an active PC configuration and using either methane or methanol as fuel. In both cases, the highest concentrations of NO are localized within the PC, where the temperature peaks occur. Generally, methane yields higher NO emissions due to its higher initial charge temperature and greater adiabatic flame temperature. A particularly pronounced NO accumulation is observed near the piston walls, corresponding to the regions where the turbulent jets from the PC impinge. Starting from approximately 10° ATDC, a substantial amount of NO begins to transfer from the PC to the MC, as elevated temperatures within the PC enhance NO formation, which subsequently diffuses into the MC during the expansion phase. Figure 6.51b presents, on a reduced scale, a direct comparison between the active and passive PC configurations, clearly illustrating the significant reduction in NO emissions associated with the passive setup. The absence of enriched combustion in the passive PC results in markedly lower temperatures, and consequently, in substantially reduced NO formation.

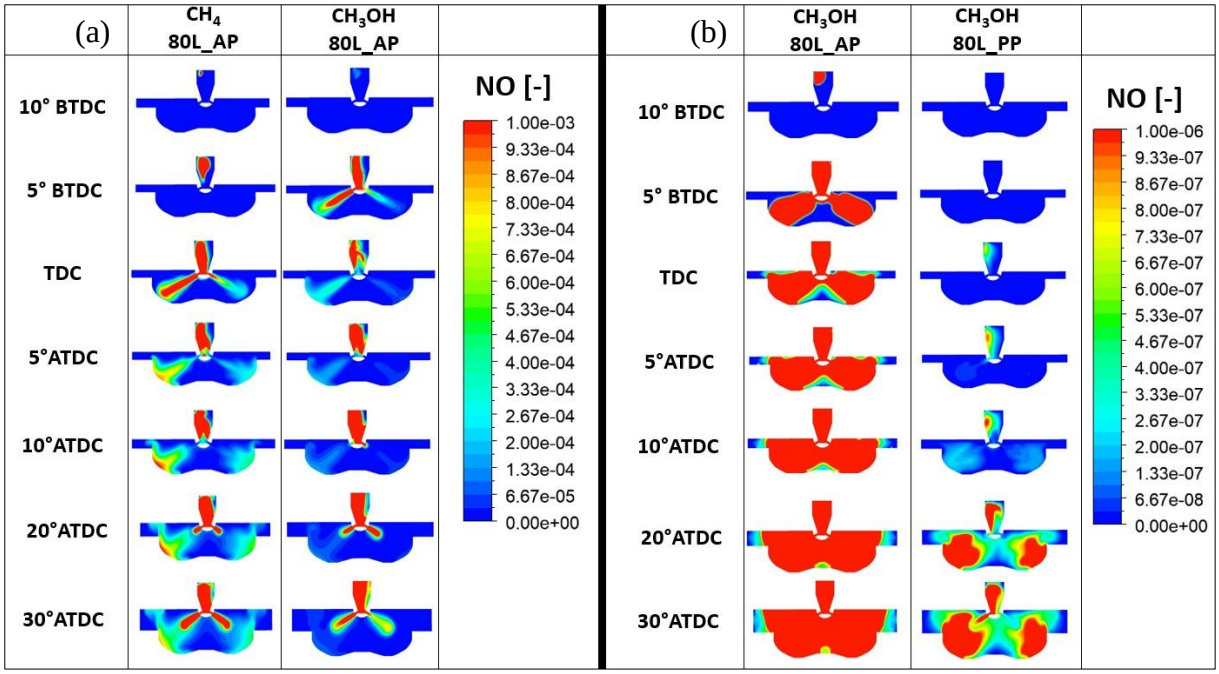

Figure 6.51: NO distributions at different CAs in a longitudinal section for the CH4_80L_AP and CH3OH_80L_AP cases (a), and for the CH3OH_80L_AP and CH3OH_80L_PP (b) cases

Low Load

Low-load operation at 20% engine capacity typically occurs during specific scenarios such as port maneuvering or prolonged idling. While less frequent in typical marine propulsion cycles, these conditions are still relevant for performance and emissions analysis. The trends in pressure and heat release at 20% load resemble those observed at 80% load, but with systematically lower peak values due to the reduced fuel mass, as illustrated in Figure 6.52a. Nevertheless, the energetic turbulent jets from the PC remain sufficient to ignite the lean mixture in the MC, enabling stable combustion for both methane and methanol across the active and passive PC configurations. It is worth noting that the difference in pressure rise rate between methanol and methane, prominent at high load, slightly decreases at low load due to the lower energy content of the mixture. Despite this, methanol combustion remains slightly faster than methane. The pressure rise rate in the CH_4_20L_AP case shows a 35% decrease compared to CH_4_80L_AP, while the reduction is more significant for methanol: 60% for CH_3OH_20L_AP and 70% for CH_3OH_20L_PP relative to their corresponding 80% load counterparts, as shown in Figure 6.52b. These variations in pressure rise correlate directly with the chemical ROHR and, consequently, with the temperature gradients that influence NO_x formation.

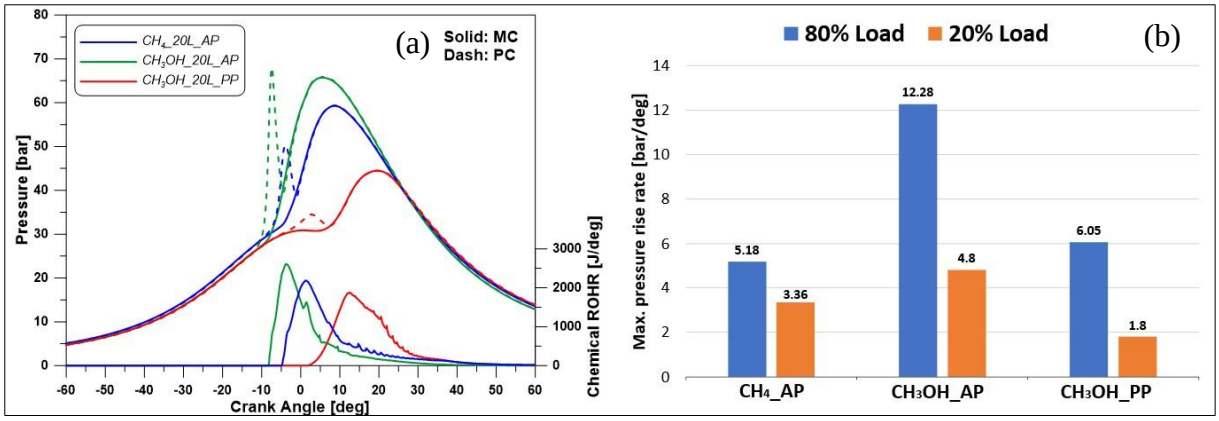

Figure 6.52:Pressure (MC and PC) and ROHR for the 20% load cases (a) and comparison of maximum pressure rise rate for the 80% and 20% load cases (b).

As shown in Figure 6.53, methane combustion leads to higher NO concentrations under low load due to more complete combustion and higher localized temperatures. In contrast, NO formation is substantially suppressed in the passive PC configuration, where combustion is less intense and the mixture in the PC is leaner. Using a scaled range [0; 1e-3], the presence of NO species becomes virtually negligible in the passive PC case due to the absence of the high-temperature zones necessary for thermal NO formation.

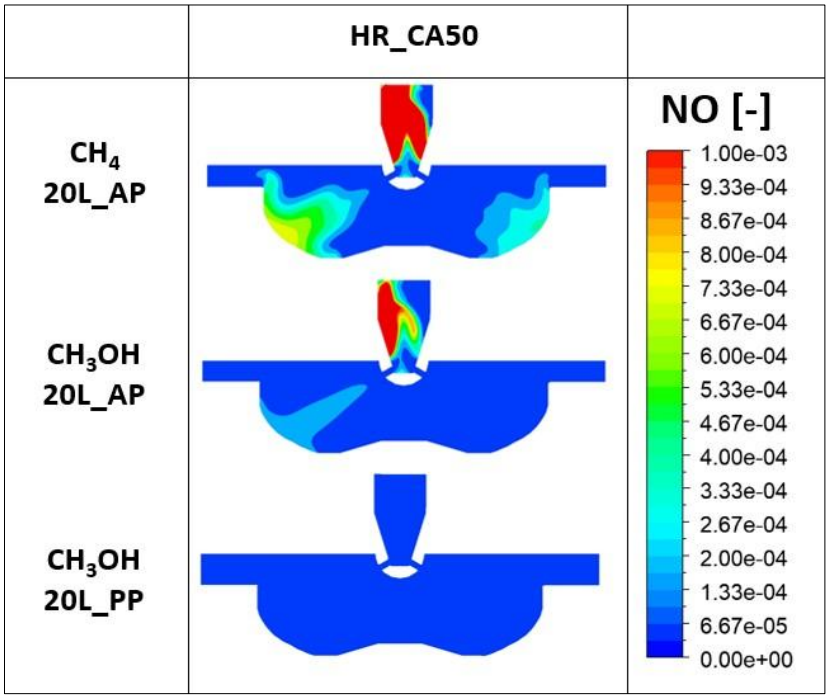

Figure 6.53: NO distributions at HR_CA50 for the low load cases in a longitudinal section

At 20% load, the lower combustion intensity leads to weaker jets, which can occasionally fail to initiate complete combustion in the MC. This results in partial oxidation and the formation of unburned species such as CO. Figure 6.54 shows the CO mass fraction distributions at EVO. In the CH_3OH_20L_PP case, elevated CO concentrations are observed along the cylinder liner

walls and to a lesser extent within the PC, indicating incomplete oxidation. In contrast, the CH_4_20L_AP configuration shows nearly zero CO emissions, confirming its superior capability to maintain effective combustion even at low load.

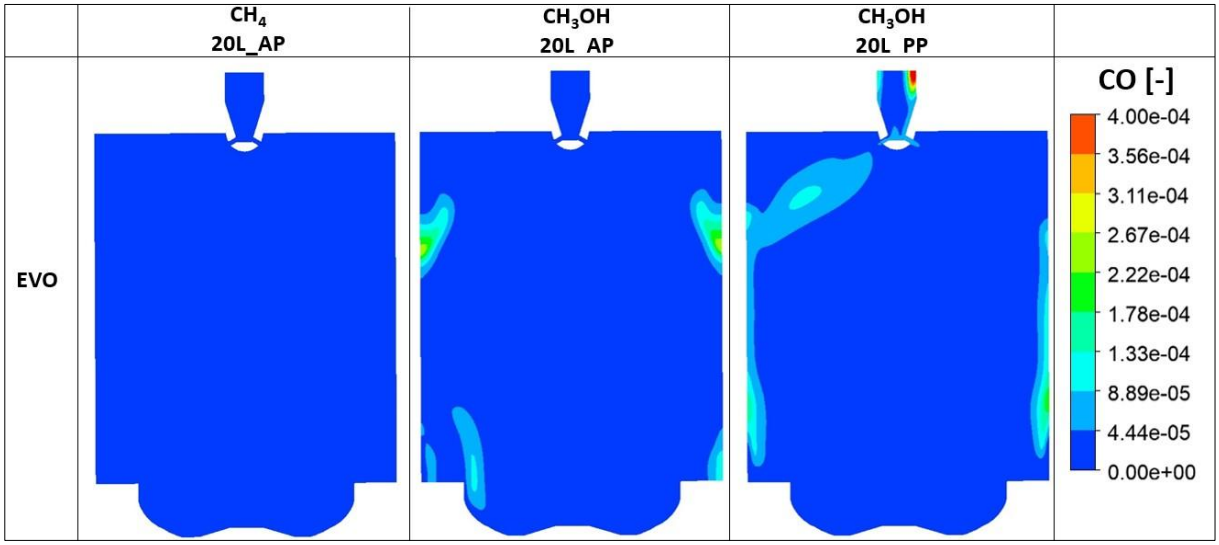

Figure 6.54: CO distributions at EVO for the low load cases in a longitudinal section.

Discussion

Table 6.15 reports the BMEP and carbon dioxide (CO_2) emissions obtained from the simulations. The objective of achieving the same BMEP at each load level was successfully met by adjusting the λ values inside the MC. However, a consistent increase in CO_2 emissions is observed for methanol across all load conditions when compared to methane. Specifically, methanol combustion leads to CO_2 increases of approximately 13%, 12%, and 8% at 100%, 80%, and 20% loads, respectively. This is primarily attributed to the lower LHV of methanol (approximately 20 MJ/kg), which necessitates a greater fuel mass input to attain the same power output, as also indicated in Table 6.15.

Table 6.15: BMEP and CO_2 emissions in g/kWh for all cases

	BMEP [bar]	**CO_2 [g/kWh]**
CH_4_100L_AP	18.45	483
CH_4_80L_AP	15.46	497
CH_4_20L_AP	5.78	622
CH_3OH_100L_AP	18.43	544
CH_3OH_80L_AP	15.46	556
CH_3OH_20L_AP	5.76	680
CH_3OH_80L_PP	15.48	557
CH_3OH_20L_PP	5.75	688

Despite methanol being operated at higher λ_{MC} values (i.e., leaner mixtures), the increased fuel mass required ultimately results in greater CO_2 emissions. Furthermore, the passive PC configuration slightly exacerbates CO_2 output due to its greater fuel demand to match the performance of the active PC setup. Consequently, CO_2 emissions in the passive configuration rise by 0.15% and 1.2% at 80% and 20% loads, respectively, relative to the active configuration. This underscores a limitation of the passive PC concept when methanol is used, as the increased fuel consumption offsets some of its environmental benefits.

Figure 6.55 displays the angular interval between the ST and the crank angle corresponding to 10% cumulative heat release (HR_CA10). Methanol exhibits a consistently shorter ST–HR_CA10 duration compared to methane across all active PC cases, with reductions of 39%, 37%, and 30% at 100%, 80%, and 20% load, respectively. This reflects the higher chemical reactivity of methanol, which leads to more rapid ignition and early flame development. As a result, the crank angle at which 50% of heat release occurs (HR_CA50) shifts closer to or even before TDC in methanol-fueled cases, in contrast to methane.

With the passive PC, the ST–HR_CA10 interval increases relative to the active configuration due to the leaner mixture in the PC, which delays ignition. Combustion duration, defined as the crank angle difference between HR_CA90 and HR_CA10, is also shorter for methanol, indicating faster combustion kinetics. Methanol cases show reductions in combustion duration of 21%, 29%, and 28% at 100%, 80%, and 20% loads, respectively, when compared to methane. The passive PC setup increases combustion duration by 23% at high load; however, this can be misleading, as the early combustion phase in the active configuration is considerably faster, as previously discussed. At low load, combustion durations are nearly identical between configurations, with only a 1% reduction observed for the passive case.

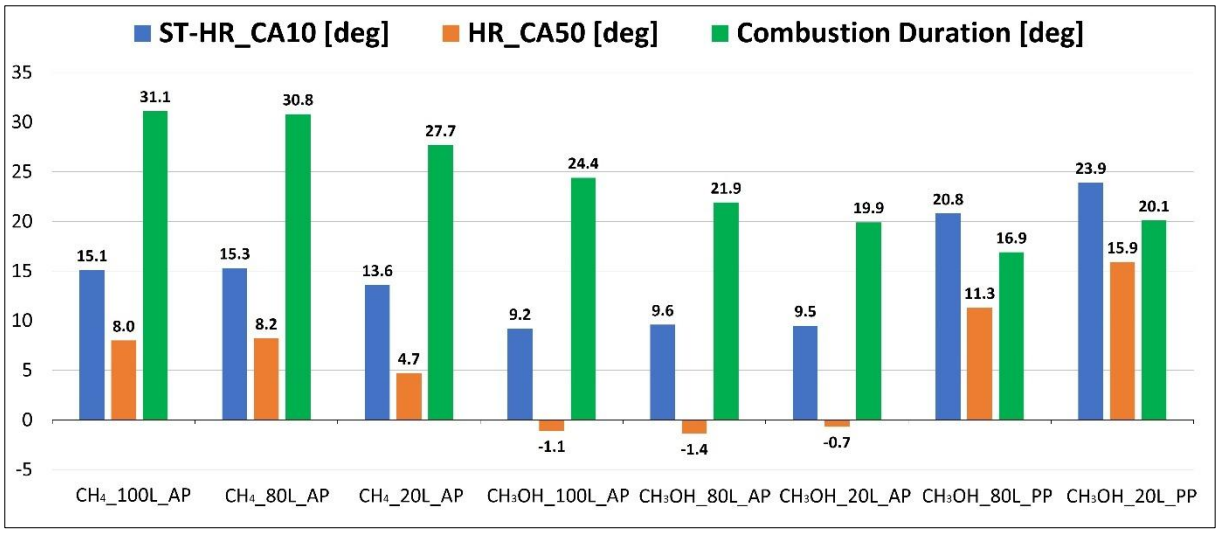

Figure 6.55: ST-HR_CA10, HR_CA50 and combustion duration for all cases

The average laminar flame speed (LFS) and TFS between HR_CA10 and HR_CA90 are illustrated in Figure 6.56. Methanol consistently exhibits a higher LFS than methane at all loads, attributable to its enhanced chemical reactivity. The same trend holds for the TFS, although the increase is less pronounced due to the combined effects of turbulence and reaction kinetics. The TFS-to-LFS ratio, which indicates the extent of flame acceleration due to turbulence, is especially high at low loads for both fuels. This is because lower thermal and chemical energy release makes the influence of turbulence more dominant in promoting flame front propagation. Transitioning from the active to passive PC configuration results in reduced LFS and TFS values. This is caused by the leaner, less reactive PC mixture and the absence of auxiliary fuel injection, which leads to lower jet momentum and weaker turbulence in the MC. These factors contribute to slower flame propagation and diminished combustion intensity.

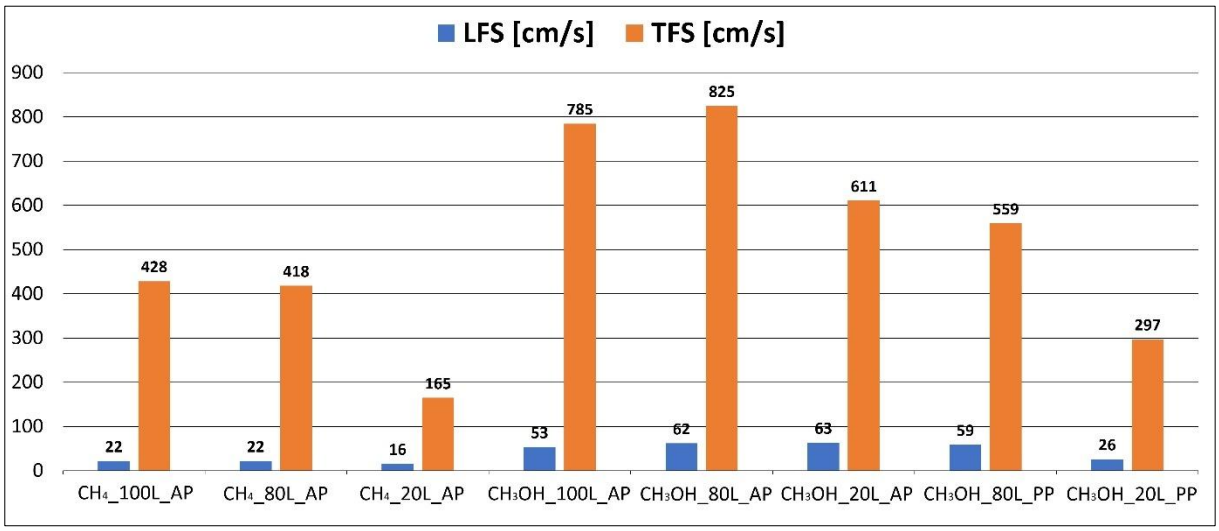

Figure 6.56: LFS and TFS mean values for all cases.

Figure 6.57 presents the thermal efficiency and the key emissions, NO_x and CO. Thermal efficiency, defined as the ratio of indicated work to the thermal energy released during combustion, is a critical metric for evaluating engine performance. Replacing methane with methanol yields noticeable gains in thermal efficiency across all load conditions, with improvements of approximately 8%, 8%, and 6% at 100%, 80%, and 20% loads, respectively. These gains are largely due to the leaner operating conditions achievable with methanol and its more complete combustion characteristics.

Switching to the passive PC configuration results in a decrease in thermal efficiency of 3.4% at 80% load and 4.6% at 20% load compared to the active configuration. This reduction is mainly due to suboptimal mixing and slower combustion in the passive layout.

Methanol combustion also produces significantly lower NO_x emissions than methane, owing to its lower adiabatic flame temperature and the reduced initial gas temperature at IVC. The latter results from methanol evaporation in the intake port, which absorbs heat and cools the charge, thereby lowering peak combustion temperatures, critical for NO_x formation. Reductions in NOx emissions with methanol reach approximately 64%, 66%, and 75% at 100%, 80%, and 20% loads, respectively, compared to methane. The passive PC configuration yields even more pronounced NOx reductions: 98% at 80% load and 99% at 20% load. These ultra-low levels are primarily due to the more homogeneous combustion and lower temperature fields, and they enable compliance with IMO Tier III regulations, which impose a stringent NO_x limit of around 3 g/kWh at low engine speeds.

Regarding CO emissions, methanol demonstrates lower emissions than methane at high loads, with reductions of 35% and 88% at 100% and 80% load, respectively. This improvement is due to leaner combustion and higher oxidation efficiency. However, at 20% load, CO emissions from methanol increase significantly compared to methane, due to incomplete combustion at low temperatures and under-lean conditions, which hinder CO oxidation.

When using the passive PC configuration, CO emissions increase by 72% at 80% load and 78% at 20% load relative to the active configuration. This is attributed to less effective mixing, reduced turbulence, and diminished oxidation efficiency, which collectively result in higher residual CO.

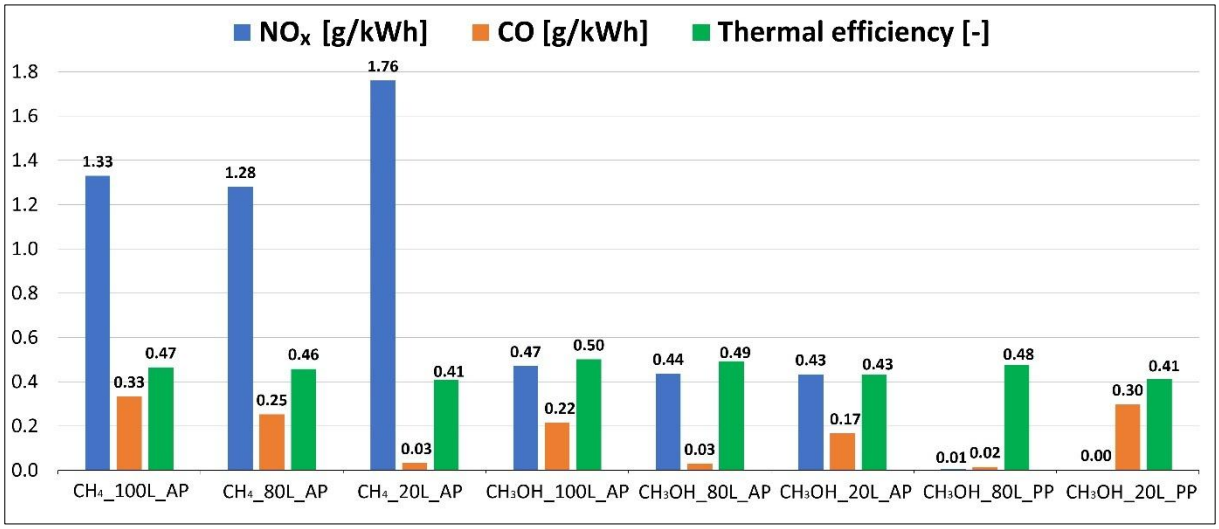

Figure 6.57: NO_x and CO emissions in g/kWh and thermal efficiency for all cases.

Chapter 7

7. PROPOSAL OF AN INNOVATIVE MARINE SYSTEM

In this chapter, a complete marine system designed to supply both propulsion and electrical loads is proposed. As observed in the previous chapters, the Rolls-Royce PC engine delivered rather promising results, especially considering its high efficiency (approaching 0.5). Moreover, its large size makes it particularly suitable for applications on large vessels. For these reasons, this engine (described in Chapter 6) was selected to equip the integrated marine system proposed in the following chapter, assuming it operates with its original fuel, namely methane. This system is an integrated combined heat and power (CHP) hybrid power generation system with an ICE, a steam methane reformer, a high temperature-proton exchange membrane fuel cell (HT-PEMFC) assisted with a battery energy storage system (BESS) for marine applications is presented. The addition of a steam methane reformer allows the on-board production of hydrogen, which is used to supply the FC. The system also includes on-board CO_2 capture after reforming. Two operating modes for FC integration are analyzed: direct connection to the ship's grid and independent operation for auxiliary loads, assisted by the BESS. The system, composed of four Rolls-Royce engines of 2430 kW each (total installed power of 9720 kW) and a 500 kW FC, is simulated using Thermoflex, a commercial lumped parameter code, and Simulink-Matlab model for the detailed description of HT-PEMFC and BESS. The results of this chapter are based on the work [202].

7.1 Background

As outlined earlier in the thesis, the maritime transport sector plays a significant role in global emissions, contributing approximately 3% of global CO_2 emissions. According to data from the IMO, emissions from maritime activities increased from 977 million tons in 2012 to 1076 million tons in 2018, mainly due to the sector's heavy reliance on fossil fuels for international shipping [1]. In response to regulatory pressure for decarbonization, electrification and hydrogen-based propulsion systems are emerging as viable solutions to achieve emission reduction targets [203]. In this context, fuel cells represent one of the most promising energy conversion technologies, thanks to their high energy efficiency and zero carbon emissions when powered by hydrogen [204]. Indeed, hydrogen fuel cells convert chemical energy directly into electricity, emitting only water vapor and offering significant environmental benefits [205].

Despite these advantages, the storage and long-distance transport of hydrogen remain challenging, often resulting in high operational costs [38]. A promising alternative to centralized supply is on-board hydrogen production, which helps overcome logistical constraints and supports local generation of hydrogen for fuel cell use. Additionally, using hydrogen to supply auxiliary systems through FCs can enhance the overall energy efficiency and sustainability of marine vessels. One of the most mature technologies for hydrogen generation is SMR, which relies on methane as a feedstock, although ammonia is also being investigated as a hydrogen carrier in some applications [206]. In SMR, methane (CH_4) reacts endothermically with steam (H_2O) at high temperatures (700–1000 °C), producing syngas, a mixture of hydrogen (H_2), carbon monoxide (CO), and carbon dioxide (CO_2) [207]. The water required for the SMR process can be supplied by a desalination system, which converts seawater into freshwater and is already widely used on ships, with typical production rates of about 30 tons of freshwater per day per vessel. The steam needed for reforming can then be generated simply by heating a portion of this treated water and feeding it directly to the steam reformer, without the need for additional dedicated treatment units [208]. To achieve high-purity hydrogen, a final purification step, such as Pressure Swing Adsorption (PSA), is applied to remove impurities including CO [209].

SMR-based systems have been widely explored as hydrogen sources for HT-PEMFCs, especially in stationary CHP applications like residential or industrial cogeneration. These fuel cells offer several advantages, including simplified water and heat management, tolerance to CO, and higher-quality thermal output, making them particularly suitable for CHP integration [210]. For instance, Jannelli et al. [211] conducted a comparative analysis of CHP systems using three types of fuel cells: a low-temperature PEM with a Nafion™ membrane, and two HT-PEMFCs with aromatic polyether membranes. Their results highlighted that HT-PEM systems reached an electrical efficiency of ~40% and a first-law efficiency of 79%. Similar results were obtained by Arsalis et al. [212], who reported an electrical efficiency of 41% in a micro-CHP configuration.

To maximize energy efficiency, integrating an HT-PEMFC with an SMR unit and ICE offers a promising solution. Although most existing studies focus on Solid Oxide Fuel Cell (SOFC) integrations [213-215], some efforts have explored the coupling of PEMFCs with reformers and ICEs running on methanol [216] or ammonia/hydrogen blends [217]. However, these applications have been primarily studied in stationary contexts, and research in non-stationary or maritime scenarios remains limited. In the marine sector, current research has largely

concentrated on standalone PEMFC-powered ships [218], leaving a gap in the exploration of hybrid and integrated propulsion architectures.

To fill this gap, the present section of the thesis investigates the integration of an HT-PEMFC and a SMR system onboard a marine vessel, working in conjunction with an ICE optimized for maritime operation. In this proposed configuration, hydrogen produced via reforming is used exclusively to power the HT-PEMFC, while the ICE runs on natural gas. The system also incorporates on-board CO_2 capture, minimizing the environmental footprint. Additionally, the integration of a battery energy storage system is proposed to stabilize the operating point of the fuel cell and further enhance system performance.

7.2 System Description and Methodology

A CHP hybrid system is proposed, consisting of a HT-PEMFC and the PC ICE described in the previous chapter (Rolls-Royce engine). The system is designed for marine applications and is powered by hydrogen produced via SMR. As a reminder, the ICE is a Rolls-Royce C26:33 L9PG, a nine-cylinder marine engine fueled with natural gas, delivering a maximum continuous rating of 2430 kW at 1000 rpm. The full propulsion system includes four engines, for a total installed power of 9720 kW.

In the hybrid configuration, exhaust gases from the ICE at about 495 °C provide thermal energy to a Heat Recovery Steam Generator (HRSG). The generated steam is then utilized in the endothermic reactions of the SMR, producing syngas. The reformer is modeled as a Fired Tubular Reformer. The key reactions occurring within the reformer are:

$$CH_4 + H_2O \rightarrow CO + 3H_2 \qquad \Delta H_0 = +206\ kJ/mol \tag{7.1}$$

$$CH_4 + 2H_2O \rightarrow CO_2 + 4H_2 \qquad \Delta H_0 = +165\ kJ/mol \tag{7.2}$$

The steam/natural gas mixture is preheated to 850 °C using combustion products from an integrated combustor, which is itself fueled with a mixture of pure hydrogen and syngas exiting the Pressure Swing Adsorption (PSA) purification unit. This configuration is a well-established strategy to ensure energy self-sufficiency of the reforming process, eliminating the need for external fuels such as natural gas, thereby enhancing overall system efficiency.

The hydrogen extracted from syngas is directly fed to the fuel cell, thus bypassing the need for hydrogen storage. This setup enables the production of additional electricity and recoverable heat, the latter primarily sourced from the FC cooling system. A portion of the generated hydrogen is also recirculated to the reformer burner, maintaining the thermal self-sufficiency of the system. To further reduce the environmental impact, a CCS is installed downstream of

the reformer. This integrated hybrid configuration achieves a significantly lower environmental footprint, improving competitiveness compared to conventional marine thermal power systems. Under normal navigation conditions, corresponding to 80% engine load, the overall plant delivers a net electrical output of 1855 kWe, with a global electrical efficiency of 39.9%, accounting for auxiliary power losses. Additionally, it provides a thermal output of 1318 kWt, including the heat recovered from the FC.

Table 7.1 and Table 7.2 summarize the technical specifications and operating conditions of the fuel cell stack used in the analysis. The HT-PEMFC considered has a nominal power of 500 kW, composed of 145 modules connected in parallel, each capable of delivering 3.465 kW under nominal conditions. The operating temperature is set at 165 °C, and both anode and cathode are supplied with reactants at 1.5 bar.

Table 7.1:HT-PEMFC technical data

FC model [rpm]	H3-500 SERENERGY
Fuel	Hydrogen
Efficiency (LHV)	52%
Power [kW]	500
Number of modules	145
Module power [kW]	3.456

Table 7.2: HT-PEMFC operating conditions

Temperature [°C]	165
Pressure [bar]	1.5
H_2 mass flow rate [kg/s]	0.008
Open circuit voltage/single module [V]	102
Nominal voltage [V]	77
Nominal current [A]	45

Figure 7.1 shows the characteristic curves for a single fuel cell module, representing the voltage-current and power-current relationships. At an operating current of 45 A, the module delivers a voltage of 77 V, corresponding to the rated power output of 3.465 kW. At this point, the cell has passed the activation loss region, and ohmic losses dominate. The relatively high voltage ensures good electrical efficiency while minimizing electrochemical stress, making this an optimal point for stable and durable operation.

Although maximum power is reached around 68 A (4.76 kW), the selected operating point of 45 A offers a balanced trade-off between efficiency and reliability, avoiding high-stress regions where degradation accelerates. This current also ensures favorable thermal balance and long-term system stability, making it ideal for continuous operation.

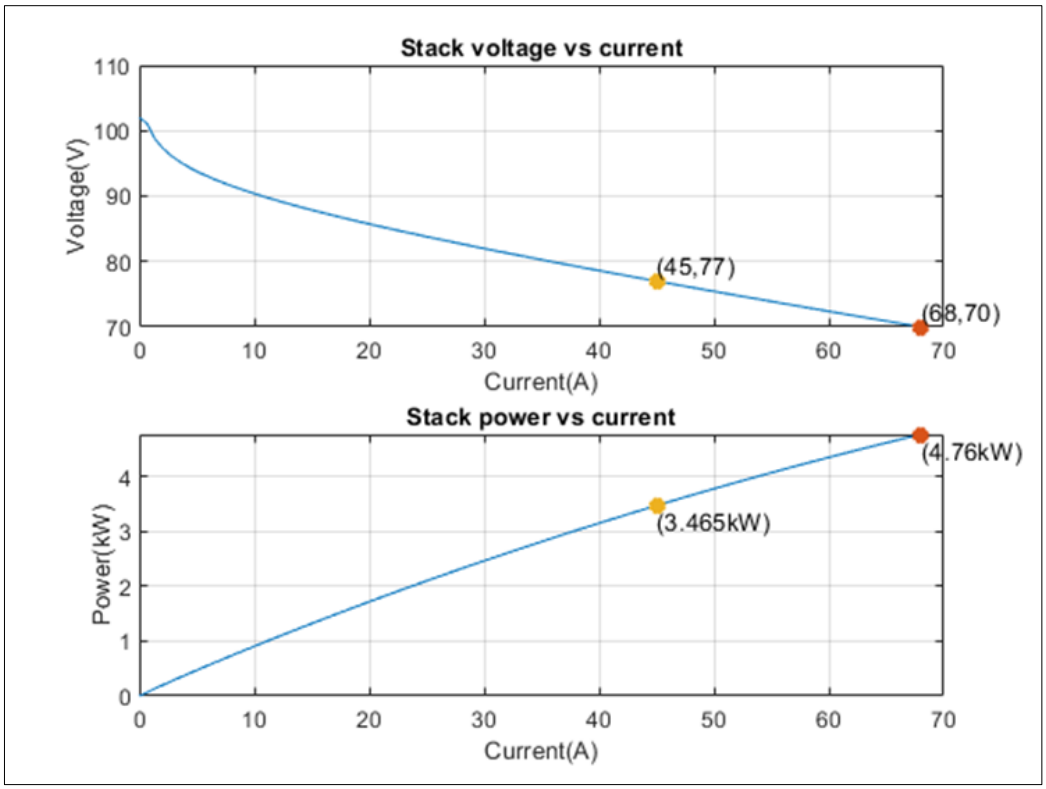

Figure 7.1: Single cell operating point

Two hybrid integration configurations were evaluated and are shown in Figure 7.2 and Figure 7.3:

- In Figure 7.2, the ICE and HT-PEMFC are both directly connected to the on-board electrical grid. The generated power is supplied to ship systems without intermediate storage.
- In Figure 7.3, the HT-PEMFC supplies only auxiliary loads, while the ICE handles propulsion. In this setup, the FC is coupled with a BESS, which absorbs load fluctuations and allows the FC to operate at a constant, optimized setpoint.

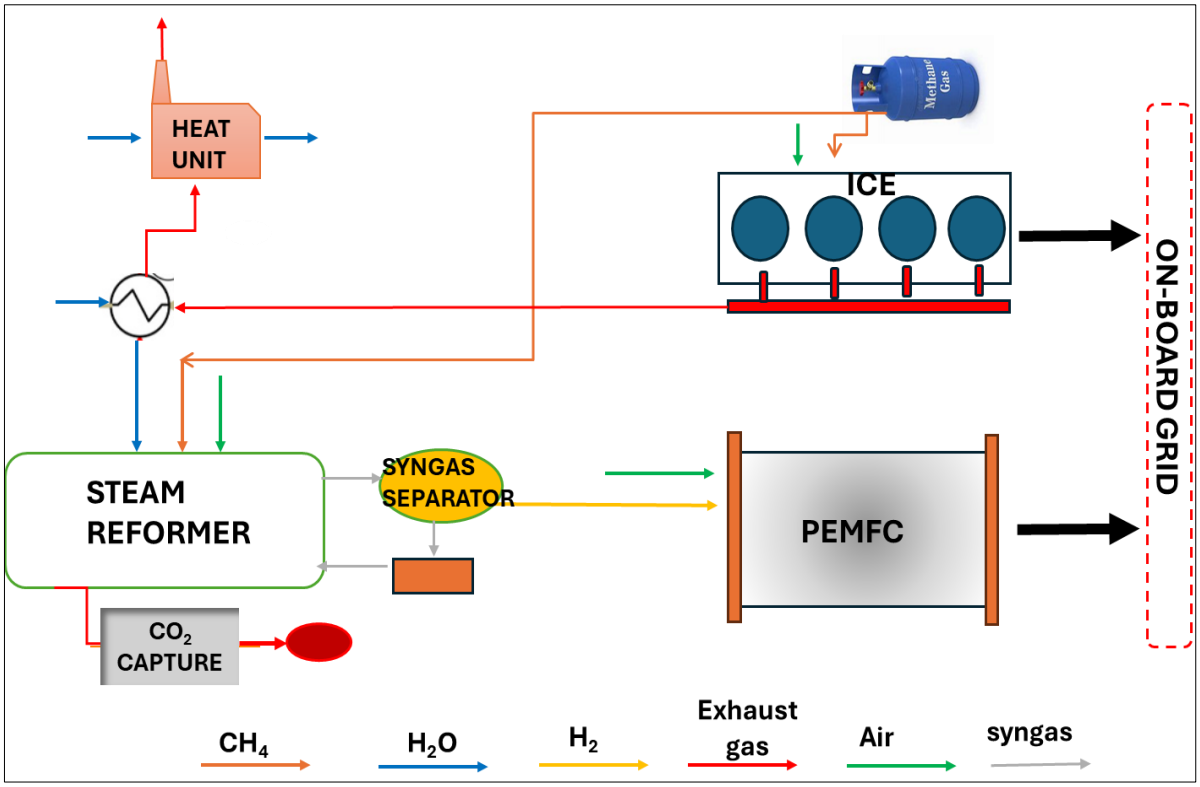

Figure 7.2: Schematic of the proposed PEM-SMR–ICE hybrid system

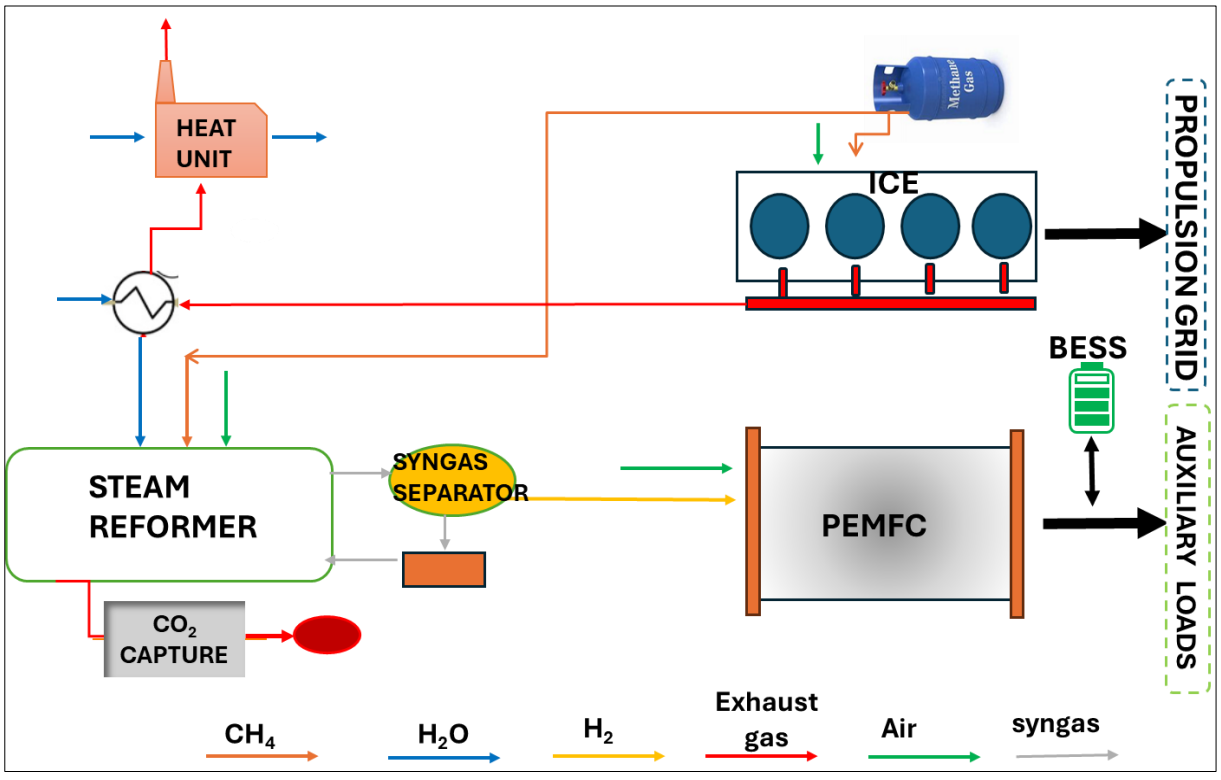

Figure 7.3: Schematic of the proposed PEM–SMR–ICE–BESS hybrid system

In both cases, the HT-PEMFC operates at fixed load, while the battery (only in the second configuration) compensates for variations in demand. This approach simplifies FC control strategy and maximizes efficiency. Operating the fuel cell dynamically would require more

complex control algorithms, as reported in [219]. The battery system, used to support and decouple fuel cell operation, is sized based on technical specifications summarized in Table 7.3 [220].

Table 7.3: Battery cell specifications

Rated voltage [V]	3.6
Maximum voltage [V]	4.2
Internal resistance [mΩ]	17
Rated capacity [V]	3
Cell mass [kg]	0.046

7.2.1 ICE, SMR and CCS Model

The thermal section of the hybrid plant, comprising the ICE, SMR, and CCS, is modeled using the Thermoflex® software [221], a lumped-parameter thermodynamic modeling tool based on mass and energy balance calculations.

Figure 7.4 illustrates the complete system layout, detailing all thermal components. The system is centered around the natural gas-fueled ICE. The exhaust gases, leaving the engine at 495 °C (Point 6), are utilized to produce superheated steam via a HRSG. This steam is then directed to both the methane reformer (Point 5) and the CO_2 capture unit (Point 8). Within the HRSG, water flows counter-currently to the exhaust gases at a pressure slightly above 20 bar, ensuring the generation of superheated steam at the conditions required for SMR operation.

A steam stream of 0.2926 kg/s (Point 2) is extracted downstream of the evaporator and distributed between the CO_2 capture process (Point 8) and the process steam generation unit (Point 1). The remaining saturated steam (0.0568 kg/s) is routed to the superheater, exiting at 468 °C (Point 5).

Natural gas for reforming is compressed to 21 bar, slightly above the operating pressure of the reformer (~20 bar), to overcome pressure drops in piping and downstream components. After compression, the natural gas is preheated in Heat Exchanger HX1 to 630 °C (Point 14), followed by a desulfurization stage (Point 13) to protect the reformer's nickel catalyst from irreversible poisoning and to suppress solid carbon formation.

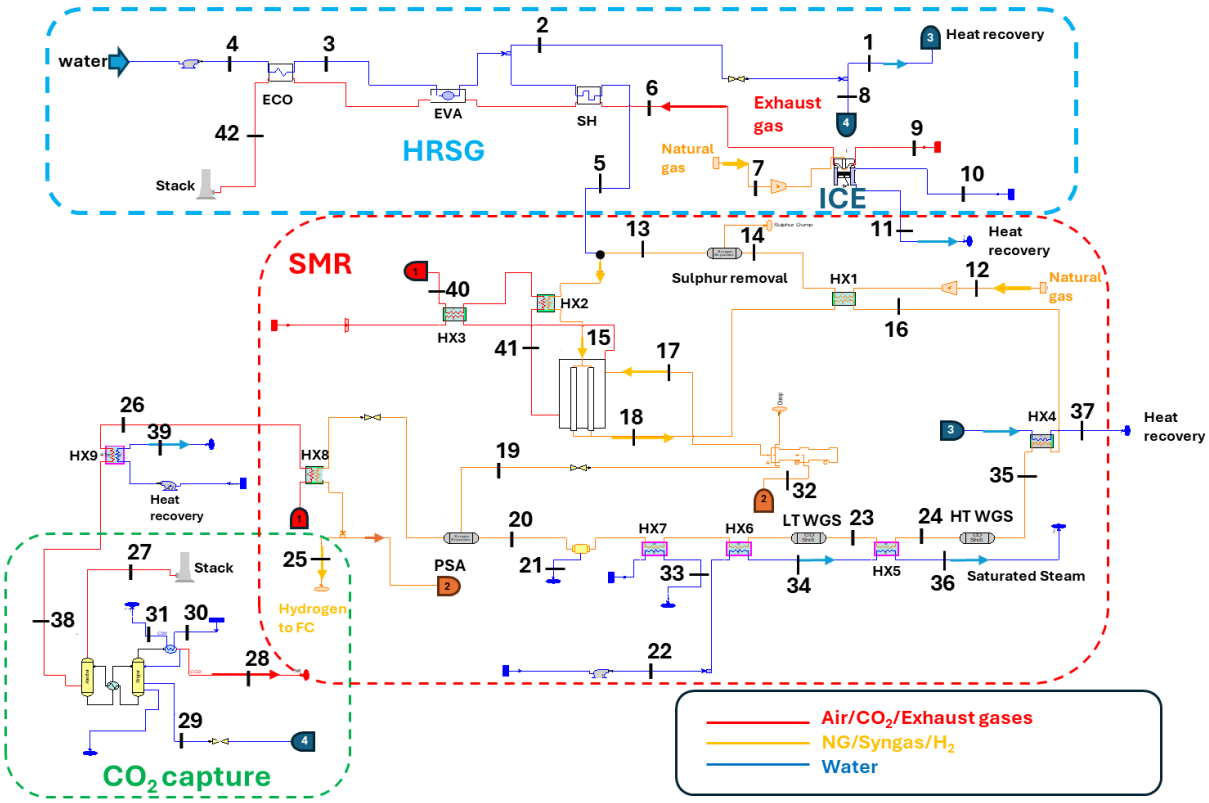

Figure 7.4: Thermal system diagram

The desulfurized gas is then mixed with superheated steam (S/C ratio = 2.5) and further heated in HX2 using the SMR combustor flue gases (Point 15), reaching 850 °C at the reformer inlet. Inside the reformer, methane reacts endothermically with steam, producing syngas. The heat required for this highly endothermic process is supplied by an integrated burner fueled by a mixture of excess pure hydrogen (Point 32) and dehydrogenated syngas (Point 19), at 950 °C (Point 41), with a lower heating value of 5380 kJ/kg.

The reformer outlet produces 0.08 kg/s of crude syngas at 650 °C (Point 18), whose volumetric composition is reported in Table 5. The syngas is cooled via HX1 and HX4 (Point 35), with heat recovered for auxiliary uses (Point 37), then passed through a two-stage Water-Gas Shift (WGS) reactor to convert CO to H_2. The high-temperature WGS (HT-WGS) stage at 312 °C achieves a 96% CO conversion (Point 24), while the low-temperature WGS (LT-WGS) stage at 200 °C increases conversion efficiency to 99%. A heat exchanger between the stages transfers heat from the syngas to saturated water (Point 36).

The WGS outlet composition is reported in Table 6. After cooling to 50 °C in HX6 and HX7, the syngas is dehydrated in a condensate separator and purified in a PSA unit (Point 20). The PSA system achieves hydrogen purity >99.9%, delivering two output streams:

A dehydrogenated syngas stream (Point 19) with a lower heating value of 5141 kJ/kg, directed to the reformer burner.

A pure hydrogen stream (0.0081 kg/s), split between the HT-PEMFC stack (throttled to 1.5 bar and preheated to 165 °C, Point 25) and the reformer burner (Point 32).

The SMR produces 0.153 kg/s of flue gas at 950 °C (Point 41), which is utilized for heat recovery before reaching the CCS system.

The CCS, simulated in Thermoflex (Figure 7.5), adopts a chemical absorption process using amine-based solvents (e.g., MEA). The target stream is the reformer flue gas, rich in CO_2 due to syngas and hydrogen combustion. The system cools flue gases to ~30 °C before they enter an absorber, where CO_2 is chemically bound by the solvent. The CO_2-rich solvent is then sent to a stripper (regeneration column), where steam decomposes the compound and releases CO_2, regenerating the solvent. The regenerated solvent is recirculated, while the CO_2-rich gas is cooled in a condenser and separated from condensate in a knockout drum. The purified CO_2 is finally compressed to 151 bar, reaching supercritical conditions suitable for transportation.

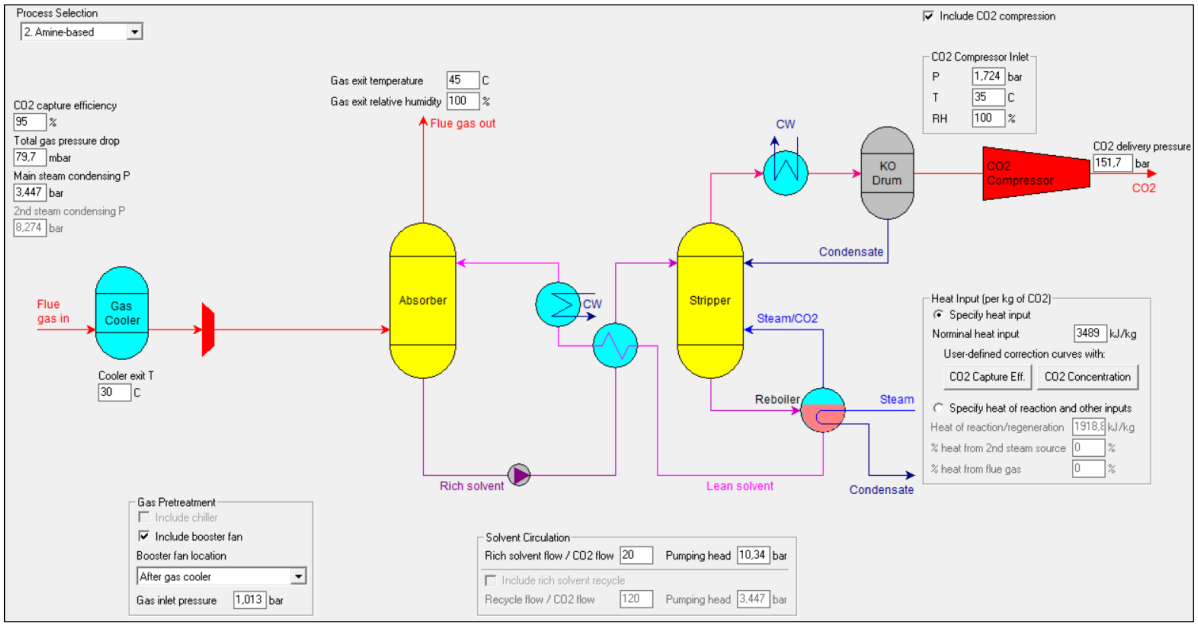

Figure 7.5: Schematics of the CCS

Simulation results show that the system captures 4.975 tonnes/day of CO_2 with 99.9% purity. Amine losses are limited to 0.002 tonnes/day. The system reduces CO_2 emissions by 95%, from 5.235 tonnes/day (no capture) to 0.2618 tonnes/day. The CCS process consumes 22.36 kW of electricity (of which 18.92 kW is for CO_2 compression) and requires 200.8 kW of thermal energy (3489 kJ/kgCO_2), primarily for solvent regeneration, supplied by 0.088 kg/s of steam at 165 °C and 2.3 bar. A detailed summary of all stream data corresponding to the points in Figure 7.4 is provided in Table 7.4.

Table 7.4: Thermodynamic properties of system state points

Steam Point	**1**	**2**	**3**	**4**	**5**	**6**
Temperature [°C]	212.6	214.3	209.8	16.42	468	495
Pressure [bar]	20	20.79	20.79	21.2	20.38	1.023
Mass flow rate [kg/s]	0.2043	0.2926	0.3529	0.3529	0.0568	2.385
Enthalpy [kJ/kg]	2797.8	2797.8	894.8	70.64	3396	522
Steam Point	**7**	**8**	**9**	**10**	**11**	**12**
Temperature [°C]	25	212.6	15	15	90	25
Pressure [bar]	1	20	1.013	1.013	0.92	3
Mass flow rate [kg/s]	0.0556	0.0883	2.306	1.975	1.975	0.0232
Enthalpy [kJ/kg]	46286	2797.8	-10.13	63	377	46514
Steam Point	**13**	**14**	**15**	**16**	**17**	**18**
Temperature [°C]	630	630	850	492	41	650
Pressure [bar]	20.38	20.59	19.98	19.8	1.724	19.98
Mass flow rate [kg/s]	0.0232	0.0232	0.08	0.08	0.0527	0.08
Enthalpy [kJ/kg]	48378	48378	15530	17129	5381	17591
Steam Point	**19**	**20**	**21**	**22**	**23**	**24**
Temperature [°C]	56	50	50.32	26.2	200	311.7
Pressure [bar]	17.74	18.63	3	20.14	18.88	19.04
Mass flow rate [kg/s]	0.0526	0.0607	0.0193	0.0606	0.08	0.08
Enthalpy [kJ/kg]	5141	20559	210.8	111.6	16027	16335
Steam Point	**25**	**26**	**27**	**28**	**29**	**30**
Temperature [°C]	165	215.3	45	35	165.3	15
Pressure [bar]	2.478	1.022	1.013	152	2.3	2
Mass flow rate [kg/s]	0.008	0.153	0.0867	0.0576	0.0883	5.98
Enthalpy [kJ/kg]	122083	205.2	21.6	-234	2798	63.13
Steam Point	**31**	**32**	**33**	**34**	**35**	**36**
Temperature [°C]	25	165	90	187	311.7	212.4
Pressure [bar]	0.62	2.478	2.91	20.04	19.43	20
Mass flow rate [kg/s]	5.98	0.0001	0.1309	0.0606	0.08	0.0606
Enthalpy [kJ/kg]	105	122083	377	794	16624	1197
Steam Point	**37**	**38**	**39**	**40**	**41**	**42**

Temperature [°C]	286	50	90	290	950	122
Pressure [bar]	19.61	1.013	3	1.043	1.085	1.013
Mass flow rate [kg/s]	0.2043	0.153	0.115	0.153	0.153	2.385
Enthalpy [kJ/kg]	3095	-33	377	289	1117	104

7.2.2 HT-PEMFC Model

The integration of fuel cells into DC or AC microgrids typically requires regulation of the electrical power supplied to the load. This necessity often leads to the development of complex control algorithms and regulation strategies, which may introduce inefficiencies into the overall energy system. One of the main limitations of fuel cells is their inherently slow dynamic response, which restricts their ability to accommodate rapid fluctuations in electrical demand. As a result, nearly all fuel cell systems are implemented in a hybrid configuration, combining the fuel cell with a fast-response energy storage system. Among the available technologies, electrochemical batteries currently offer the best trade-off in terms of energy density, power delivery capability, integration flexibility, and control simplicity. In this work, a BESS has been selected to complement the HT-PEMFC.

The schematic diagram of the system, developed in the Simulink environment, is presented in Figure 7.6.

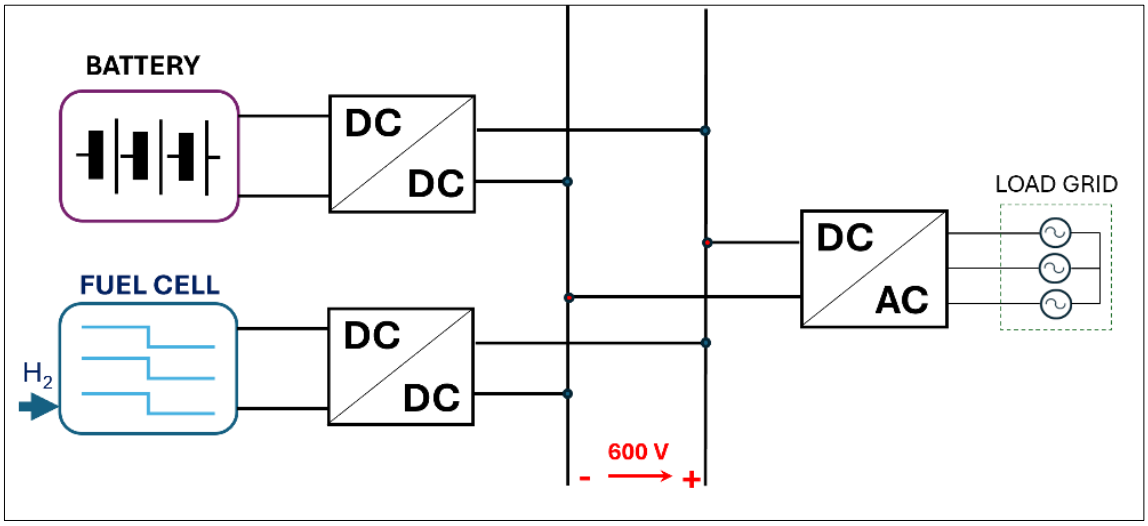

Figure 7.6: Schematic of the considered plant

The BESS is connected in parallel with the fuel cell to the DC bus of the microgrid. From this bus, power can be delivered either directly to DC loads or, via a DC–AC inverter, to the AC section of the microgrid, which also includes the electric generator associated with the ICE. To enable the inverter to supply a standard 400 V three-phase AC output, the DC bus voltage must

be maintained at a stable 600 V. Consequently, both the fuel cell and the battery system are interfaced with the DC bus through dedicated DC–DC Boost Converters. Each converter is equipped with a double-loop Proportional–Integral controller to regulate the output voltage and current. The Simulink simulation framework is shown in Figure 7.7. Thermal parameters derived from the Thermoflex simulations are imported into a Simulink block. The dynamic simulation is executed in continuous mode with a maximum time step of 1 ms to accurately capture fast transients.

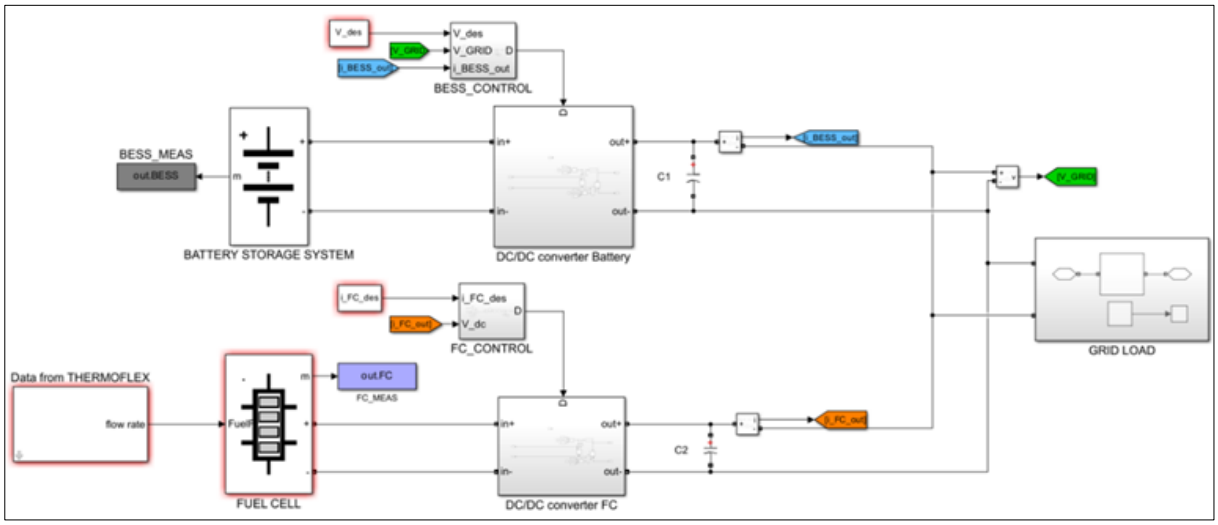

Figure 7.7: Simulink layout

The hydrogen-air fuel cell stack model used in this work is based on the detailed HT-PEMFC model implemented in MATLAB/Simulink as proposed in [222]. The three main electrochemical reactions in the cell are:

1. Anode (oxidation)

   $2H_2 \rightarrow 4H^+ + 4e^-$

2. Cathode (reduction)

   $O_2 + 4H^+ + 4e^- \rightarrow 2H_2O$

3. Overall Cell reaction

   $2H_2 + O_2 \rightarrow 2H_2O$

The fuel input to the HT-PEMFC is the hydrogen flow rate obtained from the Thermoflex thermal model. The model computes the fuel cell voltage according to:

$$V_{fc} = E_{oc} - V_{drop} - V_a \tag{7.3}$$

where:

- E_{OC} is the open circuit voltage of the fuel cell and depends on by the working temperature of the cell, the hydrogen and air pressures and many other costants;
- V_{drop} is the drop voltage due to the internal resistance of the HT-PEMFC;
- V_a is the activation voltage drop which influences also the dynamic of the HT-PEMFC;

The model also considers the effect of operating parameters—including pressure, temperature, and reactant flow rates—on the electrochemical behavior. The exchange current density is expressed by:

$$i_0 = \frac{n \cdot F \cdot k_{Pl} \cdot (p_{H2} + p_{O2})}{R \cdot h} \cdot exp\left(\frac{-\Delta G}{R \cdot T_{FC}}\right) \tag{7.4}$$

Where F is the Faraday constant k_{Pl} is Planck's constant, p_{H2} and p_{O2} are the partial pressures of hydrogen and oxygen, ΔG is the Gibbs free energy change and T_{FC} is the cell temperature.
The open-circuit voltage is estimated as:

$$E_{OC} = K_c \cdot E_n \tag{7.5}$$

Where K_c is the nominal cell voltage coefficient, and E_n is the Nerst potential, calculated (for T>373 K) as:

$$E_n = 1.229 + (T - 298) \cdot \frac{-44.43}{n \cdot F} + \left(\frac{R \cdot T}{n \cdot F}\right) \cdot ln\left(\frac{p_{H2} \cdot p_{o2}^{1/2}}{p_{H2}}\right) \tag{7.6}$$

The fuel cell system analyzed in this work has a rated power of 500 kW, representing approximately 5% of the total output of 9720 kW from the four ICE units. This power level is consistent with the typical electrical demand of on-board auxiliary loads [223].
The HT-PEMFC is composed of 145 H3-5000 modules [224], each characterized by the parameters listed in Table 7.1 and Table 7.2. Figure 7.8 and Figure 7.9 present the voltage–current characteristics of the fuel cell module at varying operating temperatures (with fixed fuel pressure of 1.5 bar) and at varying fuel pressures (at constant temperature of 165 °C), respectively. The observed trends are in agreement with data reported in the literature [225].

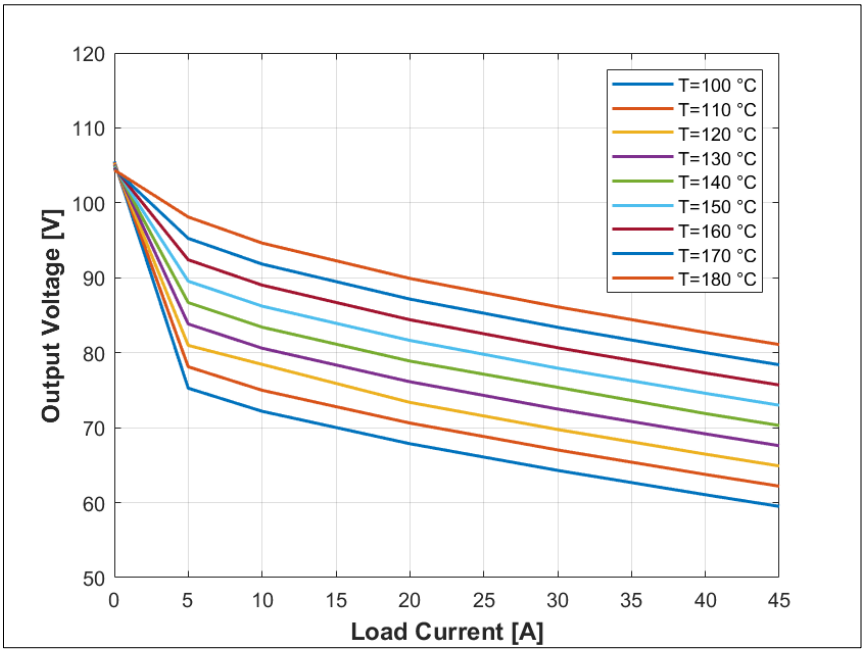

Figure 7.8: HT-PEMFC voltage-current characteristics by varying operating temperature at p=1.5 bar.

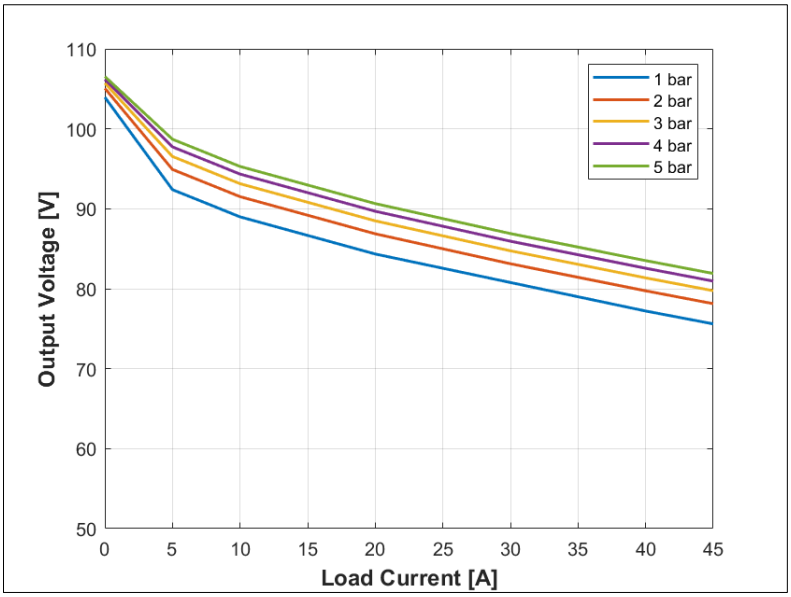

Figure 7.9: HT-PEMFC voltage-current characteristics by varying operating temperature at p=165 °C.

7.2.3 Load Model and BESS Weight Determination

Considering the scheme presented in Figure 7.3, an additional analysis was performed to evaluate the independent operation of the HT-PEMFC for supplying on-board auxiliary loads. In this configuration, a BESS is required to manage the power imbalance, i.e., the surplus or deficit, between the fluctuating load demand and the constant power supplied by the fuel cell. To realistically simulate the variable nature of electrical load, a Gaussian distribution of

electrical power demand is assumed, following the approach in [226]. Two operational scenarios are considered:

1. Continuous operation scenario, where the mean of the Gaussian distribution is equal to the rated power output of the fuel cell.
2. Harbor-mode scenario, which simulates the vessel being docked in a port. In this case, the battery is assumed to be recharged during the cruise phase, allowing the fuel cell to operate flexibly during stationary periods.

For both scenarios, the BESS sizing is formulated as an optimization problem aimed at minimizing the overall weight of the battery pack:

$$\min(BESS\ cell\ weight) \tag{7.7}$$

This optimization is subject to the following set of inequality constraints:

$$\begin{cases} \min(SOC) \geq 0.2 \\ \max\,(I_d) \leq 3C \\ \max\,(I_c) \leq 1C \\ \max(V_{batt}) \leq 420\ V \end{cases} \tag{7.8}$$

Where:

- SOC is the state of charge of the battery,
- I_d and I_c represent the discharge and charge currents, respectively,
- V_{batt} is the total output voltage of the battery pack.

These limits are imposed to preserve battery health by avoiding deep discharges, reducing thermal stress, and minimizing aging caused by high current rates. In particular, the restriction on the minimum SOC and current limits ensures higher cycle life and improved thermal management. The optimization problem is solved using a brute-force search algorithm, given the presence of integer decision variables, such as the number of cells in series and parallel configurations. A simplified electrochemical model of the BESS is adopted for simulation purposes, based on the methodology proposed in [227].

7.3 Results and Discussion

In order to evaluate the plant's overall performance, key performance indicators were employed.

- Efficiency of the fuel cell and methane reformer system, which considers the ratio between the electrical power generated by the fuel cell (P_{el_FC}) and the flow rate of natural gas to be reformed multiplied by its calorific value:

$$\eta_{FC/SMR} = \frac{P_{el\_FC}}{\dot{m}_{SMR} \cdot LHV_{NG}} \tag{7.9}$$

- Efficiency of the natural gas to hydrogen conversion system, considering the total flow rate of hydrogen produced ($\dot{m}_{H_2}$) and that of natural gas entering the SMR ($\dot{m}_{SMR}$):

$$\varepsilon_{FC/SMR} = \frac{\dot{m}_{H_2} \cdot LHV_{H_2}}{\dot{m}_{SMR} \cdot LHV_{NG}} \tag{7.10}$$

- Fuel utilization index, used to estimate the performance of a cogeneration plant:

$$I_U = \frac{P_{el\_TOT} + \dot{Q}_U + \dot{Q}_{FC}}{\dot{m}_{TOT\_NG} \cdot LHV_{NG}} \tag{7.11}$$

- ICE efficiency:

$$\eta_{ICE} = \frac{P_{el\_ICE}}{\dot{m}_{ICE} \cdot LHV_{NG}} \tag{7.12}$$

- HT-PEMFC efficiency:

$$\eta_{FC} = \frac{P_{el\_FC}}{\dot{m}_{H_2} \cdot LHV_{H_2}} \tag{7.13}$$

- Overall electrical efficiency, defined as the ratio between the total electrical power generated by the ICE/FC system ($P_{el\_ICE} + P_{el\_FC}$) and the natural gas flow rate multiplied by its lower calorific value, or:

$$\eta_{gl} = \frac{P_{el\_ICE} + P_{el\_FC} - P_{aux}}{(\dot{m}_{ICE} + \dot{m}_{SMR}) \cdot LHV_{NG}} \tag{7.14}$$

The total electrical power output is defined as the sum of the electrical power generated by the ICE and that produced by the fuel cell. The term $\dot{Q}_U$ refers to the useful thermal power, i.e., the portion of thermal energy that is effectively recovered by the system and can be delivered to the user. Conversely, $\dot{m}_{TOT\_NG}$ denotes the total mass flow rate of natural gas entering the system, which includes both the quantity used directly by the engine and the portion reformed to produce hydrogen. Table 7.5 summarizes the parameters required to calculate the performance indicators, derived partly from the Thermoflex simulation and partly from fuel cell data. To estimate the recoverable thermal power from the fuel cell's cooling system, the following empirical correlation was adopted [228]:

$$\dot{Q}_{FC} = P_{el\,FC} \cdot \left(\frac{1.25}{V_{cell}} - 1\right) \cdot \varepsilon_u \tag{7.15}$$

In this equation:

- The value 1.25 V represents the theoretical voltage of an ideal hydrogen fuel cell operating with water expelled as vapor;
- V_{cell} is the actual voltage of a single cell in the stack, set to 0.64 V in this study;
- ε_u is an empirical coefficient, set to 0.7, accounting for the fact that only a portion of the fuel cell's generated heat is recoverable. The rest is lost to the environment through radiation, convection, or dissipated by auxiliary components.

Table 7.5: Results of the entire marine system

$\mathbf{P_{el\_ICE}}$ **[kW]**	7675
$\mathbf{P_{el\_FC}}$ **[kW]**	500
$\mathbf{\dot{m}_{ICE}}$**[kg/s]**	0.3168
$\mathbf{\dot{m}_{SMR}}$ **[kg/s]**	0.0232
$\mathbf{\dot{m}_{H2}}$ **[kg/s]**	0.081
$\mathbf{\dot{Q}_{FC}}$ **[kW$_t$]**	333.5
$\mathbf{\dot{Q}_{U}}$ **[kW$_t$]**	2050.5

Table 7.6 lists the final values of the energy and performance indices calculated using the aforementioned parameters and equations.

Table 7.6: Index values

$\boldsymbol{\eta_{gl}}$	0.517
$\boldsymbol{\eta_{FC/SMR}}$	0.463
$\boldsymbol{\varepsilon_{FC/SMR}}$	0.901
$\mathbf{I_U}$	0.771

The efficiency of the integrated fuel cell and methane reformer system exceeds 0.46, a value that stands out when compared to typical efficiencies of commercially available small-to-medium-sized thermal engines (<1 MW). For reference, the current benchmark technology in ICEs generally achieves electrical efficiencies in the range of 0.35 to 0.40. As a result, replacing the SMR/HT-PEMFC subsystem with a reciprocating engine delivering the same net power output (500 kW) would lead to a measurable decrease in the overall plant efficiency compared to the configuration analyzed in this study.

Moreover, the system achieves a conversion efficiency exceeding 90%, primarily due to the optimization of the reformer's operating parameters, such as the steam-to-carbon (S/C) ratio, temperature, and operating pressure, and to the effective integration of thermal waste streams. Most of these thermal streams are reused to meet the energy demand of the reformer itself, reducing the amount of syngas and hydrogen combusted in the auxiliary burner. This strategy minimizes energy losses and maximizes conversion efficiency.

Figure 7.10 provides a breakdown of the electrical power consumption by each auxiliary component, expressed both in absolute terms and as a percentage of the total auxiliary load. The total power absorbed by auxiliaries, including generator transformation losses, amounts to 85.09 kW. Among all components, the CCS is the most energy-intensive, consuming 22.36 kW, or 26.28% of the total auxiliary power demand. This finding highlights the trade-off between carbon capture and system efficiency.

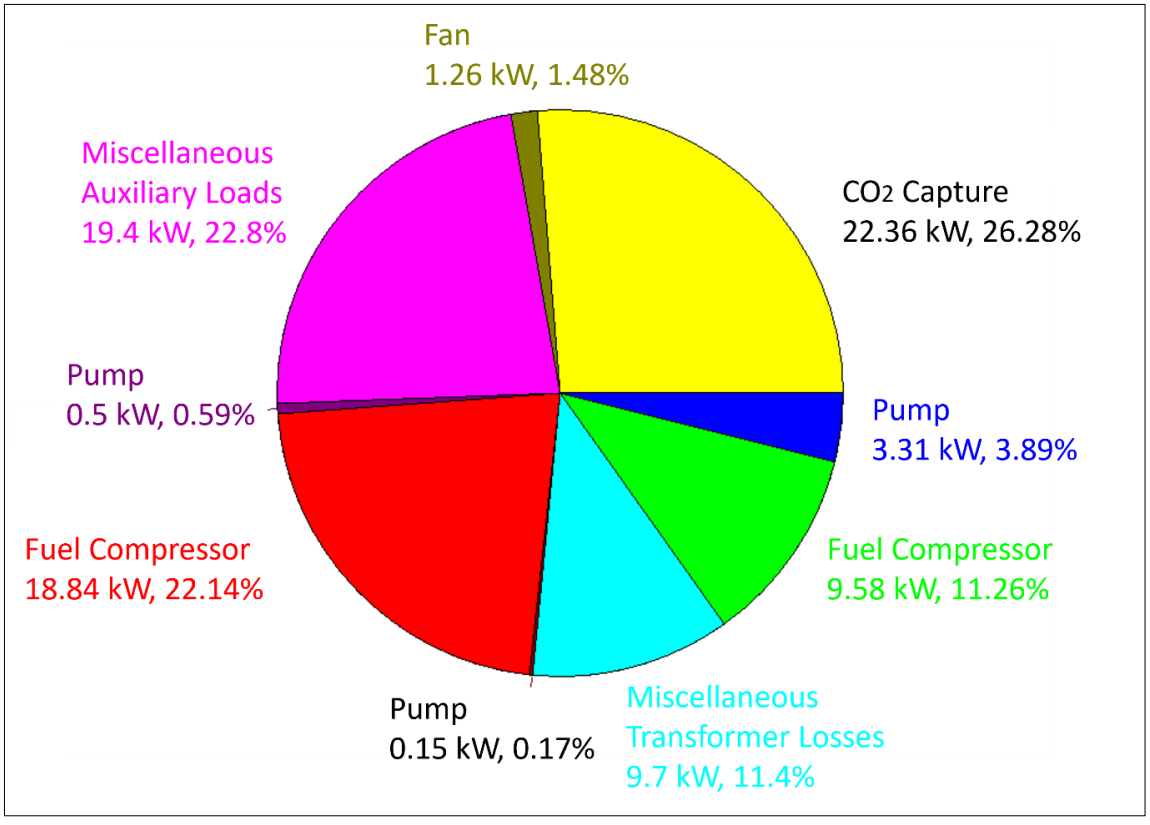

Figure 7.10: Auxiliary system consumption

While the CCS subsystem significantly reduces CO_2 emissions, its substantial power requirement negatively impacts the net plant efficiency. This efficiency penalty is an inherent limitation of all post-combustion capture technologies, as energy must be expended for gas separation, purification, and compression. Consequently, the optimal system design depends on

the priority assigned to environmental benefits versus efficiency constraints, which may vary based on specific operational goals or regulatory frameworks.

Finally, a comparative performance assessment was carried out to evaluate the system in terms of primary energy savings and CO_2 emission reductions. The analysis assumes 7,000 operating hours per year at cruise conditions. The proposed hybrid system was benchmarked against a conventional configuration in which the HT-PEMFC is replaced with a 500 kW reciprocating ICE (Caterpillar), specifically a Caterpillar model whose technical specifications are detailed in Table 7.7. All other components and operating conditions of the plant remain unchanged in this comparative assessment.

Table 7.7: Caterpillar engine data

Type	0.517
Fuel	Natural gas
Speed [rpm]	1000
Power [kW]	500
Efficiency	0.354

Simulation results indicate that the all-thermal configuration achieves a lower overall electrical efficiency (48.1%) compared to the 51.7% obtained by the hybrid system. Table 7.8 summarizes the instantaneous and annual fuel consumption for both configurations.

Table 7.8: Fuel consumption

Power system	Instantaneous rate of consumption [kg/h]	Annual rate of consumption [tonnes/year]
Hybrid with HT-PEMFC	1221	10697
Plant with ICE	1246	10918

The annual CO_2 emissions estimated through the simulations for both configurations are presented in Table 7.9, highlighting the improved environmental performance of the hybrid architecture. Indeed, the analysis indicates that the hybrid configuration offers substantial environmental benefits. Specifically, the proposed system achieves a reduction in CO_2 emissions of 2403 tonnes per year, which corresponds to an 8.4% decrease compared to the baseline configuration where the fuel cell is replaced by a second ICE (Caterpillar).

Table 7.9: CO_2 emissions

CO_2 hybrid [tonnes/year]	26219
CO_2 with only ICEs [tonnes/year]	28622

In the configuration illustrated in Figure 7.3, which includes an energy storage system, the BESS has been sized to accommodate the varying load demands of the on-board auxiliary systems.

A first scenario representing the auxiliary load profile is shown in Figure 7.11. In this case, the fuel cell operates at a constant power output of 500 kW (blue line), while the auxiliary load follows a Gaussian distribution centered at the same value (500 kW), with a standard deviation of 5 kW to introduce realistic fluctuations.

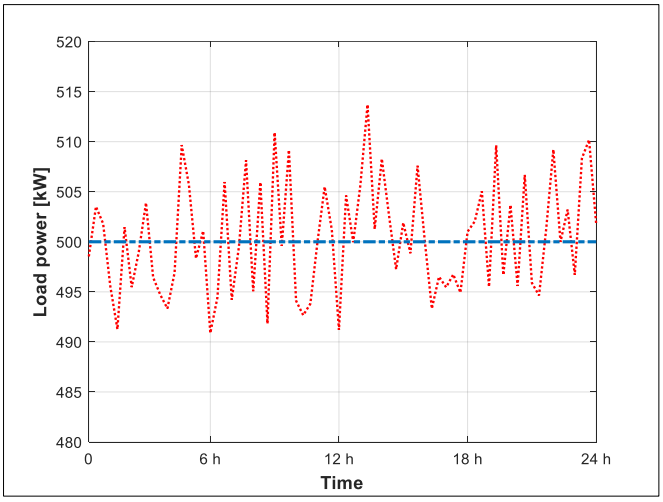

Figure 7.11: Example of auxiliar load variation using a normal distribution with mean 500 kW and standard deviation of 5 kW. The blue line is the power provided by the HT-PEMFC

The results of the optimization for various standard deviation values are presented in Table 7.10. The analysis reveals that, for the examined scenarios, the estimated mass of the BESS cells remains within acceptable limits for marine applications.

Table 7.10: BESS sizes with different load conditions

Mean value of load [kW]	**Standard deviation of load [kW]**	**Energy stored in the BESS [kWh]**	**Estimated mass of the BESS cells [kg]**
500	5	95.2	405.5
500	10	139	592.2
500	15	304.2	1295.7

A second scenario is illustrated in Figure 7.12, where a different auxiliary load condition is simulated. Here, the average power demand is assumed to be 200 kW, but short-duration peak

loads of up to 1 MW are introduced. This condition represents operational scenarios in harbor, such as during loading/unloading operations or docked system activities, where a sudden increase in power demand must be met. In this configuration, the objective is to manage the peak power requirements using the BESS, without altering the steady operating point of the fuel cell or engaging the on-board electrical generator.

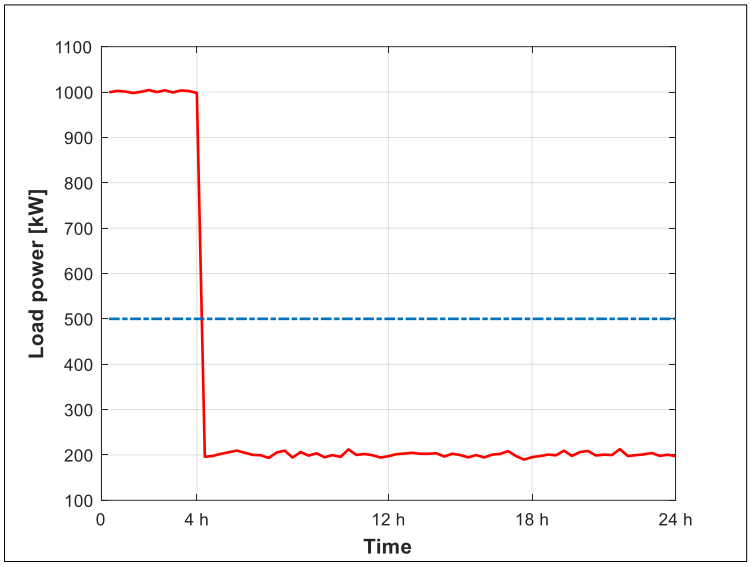

Figure 7.12: Example of auxiliar load variation using a normal distribution with mean 1 MW and standard deviation of 5 kW for the first 4 h and 200 kW and 5 kW of standard deviation for the rest of the time. The blue line is the power provided by the HT-PEMFC

The results of this analysis are summarized in Table 7.11.

Table 7.11: BESS sizes with load peak

Mean value of load [kW]	Standard deviation of load [kW]	Energy stored in the BESS [kWh]	Estimated mass of the BESS cells [kg]
1000 for 4h 200 for 18 h	5	2162	9211.3
1000 for 4 h 200 for 18 h	10	2166	9226.3
1000 for 4 h 200 for 18 h	15	2173	9254.6

It is worth noting that, under peak load conditions, the influence of the standard deviation on the sizing of the BESS becomes negligible. The battery mass and capacity requirements are primarily driven by the magnitude and duration of the peak power demand. Although the BESS weight in this case may be significant, it is nonetheless justified by the specific energy management needs. Importantly, the optimization algorithm employed also ensures the system's ability to fully recharge the BESS once the peak load event has passed, thereby maintaining the overall energy balance of the system.

Conclusions

The doctoral research has investigated the role of advanced combustion strategies and alternative fuels as enabling technologies for the decarbonization of the marine sector. Through an integrated approach combining high-fidelity CFD modeling, experimental validation, and system-level analyses, the work has addressed the complex interaction between fuel properties, combustion behavior, engine performance, and emission formation in marine propulsion systems. The findings provide fundamental insights and practical directions for the development of cleaner, more efficient powertrains that align with the IMO's decarbonization targets. In particular, this thesis has demonstrated that the use of alternative fuels in marine engines—also employing alternative combustion systems—is feasible. Across all investigated configurations, and with the adoption of suitable operating strategies, it was possible to achieve stable and efficient combustion of such fuels. Notably, a significant reduction in CO_2 emissions can be obtained compared to conventional fuels. The use of 3D numerical simulations proved to be a valuable preliminary tool, paving the way for more extensive experimental investigations on these alternative fuels. Furthermore, the study has shown that it is possible to integrate a complete marine power system by coupling the engine with a fuel cell, enabling on-board hydrogen production. In the following sections, the main conclusions corresponding to each results chapter are presented and discussed in greater detail.

1. Advanced DF CI Combustion

A major contribution of this work lies in the detailed numerical investigation of DF compression-ignition engines operating with hydrogen, methane, and ammonia, either pure or in blended configurations. A comprehensive CFD framework was developed and validated against experimental data derived from literature of a Wärtsilä 20DF engine, including detailed mesh sensitivity studies, kinetic and atomization model calibration, and validation of in-cylinder pressure traces and heat release rates. The results emphasized the critical influence of fuel blending strategies on ignition delay, combustion phasing, and pollutant formation. Hydrogen addition improved engine performance but significantly increased NO_x emissions, requiring after-treatment systems for compliance. Ammonia, a promising carbon-free fuel supported by existing distribution infrastructure, showed potential as a low-reactivity fuel (LRF) when combined with diesel and hydrogen pilot injections. However, improving its combustion efficiency required higher pilot diesel quantities and optimized hydrogen addition, since high hydrogen content exacerbated NO_x formation due to both thermal and fuel mechanisms. Injection strategies were also optimized to improve combustion stability and

efficiency. In particular, split injection using sinusoidal mass profiles for both pilot and main injections, along with proper start-of-injection calibration, allowed comparable performance to methane-only DF operation, though NO_x emissions remained intrinsically high.

Overall, the study demonstrated that CI DF engines, when properly adapted, can serve as effective transitional solutions toward low-carbon shipping, offering operational flexibility and substantial CO_2 reduction potential.

2. Spark-Ignition and PC Combustion with Alternative Fuels

The second research pillar focused on traditional spark-ignition and pre-chamber SI combustion using ethanol and methanol as low-carbon fuels, supported by the integration of 1D and 3D simulations.

Initially, the study compared closed-valves and open-valves modeling approaches. Results demonstrated that although the open-valves configuration provides a more detailed representation of the in-cylinder flow field, the closed-valves approach yields similar combustion predictions with significantly lower computational cost. This validation, supported by experimental data from literature and detailed geometry, confirmed the reliability of the closed-valves assumption for future CFD studies for premixed blends.

For ethanol-fueled SI operation, simulations showed that considering approximately 30% of ethanol in liquid state provided the most realistic in-cylinder behavior, closely matching experimental performance data. The results also indicated that multi-point injection enhances combustion efficiency. Ethanol was found to oxidize completely, but limited oxygen availability led to high CO emissions, which could be mitigated by increasing air supply to promote full oxidation, thereby improving mechanical efficiency. The coupled CFD–1D approach effectively quantified the performance benefits of optimized air–fuel delivery, confirming that stoichiometric operation enhances engine efficiency.

Regarding methanol combustion in PC systems, the study compared active and passive PC configurations against a reference methane case. Methanol allowed operation with leaner air–fuel mixtures while maintaining comparable performance. However, passive PC operation required a slightly richer mixture to achieve the same output. Methanol's higher flame speed resulted in faster and more complete combustion, improving engine efficiency and lowering NO_x emissions due to its lower adiabatic flame temperature. Conversely, CO emissions increased in the passive PC configuration, particularly at low loads, due to partial oxidation of methanol.

3. System-Level Integration and Decarbonization Potential

Building on the engine-level findings, the research proposed an innovative integrated marine power system combining internal combustion engines (ICEs) with a high-temperature proton exchange membrane fuel cell (HT-PEMFC), a steam methane reformer, carbon capture units, and a battery energy storage system. In the proposed architecture, four active PC Rolls-Royce engines provide propulsion, while the HT-PEMFC supplies auxiliary power through on-board hydrogen production. System-level simulations demonstrated that such hybrid architectures can achieve significant CO_2 emission reductions and enhanced overall efficiency compared to conventional marine propulsion systems, while maintaining operational flexibility.

4. Overall Contributions and Implications

The research presented in this dissertation advances the state of knowledge in three key areas:

- Fundamental understanding: It provides a detailed characterization of advanced combustion processes with alternative fuels in both CI DF and SI PC engines, clarifying how fuel properties and engine architectures interact to influence emissions and efficiency.
- Modeling methodology: It demonstrates the effectiveness of CFD-based approaches, with both open and closed-valves geometries combined with experimental validation and 1D modeling, for predicting complex combustion phenomena in marine engines with high accuracy.
- System innovation: It shows how advanced engine concepts can be integrated into hybrid marine power systems, offering practical pathways to decarbonization without sacrificing the efficiency.

5. Future Perspectives

While the research has yielded promising results, several challenges remain open for further investigation. First, NO_x mitigation under hydrogen-rich and ammonia-fueled engines must be addressed through a combination of in-cylinder control and exhaust treatment technologies. In addition, the processes of liquid fuel injection, atomization, and vaporization, particularly for fuels that are typically in liquid form, such as ammonia, methanol, and ethanol, require further investigation.

References

1. *Fourth IMO Greenhouse Gas Study*; 2020;
2. Nady, S.; El Fadil, H.; El Idrissi, Z.; Lassioui, A.; Intidam, A.; Anwar, H. Development and Experimental Validation of High-Order Sliding Mode Control for Quadratic Boost Converters in Fuel Cell Electric Vehicles. *Sci Afr* **2024**, *26*, e02417, doi:10.1016/j.sciaf.2024.e02417.
3. Feng, C.; Ge, S.; Zeng, J.; He, L.; Ye, G. Mapping the Global Carbon Emissions of Marine Sectors. *Environ Sci Technol* **2024**, *58*, 18508–18519, doi:10.1021/acs.est.4c09209.
4. IMO Https://Www.Imo.Org/En/Ourwork/Environment/Pages/Short-Term-Ghg-Reduction-Measure.Aspx.
5. Lauriant, G. Https://Www.Ajot.Com/Premium/Ajot-Reefers-and-Decarbonization.
6. https://marineandoffshoreinsight.com/list-of-emission-control-area-eca-names-2025/ Marine and Offshore Insight.
7. Bilousov, I.; Bulgakov, M.; Savchuk, V. *Modern Marine Internal Combustion Engines*; Springer International Publishing: Cham, 2020; Vol. 8; ISBN 978-3-030-49748-4.
8. Heywood, J. Internal Combustion Engine Fundamentals. *McGraw-Hill Education*.
9. Peng, B. A Review of Research on Marine Main Propulsion Systems. *Journal of Education and Educational Research* **2024**, *9*, 189–192, doi:10.54097/n0y36x16.
10. MAN Energy Solutions Basic Principles of Ship Propulsion.
11. Foretich, A.; Zaimes, G.G.; Hawkins, T.R.; Newes, E. Challenges and Opportunities for Alternative Fuels in the Maritime Sector. *Maritime Transport Research* **2021**, *2*, 100033, doi:10.1016/j.martra.2021.100033.
12. International Maritime Organization List of Special Areas, Emission Control Areas and Particularly Sensitive Sea Areas .
13. International Maritime Organization MARPOL Annex VI – Regulations for the Prevention of Air Pollution from Ships.
14. ABS Advisory on NOx Tier III Compliance.
15. Shih, Y.-C.; Tzeng, Y.-A.; Cheng, C.-W.; Huang, C.-H. Speed Optimization in Bulk Carriers: A Weather-Sensitive Approach for Reducing Fuel Consumption. *J Mar Sci Eng* **2023**, *11*, 2000, doi:10.3390/jmse11102000.
16. Nuran, M.; Bayraktar, M.; Yuksel, O. Simulation of a Hybrid Propulsion System on Tugboats Operating in the Strait of Istanbul. *Sustainability* **2025**, *17*, 5834, doi:10.3390/su17135834.
17. Miller, T.; Durlik, I.; Kostecka, E.; Kozlovska, P.; Jakubowski, A.; Łobodzińska, A. Waste Heat Utilization in Marine Energy Systems for Enhanced Efficiency. *Energies (Basel)* **2024**, *17*, 5653, doi:10.3390/en17225653.
18. -, A.S. Benefits of RCM (Reliability-Centered Maintenance) in the Maritime Industry. *International Journal For Multidisciplinary Research* **2025**, *7*, doi:10.36948/ijfmr.2025.v07i01.37054.
19. Kassa, M.; Hall, C. Dual-Fuel Combustion. In *The Future of Internal Combustion Engines*; IntechOpen, 2019.
20. Xiang, L.; Theotokatos, G.; Cui, H.; Xu, K.; Ben, H.; Ding, Y. Parametric Knocking Performance Investigation of Spark Ignition Natural Gas Engines and Dual Fuel Engines. *J Mar Sci Eng* **2020**, *8*, 459, doi:10.3390/jmse8060459.
21. Misra, A.; Yadav, M.; Sharma, A.; Singh, G. Methane–Diesel Dual Fuel Engine: A Comprehensive Review. In; 2020; pp. 327–337.
22. Vollbrandt, J.; Coraddu, A.; Geertsma, R. Hybrid Turbocharging for Alternatively Fueled Internal Combustion Engines in Naval Applications 2024.
23. Lu, C.; Song, E.; Xu, C.; Ni, Z.; Yang, X.; Dong, Q. Analysis of Performance of Passive Pre-Chamber on a Lean-Burn Natural Gas Engine under Low Load. *J Mar Sci Eng* **2023**, *11*, 596, doi:10.3390/jmse11030596.

24. Song, H.; Kim, H.J. Effects of Knocking on the Performance and Emissions of a Single Cylinder SI Engine Fueled with a Fuel Blend of Iso-Octane and Aromatic Hydrocarbons. *Fuel* **2020**, *279*, 118464, doi:10.1016/j.fuel.2020.118464.
25. Zhu, S.; Akehurst, S.; Lewis, A.; Yuan, H. A Review of the Pre-Chamber Ignition System Applied on Future Low-Carbon Spark Ignition Engines. *Renewable and Sustainable Energy Reviews* **2022**, *154*, 111872, doi:10.1016/j.rser.2021.111872.
26. Calgaro, L.; Giubilato, E.; Aghito, M.; Jalkanen, J.-P.; Majamaki, E.; Ferrarin, C.; Hänninen, R.; Palamarchuk, Y.; Sofiev, M.; Semenzin, E.; et al. Influence of Shipping Activities on Air and Water Quality in the Northern Adriatic Sea: A High-Resolution Modelling Study. *Mar Pollut Bull* **2025**, *217*, 118102, doi:10.1016/j.marpolbul.2025.118102.
27. Wu, M.; Cova-Bonillo, A.; Gabana, P.; Brinklow, G.; Khedkar; Herreros, J.M.; Rezaei, S.Z.; Tsolakis, A.; Millington, P.; Clave, S.A.; et al. Addressing the Challenge of Ammonia Slip and Nitrous Oxide Emissions from Zero-Carbon Fuelled Engines through Catalytic Aftertreatment Solutions. *Int J Hydrogen Energy* **2024**, *94*, 848–861, doi:10.1016/j.ijhydene.2024.11.173.
28. Fluegge, K. Does Environmental Exposure to the Greenhouse Gas, N 2 O, Contribute to Etiological Factors in Neurodevelopmental Disorders? A Mini-Review of the Evidence. *Environ Toxicol Pharmacol* **2016**, *47*, 6–18, doi:10.1016/j.etap.2016.08.013.
29. Aakko-Saksa, P.T.; Lehtoranta, K.; Kuittinen, N.; Järvinen, A.; Jalkanen, J.-P.; Johnson, K.; Jung, H.; Ntziachristos, L.; Gagné, S.; Takahashi, C.; et al. Reduction in Greenhouse Gas and Other Emissions from Ship Engines: Current Trends and Future Options. *Prog Energy Combust Sci* **2023**, *94*, 101055, doi:10.1016/j.pecs.2022.101055.
30. Glassman, I.; Yetter, R.A.; Glumac, N.G. *Combustion*; 5th edition.; Academic Press, 2014;
31. Thomson, H.; Corbett, J.J.; Winebrake, J.J. Natural Gas as a Marine Fuel. *Energy Policy* **2015**, *87*, 153–167, doi:10.1016/j.enpol.2015.08.027.
32. Mitu, M.; Movileanu, C.; Giurcan, V. The Laminar Burning Velocities of Stoichiometric Methane–Air Mixture from Closed Vessels Measurements. *Energies (Basel)* **2022**, *15*, 5058, doi:10.3390/en15145058.
33. Mokhatab, S.; Poe, W.A. Natural Gas Fundamentals. In *Handbook of Natural Gas Transmission and Processing*; Elsevier, 2012; pp. 1–42.
34. Kalikatzarakis, M.; Theotokatos, G.; Coraddu, A.; Sayan, P.; Wong, S.Y. Model Based Analysis of the Boil-off Gas Management and Control for LNG Fuelled Vessels. *Energy* **2022**, *251*, 123872, doi:10.1016/j.energy.2022.123872.
35. Nubli, H.; Jung, D.; Kim, S.J.; Sohn, J.M. Structural Impact under Accidental LNG Release on the LNG Bunkering Ship: Implementation of Advanced Cryogenic Risk Analysis. *Process Safety and Environmental Protection* **2024**, *186*, 329–347, doi:10.1016/j.psep.2024.03.109.
36. Jayabal, R. Hydrogen Energy Storage in Maritime Operations: A Pathway to Decarbonization and Sustainability. *Int J Hydrogen Energy* **2025**, *109*, 1133–1144, doi:10.1016/j.ijhydene.2025.02.207.
37. Kelly, N.A. Hydrogen Production by Water Electrolysis. In *Advances in Hydrogen Production, Storage and Distribution*; Elsevier, 2014; pp. 159–185.
38. Hossain Bhuiyan, M.M.; Siddique, Z. Hydrogen as an Alternative Fuel: A Comprehensive Review of Challenges and Opportunities in Production, Storage, and Transportation. *Int J Hydrogen Energy* **2025**, *102*, 1026–1044, doi:10.1016/j.ijhydene.2025.01.033.
39. Brouzas, S.; Zadeh, M.; Lagemann, B. Essentials of Hydrogen Storage and Power Systems for Green Shipping. *Int J Hydrogen Energy* **2025**, *100*, 1543–1560, doi:10.1016/j.ijhydene.2024.12.253.
40. Cheng, Q.; Muhammad, A.; Kaario, O.; Ahmad, Z.; Martti, L. Ammonia as a Sustainable Fuel: Review and Novel Strategies. *Renewable and Sustainable Energy Reviews* **2025**, *207*, 114995, doi:10.1016/j.rser.2024.114995.

41. Erfani, N.; Baharudin, L.; Watson, M. Recent Advances and Intensifications in Haber-Bosch Ammonia Synthesis Process. *Chemical Engineering and Processing - Process Intensification* **2024**, *204*, 109962, doi:10.1016/j.cep.2024.109962.
42. Al-Aboosi, F.Y.; El-Halwagi, M.M.; Moore, M.; Nielsen, R.B. Renewable Ammonia as an Alternative Fuel for the Shipping Industry. *Curr Opin Chem Eng* **2021**, *31*, 100670, doi:10.1016/j.coche.2021.100670.
43. Kobayashi, H.; Hayakawa, A.; Somarathne, K.D.K.A.; Okafor, E.C. Science and Technology of Ammonia Combustion. *Proceedings of the Combustion Institute* **2019**, *37*, 109–133, doi:10.1016/j.proci.2018.09.029.
44. Duong, P.A.; Kang, H. Ammonia as Fuel for Marine Dual-Fuel Technology: A Comprehensive Review. *Fuel Processing Technology* **2025**, *272*, 108205, doi:10.1016/j.fuproc.2025.108205.
45. Zheng, Q.; Tang, J.; Wang, W.; Deveci, M.; Mardani, A. Analyzing the Risk of the Ammonia Storage Facility Using Extended FMEA Model Based on Probabilistic Linguistic GLDS Method with Consensus Reaching. *Int J Hydrogen Energy* **2024**, *62*, 1231–1244, doi:10.1016/j.ijhydene.2024.03.103.
46. Panchuk, A.; Panchuk, M.; Sładkowski, A.; Kryshtopa, S.; Kryshtopa, L. Methanol Potential as an Environmentally Friendly Fuel for Ships. *Naše more* **2024**, *71*, 75–83, doi:10.17818/NM/2024/2.5.
47. Cui, X.; Kær, S.K.; Nielsen, M.P. Energy Analysis and Surrogate Modeling for the Green Methanol Production under Dynamic Operating Conditions. *Fuel* **2022**, *307*, 121924, doi:10.1016/j.fuel.2021.121924.
48. Parris, D.; Spinthiropoulos, K.; Ragazou, K.; Giovou, A.; Tsanaktsidis, C. Methanol, a Plugin Marine Fuel for Green House Gas Reduction—A Review. *Energies (Basel)* **2024**, *17*, 605, doi:10.3390/en17030605.
49. Wouters, C.; Burkardt, P.; Steeger, F.; Fleischmann, M.; Pischinger, S. Comprehensive Assessment of Methanol as an Alternative Fuel for Spark-Ignition Engines. *Fuel* **2023**, *340*, 127627, doi:10.1016/j.fuel.2023.127627.
50. Zhen, X.; Wang, Y. An Overview of Methanol as an Internal Combustion Engine Fuel. *Renewable and Sustainable Energy Reviews* **2015**, *52*, 477–493, doi:10.1016/j.rser.2015.07.083.
51. IMO Methanol as Marine Fuel: Environmental Benefits, Technology Readiness, and Economic Feasiblity. **2016**.
52. Deniz, C.; Zincir, B. Environmental and Economical Assessment of Alternative Marine Fuels. *J Clean Prod* **2016**, *113*, 438–449, doi:10.1016/j.jclepro.2015.11.089.
53. Rajeswari, S.; Baskaran, D.; Saravanan, P.; Rajasimman, M.; Rajamohan, N.; Vasseghian, Y. Production of Ethanol from Biomass – Recent Research, Scientometric Review and Future Perspectives. *Fuel* **2022**, *317*, 123448, doi:10.1016/j.fuel.2022.123448.
54. Jain, S.; Verma, D. The Consideration of Economics during the Processing of Biofuels. In *Biomass, Biopolymer-Based Materials, and Bioenergy*; Elsevier, 2019; pp. 483–493.
55. Ma, Y.; Wang, X.R.; Li, T.; Zhang, J.; Gao, J.; Sun, Z.Y. Hydrogen and Ethanol: Production, Storage, and Transportation. *Int J Hydrogen Energy* **2021**, *46*, 27330–27348, doi:10.1016/j.ijhydene.2021.06.027.
56. Mendiburu, A.Z.; Lauermann, C.H.; Hayashi, T.C.; Mariños, D.J.; Rodrigues da Costa, R.B.; Coronado, C.J.R.; Roberts, J.J.; de Carvalho, J.A. Ethanol as a Renewable Biofuel: Combustion Characteristics and Application in Engines. *Energy* **2022**, *257*, 124688, doi:10.1016/j.energy.2022.124688.
57. Raman, R.K.; Dewang, Y.; Raghuwanshi, J. A Review on Applications of Computational Fluid Dynamics. *International Journal of LNCT* **2018**, *2*.
58. Blazek, J. Principles of Grid Generation. In *Computational Fluid Dynamics: Principles and Applications*; Elsevier, 2015; pp. 357–393.

59. Blazek, J. Governing Equations. In *Computational Fluid Dynamics: Principles and Applications*; Elsevier, 2015; pp. 7–27.
60. Ferziger, J.H.; Perić, M. *Computational Methods for Fluid Dynamics*; Springer, 2002;
61. Blazek, J. Consistency, Accuracy, and Stability. In *Computational Fluid Dynamics: Principles and Applications*; Elsevier, 2015; pp. 337–356.
62. Reitz, R.D. Modeling Atomization Processes in High-Pressure Vaporizing Sprays. **1987**.
63. Reitz, R.D.; Beale, J.C. MODELING SPRAY ATOMIZATION WITH THE KELVIN-HELMHOLTZ/RAYLEIGH-TAYLOR HYBRID MODEL. *Atomization and Sprays* **1999**, *9*, 623–650, doi:10.1615/AtomizSpr.v9.i6.40.
64. Li, H.; Jia, M.; Ding, R.; Li, X.; Zhang, Z.; Zhang, Y. An Improved Kelvin-Helmholtz Rayleigh-Taylor (KH-RT) Breakup Model with Wide Fuel Applicability Based on Data-Driven Techniques. *Energy* **2025**, *334*, 137661, doi:10.1016/j.energy.2025.137661.
65. Yu, D.; Chen, Z. Theoretical Analysis on Droplet Vaporization at Elevated Temperatures and Pressures. *Int J Heat Mass Transf* **2021**, *164*, 120542, doi:10.1016/j.ijheatmasstransfer.2020.120542.
66. Ra, Y.; Reitz, R.D. A Vaporization Model for Discrete Multi-Component Fuel Sprays. *International Journal of Multiphase Flow* **2009**, *35*, 101–117, doi:10.1016/j.ijmultiphaseflow.2008.10.006.
67. Ra, Y.; Reitz, R.D. The Application of a Multicomponent Droplet Vaporization Model to Gasoline Direct Injection Engines. *International Journal of Engine Research* **2003**, *4*, 193–218, doi:10.1243/146808703322223388.
68. Sirignano, W.A. Fuel Droplet Vaporization and Spray Combustion Theory. *Prog Energy Combust Sci* **1983**, *9*, 291–322, doi:10.1016/0360-1285(83)90011-4.
69. Alexakis, A.; Biferale, L. Cascades and Transitions in Turbulent Flows. *Phys Rep* **2018**, *767–769*, 1–101, doi:10.1016/j.physrep.2018.08.001.
70. Blazek, J. Turbulence Modeling. In *Computational Fluid Dynamics: Principles and Applications*; Elsevier, 2015; pp. 213–252.
71. Han, Z.; Reitz, R.D. Turbulence Modeling of Internal Combustion Engines Using RNG κ-ε Models. *Combustion Science and Technology* **1995**, 267–295.
72. Magnussen, B.F.; Hjertager, B.H. On Mathematical Modeling of Turbulent Combustion with Special Emphasis on Soot Formation and Combustion. *Symposium (International) on Combustion* **1977**, *16*, 719–729, doi:10.1016/S0082-0784(77)80366-4.
73. Li, Z.; Ferrarotti, M.; Cuoci, A.; Parente, A. Finite-Rate Chemistry Modelling of Non-Conventional Combustion Regimes Using a Partially-Stirred Reactor Closure: Combustion Model Formulation and Implementation Details. *Appl Energy* **2018**, *225*, 637–655, doi:10.1016/j.apenergy.2018.04.085.
74. MAGNUSSEN, B. On the Structure of Turbulence and a Generalized Eddy Dissipation Concept for Chemical Reaction in Turbulent Flow. In Proceedings of the 19th Aerospace Sciences Meeting; American Institute of Aeronautics and Astronautics: Reston, Virigina, January 12 1981.
75. Kong, S.-C.; Reitz, R.D. Use of Detailed Chemical Kinetics to Study HCCI Engine Combustion With Consideration of Turbulent Mixing Effects. *J Eng Gas Turbine Power* **2002**, *124*, 702–707, doi:10.1115/1.1413766.
76. Metghalchi, M.; Keck, J.C. Burning Velocities of Mixtures of Air with Methanol, Isooctane, and Indolene at High Pressure and Temperature. *Combust Flame* **1982**, *48*, 191–210, doi:10.1016/0010-2180(82)90127-4.
77. Gülder, Ö.L. Correlations of Laminar Combustion Data for Alternative S.I. Engine Fuels. *SAE Technical Paper 841000* **1984**, doi:10.4271/841000.
78. Matalon, M.; Matkowsky, B.J. Flames as Gasdynamic Discontinuities. *J Fluid Mech* **1982**, *124*, 239–259, doi:10.1017/S0022112082002481.

79. Demesoukas, S.; Brequigny, P.; Caillol, C.; Halter, F.; Mounaïm-Rousselle, C. 0D Modeling Aspects of Flame Stretch in Spark Ignition Engines and Comparison with Experimental Results. *Appl Energy* **2016**, *179*, 401–412, doi:10.1016/j.apenergy.2016.07.007.
80. Detomaso, N.; Hok, J.-J.; Dounia, O.; Laera, D.; Poinsot, T. A Generalization of the Thickened Flame Model for Stretched Flames. *Combust Flame* **2023**, *258*, 113080, doi:10.1016/j.combustflame.2023.113080.
81. Nejaamtheen, M.N.; Choi, J.-Y. A Comprehensive Review of Flamelet Methods: Future Directions and Emerging Challenges. *Energies (Basel)* **2024**, *18*, 45, doi:10.3390/en18010045.
82. Dekena, M.; Peters, N. Combustion Modeling with the G-Equation. *Oil & Gas Science and Technology* **1999**, *54*.
83. Fan, L.; Reitz, R.D. Development of an Ignition and Combustion Model for Spark-Ignition Engines. *SAE Technical Paper 2000-01-2809* **2000**, doi:10.4271/2000-01-2809.
84. Han, Z.; Reitz, R.D. A Temperature Wall Function Formulation for Variable-Density Turbulent Flows with Application to Engine Convective Heat Transfer Modeling. *Int J Heat Mass Transf* **1997**, *40*, 613–625, doi:10.1016/0017-9310(96)00117-2.
85. Blazek, J. Boundary Conditions. In *Computational Fluid Dynamics: Principles and Applications*; Elsevier, 2015; pp. 253–281.
86. Abadie, L.M.; Goicoechea, N. Powering Newly Constructed Vessels to Comply with ECA Regulations under Fuel Market Prices Uncertainty: Diesel or Dual Fuel Engine? *Transp Res D Transp Environ* **2019**, *67*, 433–448, doi:10.1016/j.trd.2018.12.012.
87. Sinha, R.P.; Wan Nik, W.M.N. Investigation of Propulsion System for Large LNG Ships. *IOP Conf Ser Mater Sci Eng* **2012**, *36*, 012004, doi:10.1088/1757-899X/36/1/012004.
88. Yu, H.; Wang, W.; Sheng, D.; Li, H.; Duan, S. Performance of Combustion Process on Marine Low Speed Two-Stroke Dual Fuel Engine at Different Fuel Conditions: Full Diesel/Diesel Ignited Natural Gas. *Fuel* **2022**, *310*, 122370, doi:10.1016/J.FUEL.2021.122370.
89. De Bellis, V.; Malfi, E.; Lanotte, A.; Fasulo, G.; Bozza, F.; Cafari, A.; Caputo, G.; Hyvönen, J. Development of a Phenomenological Model for the Description of RCCI Combustion in a Dual-Fuel Marine Internal Combustion Engine. *Appl Energy* **2022**, *325*, 119919, doi:10.1016/j.apenergy.2022.119919.
90. Nemati, A.; Ong, J.C.; Pang, K.M.; Mayer, S.; Walther, J.H. A Numerical Study of the Influence of Pilot Fuel Injection Timing on Combustion and Emission Formation under Two-Stroke Dual-Fuel Marine Engine-like Conditions. *Fuel* **2022**, *312*, 122651, doi:10.1016/j.fuel.2021.122651.
91. Kochunni, S.K.; Chowdhury, K. Concept and Evaluation of Energy-Efficient Boil-off Gas Reliquefiers in LNG Carrier Ships Propelled by Dual-Fuel Engines. *Cryogenics (Guildf)* **2022**, *123*, 103453, doi:10.1016/j.cryogenics.2022.103453.
92. Zhang, Z.; Lv, J.; Li, W.; Long, J.; Wang, S.; Tan, D.; Yin, Z. Performance and Emission Evaluation of a Marine Diesel Engine Fueled with Natural Gas Ignited by Biodiesel-Diesel Blended Fuel. *Energy* **2022**, *256*, 124662, doi:10.1016/j.energy.2022.124662.
93. Cavalcanti, E.J.C. Energy, Exergy and Exergoenvironmental Analyses on Gas-Diesel Fuel Marine Engine Used for Trigeneration System. *Appl Therm Eng* **2021**, *184*, 116211, doi:10.1016/j.applthermaleng.2020.116211.
94. De Robbio, R.; Cameretti, M.C.; Mancaruso, E.; Tuccillo, R.; Vaglieco, B.M. CFD Analysis of Different Methane/Hydrogen Blends in a CI Engine Operating in Dual Fuel Mode.; August 30 2022.
95. Papagiannakis, R.G.; Rakopoulos, C.D.; Hountalas, D.T.; Rakopoulos, D.C. Emission Characteristics of High Speed, Dual Fuel, Compression Ignition Engine Operating in a Wide Range of Natural Gas/Diesel Fuel Proportions. *Fuel* **2010**, *89*, 1397–1406, doi:10.1016/j.fuel.2009.11.001.

96. Xiang, L.; Theotokatos, G.; Ding, Y. Parametric Investigation on the Performance-Emissions Trade-off and Knocking Occurrence of Dual Fuel Engines Using CFD. *Fuel* **2023**, *340*, 127535, doi:10.1016/j.fuel.2023.127535.
97. Hariharan, D.; Rajan Krishnan, S.; Kumar Srinivasan, K.; Sohail, A. Multiple Injection Strategies for Reducing HC and CO Emissions in Diesel-Methane Dual-Fuel Low Temperature Combustion. *Fuel* **2021**, *305*, 121372, doi:10.1016/j.fuel.2021.121372.
98. Pinto, G.M.; de Souza, T.A.Z.; da Costa, R.B.R.; Roque, L.F.A.; Frez, G.V.; Coronado, C.J.R. Combustion, Performance and Emission Analyses of a CI Engine Operating with Renewable Diesel Fuels (HVO/FARNESANE) under Dual-Fuel Mode through Hydrogen Port Injection. *Int J Hydrogen Energy* **2023**, *48*, 19713–19732, doi:10.1016/j.ijhydene.2023.02.020.
99. Kumar, R.S.; Loganathan, M.; Gunasekaran, E.J. Performance, Emission and Combustion Characteristics of CI Engine Fuelled with Diesel and Hydrogen. *Frontiers in Energy* **2015**, *9*, 486–494, doi:10.1007/s11708-015-0368-4.
100. Saravanan, N.; Nagarajan, G. Performance and Emission Studies on Port Injection of Hydrogen with Varied Flow Rates with Diesel as an Ignition Source. *Appl Energy* **2010**, *87*, 2218–2229, doi:10.1016/j.apenergy.2010.01.014.
101. Hosseini, S.H.; Tsolakis, A.; Alagumalai, A.; Mahian, O.; Lam, S.S.; Pan, J.; Peng, W.; Tabatabaei, M.; Aghbashlo, M. Use of Hydrogen in Dual-Fuel Diesel Engines. *Prog Energy Combust Sci* **2023**, *98*, 101100, doi:10.1016/j.pecs.2023.101100.
102. Subramanian, B.; Thangavel, V. Experimental Investigations on Performance, Emission and Combustion Characteristics of Diesel-Hydrogen and Diesel-HHO Gas in a Dual Fuel CI Engine. *Int J Hydrogen Energy* **2020**, *45*, 25479–25492, doi:10.1016/j.ijhydene.2020.06.280.
103. Karagöz, Y.; Güler, İ.; Sandalcı, T.; Yüksek, L.; Dalkılıç, A.S. Effect of Hydrogen Enrichment on Combustion Characteristics, Emissions and Performance of a Diesel Engine. *Int J Hydrogen Energy* **2016**, *41*, 656–665, doi:10.1016/j.ijhydene.2015.09.064.
104. Karagöz, Y.; Sandalcı, T.; Yüksek, L.; Dalkılıç, A.S.; Wongwises, S. Effect of Hydrogen–Diesel Dual-Fuel Usage on Performance, Emissions and Diesel Combustion in Diesel Engines. *Advances in Mechanical Engineering* **2016**, *8*, 168781401666445, doi:10.1177/1687814016664458.
105. Lata, D.B.; Misra, A. Analysis of Ignition Delay Period of a Dual Fuel Diesel Engine with Hydrogen and LPG as Secondary Fuels. *Int J Hydrogen Energy* **2011**, *36*, 3746–3756, doi:10.1016/j.ijhydene.2010.12.075.
106. Talibi, M.; Hellier, P.; Morgan, R.; Lenartowicz, C.; Ladommatos, N. Hydrogen-Diesel Fuel Co-Combustion Strategies in Light Duty and Heavy Duty CI Engines. *Int J Hydrogen Energy* **2018**, *43*, 9046–9058, doi:10.1016/j.ijhydene.2018.03.176.
107. Talibi, M.; Hellier, P.; Balachandran, R.; Ladommatos, N. Effect of Hydrogen-Diesel Fuel Co-Combustion on Exhaust Emissions with Verification Using an in–Cylinder Gas Sampling Technique. *Int J Hydrogen Energy* **2014**, *39*, 15088–15102, doi:10.1016/j.ijhydene.2014.07.039.
108. Shin, B.; Cho, Y.; Han, D.; Song, S.; Min Chun, K. Investigation of the Effects of Hydrogen on Cylinder Pressure in a Split-Injection Diesel Engine at Heavy EGR. *Int J Hydrogen Energy* **2011**, *36*, 13158–13170, doi:10.1016/j.ijhydene.2011.07.050.
109. Saravanan, N.; Nagarajan, G. Experimental Investigation in Optimizing the Hydrogen Fuel on a Hydrogen Diesel Dual-Fuel Engine. *Energy & Fuels* **2009**, *23*, 2646–2657, doi:10.1021/ef800962k.
110. Saravanan, N.; Nagarajan, G. Hydrogen-Diesel Dual Fuel Combustion in a Direct Injection Diesel Engine. *International Journal of Renewable Energy Technology* **2011**, *2*, 259, doi:10.1504/IJRET.2011.040863.

111. Seyam, S.; Dincer, I.; Agelin-Chaab, M. Investigation and Comparative Evaluation of a Hybridized Marine Engine Powered by Eco-Friendly Fuels Including Hydrogen. *Int J Hydrogen Energy* **2023**, *48*, 4812–4829, doi:10.1016/j.ijhydene.2022.11.008.
112. Pan, H.; Pournazeri, S.; Princevac, M.; Miller, J.W.; Mahalingam, S.; Khan, M.Y.; Jayaram, V.; Welch, W.A. Effect of Hydrogen Addition on Criteria and Greenhouse Gas Emissions for a Marine Diesel Engine. *Int J Hydrogen Energy* **2014**, *39*, 11336–11345, doi:10.1016/j.ijhydene.2014.05.010.
113. Tan, D.; Wu, Y.; Lv, J.; Li, J.; Ou, X.; Meng, Y.; Lan, G.; Chen, Y.; Zhang, Z. Performance Optimization of a Diesel Engine Fueled with Hydrogen/Biodiesel with Water Addition Based on the Response Surface Methodology. *Energy* **2023**, *263*, 125869, doi:10.1016/j.energy.2022.125869.
114. Zhang, Z.; Lv, J.; Xie, G.; Wang, S.; Ye, Y.; Huang, G.; Tan, D. Effect of Assisted Hydrogen on Combustion and Emission Characteristics of a Diesel Engine Fueled with Biodiesel. *Energy* **2022**, *254*, 124269, doi:10.1016/j.energy.2022.124269.
115. Gholami, A.; Jazayeri, S.A.; Esmaili, Q. A Detail Performance and CO2 Emission Analysis of a Very Large Crude Carrier Propulsion System with the Main Engine Running on Dual Fuel Mode Using Hydrogen/Diesel versus Natural Gas/Diesel and Conventional Diesel Engines. *Process Safety and Environmental Protection* **2022**, *163*, 621–635, doi:10.1016/j.psep.2022.05.069.
116. Atelge, M.R. Experimental Study of a Blend of Diesel/Ethanol/n-Butanol with Hydrogen Additive on Combustion and Emission and Exegetic Evaluation. *Fuel* **2022**, *325*, 124903, doi:10.1016/j.fuel.2022.124903.
117. Maitlo, H.A.; Maitlo, G.; Song, X.; Zhou, M.; Kim, K.-H. A Figure of Merits-Based Performance Comparison of Various Advanced Functional Nanomaterials for Adsorptive Removal of Gaseous Ammonia. *Science of The Total Environment* **2022**, *822*, 153428, doi:10.1016/j.scitotenv.2022.153428.
118. Manigandan, S.; Ryu, J.I.; Praveen Kumar, T.R.; Elgendi, M. Hydrogen and Ammonia as a Primary Fuel – A Critical Review of Production Technologies, Diesel Engine Applications, and Challenges. *Fuel* **2023**, *352*, 129100, doi:10.1016/j.fuel.2023.129100.
119. Zhou, X.; Li, T.; Wang, N.; Wang, X.; Chen, R.; Li, S. Pilot Diesel-Ignited Ammonia Dual Fuel Low-Speed Marine Engines: A Comparative Analysis of Ammonia Premixed and High-Pressure Spray Combustion Modes with CFD Simulation. *Renewable and Sustainable Energy Reviews* **2023**, *173*, 113108, doi:10.1016/j.rser.2022.113108.
120. Yousefi, A.; Guo, H.; Dev, S.; Liko, B.; Lafrance, S. Effects of Ammonia Energy Fraction and Diesel Injection Timing on Combustion and Emissions of an Ammonia/Diesel Dual-Fuel Engine. *Fuel* **2022**, *314*, 122723, doi:10.1016/j.fuel.2021.122723.
121. Wang, B.; Wang, H.; Hu, D.; Yang, C.; Duan, B.; Wang, Y. Study on the Performance of Premixed Natural Gas/Ammonia Engine with Diesel Ignition. *Energy* **2023**, *271*, 127056, doi:10.1016/j.energy.2023.127056.
122. Xu, L.; Xu, S.; Bai, X.-S.; Repo, J.A.; Hautala, S.; Hyvönen, J. Performance and Emission Characteristics of an Ammonia/Diesel Dual-Fuel Marine Engine. *Renewable and Sustainable Energy Reviews* **2023**, *185*, 113631, doi:10.1016/j.rser.2023.113631.
123. Shin, J.; Park, S. Numerical Analysis for Optimizing Combustion Strategy in an Ammonia-Diesel Dual-Fuel Engine. *Energy Convers Manag* **2023**, *284*, 116980, doi:10.1016/j.enconman.2023.116980.
124. Rodríguez, C.G.; Lamas, M.I.; Rodríguez, J. de D.; Abbas, A. Possibilities of Ammonia as Both Fuel and NOx Reductant in Marine Engines: A Numerical Study. *J Mar Sci Eng* **2022**, *10*, 43, doi:10.3390/jmse10010043.

125. Zhu, J.; Zhou, D.; Yang, W.; Qian, Y.; Mao, Y.; Lu, X. Investigation on the Potential of Using Carbon-Free Ammonia in Large Two-Stroke Marine Engines by Dual-Fuel Combustion Strategy. *Energy* **2023**, *263*, 125748, doi:10.1016/j.energy.2022.125748.
126. Li, Z.; Zhang, Z.; Fan, Y.; Li, J.; Wu, K.; Gao, Z.; Li, A.; Zhu, L.; Huang, Z. Fuel Reactivity Stratification Assisted Jet Ignition for Low-Speed Two-Stroke Ammonia Marine Engine. *Int J Hydrogen Energy* **2024**, *49*, 570–585, doi:10.1016/j.ijhydene.2023.08.256.
127. Li, T.; Zhou, X.; Wang, N.; Wang, X.; Chen, R.; Li, S.; Yi, P. A Comparison between Low- and High-Pressure Injection Dual-Fuel Modes of Diesel-Pilot-Ignition Ammonia Combustion Engines. *Journal of the Energy Institute* **2022**, *102*, 362–373, doi:10.1016/j.joei.2022.04.009.
128. Jin, Z.; Mi, S.; Zhou, D.; Zhu, J.; Schirru, A.; Zhao, W.; Qian, Y.; Lucchini, T.; Lu, X. Insights into the Combustion Characteristics, Emission Formation Sources, and Optimization Strategy of an Ammonia-Diesel Dual-Fuel Engine under High Ammonia Ratio Conditions. *Appl Energy* **2024**, *373*, 123894, doi:10.1016/j.apenergy.2024.123894.
129. Qian, F.; Zhang, S.; Wang, J.; Zhu, N.; Bao, X.; Yang, H.; Xu, X.; Alshahrani, W.A.; Helal, M.H.; Guo, Z. Ammonia Energy Fraction Effect on the Combustion and Reduced NOX Emission of Ammonia/Diesel Dual Fuel. *Environ Res* **2024**, *261*, 119530, doi:10.1016/j.envres.2024.119530.
130. Jin, Z.; Mi, S.; Zhou, D.; Qian, Y.; Lu, X. The Characteristics Analysis and Feasible Improvement Strategy Evaluation for Ammonia-Diesel Dual-Fuel Engine under Heavy Load and High Ammonia Ratio Conditions. *Fuel* **2025**, *383*, 133911, doi:10.1016/j.fuel.2024.133911.
131. Yang, C.; Wang, Z.; Li, J.; Cheng, X. Effects of Ammonia Energy Fractions, Diesel Injection Timings, and Loads on Combustion and Emission Characteristics of PFI-DI Ammonia-Diesel Engines. *International Journal of Engine Research* **2024**, *25*, 743–757, doi:10.1177/14680874231207435.
132. Shi, C.; Cheng, T.; Yang, X.; Zhang, Z.; Duan, R.; Li, X. Implementation of Various Injection Rate Shapes in an Ammonia/Diesel Dual-Fuel Engine with Special Emphasis on Combustion and Emissions Characteristics. *Energy* **2024**, *304*, 132035, doi:10.1016/j.energy.2024.132035.
133. De Robbio, R.; Cameretti, M.C.; Palomba, M.; Tuccillo, R.; Mancaruso, E. CFD Analysis of the Injection Strategy of a Dual Fuel Compression Ignition Engine Supplied with Hydrogen.; August 28 2023.
134. Altinkurt, M.D.; Merts, M.; Tunér, M.; Turkcan, A. Effects of Split Diesel Injection Strategies on Combustion, Knocking, Cyclic Variations and Emissions of a Natural Gas-Diesel Dual Fuel Medium Speed Engine. *Fuel* **2023**, *347*, 128517, doi:10.1016/j.fuel.2023.128517.
135. Marques, J.C.; Gasi, F.; Lourenço, S.R. Biofuel in the Automotive Sector: Viability of Sugarcane Ethanol. *Sustainability* **2024**, *16*, 2674, doi:10.3390/su16072674.
136. Puentes, J.; Mateo, S.; Sánchez, S.; Roberto, I.; Moya, A. Bioconversion Study of Olive Tree Biomass Hemicellulosic Hydrolysates by Candida Guilliermondii at Different Scales for Ethanol and Xylitol Production. *Fermentation* **2023**, *9*, 553, doi:10.3390/fermentation9060553.
137. Talebnia, F.; Karakashev, D.; Angelidaki, I. Production of Bioethanol from Wheat Straw: An Overview on Pretreatment, Hydrolysis and Fermentation. *Bioresour Technol* **2010**, *101*, 4744–4753, doi:10.1016/j.biortech.2009.11.080.
138. Pachón, E.R.; Mandade, P.; Gnansounou, E. Conversion of Vine Shoots into Bioethanol and Chemicals: Prospective LCA of Biorefinery Concept. *Bioresour Technol* **2020**, *303*, 122946, doi:10.1016/j.biortech.2020.122946.
139. Garcia-Ochoa, F.; Vergara, P.; Wojtusik, M.; Gutiérrez, S.; Santos, V.E.; Ladero, M.; Villar, J.C. Multi-Feedstock Lignocellulosic Biorefineries Based on Biological Processes: An Overview. *Ind Crops Prod* **2021**, *172*, 114062, doi:10.1016/j.indcrop.2021.114062.

140. Yousufuddin, S.; Masood, M. Effect of Ignition Timing and Compression Ratio on the Performance of a Hydrogen–Ethanol Fuelled Engine. *Int J Hydrogen Energy* **2009**, *34*, 6945–6950, doi:10.1016/j.ijhydene.2009.05.122.
141. Iliev, S. A Comparison of Ethanol, Methanol, and Butanol Blending with Gasoline and Its Effect on Engine Performance and Emissions Using Engine Simulation. *Processes* **2021**, *9*, 1322, doi:10.3390/pr9081322.
142. Catapano, F.; Di Iorio, S.; Luise, L.; Sementa, P.; Vaglieco, B.M. Influence of Ethanol Blended and Dual Fueled with Gasoline on Soot Formation and Particulate Matter Emissions in a Small Displacement Spark Ignition Engine. *Fuel* **2019**, *245*, 253–262, doi:10.1016/j.fuel.2019.01.173.
143. Dirrenberger, P.; Glaude, P.A.; Bounaceur, R.; Le Gall, H.; da Cruz, A.P.; Konnov, A.A.; Battin-Leclerc, F. Laminar Burning Velocity of Gasolines with Addition of Ethanol. *Fuel* **2014**, *115*, 162–169, doi:10.1016/j.fuel.2013.07.015.
144. Zheng, Z.; Fang, X.; Liu, H.; Geng, C.; Yang, Z.; Feng, L.; Wang, Y.; Yao, M. Study on the Flame Development Patterns and Flame Speeds from Homogeneous Charge to Stratified Charge by Fueling N-Heptane in an Optical Engine. *Combust Flame* **2019**, *199*, 213–229, doi:10.1016/j.combustflame.2018.10.027.
145. Turner, D.; Xu, H.; Cracknell, R.F.; Natarajan, V.; Chen, X. Combustion Performance of Bio-Ethanol at Various Blend Ratios in a Gasoline Direct Injection Engine. *Fuel* **2011**, *90*, 1999–2006, doi:10.1016/j.fuel.2010.12.025.
146. Ilves, R.; Küüt, A.; Olt, J. Ethanol as Internal Combustion Engine Fuel. In *Ethanol*; Elsevier, 2019; pp. 215–229.
147. Cooney, C.P.; Yeliana; Worm, J.J.; Naber, J.D. Combustion Characterization in an Internal Combustion Engine with Ethanol−Gasoline Blended Fuels Varying Compression Ratios and Ignition Timing. *Energy & Fuels* **2009**, *23*, 2319–2324, doi:10.1021/ef800899r.
148. Hsieh, W.-D.; Chen, R.-H.; Wu, T.-L.; Lin, T.-H. Engine Performance and Pollutant Emission of an SI Engine Using Ethanol–Gasoline Blended Fuels. *Atmos Environ* **2002**, *36*, 403–410, doi:10.1016/S1352-2310(01)00508-8.
149. Pourkhesalian, A.M.; Shamekhi, A.H.; Salimi, F. Alternative Fuel and Gasoline in an SI Engine: A Comparative Study of Performance and Emissions Characteristics. *Fuel* **2010**, *89*, 1056–1063, doi:10.1016/j.fuel.2009.11.025.
150. Celik, M.B. Experimental Determination of Suitable Ethanol–Gasoline Blend Rate at High Compression Ratio for Gasoline Engine. *Appl Therm Eng* **2008**, *28*, 396–404, doi:10.1016/j.applthermaleng.2007.10.028.
151. Al-Hasan, M. Effect of Ethanol–Unleaded Gasoline Blends on Engine Performance and Exhaust Emission. *Energy Convers Manag* **2003**, *44*, 1547–1561, doi:10.1016/S0196-8904(02)00166-8.
152. İlhak, M.İ.; Doğan, R.; Akansu, S.O.; Kahraman, N. Experimental Study on an SI Engine Fueled by Gasoline, Ethanol and Acetylene at Partial Loads. *Fuel* **2020**, *261*, 116148, doi:10.1016/j.fuel.2019.116148.
153. Liu, S.; Zhang, H.; Fan, Q.; Wang, W.; Qi, Y.; Wang, Z. Investigation of Combustion and Particle Number (PN) Emissions in a Spark Induced Compression Ignition (SICI) Engine for Ethanol-Gasoline Blends. *Fuel* **2022**, *316*, 123155, doi:10.1016/j.fuel.2022.123155.
154. Balki, M.K.; Sayin, C. The Effect of Compression Ratio on the Performance, Emissions and Combustion of an SI (Spark Ignition) Engine Fueled with Pure Ethanol, Methanol and Unleaded Gasoline. *Energy* **2014**, *71*, 194–201, doi:10.1016/j.energy.2014.04.074.
155. Anderson, J.E.; Kramer, U.; Mueller, S.A.; Wallington, T.J. Octane Numbers of Ethanol− and Methanol−Gasoline Blends Estimated from Molar Concentrations. *Energy & Fuels* **2010**, *24*, 6576–6585, doi:10.1021/ef101125c.

156. Cao, J.; Li, T.; Huang, S.; Chen, R.; Li, S.; Kuang, M.; Yang, R.; Huang, Y. Co-Optimization of Miller Degree and Geometric Compression Ratio of a Large-Bore Natural Gas Generator Engine with Novel Knock Models and Machine Learning. *Appl Energy* **2023**, *352*, 121957, doi:10.1016/j.apenergy.2023.121957.
157. Suijs, W.; De Graeve, R.; Verhelst, S. An Exploratory Study of Knock Intensity in a Large-Bore Heavy-Duty Methanol Engine. *Energy Convers Manag* **2024**, *302*, 118089, doi:10.1016/j.enconman.2024.118089.
158. Kowalewicz, A. Methanol as a Fuel for Spark Ignition Engines: A Review and Analysis. *Proceedings of the Institution of Mechanical Engineers, Part D: Journal of Automobile Engineering* **1993**, *207*, 43–52, doi:10.1243/PIME_PROC_1993_207_158_02.
159. Vancoillie, J.; Demuynck, J.; Sileghem, L.; Van De Ginste, M.; Verhelst, S.; Brabant, L.; Van Hoorebeke, L. The Potential of Methanol as a Fuel for Flex-Fuel and Dedicated Spark-Ignition Engines. *Appl Energy* **2013**, *102*, 140–149, doi:10.1016/j.apenergy.2012.05.065.
160. Balki, M.K.; Sayin, C.; Canakci, M. The Effect of Different Alcohol Fuels on the Performance, Emission and Combustion Characteristics of a Gasoline Engine. *Fuel* **2014**, *115*, 901–906, doi:10.1016/j.fuel.2012.09.020.
161. Wei, Y.; Liu, S.; Liu, F.; Liu, J.; Zhu, Z.; Li, G. Formaldehyde and Methanol Emissions from a Methanol/Gasoline-Fueled Spark-Ignition (SI) Engine. *Energy & Fuels* **2009**, *23*, 3313–3318, doi:10.1021/ef900175h.
162. Zhang, Z.H.; Cheung, C.S.; Chan, T.L.; Yao, C.D. Experimental Investigation on Regulated and Unregulated Emissions of a Diesel/Methanol Compound Combustion Engine with and without Diesel Oxidation Catalyst. *Science of The Total Environment* **2010**, *408*, 865–872, doi:10.1016/j.scitotenv.2009.10.060.
163. Güdden, A.; Pischinger, S.; Geiger, J.; Heuser, B.; Müther, M. An Experimental Study on Methanol as a Fuel in Large Bore High Speed Engine Applications – Port Fuel Injected Spark Ignited Combustion. *Fuel* **2021**, *303*, 121292, doi:10.1016/j.fuel.2021.121292.
164. Hlaing, P.; Echeverri Marquez, M.; Burgos, P.; Cenker, E.; Ben Houidi, M.; Johansson, B. Analysis of Fuel Properties on Combustion Characteristics in a Narrow-Throat Pre-Chamber Engine. *SAE Int J Adv Curr Pract Mobil* **2021**, *3*, 2021-01–0474, doi:10.4271/2021-01-0474.
165. Hlaing, P.; Said, A.; Cenker, E.; Im, H.G.; Turner, J. Comparing Unburned Fuel Emission from a Pre-Chamber Engine Operating on Alcohol Fuels Using FID and FTIR Analyzers.; August 30 2022.
166. Liu, X.; Sharma, P.; Silva, M.; AlRamadan, A.S.; Cenker, E.; Tang, Q.; Magnotti, G.; Im, H.G. Computational Investigation of Methanol Pre-Chamber Combustion in a Heavy-Duty Engine. *Applications in Energy and Combustion Science* **2023**, *15*, 100192, doi:10.1016/j.jaecs.2023.100192.
167. Leng, X.; Deng, Y.; He, D.; Wei, S.; He, Z.; Wang, Q.; Long, W.; Zhu, S. A Preliminary Numerical Study on the Use of Methanol as a Mono-Fuel for a Large Bore Marine Engine. *Fuel* **2022**, *310*, 122309, doi:10.1016/j.fuel.2021.122309.
168. Cameretti, M.C.; De Robbio, R.; Mancaruso, E.; Palomba, M. CFD Study of Dual Fuel Combustion in a Research Diesel Engine Fueled by Hydrogen. *Energies (Basel)* **2022**, *15*, doi:10.3390/en15155521.
169. Cameretti, M.C.; De Robbio, R.; Palomba, M. Numerical Analysis of Dual Fuel Combustion in a Medium Speed Marine Engine Supplied with Methane/Hydrogen Blends. *Energies (Basel)* **2023**, *16*, 6651, doi:10.3390/en16186651.
170. Cameretti, M.C.; De Robbio, R.; Palomba, M.; Zucareli de Souza, T. Strategies to Improve Ammonia Combustion in a Dual Fuel Marine Engine by Using CFD. *Fuel* **2025**, *381*, 133440, doi:10.1016/j.fuel.2024.133440.

171. Cameretti, M.C.; De Robbio, R.; Palomba, M. Numerical Investigation on an Injection Strategy Optimization for Dual Fuel Marine Engine Fuelled by Ammonia. *SAE Technical Paper* **2025**, doi:10.4271/2025-24-0013.
172. https://www.wartsila.com/marine/products/engines-and-generating-sets/dual-fuel-engines/wartsila-20df Wärtsilä 20DF.
173. Wärtsilä 20DF Product Guide.
174. García Valladolid, P.; Tunestål, P.; Monsalve-Serrano, J.; García, A.; Hyvönen, J. Impact of Diesel Pilot Distribution on the Ignition Process of a Dual Fuel Medium Speed Marine Engine. *Energy Convers Manag* **2017**, *149*, 192–205, doi:10.1016/j.enconman.2017.07.023.
175. Cameretti, M.C.; De Robbio, R.; Tuccillo, R. Performance Improvement and Emission Control of a Dual Fuel Operated Diesel Engine.; September 4 2017.
176. Woschni, G. A Universally Applicable Equation for the Instantaneous Heat Transfer Coefficient in the Internal Combustion Engine.; February 1 1967.
177. Patankar, S. V. *Numerical Heat Transfer and Fluid Flow*; CRC Press, 2018; ISBN 9781315275130.
178. Yakhot, V.; Orszag, S.A. Renormalization Group Analysis of Turbulence. I. Basic Theory. *J Sci Comput* **1986**, *1*, 3–51, doi:10.1007/BF01061452.
179. Lamas, M.I.; Rodríguez, C.G. Numerical Model to Study the Combustion Process and Emissions in the Wärtsilä 6L 46 Four-Stroke Marine Engine. *Polish Maritime Research* **2013**, *20*, 61–66, doi:10.2478/pomr-2013-0017.
180. Wang, H.; Ra, Y.; Jia, M.; Reitz, R.D. Development of a Reduced N-Dodecane-PAH Mechanism and Its Application for n-Dodecane Soot Predictions. *Fuel* **2014**, *136*, 25–36, doi:10.1016/j.fuel.2014.07.028.
181. Ranzi, E.; Frassoldati, A.; Stagni, A.; Pelucchi, M.; Cuoci, A.; Faravelli, T. Reduced Kinetic Schemes of Complex Reaction Systems: Fossil and Biomass-Derived Transportation Fuels. *Int J Chem Kinet* **2014**, *46*, 512–542, doi:10.1002/kin.20867.
182. Otomo, J.; Koshi, M.; Mitsumori, T.; Iwasaki, H.; Yamada, K. Chemical Kinetic Modeling of Ammonia Oxidation with Improved Reaction Mechanism for Ammonia/Air and Ammonia/Hydrogen/Air Combustion. *Int J Hydrogen Energy* **2018**, *43*, 3004–3014, doi:10.1016/j.ijhydene.2017.12.066.
183. Brulatout, J.; Garnier, F.; Mounaïm-Rousselle, C.; Seers, P. Calibration Strategy of Diesel-Fuel Spray Atomization Models Using a Design of Experiment Method. *International Journal of Engine Research* **2016**, *17*, 713–731, doi:10.1177/1468087415611030.
184. Amendments to the Annex of the Protocol of 1997 to Amend the International Convention for the Prevention of Pollution from Ships, 1973- 176(58), as Modified by the Protocol of 1978 Relating Thereto (Revised MARPOL Annex VI). **2011**.
185. Shi, C.; Cheng, T.; Yang, X.; Zhang, Z.; Duan, R.; Li, X. Implementation of Various Injection Rate Shapes in an Ammonia/Diesel Dual-Fuel Engine with Special Emphasis on Combustion and Emissions Characteristics. *Energy* **2024**, *304*, 132035, doi:10.1016/j.energy.2024.132035.
186. Huang, L.; Zheng, L.; Zhang, R.; Wang, W.; Pan, J.; Feng, M. Experimental Study on Combustion and Emissions of an Ammonia/Diesel Dual-Fuel Engine Using Split-Injection Strategy. *Fuel* **2024**, *378*, 132869, doi:10.1016/j.fuel.2024.132869.
187. Cameretti, M.C.; De Robbio, R.; Tuccillo, R.; Perrone, D.; Castiglione, T. CFD Modelling and Experimental Validation of an Ethanol Spark-Ignition Heavy-Duty Engine. *Energies (Basel)* **2025**, *18*, 3349, doi:10.3390/en18133349.
188. De Robbio, R.; Cameretti, M.C.; Palomba, M.; Tuccillo, R. Computational Fluid-Dynamics Analysis of the Effect of Ethanol-Air Mixture Supply in a Heavy-Duty Engine. *SAE Technical Paper* **2025**, doi:10.4271/2025-24-0029.
189. Altosole, M.; Cameretti, M.C.; Campora, U.; De Robbio, R.; Palomba, M.; Scamardella, F. A Preliminary Numerical Study of a Medium Speed Marine Engine Fueled by Methanol. In

Proceedings of the 2024 International Symposium on Power Electronics, Electrical Drives, Automation and Motion (SPEEDAM); 2024.
190. Roy, S.; Mishra, R.; Askari, O.; Jarrahbashi, D. Reduced Ethanol Skeleton Mechanism for Multi-Dimensional Engine Simulation. *Journal of the Energy Institute* **2023**, *106*, 101147, doi:10.1016/j.joei.2022.11.007.
191. University of Galway Https://Www.Universityofgalway.Ie/Combustionchemistrycentre/Mechanismdownloads/.
192. Wu, Y.; Panigrahy, S.; Sahu, A.B.; Bariki, C.; Beeckmann, J.; Liang, J.; Mohamed, A.A.E.; Dong, S.; Tang, C.; Pitsch, H.; et al. Understanding the Antagonistic Effect of Methanol as a Component in Surrogate Fuel Models: A Case Study of Methanol/n-Heptane Mixtures. *Combust Flame* **2021**, *226*, 229–242, doi:10.1016/j.combustflame.2020.12.006.
193. Fagundez, J.L.S.; Sari, R.L.; Garcia, A.; Pereira, F.M.; Martins, M.E.S.; Salau, N.P.G. A Chemical Kinetics Based Investigation on Laminar Burning Velocity and Knock Occurrence in a Spark-Ignition Engine Fueled with Ethanol–Water Blends. *Fuel* **2020**, *280*, 118587, doi:10.1016/j.fuel.2020.118587.
194. Zhao, Z.; Yu, X.; Huang, Y.; Sang, T.; Guo, Z.; Du, Y.; Yu, L.; Li, D. Study on Combustion and Emissions of a Combined Injection Spark Ignition Engine with Natural Gas Direct Injection Plus Ethanol Port Injection under Lean-Burn Conditions. *ACS Omega* **2022**, *7*, 21901–21911, doi:10.1021/acsomega.2c02154.
195. Bui, V.G.; Tran, V.N.; Nguyen, V.D.; Nguyen, Q.T.; Huynh, T.T. Octane Number Stratified Mixture Preparation by Gasoline–Ethanol Dual Injection in SI Engines. *International Journal of Environmental Science and Technology* **2019**, *16*, 3021–3034, doi:10.1007/s13762-018-1942-1.
196. Rolls-Royce *Project Guide C2633L BERGEN Gas ENGINE*;
197. Pichler, C.; Nilsson, E.J.K. Reduced Kinetic Mechanism for Methanol Combustion in Spark-Ignition Engines. *Energy & Fuels* **2018**, *32*, 12805–12813, doi:10.1021/acs.energyfuels.8b02136.
198. Sforza, L.; Lucchini, T.; Gianetti, G.; D'Errico, G.; Onofrio, G.; Beatrice, C.; Tunestal, P. A 3D-CFD Methodology for Combustion Modeling in Active Prechamber SI Engines Operating with Natural Gas. *SAE Technical Paper 2022-01-0470* **2022**, doi:10.4271/2022-01-0470.
199. Shah, A.; Tunestal, P.; Johansson, B. Effect of Relative Mixture Strength on Performance of Divided Chamber 'Avalanche Activated Combustion' Ignition Technique in a Heavy Duty Natural Gas Engine.; April 1 2014.
200. Shah, A.; Tunestal, P.; Johansson, B. Effect of Pre-Chamber Volume and Nozzle Diameter on Pre-Chamber Ignition in Heavy Duty Natural Gas Engines.; April 14 2015.
201. *Pounder's Marine Diesel Engines and Gas Turbines*; Elsevier, 2021; ISBN 9780081027486.
202. Palomba, M.; Cameretti, M.C.; Pio Di Noia, L. Numerical Analysis of a PEM Fuel Cell Fed by a Steam Reformer Integrated into an Internal Combustion Engine. In Proceedings of the 2025 International Conference on Clean Electrical Power (ICCEP); IEEE, June 24 2025; pp. 836–841.
203. Genovese, M.; Schlüter, A.; Scionti, E.; Piraino, F.; Corigliano, O.; Fragiacomo, P. Power-to-Hydrogen and Hydrogen-to-X Energy Systems for the Industry of the Future in Europe. *Int J Hydrogen Energy* **2023**, *48*, 16545–16568, doi:10.1016/j.ijhydene.2023.01.194.
204. Fan, L.; Tu, Z.; Chan, S.H. Recent Development of Hydrogen and Fuel Cell Technologies: A Review. *Energy Reports* **2021**, *7*, 8421–8446, doi:10.1016/j.egyr.2021.08.003.
205. Sazali, N.; Wan Salleh, W.N.; Jamaludin, A.S.; Mhd Razali, M.N. New Perspectives on Fuel Cell Technology: A Brief Review. *Membranes (Basel)* **2020**, *10*, 99, doi:10.3390/membranes10050099.
206. Ighalo, J.O.; Amama, P.B. Recent Advances in the Catalysis of Steam Reforming of Methane (SRM). *Int J Hydrogen Energy* **2024**, *51*, 688–700, doi:10.1016/j.ijhydene.2023.10.177.

207. Szablowski, L.; Wojcik, M.; Dybinski, O. Review of Steam Methane Reforming as a Method of Hydrogen Production. *Energy* **2025**, *316*, 134540, doi:10.1016/j.energy.2025.134540.
208. Lim, T.-W.; Hwang, D.-H.; Choi, Y.-S. Design and Optimization of a Steam Methane Reformer for Ship-Based Hydrogen Production on LNG-Fueled Ship. *Appl Therm Eng* **2024**, *243*, 122588, doi:10.1016/j.applthermaleng.2024.122588.
209. You, Y.-W.; Lee, D.-G.; Yoon, K.-Y.; Moon, D.-K.; Kim, S.M.; Lee, C.-H. H2 PSA Purifier for CO Removal from Hydrogen Mixtures. *Int J Hydrogen Energy* **2012**, *37*, 18175–18186, doi:10.1016/j.ijhydene.2012.09.044.
210. Nalbant, Y.; Colpan, C.O.; Devrim, Y. Energy and Exergy Performance Assessments of a High Temperature-Proton Exchange Membrane Fuel Cell Based Integrated Cogeneration System. *Int J Hydrogen Energy* **2020**, *45*, 3584–3594, doi:10.1016/j.ijhydene.2019.01.252.
211. Jannelli, E.; Minutillo, M.; Perna, A. Analyzing Microcogeneration Systems Based on LT-PEMFC and HT-PEMFC by Energy Balances. *Appl Energy* **2013**, *108*, 82–91, doi:10.1016/j.apenergy.2013.02.067.
212. Arsalis, A.; Nielsen, M.P.; Kær, S.K. Modeling and Optimization of a 1 KWe HT-PEMFC-Based Micro-CHP Residential System. *Int J Hydrogen Energy* **2012**, *37*, 2470–2481, doi:10.1016/j.ijhydene.2011.10.081.
213. Sapra, H.; Stam, J.; Reurings, J.; van Biert, L.; van Sluijs, W.; de Vos, P.; Visser, K.; Vellayani, A.P.; Hopman, H. Integration of Solid Oxide Fuel Cell and Internal Combustion Engine for Maritime Applications. *Appl Energy* **2021**, *281*, 115854, doi:10.1016/j.apenergy.2020.115854.
214. Cho, M.; Kim, Y.; Ho Song, H. Solid Oxide Fuel Cell–Internal Combustion Engine Hybrid System Utilizing an Internal Combustion Engine for Anode off-Gas Recirculation, External Reforming, and Additional Power Generation. *Appl Energy* **2022**, *328*, 120146, doi:10.1016/j.apenergy.2022.120146.
215. Choi, W.; Kim, J.; Kim, Y.; Song, H.H. Solid Oxide Fuel Cell Operation in a Solid Oxide Fuel Cell–Internal Combustion Engine Hybrid System and the Design Point Performance of the Hybrid System. *Appl Energy* **2019**, *254*, 113681, doi:10.1016/j.apenergy.2019.113681.
216. Leng, S.; Xu, S.; Li, C.; Ha, C.; Liu, Z.; Qin, J.; Wang, Z.; Wang, J.; Chen, Z.; Liao, M. Performance Analysis of an Internal Combustion Engine with Thermochemical Recovery and High Temperature Proton Exchange Membrane Fuel Cell Combined Power Generation System. *Fuel* **2025**, *384*, 133913, doi:10.1016/j.fuel.2024.133913.
217. Chen, Y.; Lu, J.; Liu, Z.; Liu, Y.; Huang, T.; Ren, X.; Wang, X.; Wan, Z. Comprehensive Evaluation on a Heat Self-Balanced Low-Temperature Ammonia Reforming-Based High-Power Hybrid Power Generation System Combined with Proton Exchange Membrane Fuel Cell and Internal Combustion Engine. *J Clean Prod* **2025**, *491*, 144755, doi:10.1016/j.jclepro.2025.144755.
218. Elkafas, A.G.; Rivarolo, M.; Gadducci, E.; Magistri, L.; Massardo, A.F. Fuel Cell Systems for Maritime: A Review of Research Development, Commercial Products, Applications, and Perspectives. *Processes* **2022**, *11*, 97, doi:10.3390/pr11010097.
219. Li, H.; Sun, C.; Li, J.; Mei, J.; Jiang, J.; Fan, F.; Yang, W.; Zhuo, R.; Song, K. Self-Tuning Oxygen Excess Ratio Control for Proton Exchange Membrane Fuel Cells Under Dynamic Conditions. *Processes* **2024**, *12*, 2807, doi:10.3390/pr12122807.
220. Molicel INR-18650-P30B Datasheet Https://Www.Molicel.Com/Inr-18650-P30b/.
221. Thermoflow Inc.. Available Online: Http://Www.Thermoflow.Com.
222. Njoya, S.M.; Tremblay, O.; Dessaint, L.-A. A Generic Fuel Cell Model for the Simulation of Fuel Cell Vehicles. In Proceedings of the 2009 IEEE Vehicle Power and Propulsion Conference; IEEE, September 2009; pp. 1722–1729.
223. International Maritime Organization *RESOLUTION MEPC.308(73) (Adopted on 26 October 2018)*;

224. Xie, P.; Araya, S.S.; Guerrero, J.M.; Vasquez, J.C. Dynamic Modeling and Control of High Temperature PEM Fuel Cell and Battery System for Electrical Applications. In Proceedings of the IECON 2023- 49th Annual Conference of the IEEE Industrial Electronics Society; IEEE, October 16 2023; pp. 1–6.
225. Rosli, R.E.; Sulong, A.B.; Daud, W.R.W.; Zulkifley, M.A.; Husaini, T.; Rosli, M.I.; Majlan, E.H.; Haque, M.A. A Review of High-Temperature Proton Exchange Membrane Fuel Cell (HT-PEMFC) System. *Int J Hydrogen Energy* **2017**, *42*, 9293–9314, doi:10.1016/j.ijhydene.2016.06.211.
226. Orji, U.; Sievenpiper, B.; Gerhard, K.; Leeb, S.B.; Doerry, N.; Kirtley, J.L.; McCoy, T. Load Modeling For Power System Requirement and Capability Assessment. *IEEE Transactions on Power Systems* **2015**, *30*, 1415–1423, doi:10.1109/TPWRS.2014.2348531.
227. Hu, X.; Murgovski, N.; Johannesson, L.; Egardt, B. Energy Efficiency Analysis of a Series Plug-in Hybrid Electric Bus with Different Energy Management Strategies and Battery Sizes. *Appl Energy* **2013**, *111*, 1001–1009, doi:10.1016/j.apenergy.2013.06.056.
228. Dicks, A.L.; Rand, D.A.J. *Fuel Cell Systems Explained*; Wiley, 2018; ISBN 9781118613528.